

1

CAMPINAS STATE UNIVERSITY

2

DOCTORAL THESIS

3

---

4

# Search for Z and Higgs boson decaying into $\Upsilon + \gamma$ in pp collisions at CMS/LHC

5

---

6

*Author:*

Felipe Torres da Silva de Araujo

*Supervisor:*

Dr. José Augusto Chinellato

*Co-Supervisor:*

Dr. Alberto Franco de Sá Santoro

7

*A thesis submitted in fulfillment of the requirements  
for the degree of Doctor of Physics*

8

*in the*

9

Graduate Program of  
"Gleb Wataghin" Institute of Physics

10

11

12

13

February 19, 2021

<sup>14</sup> “Sometimes science is a lot more art than science. A lot of people don’t get that.”

<sup>15</sup>

Rick Sanchez

<sup>16</sup> “Então, que seja doce. Repito todas as manhãs, ao abrir as janelas para deixar entrar o sol ou o  
<sup>17</sup> cinza dos dias, bem assim, que seja doce. Quando há sol, e esse sol bate na minha cara amassada do  
<sup>18</sup> sono ou da insônia, contemplando as partículas de poeira soltas no ar, feito um pequeno universo;  
<sup>19</sup> repito sete vezes para dar sorte: que seja doce que seja doce que seja doce e assim por diante. Mas,  
<sup>20</sup> se alguém me perguntasse o que deverá ser doce, talvez não saiba responder. Tudo é tão vago como  
<sup>21</sup> se fosse nada.”

<sup>22</sup>

Caio Fernando Abreu

23

CAMPINAS STATE UNIVERSITY

24

*Abstract*

25

*"Gleb Wataghin"* Institute of Physics

26

Doctor of Physics

27

**Search for Z and Higgs boson decaying into  $\Upsilon + \gamma$  in pp collisions at CMS/LHC**

28

by Felipe Torres da Silva de Araujo

29 This thesis presents the study on searches for rare decays of Standard Model bosons to quarkonia.  
30 The searches are performed on data collected during the 2016 data taking of the CMS detector, at  
31 center-of-mass energy  $\sqrt{s} = 13$  TeV. Standard Model Higgs and Z bosons decaying to a  $\Upsilon(1S, 2S, 3S)$   
32 and a photon, with subsequent decay of the  $\Upsilon(1S, 2S, 3S)$  to  $\mu^+ \mu^-$  are performed using integrated  
33 luminosity of  $35.86 \text{ fb}^{-1}$  from proton-proton collisions. No significant excess above the background-  
34 only assumption is observed. A limit at 95% confidence level, is set on the  $Z \rightarrow \Upsilon(1S, 2S, 3S) + \gamma$   
35 decay branching fraction at  $2.9, 2.7, 1.4 \times 10^{-6}$  and on  $H \rightarrow \Upsilon(1S, 2S, 3S) + \gamma$  decay branching  
36 fraction at  $6.9, 7.4, 5.8 \times 10^{-4}$ , using the  $CL_s$  method. Contributions given from 2016 to 2018 to  
37 the operation, maintenance and R&D for Phase-2 Upgrade of Resistive Plate Chambers (RPC) at  
38 CMS are also presented. This includes shift for the system operation, data certification for quality  
39 control, upgrade and maintenance of the online software and detector maintenance during the LHC  
40 Long Shutdown 2 (LS2.)

DRAFT

## 41 *Acknowledgements*

42 I would like to thank:

- 43 • the Campinas State University for providing the institutional support for this study;
- 44 • the Rio de Janeiro State University for the cooperation with Campinas State University in  
45 their high-energy physics program. This was a key factor for this study;
- 46 • the HEPGRID - High Energy Physics GRID (CMS computing cluster of Rio de Janeiro State  
47 University) for providing the computing resources;
- 48 • the National Council for Scientific and Technological Development (CNPq) for the financial  
49 support for this work;
- 50 • the European Laboratory for Particle Physics (CERN) for the construction and operation of  
51 the Large Hadron Collider (LHC);
- 52 • the Compact Muon Solenoid (CMS) collaboration for the construction, operation and provi-  
53 sion of the instrumental means for this study.

DRAFT

# 54 Contents

55	<b>Abstract</b>	iii
56	<b>Acknowledgements</b>	v
57	<b>1 Introduction</b>	1
58	<b>2 Standard Model and rare Z and Higgs decays to quarkonia</b>	5
59	2.1 Standard Model and Local Gauge Invariance . . . . .	5
60	2.1.1 Local Gauge Invariance . . . . .	6
61	2.1.2 The Standard Model . . . . .	8
62	Quantum Chromodinamics . . . . .	9
63	Electroweak Theory . . . . .	10
64	Standard Model Lagrangian and the Higgs Sector . . . . .	11
65	2.2 SM and Higgs results . . . . .	14
66	2.2.1 Standard Model vector bosons at CMS . . . . .	14
67	2.2.2 Higgs boson at CMS . . . . .	17
68	2.3 Rare Z and Higgs decays to quarkonia . . . . .	21
69	2.4 Recent results . . . . .	24
70	<b>3 Experimental Setup</b>	27
71	3.1 The Large Hadron Collider . . . . .	27
72	3.2 The Compact Muon Solenoid - CMS . . . . .	29
73	3.2.1 Coordinate system . . . . .	30
74	3.3 Tracker . . . . .	32
75	3.4 Electromagnetic Calorimeter . . . . .	33
76	3.5 Hadronic Calorimeter . . . . .	34
77	3.6 Muon System . . . . .	34
78	3.6.1 Drift Tubes . . . . .	35
79	3.6.2 CSC . . . . .	36
80	3.6.3 RPC . . . . .	36
81	3.7 Trigger and Data Acquisition . . . . .	37
82	3.8 Particle Flow Algorithim . . . . .	37
83	<b>4 CMS Resistive Plate Chambers - RPC</b>	41
84	4.1 Resistive Plate Chambers . . . . .	41
85	4.1.1 Principles and operation modes . . . . .	42

86	4.2 CMS Resistive Plate Chambers . . . . .	44
87	4.2.1 Performance . . . . .	46
88	4.3 Contribution to the CMS RPC project . . . . .	49
89	4.3.1 RPC Operation - Shifts and Data Certification . . . . .	49
90	4.4 RPC Online Software . . . . .	50
91	4.4.1 Improved RPC R&D . . . . .	52
92	4.4.2 LS2 and the RPC Standard Maintenance . . . . .	58
93	HV maintenance . . . . .	58
94	LV and control maintenance . . . . .	59
95	Detector commissioning . . . . .	60
96	<b>5 Physics Analysis</b>	<b>63</b>
97	5.1 Datasets and simulated events . . . . .	64
98	5.1.1 Data samples . . . . .	64
99	5.1.2 Simulated datasets . . . . .	64
100	5.2 Contribution of the $\Upsilon(nS)$ polarisation . . . . .	67
101	5.3 Kinematical studies using MC generator . . . . .	68
102	5.4 Event selection . . . . .	71
103	5.5 Trigger and physics object selection (Group I) . . . . .	71
104	5.5.1 Trigger . . . . .	71
105	5.5.2 Muon Identification . . . . .	72
106	5.5.3 Photon Identification . . . . .	73
107	5.5.4 Kinematical distributions . . . . .	73
108	5.6 Kinematical selection (Group II) . . . . .	84
109	5.7 Event categorization and yields . . . . .	92
110	5.7.1 R9 reweighting . . . . .	92
111	5.7.2 Event counting and yields . . . . .	93
112	5.8 Background modeling . . . . .	94
113	5.9 Signal modeling . . . . .	102
114	5.10 Systematic uncertainties . . . . .	108
115	5.10.1 Uncertainties on the predicted yields . . . . .	108
116	5.10.2 Uncertainties that affect the signal fits . . . . .	109
117	5.11 Modeling Cross checks . . . . .	112
118	5.12 Results and conclusion . . . . .	118
119	5.12.1 The $CL_s$ formalism for upper limits setting at CMS . . . . .	118
120	5.12.2 Branching fraction upper limits . . . . .	121
121	<b>6 Conclusion and perspectives</b>	<b>123</b>
122	<b>Bibliography</b>	<b>125</b>

# <sup>123</sup> List of Figures

<sup>124</sup> 1.1	Dimuon mass distribution collected with various dimuon triggers. The light gray continuous distribution represents events collected with inclusive dimuon triggers with high $p_T$ thresholds. The dataset corresponding to an integrated luminosity of $13.1 \text{ fb}^{-1}$ was collected during the 25 ns LHC running period at 13 TeV in 2016. Source: [6]. . . . .	2
<sup>129</sup> 2.1	Elementary particles of the Standard Model, with their masses charges and spin. Those particles can be divided in two classes: boson (the interaction/force carriers) and the fermions, which are divided in three generations. Source: [11]. . . . .	6
<sup>132</sup> 2.2	(a) Di-boson cross section ratio comparison to theory: Theory predictions updated to latest NNLO calculations where available compared to predictions in the CMS papers and preliminary physics analysis summaries. Source: [25]. (b) Summary of the cross sections of pure Electroweak (EWK) interactions among the gauge bosons presented as a ratio compared to theory. Source: [25]. . . . .	15
<sup>137</sup> 2.3	Summary of the cross section measurements of Standard Model processes at CMS. Source: [25]. . . . .	16
<sup>139</sup> 2.4	(a) Standard Model Higgs boson production cross sections at $\sqrt{s} = 13 \text{ TeV}$ as a function of Higgs boson mass. The tH production cross section accounts for $t$ -channel and $s$ -channel only (no $tWH$ production). The VBF process is indicated here as $qqH$ . The theoretical uncertainties are indicated as shaded bands around the lines. Source: [27]. (b) Standard Model Higgs boson decay branching ratios for different decay channels. The theoretical uncertainties are indicated as shaded bands around the lines. Source: [27]. . . . .	18
<sup>146</sup> 2.5	Example of leading order Standard Model Higgs boson production model diagrams. Source: [28]. . . . .	18

148	2.6	(a) The diphoton invariant-mass distribution for the 7 and 8 TeV datasets (points), with each event weighted by the predicted $S/(S + B)$ ratio of its event class. The solid and dotted lines give the results of the signal-plus-background and background- only fit, respectively. The light and dark bands represent the $\pm 1$ and $\pm 2$ standard deviation uncertainties respectively on the background estimate. The inset shows the corresponding unweighted invariant-mass distribution around $m_{\gamma\gamma} = 125$ GeV. Source: [3]. (b) Distribution of the observed four-lepton invariant mass from the combined 7 and 8 TeV data for the $H \rightarrow ZZ \rightarrow 4\ell$ analysis (points). The prediction for the expected $Z+X$ and $ZZ(Z\gamma^*)$ background are shown by the dark and light histogram, respectively. The open histogram gives the expected distribution for a Higgs boson of mass 125 GeV. Source: [3]. . . . .	19
159	2.7	Signal strength modifiers for the production modes, (a) $\mu^i$ , and for the decay channels, (b) $\mu^f$ . The thick (thin) black lines report the $1\sigma$ ( $2\sigma$ ) confidence intervals. The thick blue and red lines report the statistical and systematic components of the $1\sigma$ confidence intervals. Source: [39]. . . . .	20
163	2.8	A summary of the measured Higgs boson mass in the $H \rightarrow ZZ \rightarrow 4l$ and $H \rightarrow \gamma\gamma$ decay channels, and for the combination of the two is presented here. The statistical (wider, yellow-shaded bands), and total (black error bars) uncertainties are indicated. The (red) vertical line and corresponding (grey) shaded column indicate the central value and the total uncertainty of the Run 1 + 2016 combined measurement, respectively. Source: [35]. . . . .	21
169	2.9	(a) The $m_{\mu\mu}$ distribution for the weighted combination of all event categories used in the analysis. The upper panel is dominated by the gluon-gluon fusion categories with many data events but relatively small $S/(S + B)$ . The lower panel shows the residuals after background subtraction, with the best-fit SM $H \rightarrow \mu\mu$ signal con- tribution with $m_H = 125.38$ GeV indicated by the red line. The measured signal strength is $1.19^{+0.41}_{-0.39}(\text{stat})^{+0.17}_{-0.16}(\text{sys})$ . Source: [30]. (b) The best-fit estimates for the reduced coupling modifiers extracted for fermions and weak bosons from the resolved $\kappa$ -framework model compared to their corresponding prediction from the SM. The error bars represent 68% CL intervals for the measured parameters. The lower panel shows the ratios of the measured coupling modifiers values to their SM predictions. Source: [30]. . . . .	22
180	2.10	Example of leading order diagrams for the indirect and direct production mechanisms. In these diagrams, the $h$ can also be understood as a $Z$ or a Higgs boson. . . . .	24
182	2.11	Expected relative variation of the branching ratio for the $H \rightarrow \Upsilon(nS) + \gamma$ to $k_b$ , where $k_b = g(Hb\bar{b})/g(Hb\bar{b})_{SM}$ is the ratio for the observed and expected Yukawa coupling of $Hb\bar{b}$ . Source: [43] . . . . .	25
185	3.1	The LHC is the last ring (dark grey line) in a complex chain of particle accelerators. The smaller machines are used in a chain to help boost the particles to their final energies and provide beams to a whole set of smaller experiments. Source: [67]. . . . .	28
188	3.2	Overview of the CMS experiment and its subdetectors. Source: [72]. . . . .	30

189	3.3	Summary of the CMS coordinate system, with respect to the LHC. Source: [cms_coordinate_system]	
190	3.4	Schematic cross section through the CMS tracker. Each line represents a detector module. Double lines indicate back-to-back modules which deliver stereo hits. Source: [1]. . . . .	32
193	3.5	Longitudinal section view of the ECAL and its components. Source: [1]. . . . .	33
194	3.6	Longitudinal section view of the HCAL and its components. The barrel calorimeter (HB) covers the central region, inside the solenoid, the outer calorimeter covers also the central region, but it is positioned on the outside the solenoid. The endcap calorimeter (HE) covers the forward region and it is complemented by the forward calorimeter (HF), which uses Cherenkov light detectors made of radiation-hard quartz fibers. Source: [1]. . . . .	35
200	3.7	Longitudinal section view of the ECAL and its components. Source: [80]. . . . .	36
201	3.8	The figure illustrates how the information from each subdetector is used in order to identify the different high-level objects in the Particle-Flow algorithm. Source: [84]. . .	38
203	4.1	The Avalanche production process inside a RPC gap. (Top) The initial process and the secondary electron/ion generation. (Bottom) The overall charge distribution of an Avalanche between the electrodes. Source: [94]. . . . .	42
206	4.2	Streamer formation process. The distorted electric field around the high positive charge concentration enhances the ionization process, initiating secondary avalanches. Source: [94]. . . . .	44
209	4.3	RPC chamber installed on station RE+4 of CMS Endcap. Source: [96]. . . . .	45
210	4.4	R- $\phi$ (left) and R-Z (right) projections of the barrel Muon System. . . . .	46
211	4.5	R-Z projections of the endcap Muon System (positive Z side). This is the same configuration for the 36 $\phi$ sectors. . . . .	47
213	4.6	RPC efficiencies (per chamber) over Run2 Integrated Luminosity for Barrel (left) and Endcap (right). Red lines indicates technical stops (TS) while grey ones indicates Year-End-Technical stops (YETS). The drop in the efficiency around $110 \text{ pb}^{-1}$ is related to a known operation mistake. Source: [107]. . . . .	47
217	4.7	RPC cluster size (CLS - per chamber) over Run2 Integrated Luminosity for Barrel (left) and Endcap (right). Red lines indicates technical stops (TS) while grey ones indicates Year-End-Technical stops (YETS). The drop in the cluster size around $110 \text{ pb}^{-1}$ is related to a known operation mistake. Source: [107]. . . . .	48
221	4.8	Ohmic current history of W+0, RE+1, RE+4 and RE-4. The blank regions, from time to time, corresponds to technical stops (TS), when the detector is off. Source: [107].	49
223	4.9	(a) Luminosity delivered by the LHC, recorded one by CMS and the certified (validated), from the 22nd of April, 2016 to the 27th of October, 2016. (b) Efficiency of the certification process for each subsystem, from the 22nd of April, 2016 to the 27th of October, 2016. Total CMS efficiency is above 90%. Source: [108] . . . . .	50
227	4.10	Upgrade of the RPC online software. . . . .	51
228	4.11	Example of the updated screens, using Trigger Supervisor 5. . . . .	51

229	4.12 $\eta$ projection of the Muon System subdetectors. In purple, is labeled the iRPCS to 230 be installed during the CMS upgrade. . . . .	52
231	4.13 FEB configured 8 channels modes. Group should be understood as wire pad. Left: 232 Logical diagram for OR2. Right: Logical diagram for AND2. . . . .	54
233	4.14 FEB configured 2 channels modes. Left: Logical diagram for OR8. Group should be 234 understood as wire pad. Right: Logical diagram for OR4AND2. . . . .	54
235	4.15 Left: Setup mounted for commissioning. Two MWPC chamber on the top (chambers 236 A and B) and two (chambers C and D) on the bottom with a RPC R&D in the 237 middle. Right: Rack with all the services for the operation of these chambers. . . . .	55
238	4.16 Coincidence rate of two chambers with respect to an arbitrary distance between 239 the two top planes. Measured in 10 minutes, for 2 logical combinations (OR8 and 240 OR4AND2). Applied high voltage: 2.65 kV. Threshold: 7 pC. Active area: readout 241 of 160 mm x 160 mm per chamber. . . . .	56
242	4.17 Individual rates (chambers A, B, C and D) and coincidence rates for two chambers 243 (A AND B, C AND D), for without $\gamma$ source (blue), a shielded $\gamma$ source (orange) and 244 an unshielded $\gamma$ source (green). Source sitting on top of chamber A. Applied high 245 voltage: 2.65 kV. Threshold: 7 pC. Active area: readout of 160 mm x 320 mm per 246 chamber. Logical combination: AND2 . . . . .	57
247	4.18 Left: Proposed adapter the chamber patch panel which make it possible to replace 248 a tripolar by a jupiter HV connector. Right: Try out of the proposed HV connector 249 replacement. . . . .	59
250	4.19 RPC Front-end board (FEB) used in the barrel chambers. . . . .	60
251	4.20 RPC FEB Commissioning Analyzer. . . . .	61
252	5.1 A diagram for the reconstructed invariant mass of the $\mu\mu\gamma$ final state. The blue and 253 gray regions represent the Full Combinatorial and $\Upsilon + \gamma$ Combinatorial contributions, 254 respectively, while the yellow and red regions represent the Resonant background and 255 the signal region. . . . .	64
256	5.2 Distributions of $\cos\theta$ of $\Upsilon \rightarrow \mu\mu$ and $\gamma^* \rightarrow \mu\mu$ . The orange distribution is the 257 $Z \rightarrow \Upsilon(1S, 2S, 3S) + \gamma$ sample before reweighting (Unpolarized); the blue and gray 258 distributions are $Z \rightarrow \Upsilon(1S, 2S, 3S)$ sample after reweighting, for the Transverse and 259 Longitudinal Polarization. . . . .	68
260	5.3 Generator level distributions of main variables for $Z \rightarrow \Upsilon(1S, 2S, 3S) + \gamma$ : Transverse 261 momenta of the leading/trailing $p_T$ muon and the photon, pseudorapidity ( $\eta$ ) and $\phi$ 262 of the muons and the photon, distances $\Delta R$ between the two muons and between the 263 muons and the photon. All the distributions shown in the figure are normalized to 264 the unity of area. . . . .	69
265	5.4 Generator level distributions of main variables for $H \rightarrow \Upsilon(1S, 2S, 3S) + \gamma$ : Transverse 266 momenta of the leading/trailing $p_T$ muon and the photon, pseudorapidity ( $\eta$ ) and 267 $\phi$ of the muons and the photon, distances $\Delta R$ between the two muons and between the 268 muons and the photon. All the distributions shown in the figure are normalized 269 to the unity of area. . . . .	70

270	5.5 The $p_T$ muon distributions from data and signal events for Z decaying into $\Upsilon(1S, 2S, 3S) + \gamma$ after Group I of selection cuts, where on left are presenting the trailing muons and on right are the leading muons. The plots are normalized to the unit of area. The black dots are data collect by CMS while the blue distribution is related only to the signal Monte-Carlo generated samples. . . . .	74
275	5.6 The $\eta$ muon distributions from data and signal events of Z decaying into $\Upsilon(1S, 2S, 3S) + \gamma$ after Group I of selection cuts, where on left are presenting the trailing muons and on right are the leading muons. The plots are normalized to the unit of area. The black dots are data collect by CMS while the blue distribution is related only to the signal Monte-Carlo generated samples. . . . .	75
280	5.7 The $\phi$ muon distributions from data and signal events of Z decaying into $\Upsilon(1S, 2S, 3S) + \gamma$ after Group I of selection cuts, where on left are presenting the trailing muons and on right are the leading muons. The plots are normalized to the unit of area. The black dots are data collect by CMS while the blue distribution is related only to the signal Monte-Carlo generated samples. . . . .	75
285	5.8 The $p_T$ photon distributions from data and signal events for Z decaying into $\Upsilon(1S, 2S, 3S) + \gamma$ Group I of selection cuts. The plots normalized to the unit of area. . . . .	75
287	5.9 The $\eta$ photon distributions from data and signal events of Z decaying into $\Upsilon(1S, 2S, 3S) + \gamma$ after Group I of selection cuts. The plot is normalized to the unit of area. . . . .	76
289	5.10 The $\phi$ photon distributions from data and signal events of Z decaying into $\Upsilon(1S, 2S, 3S) + \gamma$ after Group I of selection cuts. The plot is normalized to the unit of area. . . . .	76
291	5.11 The $p_T$ distributions for the reconstructed $\Upsilon(1S, 2S, 3S)$ in the left and for Z in the right from data and signal events for Z decaying into $\Upsilon(1S, 2S, 3S) + \gamma$ after Group I of selection cuts. The plots are normalized to the unit of area. The black dots are data collect by CMS while the blue distribution is related only to the signal Monte-Carlo generated samples. . . . .	76
296	5.12 The $\eta$ distributions for $\Upsilon(1S, 2S, 3S)$ in the left and for Z in the right from data and signal events for Z decaying into $\Upsilon(1S, 2S, 3S) + \gamma$ after Group I of selection cuts. The plots are normalized to the unit of area. The black dots are data collect by CMS while the blue distribution is related only to the signal Monte-Carlo generated samples. . . . .	77
300	5.13 The $\phi$ distributions for $\Upsilon(1S, 2S, 3S)$ in the left and for Z in the right from data and signal events for Z decaying into $\Upsilon(1S, 2S, 3S) + \gamma$ after Group I of selection cuts. The plots are normalized to the unit of area. The black dots are data collect by CMS while the blue distribution is related only to the signal Monte-Carlo generated samples. . . . .	77
304	5.14 The $\Delta R$ distributions between the photon and the leading muon (left) and the trailing muon (right) for for Z decaying into $\Upsilon(1S, 2S, 3S) + \gamma$ from data and signal events after Group I of selection cuts. The plots are normalized to the unit of area. The black dots are data collect by CMS while the blue distribution is related only to the signal Monte-Carlo generated samples. . . . .	77

309	5.15 Left: The $\Delta R$ distributions between reconstructed dimuon ( $\mu\mu$ ) system and the 310 photon. Right: absolute value of the $\Delta\phi$ between the dimuon system and the photon 311 for Z decaying into $\Upsilon(1S, 2S, 3S) + \gamma$ from data and signal events after Group I of 312 selection cuts. The plots are normalized to the unit of area. The black dots are data 313 collect by CMS while the blue distribution is related only to the signal Monte-Carlo 314 generated samples. . . . .	78
315	5.16 The ratio for the transverse momentum of the reconstructed Upsilon and the re- 316 constructed Z mass ( $p_T^{\mu\mu}/M_{\mu\mu\gamma}$ - left) and the ratio for the transverse energy of the 317 reconstructed Photon and the reconstructed Z mass ( $E_T^\gamma/M_{\mu\mu\gamma}$ - right) distribution 318 for Z decaying into $\Upsilon(1S, 2S, 3S) + \gamma$ from data and signal events after Group I of 319 selection cuts. The plots are normalized to the unit of area. The black dots are data 320 collect by CMS while the blue distribution is related only to the signal Monte-Carlo 321 generated samples. . . . .	78
322	5.17 The dimuon mass distribution of the reconstructed $\Upsilon(1S, 2S, 3S)$ from data and signal 323 events for Z decaying after Group I of selection cuts. The plot is normalized to the 324 number of events. "Signal" stands for the $Z \rightarrow \Upsilon(1S, 2S, 3S) + \gamma$ sample (scaled 325 by a factor of $\times 100$ ) and "Background" corresponds to the resonant background 326 ( $Z \rightarrow \mu\mu\gamma_{FSR}$ ) sample (scaled by a factor of x3). . . . .	78
327	5.18 The $p_T$ muon distributions from data and signal events for Higgs decaying into 328 $\Upsilon(1S, 2S, 3S) + \gamma$ after Group I of selection cuts, where on left are presenting the 329 trailing muons and on right are the leading muons. The plots are normalized to the 330 unit of area. The black dots are data collect by CMS while the blue distribution is 331 related only to the signal Monte-Carlo generated samples. . . . .	79
332	5.19 The $\eta$ muon distributions from data and signal events of Higgs decaying into $\Upsilon(1S, 2S, 3S)$ 333 $+ \gamma$ after Group I of selection cuts, where on left are presenting the trailing muons 334 and on right are the leading muons. The plots are normalized to the unit of area. 335 The black dots are data collect by CMS while the blue distribution is related only to 336 the signal Monte-Carlo generated samples. . . . .	79
337	5.20 The $\phi$ muon distributions from data and signal events of Higgs decaying into $\Upsilon(1S, 2S, 3S)$ 338 $+ \gamma$ after Group I of selection cuts, where on left are presenting the trailing muons 339 and on right are the leading muons. The plots are normalized to the unit of area. 340 The black dots are data collect by CMS while the blue distribution is related only to 341 the signal Monte-Carlo generated samples. . . . .	79
342	5.21 The $p_T$ photon distributions from data and signal events for Higgs decaying into 343 $\Upsilon(1S, 2S, 3S) + \gamma$ Group I of selection cuts. The plot is normalized to the unit of area.	80
344	5.22 The $\eta$ photon distributions from data and signal events of Higgs decaying into 345 $\Upsilon(1S, 2S, 3S) + \gamma$ after Group I of selection cuts. The plot is normalized to the 346 unit of area. . . . .	80
347	5.23 The $\phi$ photon distributions from data and signal events of Higgs decaying into 348 $\Upsilon(1S, 2S, 3S) + \gamma$ after Group I of selection cuts. The plot is normalized to the 349 unit of area. . . . .	80

350	5.24 The $p_T$ distributions for $\Upsilon(1S, 2S, 3S)$ in the left and for Higgs in the right from data 351 and signal events for Higgs decaying into $\Upsilon(1S, 2S, 3S) + \gamma$ after Group I of selection 352 cuts. The plots are normalized to the unit of area. The black dots are data collect by 353 CMS while the blue distribution is related only to the signal Monte-Carlo generated 354 samples. . . . .	81
355	5.25 The $\eta$ distributions for $\Upsilon(1S, 2S, 3S)$ in the left and for Higgs in the right from data 356 and signal events for Higgs decaying into $\Upsilon(1S, 2S, 3S) + \gamma$ after Group I of selection 357 cuts. The plots are normalized to the unit of area. The black dots are data collect by 358 CMS while the blue distribution is related only to the signal Monte-Carlo generated 359 samples. . . . .	81
360	5.26 The $\phi$ distributions for $\Upsilon(1S, 2S, 3S)$ in the left and for Higgs in the right from data 361 and signal events for Higgs decaying into $\Upsilon(1S, 2S, 3S) + \gamma$ after Group I of selection 362 cuts. The plots are normalized to the unit of area. The black dots are data collect by 363 CMS while the blue distribution is related only to the signal Monte-Carlo generated 364 samples. . . . .	81
365	5.27 The $\Delta R$ distributions between the photon and the leading muon (left) and the trailing 366 muon (right) for Higgs decaying into $\Upsilon(1S, 2S, 3S) + \gamma$ from data and signal events 367 after Group I of selection cuts. The plots are normalized to the unit of area. The 368 black dots are data collect by CMS while the blue distribution is related only to the 369 signal Monte-Carlo generated samples. . . . .	82
370	5.28 Left: The $\Delta R$ distributions between reconstructed dimuon ( $\mu\mu$ ) system and the 371 photon. Right: absolute value of the $\Delta\phi$ between the dimuon system and the photon 372 for for Higgs decaying into $\Upsilon(1S, 2S, 3S) + \gamma$ from data and signal events after Group 373 I of selection cuts. The plots are normalized to the unit of area. The black dots are 374 data collect by CMS while the blue distribution is related only to the signal Monte- 375 Carlo generated samples. . . . .	82
376	5.29 The ratio for the transverse momentum of the reconstructed Upsilon and the recon- 377 structed Higgs mass ( $p_T^{\mu\mu}/M_{\mu\mu\gamma}$ - left) and the ratio for the transverse energy of the 378 reconstructed Photon and the reconstructed Higgs mass ( $E_T^\gamma/M_{\mu\mu\gamma}$ - right) distri- 379 bution for Higgs decaying into $\Upsilon(1S, 2S, 3S) + \gamma$ from data and signal events after 380 Group I of selection cuts. The plots are normalized to the unit of area. The black 381 dots are data collect by CMS while the blue distribution is related only to the signal 382 Monte-Carlo generated samples. . . . .	82
383	5.30 The dimuon mass distribution of the reconstructed $\Upsilon(1S, 2S, 3S)$ from data and signal 384 events for Higgs decaying after Group I of selection cuts. This plot is normalized 385 the expected number of events. "Signal" stands for the $H \rightarrow \Upsilon(1S, 2S, 3S) + \gamma$ 386 sample (scaled by a factor of $\times 600000$ ) and "Background" corresponds to the resonant 387 background (Higgs Dalitz Decay) sample (scaled by a factor of $\times 400$ ). . . . .	83

388	5.31 The $p_T$ muon distributions from data and signal events for Z decaying into $\Upsilon(1S, 2S, 3S)$	
389	+ $\gamma$ after Group I+II of selection cuts, where on left are presenting the trailing muons	
390	and on right are the leading muons. The plots are normalized to the number of events.	
391	Signal sample is scaled by a factor of $\times 100$ ). The black dots are data collect by CMS	
392	while the blue distribution is related only to the signal Monte-Carlo generated samples. . . . .	84
393	5.32 The $\eta$ muon distributions from data and signal events of Z decaying into $\Upsilon(1S, 2S, 3S)$	
394	+ $\gamma$ after Group I+II of selection cuts, where on left are presenting the trailing muons	
395	and on right are the leading muons. The plots are normalized to the number of events.	
396	Signal sample is scaled by a factor of $\times 100$ ). The black dots are data collect by CMS	
397	while the blue distribution is related only to the signal Monte-Carlo generated samples. . . . .	85
398	5.33 The $\phi$ muon distributions from data and signal events of Z decaying into $\Upsilon(1S, 2S, 3S)$	
399	+ $\gamma$ after Group I+II of selection cuts, where on left are presenting the trailing muons	
400	and on right are the leading muons. The plots are normalized to the number of events.	
401	Signal sample is scaled by a factor of $\times 100$ ). The black dots are data collect by CMS	
402	while the blue distribution is related only to the signal Monte-Carlo generated samples. . . . .	85
403	5.34 The $p_T$ photon distributions from data and signal events for Z decaying into $\Upsilon(1S, 2S, 3S)$	
404	+ $\gamma$ all (Group I+II) selection cuts. The plot is normalized to the number of events.	
405	Signal sample is scaled by a factor of $\times 100$ ). . . . .	85
406	5.35 The $\eta$ photon distributions from data and signal events of Z decaying into $\Upsilon(1S, 2S, 3S)$	
407	+ $\gamma$ after all (Group I+II) selection cuts. The plot is normalized to the number of	
408	events. Signal sample is scaled by a factor of $\times 100$ ). . . . .	86
409	5.36 The $\phi$ photon distributions from data and signal events of Z decaying into $\Upsilon(1S, 2S, 3S)$	
410	+ $\gamma$ after all (Group I+II) selection cuts. The plot is normalized to the number of	
411	events. Signal sample is scaled by a factor of $\times 100$ ). . . . .	86
412	5.37 The $p_T$ distributions for $\Upsilon(1S, 2S, 3S)$ in the left and for Z in the right from data and	
413	signal events for Z decaying into $\Upsilon(1S, 2S, 3S) + \gamma$ after all (Group I+II) selection	
414	cuts. The plots are normalized to the number of events. Signal sample is scaled by a	
415	factor of $\times 100$ ). The black dots are data collect by CMS while the blue distribution	
416	is related only to the signal Monte-Carlo generated samples. . . . .	86
417	5.38 The $\eta$ distributions for $\Upsilon(1S, 2S, 3S)$ in the left and for Z in the right from data and	
418	signal events for Z decaying into $\Upsilon(1S, 2S, 3S) + \gamma$ after all (Group I+II) selection	
419	cuts. The plots are normalized to the number of events. Signal sample is scaled by a	
420	factor of $\times 100$ ). The black dots are data collect by CMS while the blue distribution	
421	is related only to the signal Monte-Carlo generated samples. . . . .	87
422	5.39 The $\phi$ distributions for $\Upsilon(1S, 2S, 3S)$ in the left and for Z in the right from data and	
423	signal events for Z decaying into $\Upsilon(1S, 2S, 3S) + \gamma$ after all (Group I+II) selection	
424	cuts. The plots are normalized to the number of events. Signal sample is scaled by a	
425	factor of $\times 100$ ). The black dots are data collect by CMS while the blue distribution	
426	is related only to the signal Monte-Carlo generated samples. . . . .	87

427      5.40 The $\Delta R$ distributions between the photon and the leading muon (left) and the trailing 428      muon (right) for $\Upsilon(1S, 2S, 3S)$ from data and signal events for Z decaying after all 429      (Group I+II) selection cuts. The plots are normalized to the number of events. Signal 430      sample is scaled by a factor of $\times 100$ ). The black dots are data collect by CMS while 431      the blue distribution is related only to the signal Monte-Carlo generated samples. . . . .	87
432      5.41 The ratio for the transverse momentum of the reconstructed Upsilon and the re- 433      constructed Z mass ( $p_T^{\mu\mu}/M_{\mu\mu\gamma}$ - left) and the ratio for the transverse energy of the 434      reconstructed Photon and the reconstructed Z mass ( $E_T^\gamma/M_{\mu\mu\gamma}$ - right) distribution 435      for $\Upsilon(1S, 2S, 3S)$ from data and signal events for Z decaying after all (Group I+II) 436      selection cuts. The plots are normalized to the number of events. Signal sample is 437      scaled by a factor of $\times 100$ ). The black dots are data collect by CMS while the blue 438      distribution is related only to the signal Monte-Carlo generated samples. . . . .	88
439      5.42 The $p_T$ muon distributions from data and signal events for Higgs decaying into 440 $\Upsilon(1S, 2S, 3S) + \gamma$ after Group I of selection cuts, where on left are presenting the 441      trailing muons and on right are the leading muons. The plots are normalized to 442      the number of events. Signal sample is scaled by a factor of $\times 600000$ ). The black 443      dots are data collect by CMS while the blue distribution is related only to the signal 444      Monte-Carlo generated samples. . . . .	88
445      5.43 The $\eta$ muon distributions from data and signal events of Higgs decaying into $\Upsilon(1S, 2S, 3S)$ 446 $+ \gamma$ after Group I of selection cuts, where on left are presenting the trailing muons 447      and on right are the leading muons. The plots are normalized to the number of 448      events. Signal sample is scaled by a factor of $\times 600000$ ). The black dots are data 449      collect by CMS while the blue distribution is related only to the signal Monte-Carlo 450      generated samples. . . . .	88
451      5.44 The $\phi$ muon distributions from data and signal events of Higgs decaying into $\Upsilon(1S, 2S, 3S)$ 452 $+ \gamma$ after Group I of selection cuts, where on left are presenting the trailing muons 453      and on right are the leading muons. The plots are normalized to the number of 454      events. Signal sample is scaled by a factor of $\times 600000$ ). The black dots are data 455      collect by CMS while the blue distribution is related only to the signal Monte-Carlo 456      generated samples. . . . .	89
457      5.45 The $p_T$ photon distributions from data and signal events for Higgs decaying into 458 $\Upsilon(1S, 2S, 3S) + \gamma$ all (Group I+II) selection cuts. The plot is normalized to the 459      number of events. Signal sample is scaled by a factor of $\times 600000$ . . . . .	89
460      5.46 The $\eta$ photon distributions from data and signal events of Higgs decaying into 461 $\Upsilon(1S, 2S, 3S) + \gamma$ after all (Group I+II) selection cuts. The plot is normalized 462      to the number of events. Signal sample is scaled by a factor of $\times 600000$ . . . . .	89
463      5.47 The $\phi$ photon distributions from data and signal events of Higgs decaying into 464 $\Upsilon(1S, 2S, 3S) + \gamma$ after all (Group I+II) selection cuts. The plot is normalized 465      to the number of events. Signal sample is scaled by a factor of c). . . . .	90

466	5.48 The $p_T$ distributions for $\Upsilon(1S, 2S, 3S)$ in the left and for Higgs in the right from data 467 and signal events for Higgs decaying into $\Upsilon(1S, 2S, 3S) + \gamma$ after all (Group I+II) 468 selection cuts. The plots are normalized to the number of events. Signal sample is 469 scaled by a factor of $\times 600000$ . The black dots are data collect by CMS while the 470 blue distribution is related only to the signal Monte-Carlo generated samples. . . . .	90
471	5.49 The $\eta$ distributions for $\Upsilon(1S, 2S, 3S)$ in the left and for Higgs in the right from data 472 and signal events for Higgs decaying into $\Upsilon(1S, 2S, 3S) + \gamma$ after all (Group I+II) 473 selection cuts. The plots are normalized to the number of events. Signal sample is 474 scaled by a factor of $\times 600000$ . The black dots are data collect by CMS while the 475 blue distribution is related only to the signal Monte-Carlo generated samples. . . . .	90
476	5.50 The $\phi$ distributions for $\Upsilon(1S, 2S, 3S)$ in the left and for Higgs in the right from data 477 and signal events for Higgs decaying into $\Upsilon(1S, 2S, 3S) + \gamma$ after all (Group I+II) 478 selection cuts. The plots are normalized to the number of events. Signal sample is 479 scaled by a factor of $\times 600000$ . The black dots are data collect by CMS while the 480 blue distribution is related only to the signal Monte-Carlo generated samples. . . . .	91
481	5.51 The $\Delta R$ distributions between the photon and the leading muon (left) and the trailing 482 muon (right) for $\Upsilon(1S, 2S, 3S)$ from data and signal events for Higgs decaying after 483 all (Group I+II) selection cuts. The plots are normalized to the number of events. 484 Signal sample is scaled by a factor of $\times 600000$ . The black dots are data collect by 485 CMS while the blue distribution is related only to the signal Monte-Carlo generated 486 samples. . . . .	91
487	5.52 The ratio for the transverse momentum of the reconstructed Upsilon and the recon- 488 structed Higgs mass ( $p_T^{\mu\mu}/M_{\mu\mu\gamma}$ - left) and the ratio for the transverse energy of the 489 reconstructed Photon and the reconstructed Higgs mass ( $E_T^\gamma/M_{\mu\mu\gamma}$ - right) distribu- 490 tion for $\Upsilon(1S, 2S, 3S)$ from data and signal events for Higgs decaying after all (Group 491 I+II) selection cuts. The plots are normalized to the number of events. Signal sample 492 is scaled by a factor of $\times 600000$ . The black dots are data collect by CMS while the 493 blue distribution is related only to the signal Monte-Carlo generated samples. . . . .	91
494	5.53 Data and MC of the R9 variable, before and after the reweighting. Barrel (left) and 495 Endcap (right). . . . .	92
496	5.54 Resonant background for the $Z \rightarrow \Upsilon(1S, 2S, 3S) + \gamma$ analysis. $\mu\mu$ mass distribution 497 (left) and $\mu\mu\gamma$ invariant mass distribution (right). From top to bottom categories: 498 Inclusive, EB High R9, EB Low R9, EE. . . . .	96
499	5.55 $\Upsilon$ control sample fit with Chebychev 1 <sup>st</sup> order for the background support and 3 500 gaussian for the three $\Upsilon(1S, 2S, 3S)$ peaks. . . . .	97
501	5.56 $Z \rightarrow \Upsilon(1S, 2S, 3S) + \gamma$ Background Modeling: $\mu\mu$ distribution. Inclusive (top left); 502 EB High R9 (top right), EB Low R9 (bottom left), EE (bottom right). The pdfs 503 projections are plotted with respect to the overall best choice of the statistica test. . . . .	100
504	5.57 $Z \rightarrow \Upsilon(1S, 2S, 3S) + \gamma$ Background Modeling: $\mu\mu\gamma$ distribution. Inclusive (top left); 505 EB High R9 (top right), EB Low R9 (bottom left), EE (bottom right). The plotted 506 pdfs corresponds to the best choice by the statistical test for each family. The signal 507 region, from 80 GeV to 100 GeV was blinded. . . . .	100

508	5.58 Resonant Background for the $H \rightarrow \Upsilon(1S, 2S, 3S) + \gamma$ analysis. $m_{\mu\mu}$ invariant mass distribution (left) and $m_{\mu\mu\gamma}$ invariant mass distribution (right). . . . .	101
509		
510	5.59 $H \rightarrow \Upsilon(1S, 2S, 3S) + \gamma$ Background Modeling: $m_{\mu\mu}$ distribution. The <i>pdfs</i> projections are plotted with respect to the overall best choice of the statistical test. . . . .	101
511		
512	5.60 $H \rightarrow \Upsilon(1S, 2S, 3S) + \gamma$ Background Modeling: $\mu\mu\gamma$ distribution. The plotted <i>pdfs</i> corresponds to the best choice by the statistical test for each family. The signal region, from 115 GeV to 135 GeV was blinded. . . . .	101
513		
514		
515	5.61 Signal Modeling for the $Z \rightarrow \Upsilon(1S, 2S, 3S) + \gamma$ analysis for Inclusive category. $m_{\mu\mu}$ mass distribution (left) and $m_{\mu\mu\gamma}$ mass distribution (right). From top to bottom: $\Upsilon(1S)$ , $\Upsilon(2S)$ , $\Upsilon(3S)$ . . . . .	103
516		
517		
518	5.62 Signal Modeling for the $Z \rightarrow \Upsilon(1S, 2S, 3S) + \gamma$ analysis for EB High R9 category. $m_{\mu\mu}$ mass distribution (left) and $m_{\mu\mu\gamma}$ mass distribution (right). From top to bottom: $\Upsilon(1S)$ , $\Upsilon(2S)$ , $\Upsilon(3S)$ . . . . .	104
519		
520		
521	5.63 Signal Modeling for the $Z \rightarrow \Upsilon(1S, 2S, 3S) + \gamma$ analysis for EB Low R9 category. $m_{\mu\mu}$ mass distribution (left) and $m_{\mu\mu\gamma}$ mass distribution (right). From top to bottom: $\Upsilon(1S)$ , $\Upsilon(2S)$ , $\Upsilon(3S)$ . . . . .	105
522		
523		
524	5.64 Signal Modeling for the $Z \rightarrow \Upsilon(1S, 2S, 3S) + \gamma$ analysis for EE category. $m_{\mu\mu}$ mass distribution (left) and $m_{\mu\mu\gamma}$ mass distribution (right). From top to bottom: $\Upsilon(1S)$ , $\Upsilon(2S)$ , $\Upsilon(3S)$ . . . . .	106
525		
526		
527	5.65 Signal Modeling for the $H \rightarrow \Upsilon(1S, 2S, 3S) + \gamma$ . $m_{\mu\mu}$ mass distribution (left) and $m_{\mu\mu\gamma}$ mass distribution (right). From top to bottom: $\Upsilon(1S)$ , $\Upsilon(2S)$ , $\Upsilon(3S)$ . . . . .	107
528		
529	5.66 Examples of the toy datasets fit ( $M_{\mu\mu}$ ), for the Z decay analysis, after the toy dataset refit, for 1S, 2S and 3S (left to right), with $\mu_{true}$ equals to 20, 50, 100, 1000 (top to bottom). The red lines corresponds to the background model (B), the green lines to signal model (S), the blue lines to the total (S+B) and the dots is the toy dataset. . . . .	112
530		
531		
532		
533	5.67 Examples of the toy datasets fit ( $M_{\mu\mu\gamma}$ ), for the Z decay analysis, after the toy dataset refit, for 1S, 2S and 3S (left to right), with $\mu_{true}$ equals to 20, 50, 100, 1000 (top to bottom). The red lines corresponds to the background model (B), the green lines to signal model (S), the blue lines to the total (S+B) and the dots is the toy dataset. . . . .	113
534		
535		
536		
537	5.68 Examples of the toy datasets fit ( $M_{\mu\mu}$ ), for the Higgs decay analysis, after the toy dataset refit, for 1S, 2S and 3S (left to right), with $\mu_{true}$ equals to 100000, 200000, 300000, 1000000 (top to bottom). The red lines corresponds to the background model (B), the green lines to signal model (S), the blue lines to the total (S+B) and the dots is the toy dataset. . . . .	114
538		
539		
540		
541		
542	5.69 Examples of the toy datasets fit ( $M_{\mu\mu\gamma}$ ), for the Higgs decay analysis, after the toy dataset refit, for 1S, 2S and 3S (left to right), with $\mu_{true}$ equals to 100000, 200000, 300000, 1000000 (top to bottom). The red lines corresponds to the background model (B), the green lines to signal model (S), the blue lines to the total (S+B) and the dots is the toy dataset. . . . .	115
543		
544		
545		
546		
547	5.70 Distribution of pulls ( $\frac{\mu_{fit} - \mu_{true}}{\sigma_{fit}}$ ), for the Z decay analysis, after the toy dataset refit, for 1S, 2S and 3S (left to right), with $\mu_{true}$ equals to 20, 50, 100, 1000 (top to bottom). . . . .	116
548		

549	5.71 Distribution of pulls ( $\frac{\mu_{fit} - \mu_{true}}{\sigma_{fit}}$ ), for the Higgs decay analysis, after the toy dataset	117
550	refit, for 1S, 2S and 3S (left to right), with $\mu_{true}$ equals to 100000, 200000, 300000,	
551	1000000 (top to bottom). . . . .	
552	5.72 Example of $f(\tilde{q}_\mu   \mu, \hat{\theta}_\mu^{\text{obs}})$ $f(\tilde{q}_\mu   \mu = 0, \hat{\theta}_{\mu=0}^{\text{obs}})$ distributions generated with toy MC.	120
553	Source: [162]. . . . .	
554	5.73 Example of $f(\tilde{q}_\mu   \mu, \hat{\theta}_\mu^{\text{obs}})$ $f(\tilde{q}_\mu   \mu = 0, \hat{\theta}_{\mu=0}^{\text{obs}})$ distributions generated with toy MC. In	121
555	the figure, $q$ must be read as $\tilde{q}$ . The green area shows the $p_{s+b}$ defined in 5.13, while	
556	the yellow one shows $p_b$ defined in 5.14. Source: [159]. . . . .	

# 557 List of Tables

558      2.1	Relative strength (with respect to the strong force) and effective range of action for 559      the four fundamentals interactions. . . . .	5
560      2.2	Summary of branching ratios for $H/Z \rightarrow \Upsilon(1S, 2S, 3S) + \gamma \rightarrow \mu^+ \mu^- + \gamma$ analysis. 561      The effective cross-section will be discussed in section 5.1.2. . . . .	23
562      2.3	Observed upper limits, by the ATLAS experiment [56, 57], on the branching fractions 563      for the Higgs and Z decays (last result). Detailed comparisons with the results 564      obtained in this study will be presented in section 5.12. . . . .	25
565      2.4	Observed upper limits, by CMS, on the branching fractions for the Higgs and Z 566      decays. The number are compatible with the ones obtained by ATLAS. The results 567      presented for different polarization scenarios of the $J/\Psi$ . . . . .	26
568      5.1	Datasets simulated (MC) for 2016 conditions. Assuming that $\sigma(pp \rightarrow H)$ , taking into 569      consideration all the simulated Higgs production modes, is 55.13 pb [133] and $\sigma(pp \rightarrow$ 570 $Z \rightarrow \mu\mu$ ) is 57094.5 pb, including the next-to-next-to-leading order (NNLO) QCD 571      contributions, and the next-to-leading order (NLO) electroweak corrections from fewz 572      3.1 [134] calculated using the NLO PDF set NNPDF3.0, with the phase space selec- 573      tion in invariant mass of the dimuon system of $m_{\mu\mu} > 50$ GeV. For the Higgs Dalitz 574 $\sigma$ , we consider only the gluon fusion contribution ( $\sigma_{ggF} = 48.6$ pb) [133]. The Higgs 575      Dalitz Decay $BR_{SM}$ and the $Z \rightarrow \mu\mu\gamma_{FSR}$ were obtained with MCFM 6.6 [135] (as 576      in the CMS search for Higgs Dalitz Decay in at $\sqrt{s} = 8$ TeV [136]) and with MAD- 577      GRAPH 5 _MC@NLO, respectively. The $BR_{\Upsilon(1S,2S,3S) \rightarrow \mu\mu}^{PDG} = (2.48, 1.93, 2.18) \times 10^{-2}$ 578      is quoted from Particle Data Group report (PDG) [12]. The "Effective $\sigma$ " for the 579      signal samples is $\sigma(pp \rightarrow Z(H)) \times BR_{SM} \times BR_{\Upsilon(nS) \rightarrow \mu\mu}^{PDG}$ . . . . .	66
580      5.2	Summary of the impact of reweighted of polarization contribution using several sce- 581      narios. . . . .	67
582      5.3	Conditions for a muon to pass the strict tracker requirements. . . . .	72
583      5.4	Number of events for the Z decay, before and after the full selection, per categorization 584      scenarios. . . . .	93
585      5.5	Number of events for the H decay, before and after the full selection. . . . .	93
586      5.6	Modeling for each background source and mass component. . . . .	94
587      5.7	Modeling for each signal source and mass component. . . . .	102
588      5.8	A summary table of systematic uncertainties in the Z boson decaying into $\Upsilon(1S, 2S, 3S) +$ 589 $\gamma$ , affecting the final yields of the MC samples. . . . .	110
590      5.9	A summary table of systematic uncertainties in the Higgs boson decaying into $\Upsilon(1S, 2S, 3S) +$ 591 $\gamma$ , affecting the final yields of the MC samples. . . . .	111

592	5.10 A summary table of systematic uncertainties in the Z (H) decaying into $\Upsilon(1S, 2S, 3S) +$	
593	$\gamma$ , affecting the signal fits. . . . .	111
594	5.11 Summary table for the limits on branching ratio of $Z \rightarrow \Upsilon(1S, 2S, 3S)\gamma$ and $H \rightarrow$	
595	$\Upsilon(1S, 2S, 3S)\gamma$ decays. . . . .	121
596	5.12 Summary table for the limits on branching ratio of $Z \rightarrow \Upsilon(1S, 2S, 3S)\gamma$ , for the two	
597	possible categorization scenarios. . . . .	122

## <sup>598</sup> List of Abbreviations

<b>CERN</b>	European Center for Particle Physics
<b>LHC</b>	Large Hadron Collider
<b>CMS</b>	Compact Muon Solenoid
<b>SM</b>	Standard Model
<b>R9</b>	Photon R9 is a shower shape variable defined as the fraction of energy deposited in the 5x5 square surrounding the Super Cluster seed of the reconstructed photon.
<b>LS1, LS2</b>	Long-Shutdown 1 and 2. Long periods of maintenance and upgrade (spread over few year), in between data taking periods (Run). The LHC timescale is: Run1, LS1, Run2, LS2, Run3, ...
<b>ECAL</b>	Electromagnetic Calorimeter
<b>HCAL</b>	Hadronic Calorimeter

DRAFT

# <sup>599</sup> 1 Introduction

600 The Standard Model (SM) have been proven successful over the last decades by its accordance with  
 601 results from many particle physics experiments, the Super Proton Synchrotron (SPS) [**Synchrotron:1997188**]  
 602 and its experiments created the experimental conditions to the discovery of the electroweak bosons,  
 603  $W^\pm$  and  $Z$ . The Tevatron experiments (D0 and CDF) allowed the discovery of the top quark.  
 604 These were 3 of the four heaviest components of the SM. The missing piece was the, so called, Higgs  
 605 Boson, or any other explanation to the mass of the other SM particles.

606 In 2012, during CMS' Run1, at center-of-mass energy  $\sqrt{s} = 7$  and 8 TeV, researchers from CMS [1]  
 607 and ATLAS [2], two collaborations with experiments located at the Large Hadron Collider (LHC), a  
 608 27 km long circular proton-proton collider build and operated by CERN, announced the discovery a  
 609 new particle [3, 4], with characteristics compatibles with the Brout-Englert-Higgs boson, completing  
 610 the SM picture proposed up to fifty years ago. In 2013, Francois Englert and Peter Higgs were  
 611 awarded with the Noble Prize for "*for the [...] discovery of a mechanism that contributes to our  
 612 understanding of the origin of mass of subatomic particles, and which recently was confirmed through  
 613 the discovery of the predicted fundamental particle, by the ATLAS and CMS experiments at CERN's  
 614 Large Hadron Collider*" [5].

615 On top of the success of the Higgs program at CMS, there is much to be understood, e.g. pin down  
 616 the coupling constants of the Higgs boson with all three generations of quarks and leptons, its mass  
 617 and its full width, evaluate non-zero CP-odd components in Higgs interactions, investigate double  
 618 Higgs production and its self-coupling constant and possible extensions of the SM close to the Higgs  
 619 sector and explore rare decays of Higgs. The former one, specially rare decays involving quarkonia,  
 620 such as  $H \rightarrow M\gamma$ , where  $M$  is a meson state, are a very good scenario to investigate the Higgs  
 621 interaction with other SM particles other than the direct decay. This one would be overwhelmed  
 622 by the immense background coming from QCD events. The same analogy can be extended to the  
 623  $Z$  boson, which also serves as a benchmark for the Higgs study.

624 The present study corresponds to  $35.86 \text{ fb}^{-1}$  of data taken by CMS during 2016, during the Run2,  
 625 at center-of-mass energy  $\sqrt{s} = 13$  TeV, in which an upper limit on the branching fraction for  
 626  $H/Z \rightarrow \Upsilon(1S, 2S, 3S)(\rightarrow \mu\mu) + \gamma$  is determined.

627 Because of its narrow resolution, muons play a special role not only for this study, but for CMS,  
 628 in general. Not only the Higgs studies heavily depends of muonic final states (for decay channels,  
 629 such as  $H \rightarrow \mu\mu$  and  $H \rightarrow ZZ \rightarrow 4l$  and identification of the production modes), but also muon  
 630 final states are very important to a whole broad of physics process accessible at CMS/LHC. The  
 631 Figure 1.1 presents the distribution of dimuon invariant mass reconstructed from different double  
 632 muon triggers, with different requirements in pseudorapidity and transverse momentum. It is clear

633 how the muons at CMS broaden the set of interesting process giving access to light quark hadrons  
 634 to high transverse momentum phenomena.

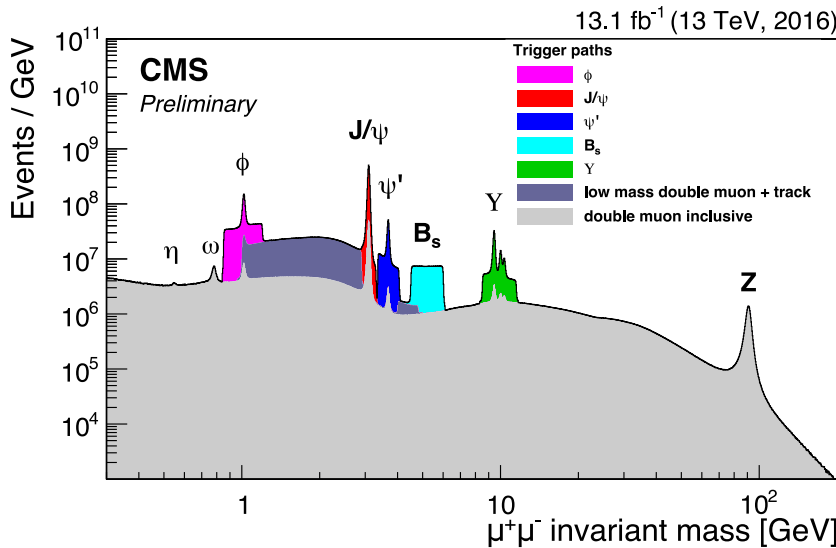


Figure 1.1: Dimuon mass distribution collected with various dimuon triggers. The light gray continuous distribution represents events collected with inclusive dimuon triggers with high  $p_T$  thresholds. The dataset corresponding to an integrated luminosity of  $13.1 \text{ fb}^{-1}$  was collected during the 25 ns LHC running period at 13 TeV in 2016. Source: [6].

635 In this scenario, a contribution to the muon system of CMS is a meaningfully one to the col-  
 636 laboration. In this document it is described the contributions given to Resistive Plate Chamber  
 637 (RPC) subdetector, including its commissioning, instrumentation for its upgrade, operation and  
 638 maintenance.

639 This document is organized as follows: Chapter 1 is this introduction. Chapter 2 is devoted to a  
 640 review of the theoretical foundations of this study and the motivations for the study of Rare Z and  
 641 Higgs decays involving quarkonia. Chapter 3 is a review of the collider and experimental setup, LHC  
 642 and CMS respectively. Chapter 4 is a reviews of the Resistive Plate Chamber technology for muon  
 643 detection at CMS and the details of the contributions given to this subdetector. Chapter 5 is a  
 644 detailed description of the data sample and the applied analysis procedure, as well as the statistical  
 645 modeling and the branching fraction upper limit extraction. Chapter 6 presents a summary and  
 646 perspectives for future developments.

647 Wherever figures and tables sources are not provided, the source is the author himself.

648 In this document, the convention of natural units is implicitly used: the vacuum speed of light ( $c$ ),  
 649 the reduced Planck constant ( $\hbar$ ) and electric permittivity ( $\epsilon_0$ ) are normalized to unity. In this way,  
 650 SI units are:

- 651 • mass ( $[m]$ ) = GeV,
- 652 • energy ( $[E]$ ) = GeV,
- 653 • momentum ( $[p]$ ) = GeV,
- 654 • time ( $[t]$ ) = 1/GeV,

- 655     • length ( $[s]$ ) = 1/GeV.

656     The summation convention is also followed. In this notation,  $y = A^i B_i$  stands for  $y = \sum_{i=0}^n A^i B_i =$   
657      $A^1 B_1 + A^2 B_2 + A^3 B_3 + \dots + A^n B_n$ .

DRAFT

DRAFT

## 658 2 Standard Model and rare Z and Higgs 659 decays to quarkonia

### 660 2.1 Standard Model and Local Gauge Invariance

661 Physics understands matter and how it interacts in terms of two components: fundamental forces  
 662 and elementary particles. From the weakest to the strongest, the fundamental forces are: Gravita-  
 663 tional, Weak, Electromagnetic and Strong. All share common characteristics like, being mediated  
 664 by particles <sup>1</sup>, being relevant within some effective range and have an associate a charge-like quan-  
 665 tity (i.e. an intrinsic characteristic of the object) that defines whether or not, particles might be  
 666 subjected to a specific interaction.

667 Along with the fundamental interactions, the Standard Model [7–10] (or simply *SM*) defines every  
 668 existing matter in the Universe as a set of fundamental quantum objects, with properties that pre-  
 669 scribes their interaction. Those objects are said to be fundamental since, in the context of the SM,  
 670 they are the smallest possible components of matter. We shall refer to them as *Fundamental Parti-*  
 671 *cles*. There four of those mediating particles (force carriers), gluon ( $g$  - for the strong interaction),  
 672 photon ( $\gamma$  - for the electromagnetic interaction), Z (neutral) and  $W^\pm$  (for weak interaction), all of  
 673 them being vector bosons (spin 1). Besides the interaction mediators, described at Table 2.1, the  
 674 fundamental particles are divided in two groups (*quarks* and *leptons*), with three generations, each.  
 675 These are not force carriers, but elementary particles, endowed with charge-like characteristics that  
 676 allow them to interact by exchange the vector bosons. Those are the building blocks of Matter in  
 677 our Universe.

678 Figure 2.1 summarizes their properties. Table 2.1 presents the relative strength and effective range,  
 679 for each one of the four fundamental interactions. It is important to stress that, the gravitational  
 680 force is not study subject of the Standard Model.

Table 2.1: Relative strength (with respect to the strong force) and effective range of action for the four fundamentals interactions.

	Mediator	Relative Strength	Effective Range
Gravitational	Graviton	$10^{-41}$	$\infty$
Weak	W and Z	$10^{-16}$	$10^{-18}$ m
Electromagnetic	Photon	$10^{-3}$	$\infty$
Strong	Gluon	1	$10^{-15}$ m

<sup>1</sup>There is no evidence of the existence of the Graviton (force carrier associated to the gravitational force), even though, it is theorized by models that wish to comprehend gravity in a quantum perspective.

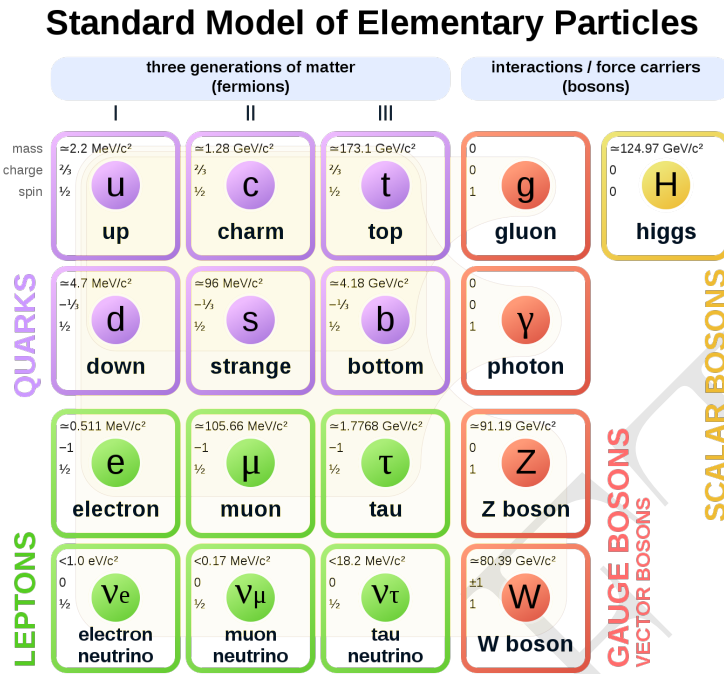


Figure 2.1: Elementary particles of the Standard Model, with their masses charges and spin. Those particles can be divided in two classes: boson (the interaction/force carriers) and the fermions, which are divided in three generations. Source: [11].

681 There are six quarks, up and down ( $u$  and  $d$  - first generation), charm and strange ( $c$  and  $s$  - second  
682 generation), top and bottom ( $t$  and  $b$  - third generation), in increasing invariant mass order of the  
683 generations. Since they interact through all the three fundamental forces of the SM, they are said  
684 to possess electrical charge (for the electromagnetic interaction), flavour (for the weak interaction)  
685 and color (for the strong). Their generational counterparts, the leptons, don't interact via strong  
686 force, that is why they are said to have only flavour and electric charge. The leptons are electron  
687 and electron neutrino ( $e$  and  $\nu_e$  - first generation), muon and muon neutrino ( $\mu$  and  $\nu_\mu$  - second  
688 generation) and tau and tau neutrino ( $\tau$  and  $\nu_\tau$  - third generation). The neutrinos, within the  
689 SM, are massless, even though, experimental measurements have shown that they actually have  
690 mass [12]. Neutrinos are also electrically neutral, meaning that they only interact through weak  
691 interactions.

692 Figure 2.1 also presents the Higgs Boson ( $H$ ) which is part of the SM and shall be discussed later.

### 693 2.1.1 Local Gauge Invariance

694 Within the Standard Model, the theoretical basis that describe the fundamental interactions are  
695 derived from a common principle: the local gauge invariance. According to Salam and Ward [13]:

696 "Our basic postulate is that it should be possible to generate strong, weak and electro-  
697 magnetic interaction terms [...], by making local gauge transformations on the kinetic-  
698 energy terms in the free Lagrangian for all particles."

699 Taking the Quantum Electrodynamics (QED) as an example: the quantum field theory that de-  
700 scribes the electromagnetic interactions, consider the Dirac equation, in the covariant form, for a  
701 particle with mass  $m$ , charge  $-e$  and spin  $1/2$ , i.e. a electron:

$$(i\gamma^\mu \partial_\mu + m)\psi(x) = 0, \quad (2.1)$$

702 where  $\psi(x)$  is a spinor, describing the wave-function and  $\gamma^\mu$  are gamma-matrices. This equation  
703 can be obtained from the lagrangian  $\mathcal{L}$ <sup>2</sup> of a free particle, in the form of

$$\mathcal{L}_0 = i\bar{\psi}(x)\gamma^\mu \partial_\mu \psi(x) - m\bar{\psi}\psi(x), \quad (2.2)$$

704 when applied to the Euler-Lagrange equation.

705 It is clear that, the Dirac Equation (2.1) and its lagrangian (2.2) are invariant under a global phase  
706 transformation.

$$\psi(x) \rightarrow \psi'(x) = \exp(-ie\alpha)\psi(x), \quad (2.3)$$

707 where  $\alpha$  is a constant (global phase shift).

708 The same is not true when  $\alpha$  is not a constant, but actually a local phase transformation, a gauge  
709 transform.

$$\psi(x) \rightarrow \psi'(x) = \exp(-ie\alpha(x))\psi(x) \quad (2.4)$$

710 In this case, the derivative of  $\alpha(x)$  will introduce a new term that would break the invariance. To  
711 recover it, the covariant derivative operator should be modified as follows:

$$\partial_\mu \rightarrow D_\mu = \partial_\mu - ieA_\mu. \quad (2.5)$$

712 This modification introduces the concept of the gauge field  $A_\mu$ , associated to a particle of spin 1  
713 and zero mass, the photon. This term should transform under gauge, in the following manner:

$$A_\mu \rightarrow A'_\mu = A_\mu - \partial_\mu \alpha(x). \quad (2.6)$$

714 Modifications 2.5 and 2.6 are sufficient not only to make the free particle Dirac Equation and its  
715 lagrangian gauge transformation invariant (Equations 2.7 and 2.8 ), but also it naturally gives rise  
716 to an interaction term associated to the gauge field  $A_\mu$ .

$$(i\gamma^\mu \partial_\mu + m)\psi(x) = -e\gamma_\mu A_\mu(x)\psi(x) \quad (2.7)$$

---

<sup>2</sup>Even though, the  $\mathcal{L}$  actually represents the lagrangian density, in this document we shall refer to it as simply lagrangian.

$$\begin{aligned}\mathcal{L} \rightarrow \mathcal{L}' &= i\bar{\psi}'(x)\gamma^\mu D_\mu\psi'(x) - m\bar{\psi}'\psi'(x) \\ \mathcal{L}' &= \mathcal{L}_0 + e\bar{\psi}(x)\gamma^\mu A_\mu\psi(x) = \mathcal{L}\end{aligned}\tag{2.8}$$

717 Interesting to notice that the  $\mathcal{L}_0$  term, on 2.8, corresponds to the electron kinetic energy plus its  
 718 mass contribution (the free particle lagrangian), while the second corresponds to the interaction of  
 719 the electron ( $\psi(x)$ ) and the electromagnetic field. On this basis,  $e$  is said to be the generator of the  
 720 electromagnetic four-potential,  $A_\mu$ . One could add the energy contribution of the electromagnetic  
 721 field itself, by adding a term like:

$$\mathcal{L}_{EM} = -\frac{1}{4}F_{\mu\nu}F^{\mu\nu},\tag{2.9}$$

where:

$$F_{\mu\nu} = \partial_\mu A_\nu - \partial_\nu A_\mu\tag{2.10}$$

722 is the electromagnetic field tensor.

723 It can be proven that applying 2.10 on the Euler-Lagrange equations, this will give us the Maxwell's  
 724 Equations for the vacuum,  $\partial_\mu F^{\mu\nu} = 0$ <sup>3</sup>. One could also expect that a field mass contribution in as  
 725 below, could be introduced, as well.

$$\frac{1}{2}m_{photon}^2 A_\mu A^\mu\tag{2.11}$$

726 This one would break the gauge invariance, therefore we can imply that the photon should be  
 727 massless.

728 The QED is said to be a gauge theory with the symmetry group  $U(1)$ . The  $U(1)$  description comes  
 729 from Lie Algebra, where 2.5 and 2.6 are transformations of gauge  $\alpha$  (in one dimension) to which  
 730 the system is symmetric (invariant), then unitary and generated by a  $1 \times 1$  matrix ( $e$ ).

### 731 2.1.2 The Standard Model

732 Taking profit of the Local Gauge Invariance as path to introduce interactions in a quantum field  
 733 theory (QFT), such as for the QED, the Standard Model can be defined as a QFT of the gauge  
 734 group  $SU_C(3) \times SU_L(2) \times U_Y(1)$ . All the experimental results we have, so far (Section 2.2), give us  
 735 support to this definition.

736 In this context there are 8 spin 1 bosons (called gluons) for the  $SU_C(3)$  component, which corre-  
 737 sponds to the strong interaction, plus 4 bosons,  $W^\pm$ ,  $Z$  and the photon for the other components  
 738 (weak and electromagnetic interactions).

739 Hadrons are defined as colorless particles that interact strongly. They are bound states of quarks,  
 740 which also interact via strong force and have non-neutral color. Hadrons are divided in mesons

---

<sup>3</sup>A non-vacuum covariant form of the Maxwell's Equations would be  $\partial_\mu F^{\mu\nu} = j^\nu$ .

<sup>741</sup> (spin integer) and barions (spin non-integer). Leptons do not interact via gluons (via the strong  
<sup>742</sup> interaction).

<sup>743</sup> **Quantum Chromodinamics**

<sup>744</sup> Quantum Chromodynamics (QCD) is the  $SU_C(3)$  component of the SM, where  $SU$  stands for special  
<sup>745</sup> unitary group, to which the  $\det(e^{i\lambda_i}) = 1$ , where  $\lambda_i$  are the Gell-Mann matrices [**PhysRev.125.1067**]  
<sup>746</sup> (the 8 generators of the  $SU(3)$ ). It corresponds to the field of gluons, responsible for the strong  
<sup>747</sup> interaction acting on a charge-like degree of freedom: colour ( $c$ ). Gluons follow the same fash-  
<sup>748</sup> ion as photons, they are massless and have spin 1, but contrary to electromagnetism, the QCD  
<sup>749</sup> is a non-abelian gauge theory. This means that the force carriers (gluons) can interact with each  
<sup>750</sup> other (self-coupling). In other words, gluons are charged (coloured). In a more formal manner, the  
<sup>751</sup> generators of this group are non-commutative, as follows.

$$[T_a, T_b] = \left[ \frac{\lambda_a}{2}, \frac{\lambda_b}{2} \right] = i \sum_{c=1}^8 f_{ab}^c \lambda_c, \quad (2.12)$$

<sup>752</sup> where  $f_{ab}^c$  are antisymmetric structure constants.

<sup>753</sup> From a experimental perspective, the idea of colour begins with the observation of  $\Lambda^{++}$  [14]. It  
<sup>754</sup> could be only be composed by three up quarks, which would break Pauli Exclusion Principle <sup>4</sup>. This  
<sup>755</sup> observation demanded the inclusion of another degree of freedom, the colour, typically refereed as  
<sup>756</sup> RED, BLUE, GREEN and its anti-colours.

<sup>757</sup> The QCD lagrangian for a quark of colour  $c$ , just the QED lagrangian for a electron of charge  $-e$ ,  
<sup>758</sup> is <sup>5</sup>:

$$\mathcal{L}_{QCD} = \bar{\psi}_c(x) (i\gamma^\mu D_\mu - m) \psi_c(x) - \frac{G_{\mu\nu}^c G_c^{\mu\nu}}{4}, \quad (2.13)$$

where

$$D_\mu = \partial_\mu + ig_s T_c G_\mu^c \quad (2.14)$$

and

$$G_{\mu\nu}^c = \partial_\mu G_\nu^c - \partial_\nu G_\mu^c - g_s f_{ab}^c G_\mu^a G_\nu^b \quad (2.15)$$

<sup>759</sup> This lagrangian is local gauge invariant when the strength tensor 2.15 as:

$$G_\mu^c \rightarrow G_\mu^{c'} = G_\mu^c - \frac{1}{g_s} \partial_\mu \alpha_c(x) - f_{ab}^c \alpha_a(x) G_\mu^b \quad (2.16)$$

<sup>760</sup> Coloured particles, such as quarks and gluons, are subjected to the phenomenon of Colour Con-  
<sup>761</sup> finement, which prohibits the direct observation of these particles. These can only be observed in  
<sup>762</sup> colourless bound states (hadrons). A isolated quark or gluon will immediately interact with the

<sup>4</sup>Two or more fermion can not be in the same quantum state.

<sup>5</sup>The total QD lagrangian would the sum over all possible states.

vacuum and initiates a hadronization process until a set of stable colourless particle is produced. As a consequence of the Colour Confinement and the self-coupling property of the QCD force carriers, a bound state or a resonance of gluons, Glueballs [15], is possible, even though there are no experimental clear evidences of its existence. This is one of the few open topics in the SM.

QCD is a perturbation theory ( $\mathcal{L} = \mathcal{L}_{\text{Free Particle}} + \mathcal{L}_{\text{Interaction}}$ ) which demands renormalization <sup>6</sup>. In a qualitative way, one could imagine that, as larger the distance on interaction is, more sea vacuum gluon pairs can contribute to the net colour charge, due to the self-coupling, increasing the total interaction strength. To cope the Colour Confinement and the self-coupling, one would redefine the strong coupling constant as  $g_s = \sqrt{4\pi\alpha_s}$  (from 2.14, 2.15 and 2.16), where  $\alpha_s(Q^2) \propto \frac{\Lambda_{QCD}^2}{\ln Q^2}$ . In this situation, the coupling strength is related to the transferred momentum  $Q^2$ , in such a way that, in a highly energetic interaction (high  $Q^2$ , hence short distance) the coupling is weaker and the quarks and gluons involved, behave like a quasi-free particles, allowing the use of perturbation theory. This effect is known as Asymptotic Freedom, and its scale have already been measured by the LHC experiments [12].

## 777 Electroweak Theory

The  $SU_L(2) \times U_Y(1)$  represents the Electroweak component of the SM. It is the unification of the Weak and Electromagnet interaction, under the same theory. Here two new degrees of freedom are introduced,  $L$  and  $Y$ . The former one is related to the chirality of  $SU(2)$  and the latter is the weak hypercharge. The generators of groups are the Pauli Matrices ( $T_i$ ) <sup>7</sup>, form the  $SU_L(2)$  and the electromagnetic generator structure for  $U_Y(1)$  (but for  $Y$ , instead of  $-e$ , as before). Since:

$$\begin{aligned}[T_a, T_b] &= i\epsilon^{abc}T_c, \\ [T_a, Y] &= 0\end{aligned}\tag{2.17}$$

where  $\epsilon^{abc}$  is the Levi-Civita tensor,  $SU_L(2)$  is also a non-abelian group.

The connection between electric charge  $Q$  and the weak hypercharge is  $\frac{Y}{2} = Q - T_3$ , as such, QED ( $U_{EM}(1)$ ), as defined in Section 2.1.1 is derived from  $U_Y(1)$ .

In the Electroweak Theory, fermions can have left-handed or right-handed components of their wave-functions, according to their chirality. Left-handed components transform as doublets of  $(T, T_3)$  with eigenvalues  $(1/2, \pm 1/2)$  under  $SU_L(2)$  and the right-handed components transform as singlets ( $T = 0$ ). Weak interactions act only on left-handed fermions. That is the reason for the  $L$  subscript in the electroweak symmetry group definition.

<sup>6</sup>A techniques to deal with infinites that might arrive when calculating quantities in a QFT. In summary the total probability for the theory is required to re-sum to unity.

<sup>7</sup>The usual  $\sigma_i$  representation for the Pauli Matrices usually is reserved for the  $SU_{spin}(2)$  group.

<sup>791</sup> **Standard Model Lagrangian and the Higgs Sector**

The SM lagrangian is given by:

$$\mathcal{L}_{SM} = \mathcal{L}_{gauge} + \mathcal{L}_{fermions} + \mathcal{L}_{Yukawa} + \mathcal{L}_{Higgs}, \quad (2.18)$$

<sup>792</sup> where  $\mathcal{L}_{gauge}$  describes gauge fields of the QCD and Electroweak theories,

$$\mathcal{L}_{gauge} = -\frac{1}{4} \sum_{c=1}^8 G_{\mu\nu}^c G_c^{\mu\nu} - \frac{1}{4} \sum_{a=1}^3 W_{\mu\nu}^a W_a^{\mu\nu} - \frac{1}{4} B_{\mu\nu} B^{\mu\nu}. \quad (2.19)$$

<sup>793</sup> The first term is related to the  $SU_C(3)$  component of the SM and last two terms are related to  
<sup>794</sup>  $SU_L(2) \times U_Y(1)$  components, respectively. The summations are related to all generators in the  
<sup>795</sup> symmetry group, 8 and 3 + 1, for QCD Electroweak. Following the same structure as in 2.15:

$$\begin{aligned} W_{\mu\nu}^a &= \partial_\mu W_\nu^a - \partial_\nu W_\mu^a - g\epsilon_{abc}W_\mu^b W_\nu^c, \\ B_{\mu\nu} &= \partial_\mu B_\nu - \partial_\nu B_\mu \end{aligned} \quad (2.20)$$

For the fermionic term of the lagrangian, we have:

$$\mathcal{L}_{fermions} = \sum_j i\bar{\psi}_L^j \not{D}^L \psi_L^j + \sum_k i\bar{\psi}_R^k \not{D}^R \psi_R^k, \quad (2.21)$$

<sup>796</sup> where the first term is summed over all  $T$  doublets (left-handed components) and the second one,  
<sup>797</sup> over all  $T$  singlets (right-handed components). The slash notation was introduced, in which  $\not{D} =$   
<sup>798</sup>  $\gamma^\mu a_\mu$ . Here, we define the covariant derivatives as:

$$\begin{aligned} D_\mu^L &= \partial_\mu + ig \sum_{a=1}^3 T_L^a W_\mu^a + ig' \frac{Y}{2} B_\mu + ig_s T_c G_\mu^c \\ D_\mu^R &= \partial_\mu + ig' \frac{Y}{2} B_\mu + ig_s T_c G_\mu^c \end{aligned} \quad (2.22)$$

<sup>799</sup> It is important to notice that, the weak interaction term ( $W_\mu$ ) is absent in the right-handed component and the QCD term of the covariant derivative is only applied to quarks. Leptons are colourless.  
<sup>800</sup>  
<sup>801</sup> Since, the electroweak components of the SM are not related to flavour and charge, but rather weak  
<sup>802</sup> hypercharge and left-handed chirality, the boson that we observe experimentally ( $Z$ ,  $W^\pm$  and  $\gamma$ )  
<sup>803</sup> are not directly related to the fields  $W_\mu^a$  and  $B_\mu$ . They are linear combination of them, as follows  
<sup>804</sup> (assuming  $T_L^a = \sigma^a/2$ , where  $\sigma^a$  are the Pauli Matrices):

$$W_\mu^\pm = \frac{1}{\sqrt{2}} W_\mu^1 \mp i W_\mu^2 \quad (2.23)$$

$$\begin{aligned} Z_\mu &= \cos\theta_w W_\mu^3 - \sin\theta_w B_\mu, \\ A_\mu &= \sin\theta_w W_\mu^3 + \cos\theta_w B_\mu, \end{aligned} \quad (2.24)$$

where  $\theta_w$  is a measurable of the theory [12].

The SM lagrangian terms, presented so far, are clearly gauge invariant, under the proper transformations. Even though this is sufficient to define the interactions, two problems arise, related to mass: the spin 1 gauge boson are, by construction, massless, which is in conflict for the measurements we have for  $Z$  and  $W^\pm$  [12]; if one include a mass term for the fermions, as expected from the previous discussion on the QED and QCD, this would break the gauge invariance of the symmetry.

To overcome these problem, another field ( $\phi$ ) is introduced. By its interaction with Electroweak bosons ( $Z$  and  $W^\pm$ ), they gain mass. Also, at the same time, a Yukawa coupling term, between the new field and the fermion, is capable to give them mass, naturally. The simplest way to achieve this is by introducing a scalar field double in  $SU_L(2)$ , the Higgs field.

$$\phi = \begin{pmatrix} \phi^+ \\ \phi^0 \end{pmatrix} \quad (2.25)$$

Therefore, the Higgs contribution to the SM lagrangian is:

$$\mathcal{L}_{Higgs} = (D_\mu \phi)^\dagger (D_\mu \phi) - V(\phi), \quad (2.26)$$

where

$$D_\mu = \partial^\mu + ig \sum_{a=1}^3 T_L^a W_\mu^a + ig' \frac{Y}{2} B_\mu \quad (2.27)$$

and

$$V(\phi) = \mu^2 \phi^\dagger \phi + \lambda (\phi^\dagger \phi)^2. \quad (2.28)$$

The key idea behind the introduction of this field, is that, at ground state, the  $SU_L(2) \times U_Y(1)$  symmetry is "spontaneously" broken, hence the name usually given to this procedure Spontaneously Symmetry Break [16–21]. In this case, to preserve unitarity and to ensure the  $V(\phi)$  has a global minimum,  $\lambda > 0$ . and  $\mu^2$  needs to be negative, in order to give mass to  $Z$  and  $W^\pm$ , otherwise, we would be adding just a scalar field of mass  $\mu$  with self-coupling of strength  $\lambda$ , but the SM bosons would still be massless.

In this case, the minimum value for  $V(\phi)$  is a set of degenerated states in a circle of radius  $\langle \phi \rangle = \sqrt{\frac{-\mu^2}{2\lambda}} = \frac{v}{\sqrt{2}}$ ,  $v = \sqrt{-\mu^2/\lambda}$  is the vacuum expectation value (VEV). Without loss of generality, one can choose a direction:

$$\phi = \frac{1}{\sqrt{2}} \begin{pmatrix} 0 \\ v \end{pmatrix} \quad (2.29)$$

825 assigning hypercharge  $Y = 1$ .

826 Once again, taking profit of the perturbation theory around the ground state (VEV), one could  
827 define <sup>8</sup>:

$$\phi = \frac{1}{\sqrt{2}} \begin{pmatrix} 0 \\ v + H \end{pmatrix} \quad (2.30)$$

828 Expanding the potential  $V(\phi)$ , as is 2.28, one gets:

$$V = \mu^2 H^2 + \frac{\mu^2}{v} H^3 + \frac{\mu^2}{4v^2} H^4, \quad (2.31)$$

829 hence, a new scalar boson (the Higgs boson) is included in the theory with mass  $\sqrt{2\mu^2}$  and self-  
830 couplings terms.

In the same way, expanding 2.27 and assuming  $T_L^a = \sigma^a/2$ :

$$(D_\mu \phi)^\dagger (D_\mu \phi) = \frac{1}{2} (\partial_\mu H)^2 + \frac{1}{8} g^2 (v + H)^2 |W_\mu^1 + iW_\mu^2|^2 + \frac{1}{8} (v + H)^2 |gW_\mu^3 - g'B_\mu|^2. \quad (2.32)$$

831 Defining the SM bosons fields as:

$$\begin{aligned} W_\mu^\pm &= \frac{1}{\sqrt{2}} (W_\mu^1 \mp iW_\mu^2) \\ Z_\mu &= \frac{gW_\mu^3 - g'B_\mu}{\sqrt{g^2 + g'^2}} \\ A_\mu &= \frac{gW_\mu^3 + g'B_\mu}{\sqrt{g^2 + g'^2}}, \end{aligned} \quad (2.33)$$

832 one can naturally infer that the introduction of the Higgs fields gave the SM bosons mass values of:  
833  $M_W = vg/2$ ,  $M_Z = v\sqrt{(g^2 + g'^2)}$  and  $M_A = 0$ . In this context, the Weinberg angle,  $\theta_W$ , is related  
834 to the SM coupling constants as:

$$\begin{aligned} \cos\theta_W &= \frac{g'}{\sqrt{g^2 + g'^2}} \\ \sin\theta_W &= \frac{g}{\sqrt{g^2 + g'^2}}. \end{aligned} \quad (2.34)$$

---

<sup>8</sup>A even more general redefinition of the Higgs field would be possible ( $\phi = (\phi^+, v + H + i\chi)$ ), but the one proposed presents no loss of generality.

835 The missing piece of the SM lagragian (2.18) is the Yukawa components,  $\mathcal{L}_{Yukawa}$ , and how it gives  
 836 the fermion masses. The procedure is quite straightforward. Start including a Yukawa coupling for  
 837 each fermion to either  $\phi$  or  $\tilde{\phi} = i\sigma_2\phi^\dagger$  (this one with  $Y = -1$ ). Taking the electron as an example:

$$\begin{aligned}\mathcal{L}_{Yuk}^e &= -\lambda_e \bar{L}\phi e_R + h.c. \\ \mathcal{L}_{Yuk}^e &= -\frac{1}{\sqrt{2}}\lambda_e(\bar{\nu}^e, \bar{e}_L) \begin{pmatrix} 0 \\ v + H \end{pmatrix} e_R + h.c \\ \mathcal{L}_{Yuk}^e &= -\frac{1}{\sqrt{2}}\lambda_e(v + H)\bar{e}_L e_R + h.c,\end{aligned}\tag{2.35}$$

838 where  $\lambda_e$  is the coupling constant between the Higgs boson and the electron. This tell us that  
 839  $m_e = \frac{\lambda_e v}{\sqrt{2}}$ .

840 Similar procedure can be used for all the fermion of the SM.

## 841 2.2 SM and Higgs results

842 The Standard Model have been proven extremely successful in describing what it is proposed to  
 843 do. The discovery of the two highest invariant mass particles of the SM, the top quark [22, 23], by  
 844 the CDF and D0 collaboration, at FERMILAB, and the Higgs Boson [3, 4], by CMS and ATLAS,  
 845 at CERN, fill the two missing pieces of the SM puzzle, presented at Figure 2.1. In general, SM  
 846 measurements presents very good agreement between theory and experiment, even when the Higgs  
 847 boson is taken into account, once it mass has been established, the subsequent results tend to  
 848 be found restricted within the expectations and constrained by the statistics and experimental  
 849 sensitivity.

850 In this section, we shall briefly review some of the most relevant SM results from LHC, with special  
 851 focus to  $Z$  and Higgs boson, subjects of the study.

### 852 2.2.1 Standard Model vector bosons at CMS

853 The success of the Standard Model relies mostly on its excellent agreement between its predictions  
 854 and the measurements, even though there are still many open questions on fundamental particle  
 855 physics [24], such as: How can we explain the number of fundamental particles known so far? Why  
 856 matter and antimatter appear in the Universe in different proportions? What is the astrophysical  
 857 dark matter? How could we unify the fundamental interactions? How to quantize gravity?

858 The Figures 2.2a, 2.2b, and 2.3 presents a summary of relevant CMS results on SM measurements.  
 859 The former one presents the ratio between the observed and expected cross section ( $\sigma_{exp}/\sigma_{theo}$ )  
 860 for different di-boson production at NNLO calculations and pure electroweak processes, while the  
 861 later have a summary of cross section measurements made by CMS. When theory and experiment

agreement is not exact, one has to take into account the experimental limitations of one experiment, such as CMS and the many possible electroweak phenomena to be studied.

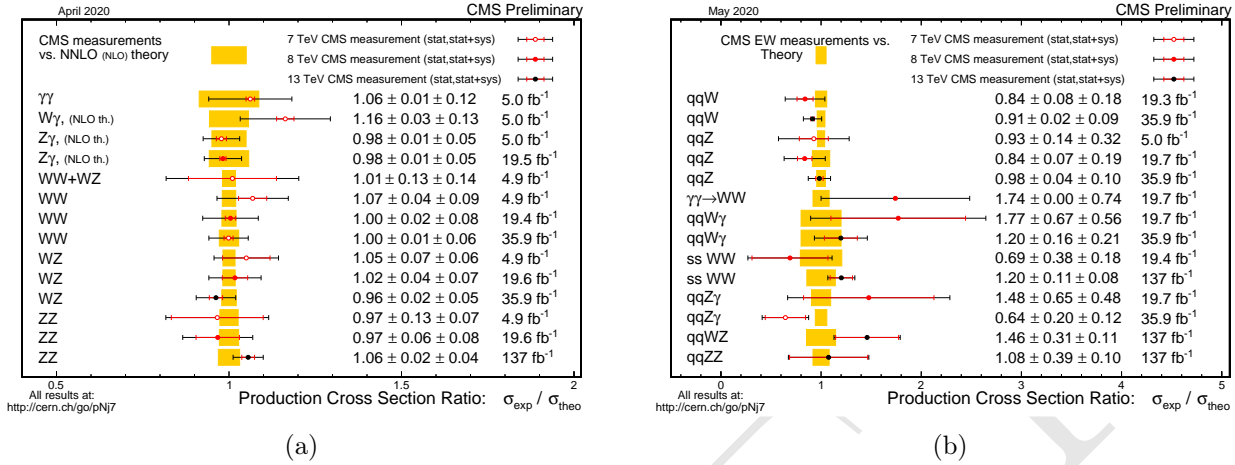


Figure 2.2: (a) Di-boson cross section ratio comparison to theory: Theory predictions updated to latest NNLO calculations where available compared to predictions in the CMS papers and preliminary physics analysis summaries. Source: [25]. (b) Summary of the cross sections of pure Electroweak (EWK) interactions among the gauge bosons presented as a ratio compared to theory. Source: [25].

The open questions above are not subjected to the SM scope, but even within the SM there still relevant precision measurements [26] that are important to understand the validity of the SM and what other questions lies about the SM, at the threshold of the LHC experiments precision.

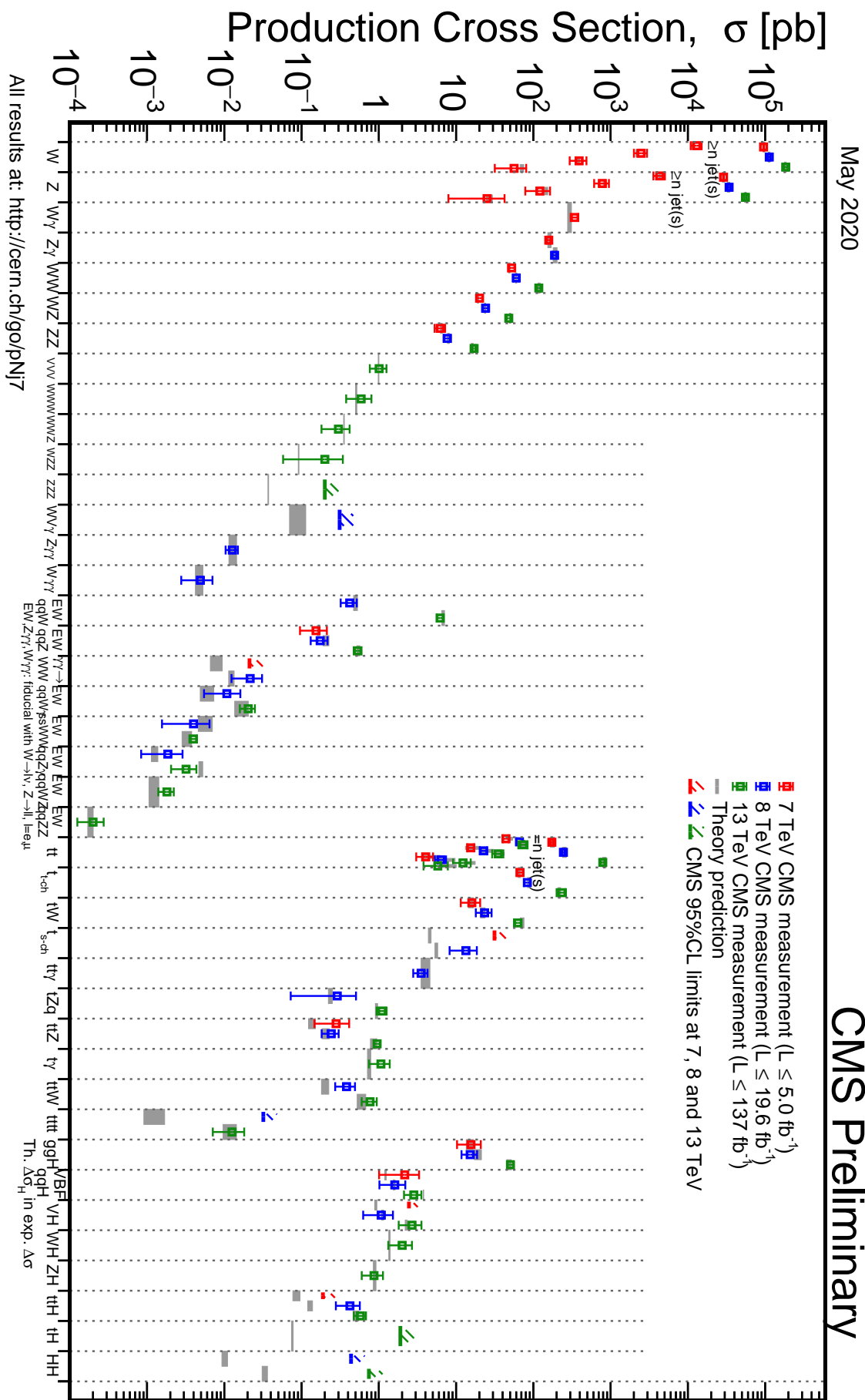


Figure 2.3: Summary of the cross section measurements of Standard Model processes at CMS. Source: [25].

### 2.2.2 Higgs boson at CMS

The Higgs may be produced at LHC proton-proton collisions by the following process, called **Production Modes**. *state-of-art* SM cross section predictions were computed by the "LHC Higgs Cross Section Working Group" [27] and are presented as a function of the Higgs mass is presented at Figure 2.4a and examples of leading order Feynmann diagrams of them are presented at Figure 2.5, for the highest cross section production modes.

The **Gluon Fusion - ggF** - is the result of a gluon-gluon interaction which is mediated by a heavy quark loop. Each quark contributing is suppressed by  $1/m_q^2$ . It is by far the one with highest cross section. Its final state is composed only by a Higgs boson, which makes it harder to identify, since there are no other auxiliary final state particle to tag it. In this decay, QCD radiative corrections are very important and have been included in the results of Figure 2.4a up to N3LO (next-to-next-to-next-to-leading order, while electroweak corrections are computed up to NNLO).

The **Associated Vector Boson Production - VH** - a SM vector boson ( $Z$  or  $W$ ) irradiate a Higgs. Due to its clear electroweak signature (a final state with a Higgs and a vector boson), this production mode enhances the signal, when the Higgs decay has a large contribution from QCD background, e.g.  $H \rightarrow b\bar{b}$ . This process is also called Higgs-Strahlung.

The third process is the **Vector Boson Fusion - VBFH** - in which the two quarks from the initial state scatter by the emission a pair of vector bosons ( $ZZ$  or  $W\pm W\mp$ ). Those would interact (fuse) and produce a Higgs in the final, associated with two back-to-back jets, from the initial state quarks. The **Associated  $t\bar{t}$  Production - ttH** - and **Associated  $b\bar{b}$  Production - bbH** are very similar process (especially in the scale of  $\sqrt{s} = 13$  TeV, where their cross sections almost match), where the coupling of the heavy quark to the Higgs boson, contrary to what happens in the ggF production, it is not with a virtual state of then.

The **Associated Single Top Production - tH** - is the production mode with the smallest cross section, due to its destructive interference with other process. Without loss of generality, it is not considered in this study.

The Higgs allowed **Decay Channel**, in the context of the Standard Model, is also a closet set, which have also been subject of study of the "LHC Higgs Cross Section Working Group" [27]. Figure 2.4b presents their expected branching ratios.

The largest branching fraction is the decay to a  $b\bar{b}$  pair, which is, at  $\sqrt{s} = 13$  TeV, more than the double of the next channel. The large cross section does not imply in being the most sensible channel for the Higgs observation. One has to take into account the experimental sensitivity to this final state (which rely on b-tagging techniques) and its enormous QCD background. Tagging on specific production modes is usually explored in this kind of study [29] to enhance the signal to background ratio. Similar to  $b\bar{b}$ , decays to other SM dileptons are also usually studied, such as dimuons [30],  $\tau\tau$  [31] and  $c\bar{c}$  [32].

Other decays include the  $VV$  state, where  $V$  is a electroweak vector boson ( $Z$  [33],  $W^\pm$  [34] and  $\gamma$  [35]). Even tough the branching fraction for these ones are relatively smaller, they offer a clear signature for event selection, with reduced QCD background. It is important to notice that  $H \rightarrow Z\gamma$

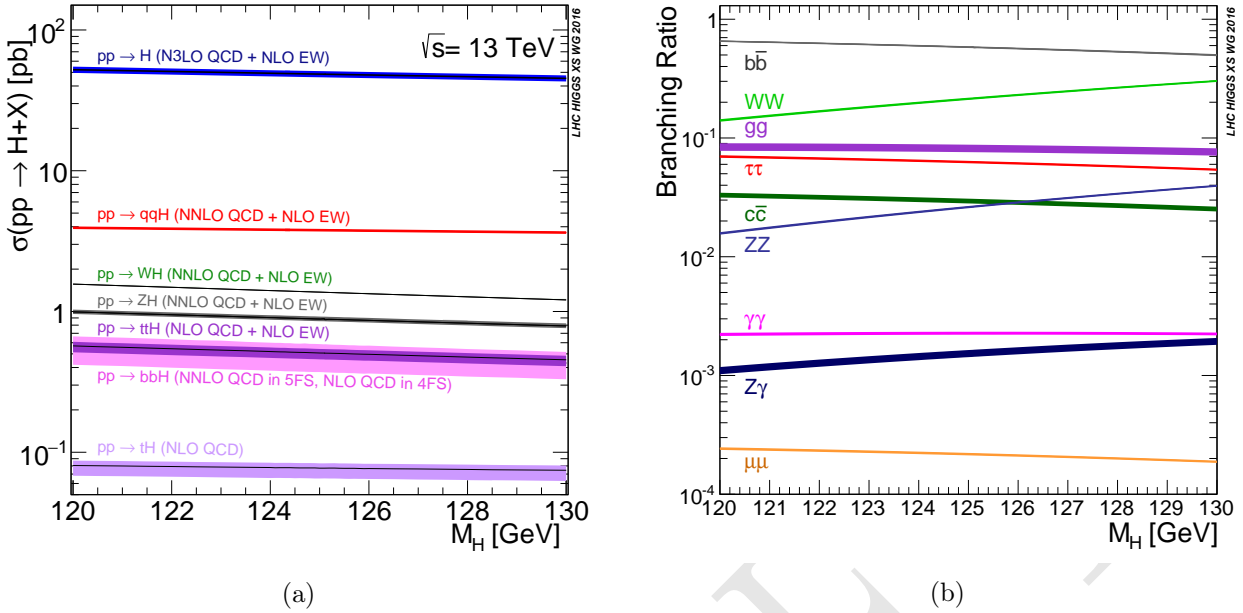


Figure 2.4: (a) Standard Model Higgs boson production cross sections at  $\sqrt{s} = 13$  TeV as a function of Higgs boson mass. The  $tH$  production cross section accounts for  $t$ -channel and  $s$ -channel only (no  $tWH$  production). The VBF process is indicated here as  $qqH$ . The theoretical uncertainties are indicated as shaded bands around the lines. Source: [27]. (b) Standard Model Higgs boson decay branching ratios for different decay channels. The theoretical uncertainties are indicated as shaded bands around the lines. Source: [27].

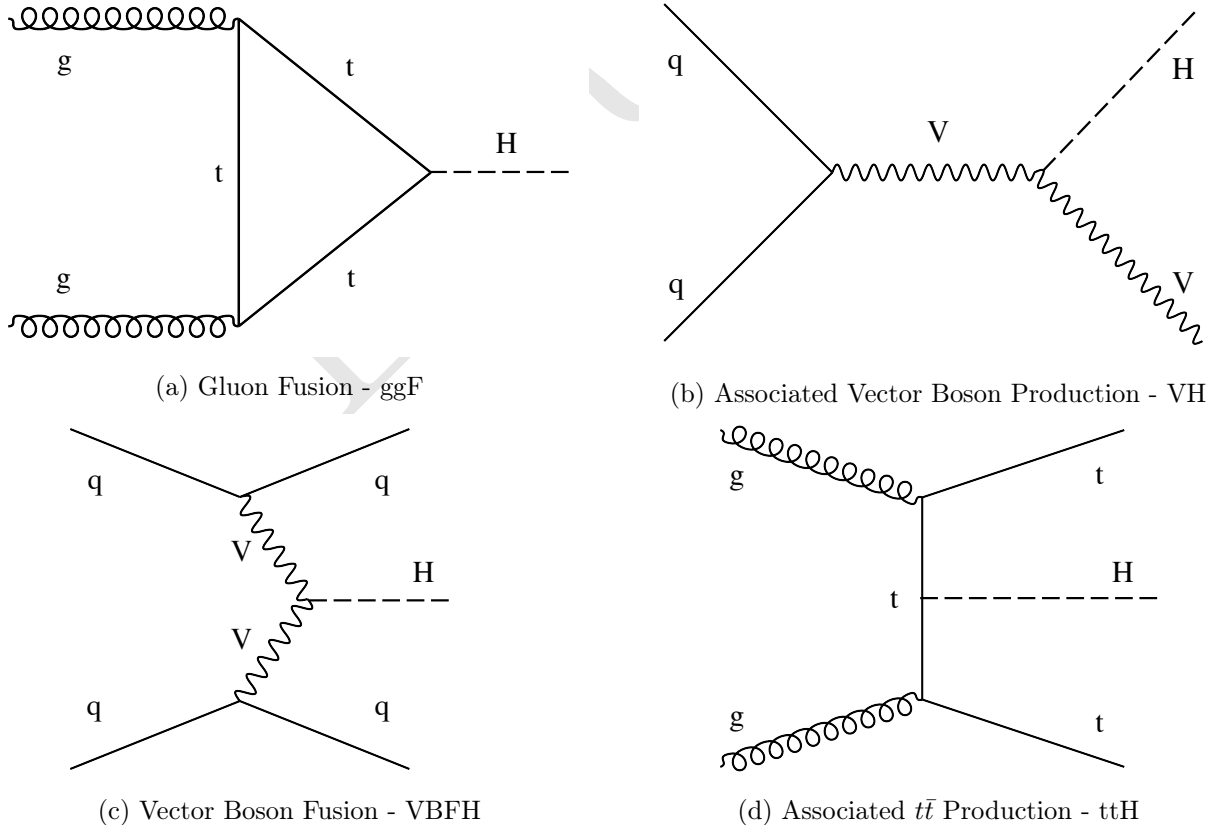


Figure 2.5: Example of leading order Standard Model Higgs boson production model diagrams. Source: [28].

also play a role in this decay mode. CMS (and ATLAS) has a very good sensitivity for leptonic final states of these bosons and for a direct measurement of photons, with resolutions to the order of 1% for the Higgs. Other channels will have resolutions larger than 10% [12].

Gluonic Higgs decays ( $H \rightarrow gg$ ) are allowed in the Standard Model, but they would be overwhelmed by the QCD background. This is considered to be measurable only in the context of a  $e^+e^-$  collider [36].

As already mentioned on Section 2.2, the Higgs was found at CMS and ATLAS in 2012, with Run1 data at  $\sqrt{s} = 7$  and 8 TeV, by investigating the  $H \rightarrow ZZ \rightarrow 4l$  and  $H \rightarrow \gamma\gamma$  decays. Figures 2.6a and 2.6b present the reconstructed final state invariant masses that lead to its discovery. Since then, a broad program have been carried out by both, ATLAS and CMS, to extend the understanding of the Higgs boson to all accessible decays, production modes and also its properties and differential cross section.

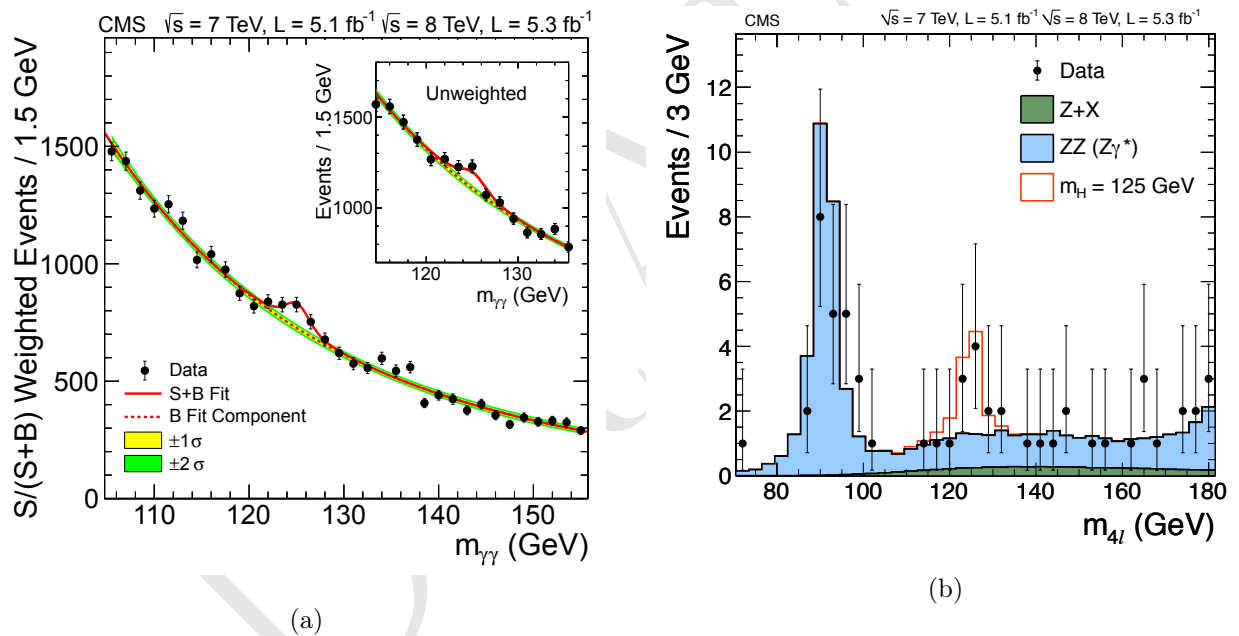


Figure 2.6: (a) The diphoton invariant-mass distribution for the 7 and 8 TeV datasets (points), with each event weighted by the predicted  $S/(S + B)$  ratio of its event class. The solid and dotted lines give the results of the signal-plus-background and background-only fit, respectively. The light and dark bands represent the  $\pm 1$  and  $\pm 2$  standard deviation uncertainties respectively on the background estimate. The inset shows the corresponding unweighted invariant-mass distribution around  $m_{\gamma\gamma} = 125$  GeV. Source: [3]. (b) Distribution of the observed four-lepton invariant mass from the combined 7 and 8 TeV data for the  $H \rightarrow ZZ \rightarrow 4\ell$  analysis (points). The prediction for the expected  $Z+X$  and  $ZZ(Z\gamma^*)$  background are shown by the dark and light histogram, respectively. The open histogram gives the expected distribution for a Higgs boson of mass 125 GeV. Source: [3].

A complete list of Higgs publications and public result from CMS can be found at [37, 38]. With the Higgs measurements being carried out per decay channel, a important effort of combination of these results in performed independently by each collaboration, as well as joint combinations. Some of the Higgs boson measurements by CMS are summarized.

922 The signal strength modifier is the ratio of the measured cross section or branching ratio over the  
 923 expected one.

$$\mu^i = \frac{\sigma^i}{\sigma_{SM}^i} \quad \mu^f = \frac{\mathcal{B}^i}{\mathcal{B}_{SM}^i}, \quad (2.36)$$

924 where  $\sigma^i$  and  $\mathcal{B}^i$  stand for the measured cross section and branching ratio of a certain production  
 925 mode or decay channel, respectively. Figure 2.7 presents the most updated measurements of  $\mu^i$  and  
 926  $\mu^f$  during Run2. The overall combined strength modifier is  $\mu = 1.02^{+0.07}_{-0.06}$  [39], for  $m_H = 125.09$   
 927 GeV, which shows very good agreement with the SM expectation.

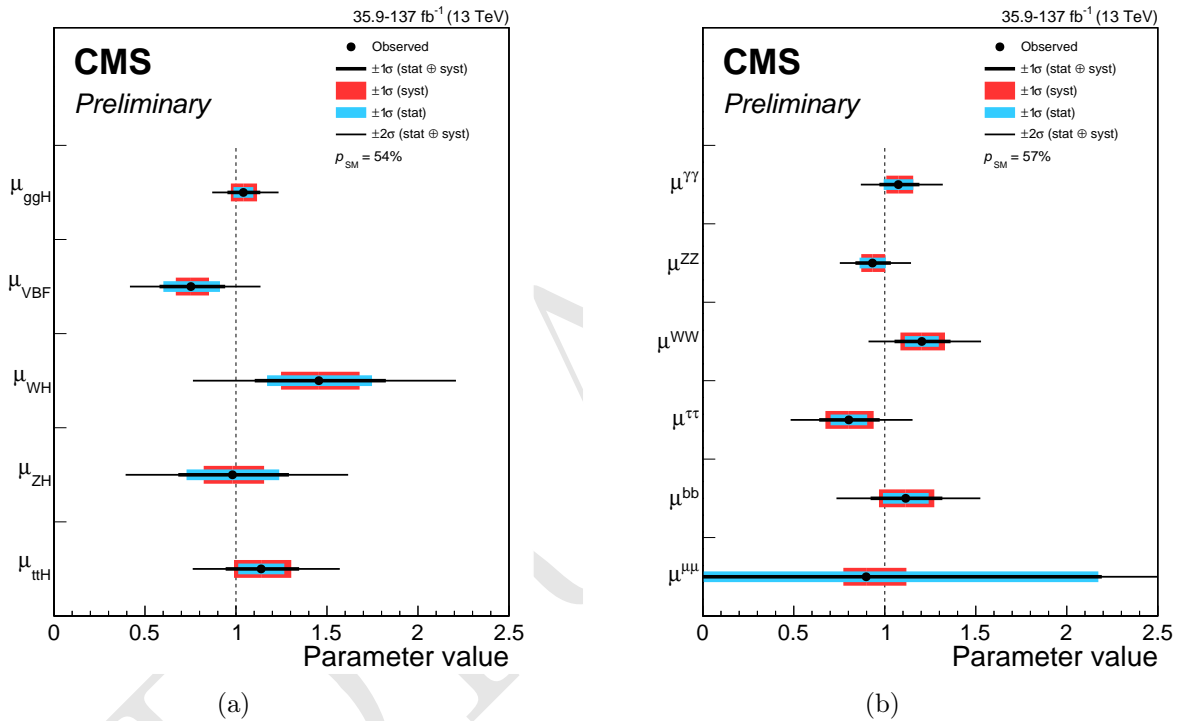


Figure 2.7: Signal strength modifiers for the production modes, (a)  $\mu^i$ , and for the decay channels, (b)  $\mu^f$ . The thick (thin) black lines report the 1 $\sigma$  (2 $\sigma$ ) confidence intervals. The thick blue and red lines report the statistical and systematic components of the 1 $\sigma$  confidence intervals. Source: [39].

928 The Higgs mass was also subject of many study, here we quote the results on Figure 2.8 [35], for  
 929 Run1 and partial Run2 datasets, for both  $H \rightarrow ZZ \rightarrow 4l$  and  $H \rightarrow \gamma\gamma$  decays. The combined  
 930 measurement is  $m_H = 125.38 \pm 0.14$  GeV. This is the *state-of-art* value for the Higgs mass.

931 Other properties studied comprehends its quantum numbers. The Landau-Yang theorem [40, 41]  
 932 rules out the spin-1 possibility, based on its observation on the  $\gamma\gamma$  channel. All the tests conducted,  
 933 so far, support the  $J^P = 0^+$  hypothesis [42].

934 A recent very relevant Higgs result published by CMS is the evidence of the  $H \rightarrow \mu\mu$  decay [30]. In  
 935 this paper it is reported an excess on data, with respect to the background only hypothesis, with  
 936 3 $\sigma$  of significance. This is the first evidence of the Higgs coupling to second generation fermions.  
 937 Figure 2.9a presents a weighted invariant mass distribution of the dimuon system ( $m_{\mu\mu}$ ) for all the  
 938 categories included in this analysis.

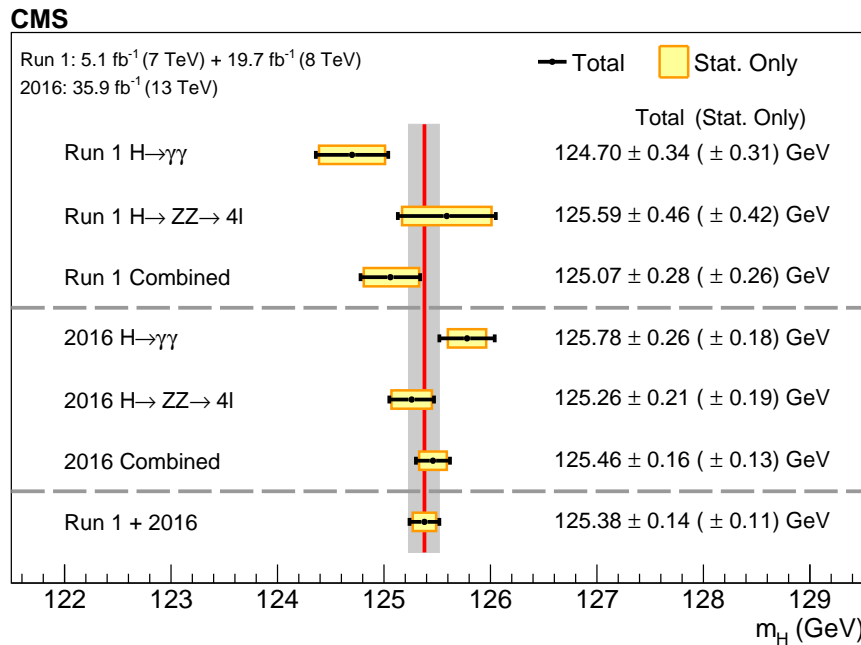


Figure 2.8: A summary of the measured Higgs boson mass in the  $H \rightarrow ZZ \rightarrow 4l$  and  $H \rightarrow \gamma\gamma$  decay channels, and for the combination of the two is presented here. The statistical (wider, yellow-shaded bands), and total (black error bars) uncertainties are indicated. The (red) vertical line and corresponding (grey) shaded column indicate the central value and the total uncertainty of the Run 1 + 2016 combined measurement, respectively. Source: [35].

939 The same note also updates the coupling constant modifier by combining the new results for  $H \rightarrow \mu\mu$   
 940 with previous Higgs results from Run2 [39]. The measured parameters are presented at Figure 2.9b  
 941 and they also present very good agreement with the SM prediction, where the coupling constants  
 942 to fermions is proportional to the fermion mass( $M_f$ ), while for electroweak boson, it is proportional  
 943 to the square of the boson mass ( $M_V$ ). The fit results are scaled to the reduced coupling strength  
 944 modifiers, defined as  $y_V = \sqrt{\kappa_V} \frac{m_V}{\nu}$  and  $y_f = \kappa_f \frac{m_F}{\nu}$ , where  $\nu$  is the vacuum expectation value of  
 945 the Higgs field of 246.22 GeV.

## 946 2.3 Rare Z and Higgs decays to quarkonia

947 The rare decays of the Higgs boson [3, 4] to a quarkonium state and a photon provide a unique  
 948 sensitivity to the magnitude of the Yukawa couplings of the Higgs boson to quarks [43–45]. These  
 949 couplings are difficult to access on hadronic collisions through direct decay of Higgs in quark-  
 950 antiquark, due to the immense background from QCD [46].

951 Among the channels available to explore Yukawa’s couplings of light quarks [44, 45] the promi-  
 952 nent candidates are those with heavy-quarkonia. The rare modes of decay of the Z boson have  
 953 attracted attention focused on establishing its sensitivity to New Physics [47], being an alternative  
 954 environment to investigate the Yukawa couplings of the Higgs boson.

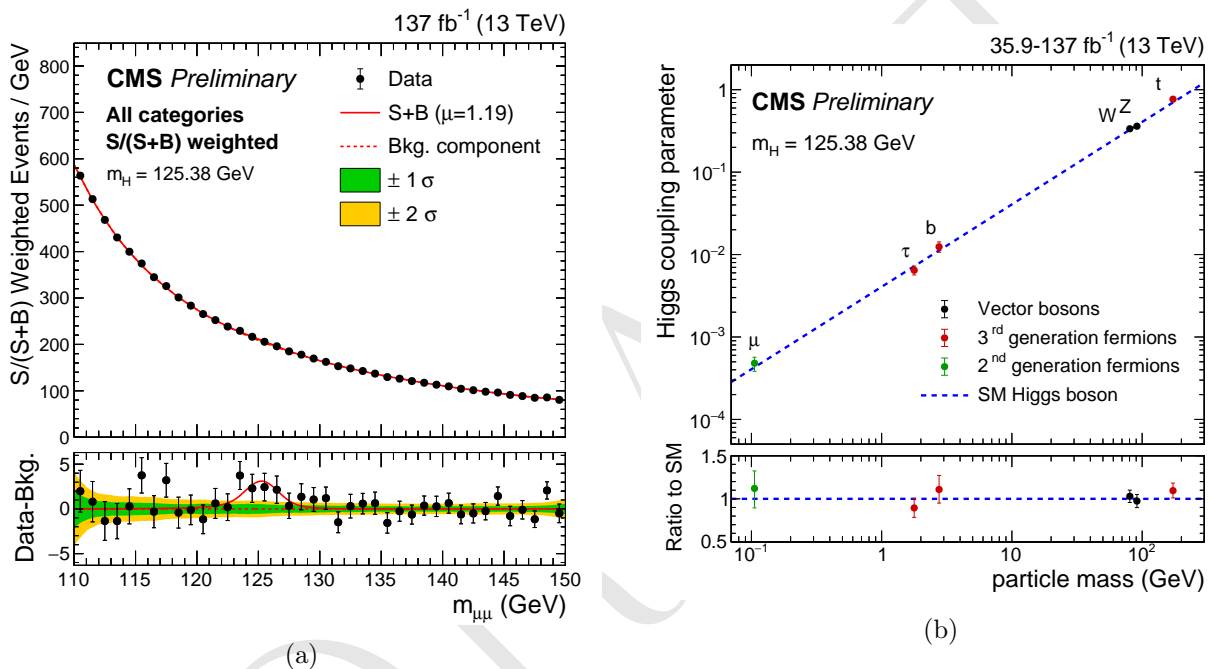


Figure 2.9: (a) The  $m_{\mu\mu}$  distribution for the weighted combination of all event categories used in the analysis. The upper panel is dominated by the gluon-gluon fusion categories with many data events but relatively small  $S/(S + B)$ . The lower panel shows the residuals after background subtraction, with the best-fit SM  $H \rightarrow \mu\mu$  signal contribution with  $m_H = 125.38$  GeV indicated by the red line. The measured signal strength is  $1.19^{+0.41}_{-0.39}(\text{stat})^{+0.17}_{-0.16}(\text{sys})$ . Source: [30]. (b) The best-fit estimates for the reduced coupling modifiers extracted for fermions and weak bosons from the resolved  $\kappa$ -framework model compared to their corresponding prediction from the SM. The error bars represent 68% CL intervals for the measured parameters. The lower panel shows the ratios of the measured coupling modifiers values to their SM predictions. Source: [30].

955 Also, the exclusive rare decays of vector bosons (Z, W) provide a favorable environment for testing  
 956 the factorization of QCD, thus allowing an approach in a context where the power of corrections  
 957 are definitely under control. The main focus of this kind of analysis are the hadronic radioactive  
 958 decays,  $Z \rightarrow M\gamma$ , where M can be a pseudoscalar or a vector meson ( $J/\psi, \phi, \Upsilon_n$ ).

959 They offer the perfect way to explore some of the leading order properties of the light-cone distri-  
 960 bution amplitudes (LCDAs) [48] of several mesons, but they present a difficulty, considering that  
 961 in the LHC energy scale the branching ratio of these processes is very small. There are theoretical  
 962 predictions [49, 50] that point out a branching ratio for several decay channels in the Standard  
 963 Model, as shown in the Table 2.2.

Table 2.2: Summary of branching ratios for  $H/Z \rightarrow \Upsilon(1S, 2S, 3S) + \gamma \rightarrow \mu^+\mu^- + \gamma$  analysis. The effective cross-section will be discussed in section 5.1.2.

Physics Processes	Branching Ratio ( $\text{BR}_{SM}$ ):
$H \rightarrow \Upsilon(1S) + \gamma$	$5.22 \times 10^{-9}$
$H \rightarrow \Upsilon(2S) + \gamma$	$1.42 \times 10^{-9}$
$H \rightarrow \Upsilon(3S) + \gamma$	$9.10 \times 10^{-10}$
$Z \rightarrow \Upsilon(1S) + \gamma$	$4.88 \times 10^{-8}$
$Z \rightarrow \Upsilon(2S) + \gamma$	$2.44 \times 10^{-8}$
$Z \rightarrow \Upsilon(3S) + \gamma$	$1.88 \times 10^{-8}$

964 Recent studies on exclusive Higgs boson decays [51–53] in final states containing a vector meson  
 965 and a photon have caused interest in these physics topics. It was proposed to use these decays as  
 966 a possible way to explore non-standard Yukawa couplings of the Higgs boson. Such measures are  
 967 quite challenging in the LHC environment. The observation of hadronic decays of vector bosons  
 968 could provide a new frontier for the nature of heavy quarkonia production in hadronic collisions.

969 Along the same lines, the simple exploration of rare SM decays, even in scenarios where anomalous  
 970 couplings are, in principle, ruled out by direct measurements [54], as in the case of this analysis  
 971 ( $H \rightarrow \Upsilon(nS) + \gamma$ ), are still important as a stress test of the SM and as reference for future  
 972 measurements. Specially the later one, when you consider that the small predicted cross sections  
 973 from Table 2.2, most probably, would imply that an observation of this decay would be unlikely  
 974 even in the HL-LHC [55].

975 This measurement is sensitive to the direct and indirect production (Figure 2.10). The *direct*  
 976 process consists in the decay of boson (Higgs or Z) to a quark anti-quark pair, in which, one of the  
 977 quarks radiates a photon and the pair hadronizes to a meson (a  $\Upsilon(nS)$ , for this study), while in  
 978 *indirect* process, the decay happens to a  $\gamma\gamma^*(Z)$ , with the subsequent decay of the  $\gamma^*(Z)$  to a quark  
 979 anti-quark that hadronizes.

980 Clearly, only the direct process is sensible to the Yukawa coupling of the boson with the quarks,  
 981 but, since both processes are indistinguishable in their final state, the indirect process needs to be  
 982 taken into account. In this study, a dimuon final state is used to tag the  $\Upsilon(nS)$ .

983 Even though there is different theoretical predictions for the cross section of this process and its  
 984 twin brother ( $H \rightarrow J/\Psi + \gamma$ ), each one taking into account different levels of complexity, the 2013

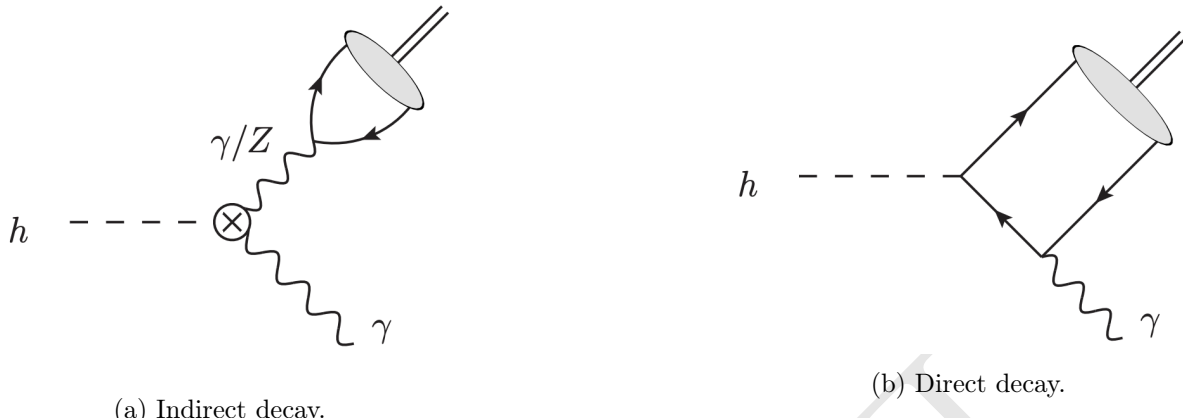


Figure 2.10: Example of leading order diagrams for the indirect and direct production mechanisms. In these diagrams, the  $h$  can also be understood as a  $Z$  or a Higgs boson.

paper [43], from G. Bodwin, F. Petriello, S. Stoynev and M. Velasco, summarizes very well and in a simpler manner, the most relevant phenomenological results on these decays. For the decay to  $J/\Psi + \gamma$ , the quantum interference with the indirect amplitude, enhances the directed production, leading to a larger, and potentially observable, cross section. This is not true for the  $\Upsilon(nS) + \gamma$  decay, since the interference is destructive, diminishing the cross sections.

Another interesting aspect of this study is that, for both  $Hc\bar{c}$  and  $Hb\bar{b}$  direct coupling measurements are not sensible to the sign of the Yukawa coupling, while the presence of the indirect process in the  $H \rightarrow M + \gamma$  ( $M$  standing for  $J/\Psi$  or  $\Upsilon(nS)$ ) decays resolve this ambiguity.

Finally, since the  $\Upsilon(nS) + \gamma$  decay has a much smaller cross section, because of the destructive quantum interference between direct and indirect production mechanisms, a small deviation in the  $Hb\bar{b}$  Yukawa coupling, can lead a large increase in the expected branching ratio, making this channel sensible any non-Standard Model process that might interfere in this final state. This becomes clear when we look to Figure 2.11.

## 2.4 Recent results

The ATLAS experiment [2] already have two results on this decays [56, 57]. The first one corresponds to data taken from 2015, while the latter one, corresponds to data from 2016 (the same data taking period to which this study refers).

To what concerns the most updated result, the study corresponded to  $36.1 \text{ fb}^{-1}$  at  $\sqrt{s} = 13 \text{ TeV}$  and no significant excess was found by the experiment. Upper limits for the decay were obtained, assuming the Standard Model branching fractions predictions, at 95% confidence level, according to table 2.3.

It is worth it to mention that the ATLAS papers present a broader analysis, including the decays to  $J/\Psi + \gamma$  and  $\Psi(2S) + \gamma$ .

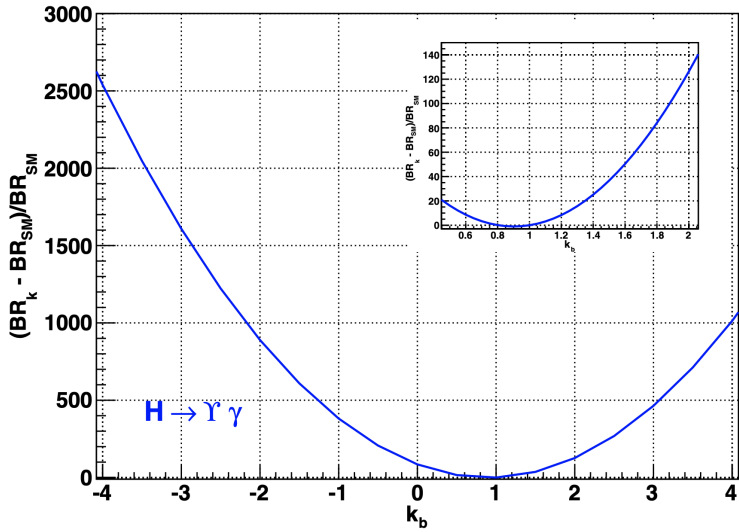


Figure 2.11: Expected relative variation of the branching ratio for the  $H \rightarrow \Upsilon(nS) + \gamma$  to  $k_b$ , where  $k_b = g(Hb\bar{b})/g(Hb\bar{b})_{SM}$  is the ratio for the observed and expected Yukawa coupling of  $Hb\bar{b}$ . Source: [43]

Table 2.3: Observed upper limits, by the ATLAS experiment [56, 57], on the branching fractions for the Higgs and Z decays (last result). Detailed comparisons with the results obtained in this study will be presented in section 5.12.

Decay	$\mathcal{B}F$ at 95% CL
$H \rightarrow J/\Psi + \gamma$	$< 4.5 \times 10^{-4}$
$H \rightarrow \Psi(2S) + \gamma$	$< 2.0 \times 10^{-3}$
$H \rightarrow \Upsilon(1S) + \gamma$	$< 4.9 \times 10^{-4}$
$H \rightarrow \Upsilon(2S) + \gamma$	$< 5.9 \times 10^{-4}$
$H \rightarrow \Upsilon(3S) + \gamma$	$< 5.7 \times 10^{-4}$
<hr/>	
$Z \rightarrow J/\Psi + \gamma$	$< 2.3 \times 10^{-6}$
$Z \rightarrow \Psi(2S) + \gamma$	$< 4.5 \times 10^{-6}$
$Z \rightarrow \Upsilon(1S) + \gamma$	$< 2.8 \times 10^{-6}$
$Z \rightarrow \Upsilon(2S) + \gamma$	$< 1.7 \times 10^{-6}$
$Z \rightarrow \Upsilon(3S) + \gamma$	$< 4.8 \times 10^{-6}$

- 1008 CMS [58] also has a result on  $J/\Psi + \gamma$  and  $\Psi(2S) + \gamma$  decay channel, of the Higgs and Z boson [59].  
1009 The observed upper limits on the branching fraction for these decays are presented in table 2.4.

Table 2.4: Observed upper limits, by CMS, on the branching fractions for the Higgs and Z decays. The numbers are compatible with the ones obtained by ATLAS. The results presented for different polarization scenarios of the  $J/\Psi$ .

Channel	Polarization	$\mathcal{BF}$ at 95% CL
$Z \rightarrow J/\Psi + \gamma$	Unpolarized	$< 1.4 \times 10^{-6}$
	Transverse	$< 1.5 \times 10^{-6}$
	Longitudinal	$< 1.2 \times 10^{-6}$
$H \rightarrow J/\Psi + \gamma$	Transverse	$< 7.6 \times 10^{-4}$

- 1010 No result on the Z and Higgs decays to  $\Upsilon(nS) + \gamma$  have been published by CMS, yet.  
1011 The results presented here are a subset of a broader topic related to the rare decays of Standard  
1012 Model (SM) boson, involving quarkonia. Sticking only to CMS results, we can cite:

- 1013 • Search for Higgs and Z boson decays to  $J/\psi$  or  $\Upsilon$  pairs in proton-proton collisions at  $\sqrt{s} =$   
1014 13 TeV [60].
- 1015 • Observation of the  $Z \rightarrow \psi\ell^+\ell^-$  decay in pp collisions at  $\sqrt{s} = 13$  TeV [61]. This one specifically,  
1016 is the first observation of such a decay, involving a Z boson.
- 1017 • Search for decays of the 125 GeV Higgs boson into a Z boson and a  $\rho$  or  $\phi$  meson [62].

# 1018 3 Experimental Setup

1019 This chapter describes the experimental setup used in this study. For the sake of brevity, brief  
1020 descriptions of the Large Hadron Collider (LHC), the Compact Muon Solenoid (CMS) and its  
1021 subdetectors are provided. Also, it is shown how the high-level physics objects are processed and  
1022 reconstructed.

## 1023 3.1 The Large Hadron Collider

1024 The Large Hadron Collider (LHC) is the world largest and powerful particle accelerator for protons  
1025 and heavy-ions ever build. It is located in a complex of other accelerator operated by the European  
1026 Organization for Nuclear Research (CERN), in the border of between Switzerland and France.  
1027 The LHC is built in the same 26.7 km extension tunnel with depth varying from 45 m to 170  
1028 m below the surface (the LHC plane is tilted 1.4% for construction reasons), once used by Large  
1029 Electron–Positron Collider. The CERN complex is a composition of many accelerators, for proton  
1030 and heavy-ions, used to provide beams of particles for smaller experiments and as a sequence of  
1031 injectors for the LHC. Figure 3.1 presents the many components of the LHC complex of accelerators.  
1032 A detailed description of the LHC can be found at [63–66].

1033 A LHC section is composed of two vacuum pipes, in which the bunch of particles travels in opposite  
1034 directions. This means that both beams are magnetically coupled by the same super-conducting  
1035 magnetic system, saving space and allowing the use of the pre-built LEP tunnel. The particle  
1036 acceleration is made by Resonant Cavities [68]. Those cavities apply to each beam a set of radio-  
1037 frequencies (RF) used to transfer energy by means of a 2 MV electric potential per cavity, at a  
1038 revolution frequency of 400.789 MHz. The acceleration is applied to bunches of particles. The  
1039 bunch configuration depends of the injection mode (configurable), but a typical  $pp$  injection would  
1040 be composed by 2808 bunches of  $1.1 \times 10^{11}$  protons each. Proper timing of the bunches injection  
1041 and the RF is a key factor for an efficient energy transfer inside the RF cavities. The cavities also  
1042 are operated in low temperatures of 4.5 K, to ensure superconducting properties and reduce energy  
1043 losses.

1044 The nominal time spacing between each bunch (bunch crossing - BX) is 25 ns. This defines the  
1045 clock frequency of the LHC at  $f_{LHC} = 40$  MHz. This frequency is propagated to all experiments  
1046 and used as a reference for timing and synchronization.

1047 In certain positions, called the interaction points (IP), those two bunches are allowed to cross, possi-  
1048 bility the particle collisions. The experiments on the LHC are located in those interaction points.

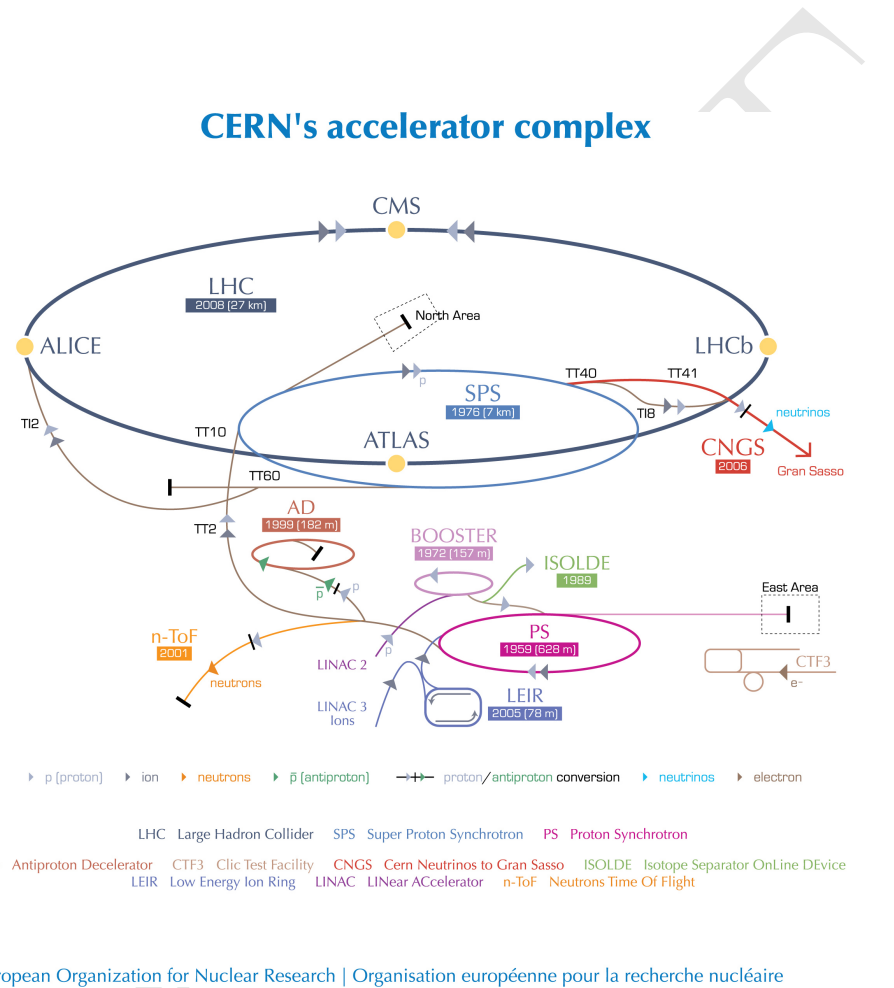


Figure 3.1: The LHC is the last ring (dark grey line) in a complex chain of particle accelerators. The smaller machines are used in a chain to help boost the particles to their final energies and provide beams to a whole set of smaller experiments. Source: [67].

1049 ATLAS (A Toroidal LHC ApparatuS) [2] and CMS (Compact Muon Solenoid, better explained in  
 1050 the next section), at P1 and P5, respectively, are so called general proposes experiments, with focus  
 1051 on different aspects of a particle interactions in the LHC energy scale, including extensive test of  
 1052 known Standard Model process (in high and low transverse momentum regime), including the Higgs  
 1053 sector and Heavy Flavour Physics (phenomena involving the hadrons composed by  $c$  and  $b$  quarks),  
 1054 exploration of Beyond Standard Model (BSM) phenomena, as well as an competitive program in  
 1055 heavy-ions collisions. The LHCb (Large Hadron Collider beauty) [69] is a experiment devoted,  
 1056 mostly, to precision measurements of CP violation and rare decays of  $B$  hadrons. The ALICE  
 1057 (A Large Ion Collider Experiment) [70] experiment is dedicated to the study of  $p\text{-}Pb$  and  $Pb\text{-}Pb$   
 1058 collisions and processes such as QCD, strongly interacting matter and the quark-gluon plasma at  
 1059 extreme values of energy density and temperature.

1060 The number of events of a certain kind  $i$ , per unit of time, is given by Equation 3.1.

$$\frac{dN^i}{dt} = \sigma^i \mathcal{L}, \quad (3.1)$$

1061 where  $\sigma^i$  is the cross-section for a certain process  $i$  and  $\mathcal{L}$  is the instantaneous luminosity delivered  
 1062 by the LHC.

1063 In order to accumulate as much statistics as possible, in the shortest amount of time (for the  
 1064 most efficiently use of the resources available, including person-power), the luminosity is a key  
 1065 factor in the exploration of the collisions. This is dependent of the number of particles per bunch,  
 1066 number of bunches per beam, revolution frequency, form factors of the bunches, crossing angles at  
 1067 the interaction points and correction factors to address relativistic and electromagnetic associated  
 1068 phenomena. For  $pp$  collisions, the LHC aims peak luminosities of, for ATLAS and CMS, around  
 1069  $2 \times 10^{34} \text{ cm}^{-2} \text{ s}^{-1}$ . For future upgrades of the LHC (called HL-LHC [71]), the peak luminosity might  
 1070 increase 10 times, allowing an accumulated luminosity <sup>1</sup> of  $3000 \text{ fb}^{-1}$ .

1071 The LHC can collide protons with center-of-mass energy  $\sqrt{s}$  up to 14 TeV. Different energy config-  
 1072 urations have been used so far, historically increasing the energy. For the operation cycle used in  
 1073 this study (Run2, from 2015 to 2018), the machine was producing collisions at  $\sqrt{s} = 13 \text{ TeV}$ . For  
 1074 the next operation cycle (Run3), to start in 2022, it is expected that the LHC might reach the 14  
 1075 TeV energy values.

## 1076 3.2 The Compact Muon Solenoid - CMS

1077 The Compact Muon Solenoid (CMS) is a multiple purpose experiment used to investigated  $pp$  as  
 1078 well as lead-lead collisions at the LHC. It is operated by the CMS Collaborations, composed by  
 1079 around 200 institutes from more than 40 countries <sup>2</sup>. The CMS is located in the city of Cessy,  
 1080 France, 100 m below the surface. The CMS apparatus has an overall length of 22 m, a diameter of

<sup>1</sup>Accumulated (or integrated) luminosity is defined as  $L = \int \mathcal{L} dt$ .

<sup>2</sup>It is important to stress that CMS is a collaboration of institutes, not researches.

1081 15 m, and weighs 14 000 tonnes. A detailed description of the CMS detector, can be found in [1].  
 1082 Figure 3.2 presents a sketch of CMS and its subdetectors.

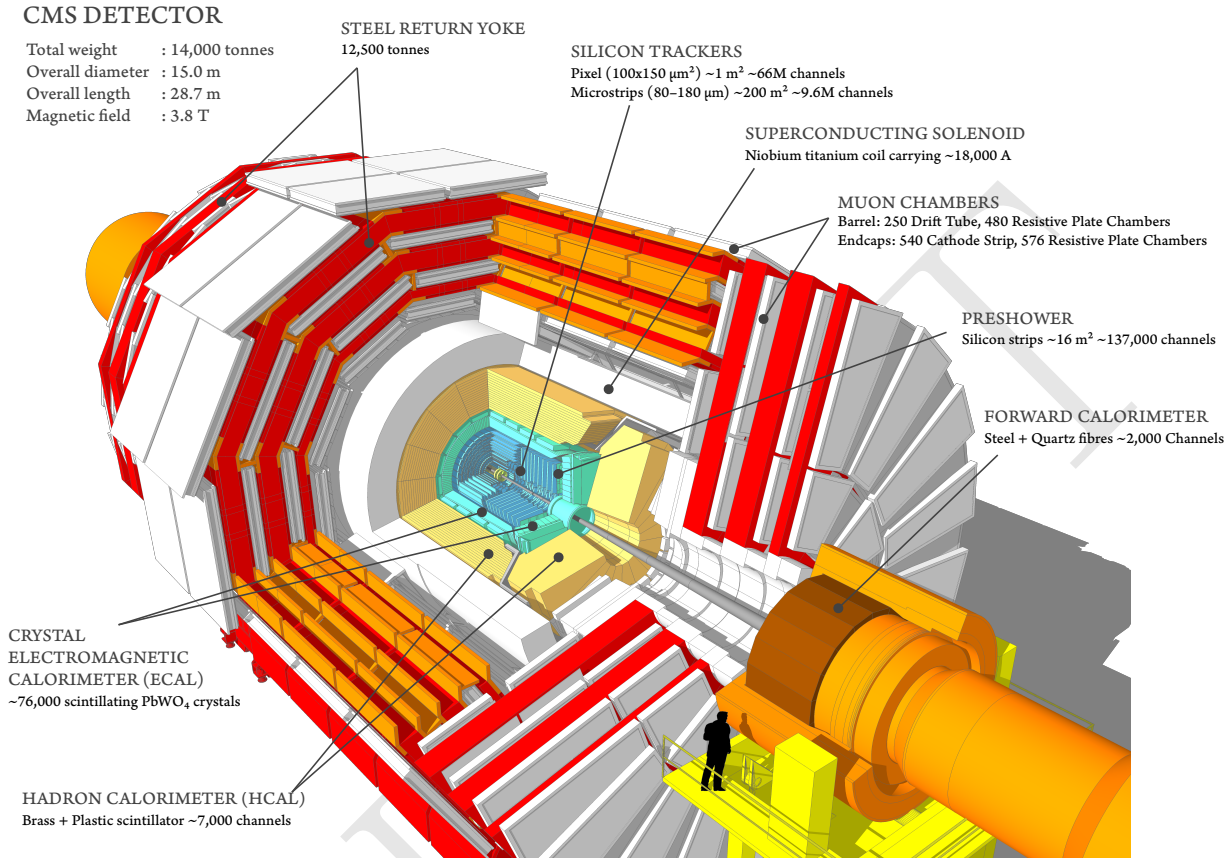


Figure 3.2: Overview of the CMS experiment and its subdetectors. Source: [72].

1083 The central feature of the CMS apparatus is a superconducting solenoid of 6 m internal diameter,  
 1084 providing a magnetic field of 3.8 T. Within the solenoid volume are a silicon pixel and strip tracker,  
 1085 a lead tungstate crystal electromagnetic calorimeter (ECAL), and a brass and scintillator hadron  
 1086 calorimeter (HCAL), each composed of a barrel and two endcap sections. Forward calorimeters ex-  
 1087 tend the pseudorapidity coverage provided by the barrel and endcap detectors. Muons are detected  
 1088 in gas-ionization chambers embedded in the steel flux-return yoke outside the solenoid.  
 1089 The following sections describes the subdetectors, mentioned above, and the CMS coordinate system,  
 1090 as well as some important variables.

### 1091 3.2.1 Coordinate system

1092 CMS uses a right-handed coordinate system (Figure 3.3), with the origin at the nominal interaction  
 1093 point, the  $x$  axis pointing to the centre of the LHC ring, the  $y$  axis pointing up (perpendicular to the  
 1094 LHC plane), and the  $z$  axis along the anticlockwise-beam direction. The polar angle  $\theta$  is measured  
 1095 from the positive  $z$  axis and the azimuthal angle  $\phi$  is measured in the  $x$ - $y$  plane.

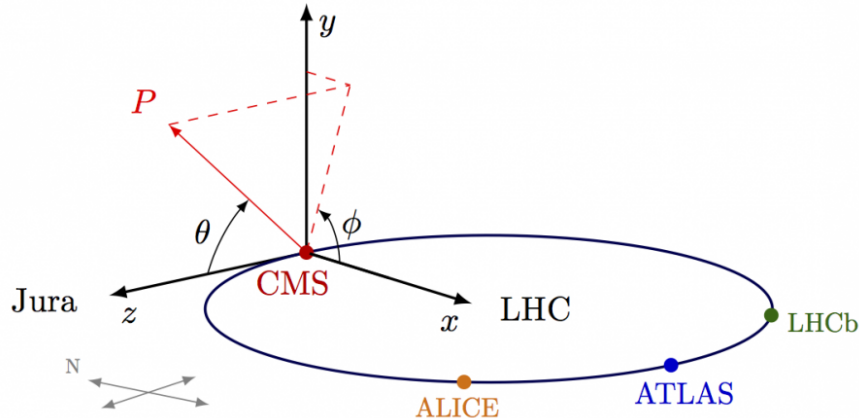


Figure 3.3: Summary of the CMS coordinate system, with respect to the LHC. Source: [cms\_coordinate\_system].

1096 It is important to define some key variables for CMS, in this study. The rapidity is defined by:

$$y = \frac{1}{2} \ln \left( \frac{E + p_z}{E - p_z} \right), \quad (3.2)$$

1097 where  $E$  is the energy of the object and  $p_z$  is the momentum of the objects along the  $z$  direction.

1098 The difference between the rapidity of two objects is known for being a lorentz invariant under a  
1099 boost.

1100 A usually more suitable variable is the pseudorapidity, which is the rapidity in the relativistic limit  
1101 of  $E \gg m$ .

$$\eta = -\ln \left[ \tan \left( \frac{\theta}{2} \right) \right], \quad (3.3)$$

1102 where  $\theta$  is the angle between the transverse plane to the beam line ( $x$ - $y$  plane) and the positive  $z$   
1103 direction. The convenience of using the pseudorapidity is its direct connection with the geometry  
1104 of the event by the  $\theta$  angle.

1105 Spatial distance, at CMS, usually is measured based on the  $\eta$ - $\phi$  space. In this sense the distance  
1106  $\Delta R$  between two objects is defined as:

$$\begin{aligned} \Delta R &= \sqrt{(\Delta\eta)^2 + (\Delta\phi)^2} \\ &= \sqrt{(\eta_1 - \eta_2)^2 + (\phi_1 - \phi_2)^2} \end{aligned} \quad (3.4)$$

1107 One last important variable is the transverse momentum component, computed as in Equation 3.5

$$\begin{aligned} p_T &= \sqrt{p_x^2 + p_y^2} \\ &= |\mathbf{p}| \cos(\theta) \end{aligned} \quad (3.5)$$

1108 **3.3 Tracker**

1109 The tracker is the closest subdetector to the interaction point, with 5.8 m length and 2.5 m diameter  
1110 cylinder. The silicon tracker measures charged particles within the pseudorapidity range  $|\eta| < 2.5$ .  
1111 The challenge of this subdetector is to cope with the high efficiency demanded for the secondary  
1112 vertices identification for long lived particles and initial momentum measurement, the required  
1113 radiation hardness for being close to the interaction point and the expected resolution demanded  
1114 to deal with the high multiplicity of a  $pp$  collisions, specially in the high pileup <sup>3</sup> regime. It consists  
1115 of 1440 silicon pixel and 15 148 silicon strip detector modules, as in Figure 3.4. For non-isolated  
1116 particles of  $1 < p_T < 10$  GeV and  $|\eta| < 1.4$ , the track resolutions are typically 1.5% in  $p_T$  and 25–90  
1117 (45–150)  $\mu\text{m}$  in the transverse (longitudinal) impact parameter [73].

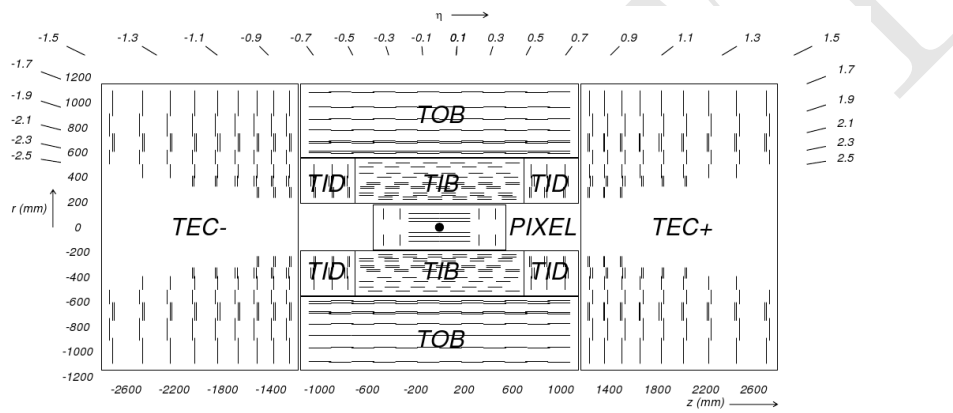


Figure 3.4: Schematic cross section through the CMS tracker. Each line represents a detector module. Double lines indicate back-to-back modules which deliver stereo hits. Source: [1].

1118 The pixel detector consists of 3 layers <sup>4</sup> on the barrel region and 4 layers on the endcap <sup>5</sup>. The pixel  
1119 is located in a region of 20 cm from the beam pipe.  
1120 Each pixel sensor has 100 by 150  $\mu\text{m}^2$ . The silicon strips detector covers a area of  $\approx 200\text{m}^2$  with  
1121  $9.3 \times 10^6$  channels. It is the largest silicon detector covered area ever built. It is divided in Tracker  
1122 Inner Barrel (TIB), with length of 130 cm covering the central part of the detector, the Tracker  
1123 Inner Disks (TID) at the inner endcap, both are surrounded by the Tracker Outer Barrel (TOB)  
1124 on the barrel, and the Tracker Endcap (TEC).

1125 The tracker is essential for a proper muon measurement in this study.

<sup>3</sup>Each LHC collision recorded by CMS, is composed not by a single  $pp$  interaction, but by bunches of protons crossing each other. In this case, a hard interaction is actually surrounded by many soft interaction between adjacent protons. The extra activity produced in these interactions, and caught by the detector, is called **pileup** and has its signal mixed with the hard one.

<sup>4</sup>After 2017, the pixel received one more layer, but this irrelevant to the context of this study, since the data analyzed was collected during 2016.

<sup>5</sup>From 2017, another layer on each side was added.

## 3.4 Electromagnetic Calorimeter

The Electromagnetic Calorimeter (ECAL) is responsible for absorb (and measure) the energy of photons and electrons produced as final state particles of the collisions. The ECAL consists of 75 848 lead tungstate ( $PbWO_4$ ) crystals, which provide coverage in pseudorapidity  $|\eta| < 1.48$  in a barrel region (EB,  $2.2 \times 2.2 cm^2$  and a length of 23 cm) and  $1.48 < |\eta| < 3.0$  in two endcap regions (EE,  $2.86 \times 2.86 cm^2$  front cross section and 22 cm long). Preshower detectors consisting of two planes of silicon sensors interleaved with a total of  $3X_0$  of lead are located in front of each EE detector [74], as shown in Figure 3.5.

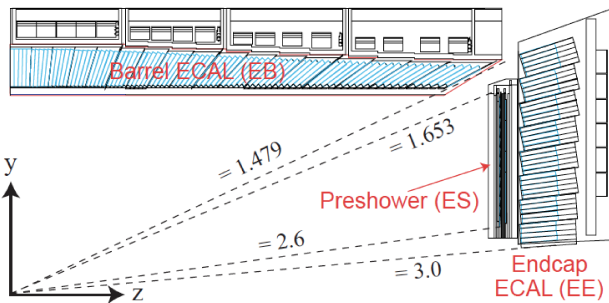


Figure 3.5: Longitudinal section view of the ECAL and its components. Source: [1].

When a electron (or photon) enters the high density region of the lead tungstate crystals ( $8.3 g/cm^3$ ), it initiates a cascade effect of pair production and photon emission via bremsstrahlung. The intensity of light produce is proportional to the energy of the particle adsorbed. With radiation length<sup>6</sup> of 0.89 cm and a small Molière radius (2.2 cm) the ECAL was built with compact size and its fine granularity. The preshower, located in front of the endcap ECAL (EE), is used to distinguish from high momentum photons and pair of photons coming from  $\pi^0$  decays, highly boosted, in such a way that they would be indistinguishable one from the other. Its first layer is composed by the lead tungstate crystal, followed by silicon strip sensor, that allow to measure the shape of the initiated cascade on the first layer and correlate this with the source of the radiation.

Each ECAL crystal is isolated by a carbon fiber layer and it is connected to two photodetectors with a gain of 50. Their signal is collected by a ADC (Analog to Digital Converter) which catches the charge from the photodetectors and convert it to a digital signal.

In the barrel section of the ECAL, an energy resolution of about 1% is achieved for unconverted or late-converting photons that have energies in the range of tens of GeV. The remaining barrel photons have a resolution of about 1.3% up to a pseudorapidity of  $|\eta| = 1$ , rising to about 2.5% at  $|\eta| = 1.4$ . In the endcaps, the resolution of unconverted or late-converting photons is about 2.5%, while the remaining endcap photons have a resolution between 3 and 4% [75]. When combining information from the entire detector, the jet energy resolution amounts typically to 15% at 10 GeV, 8% at 100 GeV, and 4% at 1 TeV, to be compared to about 40%, 12%, and 5% obtained when the ECAL and Hadronic Calorimeter (HCAL) alone are used.

<sup>6</sup>Distance an electron or a photon travels until its energy is reduced by a factor of  $1/e$ .

1154 Due to its responsibility on photon and electrons identification, the ECAL had a very important  
1155 role on the Higgs observation, specially concerning its relation with the  $\gamma\gamma$  and 4-leptons finals  
1156 states of the discovery.

### 1157 3.5 Hadronic Calorimeter

1158 The Hadronic Calorimeter (HCAL) is devoted to absorb and measure the energy of final states  
1159 hadrons. Together with the ECAL, it plays a key role on the jet reconstruction and missing energy  
1160 measurement. It is the last subdetector until the magnet coil and, as much as possible, tries to cover  
1161 the largest pseudorapidity region in order to enhance the missing transverse energy identification. It  
1162 is composed by layers of brass and steel, interleaved with plastic scintillators, with 3.7 mm thickness  
1163 each, in order to leave as much as possible space for the absorptive materials. This allows, once a  
1164 hadron hit the material, the formation of hadronic cascades. These cascades are detected by the  
1165 scintillators which emits light proportional to the amount of energy deposited.

1166 The HCAL is divided in 4 components, the HB (barrel) 9 m long in the central region

1167 In the region  $|\eta| < 1.74$ , the HCAL cells have widths of 0.087 in pseudorapidity and 0.087 in azimuth  
1168 ( $\phi$ ), corresponding to 5 to 10 interaction lengths. In the  $\eta$ - $\phi$  plane, and for  $|\eta| < 1.48$ , the HCAL  
1169 cells map on to  $5 \times 5$  arrays of ECAL crystals to form calorimeter towers projecting radially outwards  
1170 from close to the nominal interaction point. For  $|\eta| > 1.74$ , the coverage of the towers increases  
1171 progressively to a maximum of 0.174 in  $\Delta\eta$  and  $\Delta\phi$ . Within each tower, the energy deposits in  
1172 ECAL and HCAL cells are summed to define the calorimeter tower energies, which are subsequently  
1173 used to provide the energies and directions of hadronic jets. Figure 3.6 shows a longitudinal view  
1174 of the HCAL.

1175 Jets are reconstructed offline from the energy deposits in the calorimeter towers, clustered using the  
1176 anti- $k_T$  algorithm [76, 77] with a distance parameter of 0.4. In this process, the contribution from  
1177 each calorimeter tower is assigned a momentum, the absolute value and the direction of which are  
1178 given by the energy measured in the tower, and the coordinates of the tower. The raw jet energy  
1179 is obtained from the sum of the tower energies, and the raw jet momentum by the vectorial sum of  
1180 the tower momenta, which results in a nonzero jet mass. The raw jet energies are then corrected to  
1181 establish a relative uniform response of the calorimeter in  $\eta$  and a calibrated absolute response in  
1182 transverse momentum  $p_T$ .

### 1183 3.6 Muon System

1184 Muons at CMS [78] are measured in the pseudorapidity range  $|\eta| < 2.4$ , with detection planes  
1185 made using three technologies: drift tubes, cathode strip chambers, and resistive plate chambers,  
1186 as presented in Figure 3.7. The single muon trigger efficiency exceeds 90% over the full  $\eta$  range,  
1187 and the efficiency to reconstruct and identify muons is greater than 96%. Matching muons to tracks  
1188 measured in the silicon tracker results in a relative transverse momentum resolution, for muons with

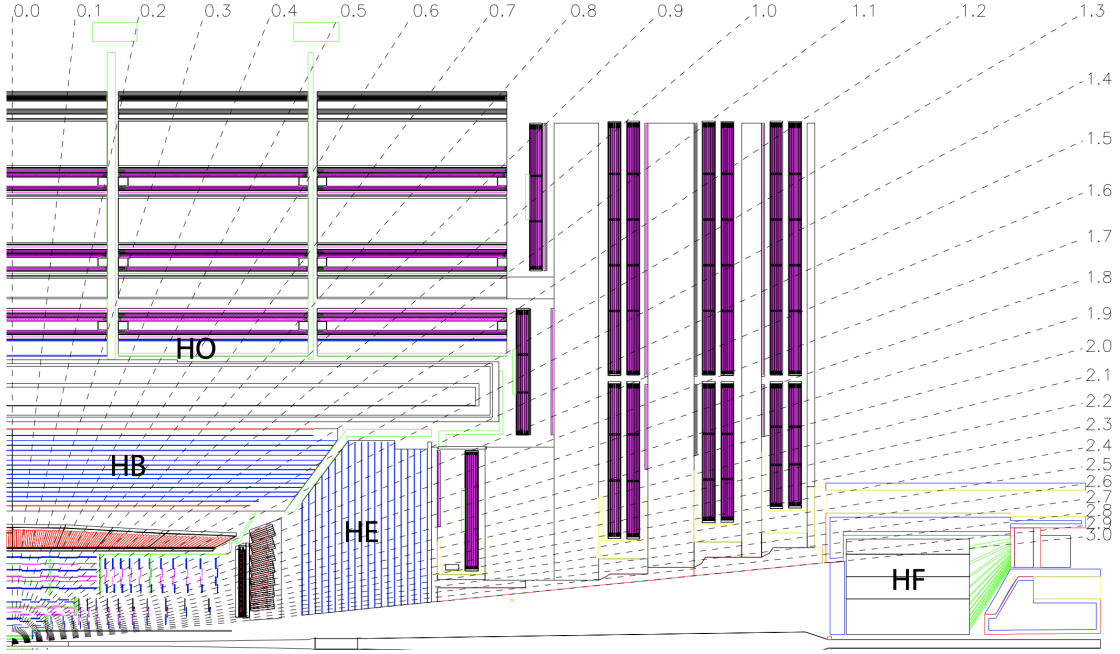


Figure 3.6: Longitudinal section view of the HCAL and its components. The barrel calorimeter (HB) covers the central region, inside the solenoid, the outer calorimeter covers also the central region, but it is positioned on the outside the solenoid. The endcap calorimeter (HE) covers the forward region and it is complemented by the forward calorimeter (HF), which uses Cherenkov light detectors made of radiation-hard quartz fibers. Source: [1].

1189  $p_T$  up to 100 GeV, of 1% in the barrel and 3% in the endcaps. The  $p_T$  resolution in the barrel is  
 1190 better than 7% for muons with  $p_T$  up to 1 TeV [79].

1191 The muon detection system has around 1 million channels. For Run3, the muon system is be-  
 1192 ing expanded and upgraded, by the inclusion of new chamber with the Gas Electron Multiplier  
 1193 (GEM) [81] technology.

### 1194 3.6.1 Drift Tubes

1195 The Drift Tubes (DT) [82] are gaseous detectors (85% Ar and 15% CO<sub>2</sub>) installed in the central  
 1196 region of CMS (Barrel - blue regions at Figure 3.7), covering the region of  $|\eta| < 1.2$ . The barrel  
 1197 is divided in 5 wheels, along  $z$ , W+2, W+1, W0, W-1 and W-2. Each wheel is composed by four  
 1198 concentric stations along  $r$ , MB 1 to MB4, and each station is divided in 12 sectors along  $\phi$ , S01  
 1199 to S12. In total, there are 205 DT chambers. Each tube has 50  $\mu\text{m}$  tick (diameter) gold-plated  
 1200 stainless steel wire, as well as, kept at positive voltage, and aluminum electrodes. The signal is read  
 1201 on the golden wire only.

1202 The tubes are arranged in layers and occupy the whole length of the chamber. The tubes are  
 1203 arranged in coaxial layers. Each set of three layers, forms a Super-Layer (SL). The first and the  
 1204 last SL are aligned in the  $r - \phi$  direction, while the middle one, in the  $r - z$  direction,  
 1205 transversal to the previous one. This arrangement give the DTs, the possibility to measure the  
 1206 passage of a muon in  $\eta$  and  $\phi$  direction, with a resolution of 100  $\mu\text{m}$ .

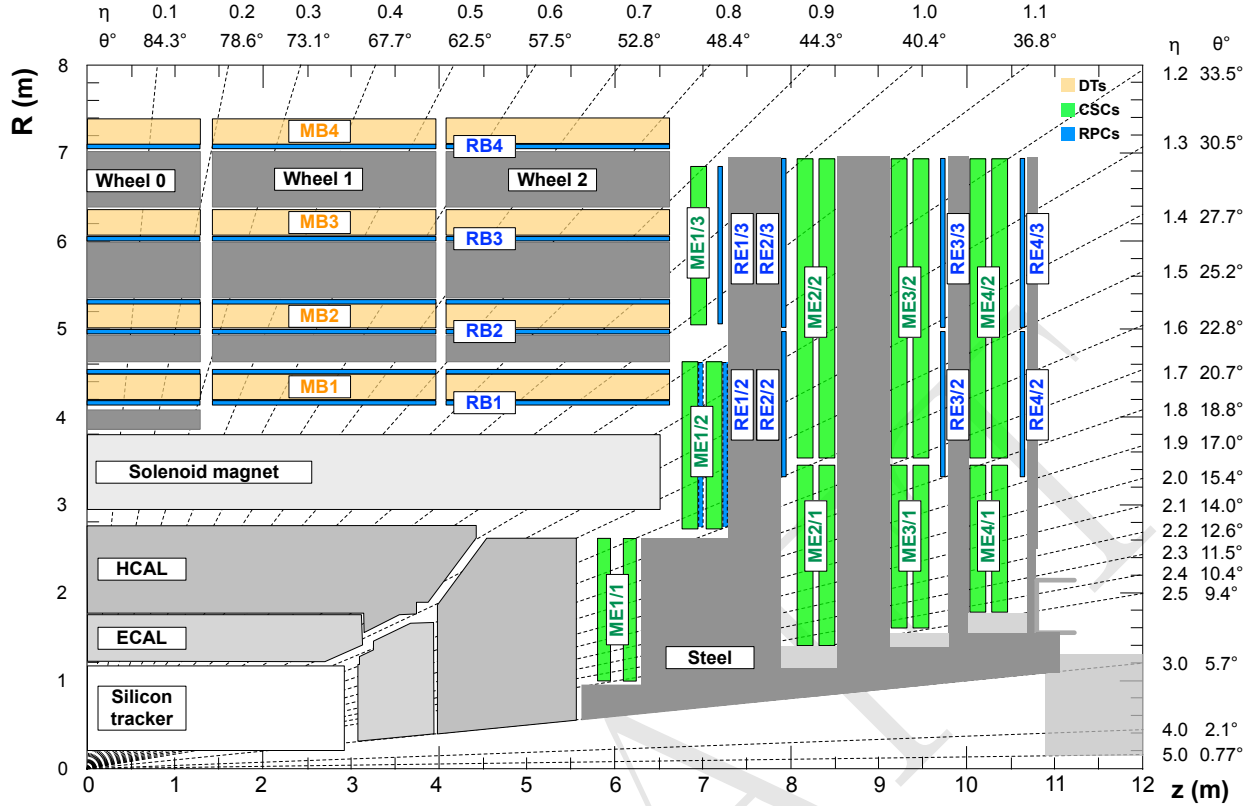


Figure 3.7: Longitudinal section view of the ECAL and its components. Source: [80].

### 1207 3.6.2 CSC

1208 The Cathode Strip Chamber (CSC) is also a gaseous detector (50% CO<sub>2</sub>, 40% Ar, and 10% CF<sub>4</sub>) of  
 1209 the Muon System which covers the endcap region, up to  $|\eta| < 2.4$  composed by wires perpendicular  
 1210 to  $\eta$  (radial measurement) and strips along  $\eta$ , the former operating at 3.9 to 3.6 kV. With 8.4 to 16  
 1211 mm strip width and a wire-distance of 2.5 to 3.16 mm depending on their location, they provide a  
 1212 75 to 150  $\mu\text{m}$  resolution.

1213 They are installed in four layers (or disk) on each side of CMS, with each disk divided in up to  
 1214 three rings.

### 1215 3.6.3 RPC

1216 The Resistive Plate Chambers (RPC) is the only muon detection technology present in both barrel  
 1217 and endcap. It has very good timing resolution and it is used mostly for triggering.

1218 Due to the particularities of the study, especially the contributions given to the RPC project of  
 1219 CMS, Chapter 4 is devoted exclusively to this subdetector.

## 1220 3.7 Trigger and Data Acquisition

1221 The LHC collides protons at 40 MHz. To process and save this amount of information would  
1222 be unmanageable. To deal with the high rate of readouts generated by the collisions and nuclear  
1223 background (around 950 TB/s) CMS uses a two-tiered trigger system [83]. The first level (L1), com-  
1224 posed of custom hardware processors, uses information from the calorimeters and muon detectors,  
1225 in the form of the so called trigger-primitives, to select events at a rate of around 100 kHz within a  
1226 time interval of less than 4  $\mu$ s. The L1 trigger relies on the processing of the optical links, coming  
1227 CMS subdetector by FPGAs (Field Programmable Gate Array) processors. This combination of  
1228 technologies allows the maximum speed in the readout information processing.

1229 The second level, known as the high-level trigger (HLT), consists of a farm of processors running a  
1230 version of the full event reconstruction software optimized for fast processing, and reduces the event  
1231 rate to around 1 kHz before data storage.

1232 Both triggers systems are designed to quickly identify the events <sup>7</sup> that have a specific set of  
1233 signatures of interesting physics, to the context of CMS. As an example, events with characteristics  
1234 of the historically widely studied soft-diffraction, are mostly (but not fully) discarded.

1235 Once a event is read by CMS, it is categorized in one or many of the defined "triggers". Each trigger  
1236 is composed by a minimum sets of requirements, e.g. a single isolated muon trigger is defined as "at  
1237 least one muon, well isolated from any other detector relevant activity, above a minimum transverse  
1238 momentum threshold". If a event falls into a L1 trigger definition and passes the prescaling <sup>8</sup> of  
1239 that trigger, a "L1 Accept" (L1A) optical signal is propagated to all subdetectors readout hardware  
1240 and the information is injected into the Data Acquisition (DAQ) system and saved at the local  
1241 computing cluster, the HLT. This decision process takes around 3.2  $\mu$ s. Saved events are processed  
1242 by an optimized version of the Particle-Flow algorithm and if it again falls into one of the HLT triggers  
1243 paths (definitions) it is saved for future analysis.

## 1244 3.8 Particle Flow Algorithm

1245 The global event reconstruction (also called particle-flow event reconstruction [84]) aims to re-  
1246 construct and identify each individual particle in an event, with an optimized combination of all  
1247 subdetector information. In this process, the identification of the particle type (photon, electron,  
1248 muon, charged hadron, neutral hadron) plays an important role in the determination of the par-  
1249 ticle direction and energy. Photons ( $e/\gamma$  coming from  $Z$  decays or from electron bremsstrahlung)  
1250 are identified as ECAL energy clusters not linked to the extrapolation of any charged particle tra-  
1251 jectory to the ECAL. Electrons are identified as a primary charged particle track and potentially  
1252 many ECAL energy clusters corresponding to this track extrapolation to the ECAL and to possible  
1253 bremsstrahlung photons emitted along the way through the tracker material. Muons are identified

<sup>7</sup>A Event can be understood the set of information from the detector channels, extracted in one readout cycle.

<sup>8</sup>Each trigger has its prescaling. For example, a prescaling 30 means that only once every 30 times that this trigger is activated, the event will be processed and forwarded into the data acquisition chain.

as tracks in the central tracker consistent with either a track or several hits in the muon system, and associated with calorimeter deposits compatible with the muon hypothesis. Charged hadrons are identified as charged particle tracks neither identified as electrons, nor as muons. Finally, neutral hadrons are identified as HCAL energy clusters not linked to any charged hadron trajectory, or as a combined ECAL and HCAL energy excess with respect to the expected charged hadron energy deposit. Figure 3.8 show the identification process for each high-level physics object, as previously described.

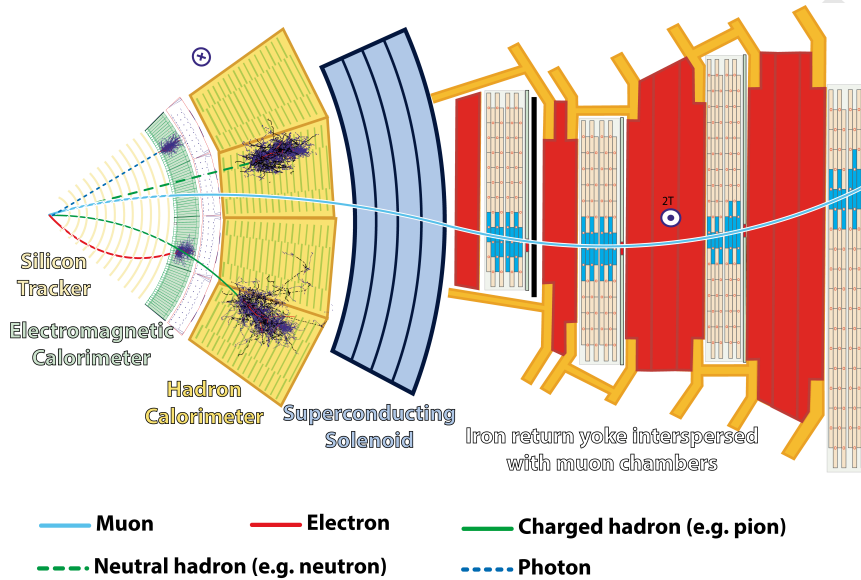


Figure 3.8: The figure illustrates how the information from each subdetector is used in order to identify the different high-level objects in the Particle-Flow algorithm. Source: [84].

The energy of photons is obtained from the ECAL measurement. The energy of electrons is determined from a combination of the track momentum at the main interaction vertex, the corresponding ECAL cluster energy, and the energy sum of all bremsstrahlung photons attached to the track. The energy of muons is obtained from the corresponding track momentum. The energy of charged hadrons is determined from a combination of the track momentum and the corresponding ECAL and HCAL energies, corrected for the response function of the calorimeters to hadronic showers. Finally, the energy of neutral hadrons is obtained from the corresponding corrected ECAL and HCAL energies.

The candidate vertex with the largest value of summed physics-object  $p_T^2$  is taken to be the primary  $pp$  interaction vertex. For each event, hadronic jets are clustered from these reconstructed particles using the infrared and collinear safe anti- $k_T$  algorithm [76, 77] with a distance parameter of 0.4. Jet momentum is determined as the vectorial sum of all particle momenta in the jet, and is found from simulation to be, on average, within 5 to 10% of the true momentum over the whole  $p_T$  spectrum and detector acceptance. Additional proton-proton interactions within the same or nearby bunch crossings (pileup) can contribute additional tracks and calorimetric energy depositions to the jet momentum. To mitigate this effect, charged particles identified to be originating from pileup vertices are discarded and an offset correction is applied to correct for remaining contributions. Jet energy corrections are derived from simulation to bring the measured response of jets to that of particle

1279 level jets on average. In situ measurements of the momentum balance in dijet, photon + jet,  $Z + \text{jet}$ ,  
1280 and multijet events are used to account for any residual differences in the jet energy scale between  
1281 data and simulation [85]. The jet energy resolution amounts typically to 15–20% at 30 GeV, 10%  
1282 at 100 GeV, and 5% at 1 TeV [85]. Additional selection criteria are applied to each jet to remove  
1283 jets potentially dominated by anomalous contributions from various subdetector components or  
1284 reconstruction failures.

1285 Anomalous high- $p_T^{\text{miss}}$  events can be due to a variety of reconstruction failures, detector malfunctions  
1286 or non collisions backgrounds. Such events are rejected by event filters that are designed to identify  
1287 more than 85–90% of the spurious high- $p_T^{\text{miss}}$  events with a mistagging rate less than 0.1% [86].

1288 Hadronic decays of top quarks are identified using the ratio between 3-subjettiness and 2-subjettiness [87],  
1289  $\tau_{32} = \tau_3/\tau_2$ , and the groomed jet mass. The groomed jet mass is calculated after applying a modified  
1290 mass-drop algorithm [88, 89], known as the *soft drop* algorithm [90], to anti- $k_T$  jets with a distance  
1291 parameter of 0.8 and parameters  $\beta = 0$ ,  $z_{\text{cut}} = 0.1$ , and  $R_0 = 0.8$ . The variables are calibrated in a  
1292 top quark-antiquark enriched sample [91].

1293 In the barrel section of the ECAL, an energy resolution of about 1% is achieved for unconverted  
1294 or late-converting photons in the tens of GeV energy range. The remaining barrel photons have  
1295 a resolution of about 1.3% up to a pseudorapidity of  $|\eta| = 1$ , rising to about 2.5% at  $|\eta| = 1.4$ .  
1296 In the endcaps, the resolution of unconverted or late-converting photons is about 2.5%, while the  
1297 remaining endcap photons have a resolution between 3 and 4% [75].

1298 The electron momentum is estimated by combining the energy measurement in the ECAL with the  
1299 momentum measurement in the tracker. The momentum resolution for electrons with  $p_T \approx 45$  GeV  
1300 from  $Z \rightarrow ee$  decays ranges from 1.7% to 4.5%. It is generally better in the barrel region than in  
1301 the endcaps, and also depends on the bremsstrahlung energy emitted by the electron as it traverses  
1302 the material in front of the ECAL [74].

1303 Muons have their momentum computed by curvature of their tracks in the muon system solo or the  
1304 matched track in the muon system and the tracker.

DRAFT

# 1305 4 CMS Resistive Plate Chambers - RPC

## **Statement of Contribution**

From September/2017 to September/2019, I received a grant from the National Council for Scientific and Technological Development (CNPq) to work at CERN, as part of my PhD graduation. During this period, I started to contribute to the RPC project at CMS. My first task was on the upgrade of the Online Software, that control the data taking process for the RPC system. Later I became the responsible for the monitoring and maintenance of this software. I also had the opportunity to work as shifter for the operation of the detector, as contact person between the CMS Run Coordination and the RPC experts, and also as Data Manager shifter, working on the prompt monitoring of the data quality (data certification).

During the course of the Long Shutdown 2 (LS2, from 2019 until middle of 2021), I vigorously worked in the maintenance of the RPC system, specially on the HV system reparation and commissioning. In the context of the task, I proposed changes in the HV connectorization of the RPC chambers, witch were later approved and implemented for recently repaired chambers in the Endcap. In the last moments of my stay at CERN, I also had the opportunity to work with Multiwire Proportional Chambers (MWPC), donated by the LHCb experiment. Those chambers were validated and commissioned by me, in order to server and baseline technology of a muon trigger to be installed in the Gamma Irradiation Facility (GIF++), at CERN, for R&D of the RPC future upgrades.

Later, I became Deputy Run Coordinator for the RPC system, were I share the responsibilities for the operation and commissioning of the system, management the operation shifters, and monitoring with RPC DAQ backend electronics and its communication with other CMS subsystems. I also represent the RPC system for CMS Run Coordination.

1306

- 1307 In the course of this PhD study, there were a lot of opportunities to work for the RPC project, in
- 1308 the context of the CMS Collaboration. The main activities consists of shifts for the RPC operation
- 1309 and data certification, upgrade and maintenance of the online software, R&D activities for the RPC
- 1310 upgrade and detector maintenance during the LHC Long Shutdown 2 (2019 to 2020).
- 1311 In this chapter, it is presented a summary of the Resistive Plate Chamber technology and the my
- 1312 contributions to the RPC project at CMS.

## 1313 4.1 Resistive Plate Chambers

- 1314 The seminal paper on the Resistive Plate Chamber (RPC) technology was presented by R. Santonico
- 1315 and R. Cardarelli, in which they described a "dc operated particle detector (...) whose constituent
- 1316 elements are two parallel electrode Bakelite plates between" [92]. The key idea behind the RPC,
- 1317 with respect to other similar gaseous detectors, is the use of two resistive plates as anode an

1318 cathode, which makes possible to have a small localized region of dead time, achieving very good  
 1319 time resolution.

1320 The working principle for RPCs relies on the idea that a ionizing particle crossing the detector, tend  
 1321 to interact with the gap between the two plates (filled with some specific gas mixture) and form a  
 1322 ionizing cascade process, in which the produced charged particle are driven by the strong uniform  
 1323 electrical field produced by the two plates.

1324 The gas mixture is a key component of a RPC. Even though the first RPCs were produced with  
 1325 a mixture of argon and butane, nowadays RPCs use a mixture of gases that would enhance an  
 1326 ionization caused by the incident particle and quench secondary (background) effects.

1327 Another feature of the RPCs is its construction simplicity and low cost. This allow the use RPC to  
 1328 cover larger at a reasonable cost.

1329 An extensive review of the RPC technology and its application can be found at [93].

#### 1330 4.1.1 Principles and operation modes

1331 The core of a RPC chamber is a gap made with two parallel high resistivity plates, separated  
 1332 by some regular distance (typically millimeters), filled with with a proper gas mixture and under  
 1333 appropriate high voltage (HV) applied on the plates (electrodes, from here on). When a ionizing  
 1334 particle crosses the gap, there is a high enough chance the particle will interact with the gas and  
 1335 produce a newly created positive ion and a electron. This pair will travel in opposite directions,  
 1336 according to the electric field from the electrodes. During this process, the electron will gain kinetic  
 1337 energy and inelastically interact with other neighboring atoms/molecules, creating excitations in their  
 1338 energy levels and, potentially, also ionizing them. The secondary ionization electrons will also follow  
 1339 the same curse, creating an **Avalanche** of positive and negative particle/ions traveling towards the  
 1340 electrodes. This process is proportional to the applied electric field. Figure 4.1 illustrates the  
 1341 avalanche production.

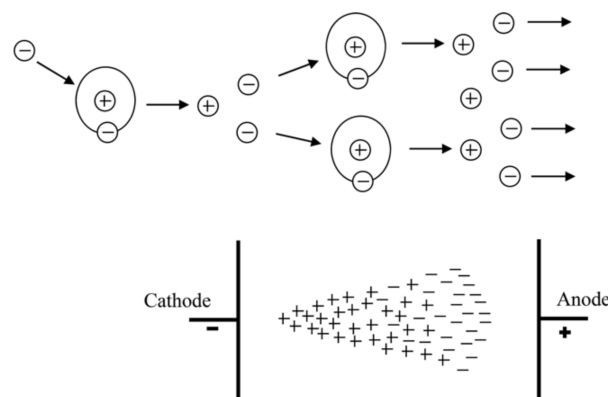


Figure 4.1: The Avalanche production process inside a RPC gap. (Top) The initial process and the secondary electron/ion generation. (Bottom) The overall charge distribution of an Avalanche between the electrodes. Source: [94].

1342 The number of particle composing the avalanche can be expressed as (assuming constant pres-  
1343 sure) [94]:

$$n_e = n_0 e^{\alpha d} = n_0 A, \quad (4.1)$$

1344 where  $n_0$  is the number of initial electrons initiating the avalanche,  $A$  is the *gas gain*, or *multiplication*  
1345 *factor* and  $d$  is the distance since the avalanche creation. This is also known as Townsend theory  
1346 for discharges and  $\alpha$  is the first Townsend coefficient.

1347 When the positive ions bunch reaches the cathode, under certain conditions (if the first ionization  
1348 energy of the ion is greater than the work function of the cathode), the recombination of the ion  
1349 with the electrode material might release electrons which will also follow the electric field. The  
1350 relative probability (with respect to the primary electron emission) of this emission to happen ( $\gamma_+$ )  
1351 is called the second Townsend coefficient.

$$n_+ = n_0 A \gamma_+. \quad (4.2)$$

1352 Another process which can occur is the secondary photoelectron production, described by a similar  
1353 equation as above:  $n_{pe} = n_0 A \gamma_{ph}$ . This production is mostly related to de-excitation of molecules  
1354 and atoms in vicinity of the avalanche. The produced photons might initiate new ionization process.

1355 As an alternative to the Townsend theory, Raether, Meek, and Loeb, proposed the *streamer-leader*  
1356 *theory* [95]. This theory is valid when there is a high enough concentration of produced ions. This  
1357 critical value is called Raether limit.

$$n_0 A > 10^8 \text{ electrons} \quad (4.3)$$

1358 In this limit, the electric field created by the space distribution is high enough to be same order  
1359 of the external field. In the vicinity of the head (or tail) of the avalanche the field gets disturbed  
1360 and intensified. The intensification of the field enhances the ionization effect and give rise to  
1361 secondary avalanches (photoelectrons). The intensified field also makes the photoelectrons produced  
1362 travel towards the head (positive ions). Their antionation generates more UV radiation and more  
1363 secondary avalanches. This whole process is called **Streamer**. If no quenching is imposed, the  
1364 streamer might evolve to a spark, fully discharging on the electrodes. If the concentration of  
1365 electrons is high enough, the avalanche tail (electrons) might also give rise to a streamer (namely,  
1366 negative streamer). Figure 4.2 illustrates the different subprocess related to streamer production.

1367 A RPC where most of the charge multiplication process happens in the form of a streamer is said  
1368 to be working in **Streamer Mode**. The advantage of the of the streamer mode is the high induced  
1369 charge which is easily caught by non-sensitive readout electronics. On the other hand, the streamer  
1370 mode, because of its highly associated charge, will have a impact in the rate capability of the  
1371 detector (the local dead time will be higher).

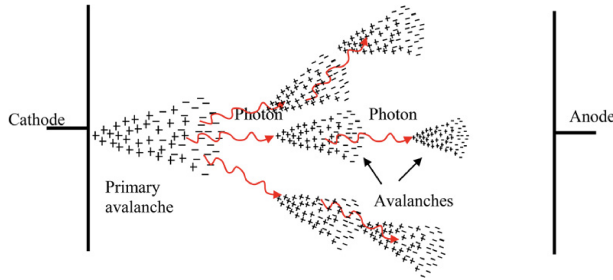


Figure 4.2: Streamer formation process. The distorted electric field around the high positive charge concentration enhances the ionization process, initiating secondary avalanches. Source: [94].

1372 Because of the high background environment of LHC, the CMS RPC operates in **Avalanche Mode**,  
1373 where de discharge is highly quenched and very well localized. On the other hand, a very sensitive  
1374 readout electronics is required to cope with the high rate demanded.

1375 A good review of electrical discharge on gases can be found at [94].

## 1376 4.2 CMS Resistive Plate Chambers

1377 At CMS, the Resistive Plate Chamber are installed in both the barrel and endcap region, forming  
1378 a redundant system with the DT (barrel) and CSC (endcap). As described in the CMS Muon  
1379 Technical Design Report (Muon-TDR) [78], the RPC are composed of 423 Endcap chambers and  
1380 633 barrel chambers. Figure 4.3 presents a picture of the CMS RPCs installed on station RE+4 of  
1381 the Endcap.

1382 Each chamber consists of two gas gaps (double gap), 2 mm tick each, made of Bakelite (phenolic  
1383 resin) with bulk resistivity of  $10^{10} - 10^{11} \Omega m$ . The choice of the bulk resistivity of the electrode has  
1384 high impact on the rate capability of the detector.

1385 Each gap has its external surface is coated with a thin layer of graphite paint, which acts as  
1386 conductive material, distributing the applied high-voltage (HV). On top of the graphite a PET  
1387 film is used for isolation. A sheet of copper strips is sandwiched between the gaps. Everything is  
1388 wrapped in aluminum case.

1389 The double gap configuration increases the efficiency of the chamber, since the signal is picked up  
1390 from the OR combination of the two gaps. A chamber with only one gap working, loses around  
1391 15% of efficiency, even though, this can be recovered by increasing the HV applied during operation  
1392 mode (working point - WP).

1393 A characteristic that differentiate the CMS RPC from previous RPC application in HEP is the  
1394 operation mode. A RPC at CMS, operates in avalanche mode, while previous experiments used the  
1395 streamer mode. Both modes are related to the applied HV, in commitment with the strength of  
1396 the generated signal, and are capable of generate a well localized signal, which can be picked up by  
1397 the readout electronics, but the avalanche mode offer a higher rate capability around  $1 \text{ kHZ}/\text{cm}^2$ ,

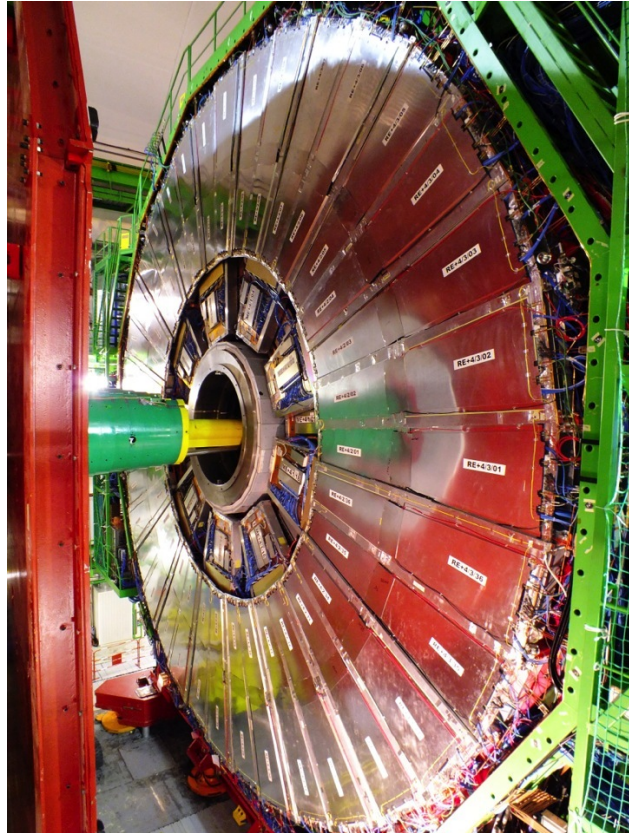


Figure 4.3: RPC chamber on installed on station RE+4 of CMS Endcap. Source: [96].

1398 while the streamer mode goes up to  $100 \text{ Hz/cm}^2$ . The high rate capability is a key factor in order  
 1399 to cope with requirements of the LHC luminosity, specially in the high background regions.

1400 Besides the rate capability, the key factors that driven the CMS RPC design were: high efficiency ( $>$   
 1401 95%), low cluster size ( $> 2$ ) for better spatial resolution (this reflects in the momentum resolution)  
 1402 and good timing in order to do the readout of the signal within the 25 ns of a LHC bunch cross  
 1403 (BX) and provide it to the CMS trigger system. These requirements have implications in the choice  
 1404 of material, dimensions, electronics and gas mixture.

1405 In the barrel, along the radial direction, there are 4 muon layers (called stations), MB1 to MB4.  
 1406 MB1 and MB2 is composed of a DT chamber sandwiched between two RPC chambers (RB1 and  
 1407 RB2) with rectangular shape. The stations MB3 and MB4 have only one RPC (RB3 and RB4) are  
 1408 composed by two RPC chambers (named - and + chambers with the increase of  $\phi$ ) attached to one  
 1409 DT chamber, except in sector 9 and 11, where there is only one RPC. RE4, sector 10 is a special  
 1410 case, since it is composed of four chambers (-, -, + and ++). These stations are replicated along  
 1411 the z direction in five different wheels of the CMS (W-2, W-1, W0, W+1 and W+2) and in twelve  
 1412 azimuthally distributed sectors (S1 to S12). Figure 4.4 show the different barrel stations and wheel.

1413 In the endcap, the RPC chambers have a trapezoidal shape and are distributed in four disks (or  
 1414 stations) each side (RE $\pm 4$ , RE $\pm 3$ , RE $\pm 2$ , RE $\pm 1$ ), each one with 72 chambers. CMS split up its  
 1415 disks in 3 rings, along the radial direction, and 36 sector in the azimuthal angle. RPCs are present  
 1416 in the two outer rings (R2 and R3), in all 36 sectors. The RE $\pm 4$  are special cases, since these

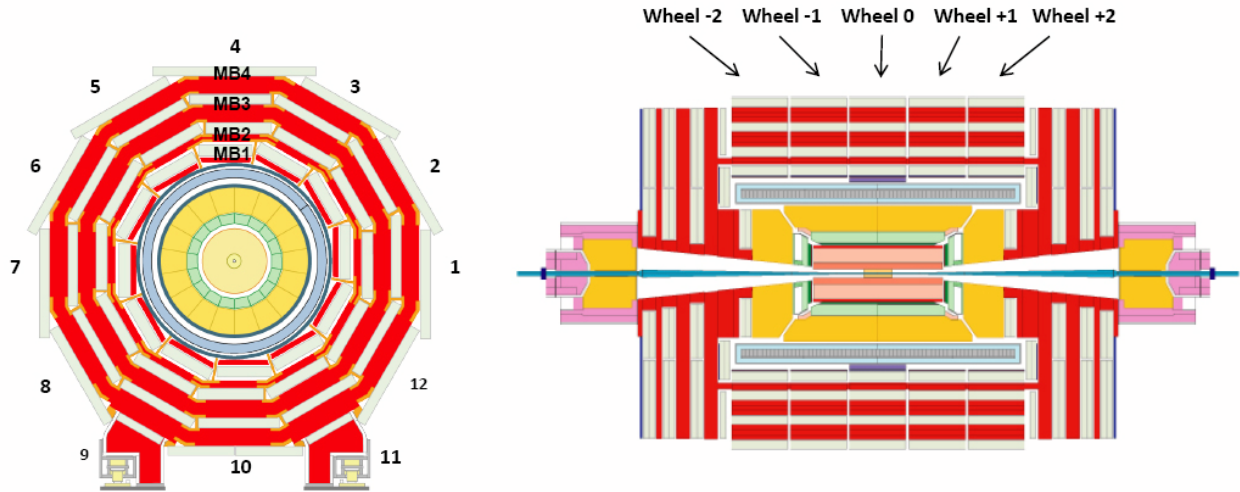


Figure 4.4: R- $\phi$  (left) and R-Z (right) projections of the barrel Muon System.

1417 chambers were installed only in 2014, a design choice was made the mechanically attached R2 and  
1418 R3 chambers, each sector, in what is called, a super-module. Figure 4.5 show the different endcap  
1419 disks.

1420 The length of the strips is chosen, for both barrel and endcap, in such a way to control the area of  
1421 each strip, in order to reduce the fake muons, due to random coincidence. This has to do with the  
1422 time-of-flight and signal propagation along the strip. In the barrel, each chamber readout is divided  
1423 in two regions (rolls), called forward and backward (along increasing  $|\eta|$ ) <sup>1</sup>. In the endcap, the strips  
1424 are divided in 3 regions, called partitions A, B and C (from inside the detector to outside).

1425 The gas mixture used in the CMS RPCs is composed by C2H2F4 (Freon R-134a, tetrafluoroethane),  
1426 C4H10 (isobutane), SF6 (sulphur hexafluoride) (95.2 : 4.5 : 0.3 ratio) and with controlled humidity  
1427 of 40% at 20-22 °C. The Freon is used to enhance the ionization and charge multiplication that  
1428 characterizes the avalanche, while the isobutane is introduced for quenching proposes, in order to  
1429 reduce the secondary ionizations that could lead to formation of streamers and the SF6 is used  
1430 to reduce the electron background. The choice of Freon over other gases, i.e. argon-based and  
1431 helium-based, was motivated by previous studies [97, 98].

1432 Since its R&D, the RPC have shown good performance over aging. This is even historical over  
1433 previous RPC experiments [99–105]. Even the most recent studies of aging, taking into account  
1434 future LHC conditions (High-Luminosity LHC - HL-LHC) plus a safety margin of 3 times the  
1435 expected background ( $600 \text{ Hz/cm}^2$ ) have shown good aging hardness [106].

#### 1436 4.2.1 Performance

1437 The RPCs, for the CMS experiment, contribute mainly with triggering inputs, due to its very good  
1438 time resolution. The important parameters which are monitored to evaluate the RPC performance  
1439 are the efficiency and cluster size. The former is related to the ratio of the registered hits over the

<sup>1</sup>Some chamber are divided in three rolls, forward, middle and backward, for trigger propose.

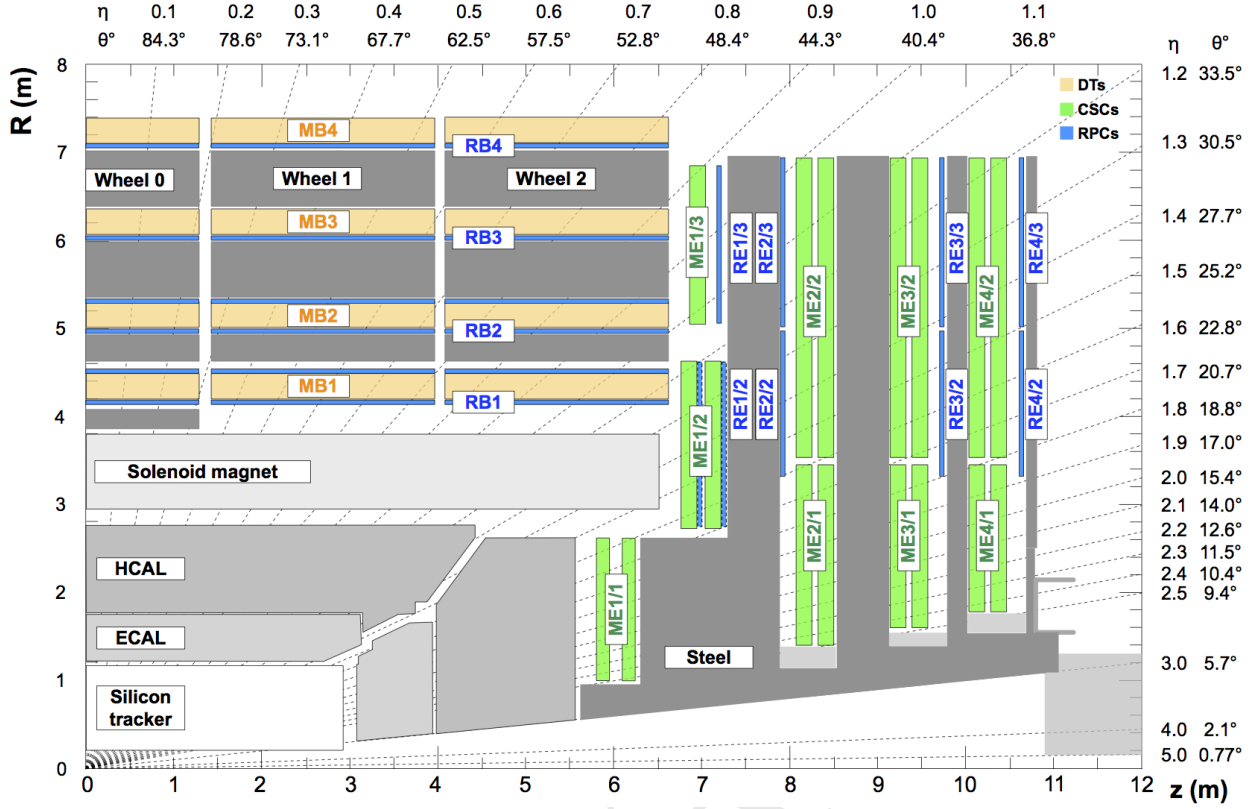


Figure 4.5: R-Z projections of the endcap Muon System (positive Z side). This is the same configuration for the  $36\phi$  sectors.

number of muons that passed through the chamber, while the former one is the number adjacent strip (minimal readout unit) that were fired (activated) per hit. Figures 4.6 and 4.7 present the historical distribution of efficiency and cluster size as a function of the integrated luminosity collect during Run2.

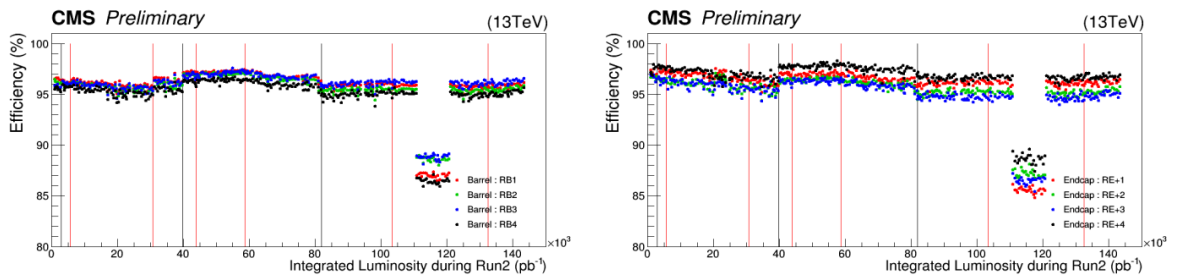


Figure 4.6: RPC efficiencies (per chamber) over Run2 Integrated Luminosity for Barrel (left) and Endcap (right). Red lines indicates technical stops (TS) while grey ones indicates Year-End-Technical stops (YETS). The drop in the efficiency around  $110\text{ pb}^{-1}$  is related to a known operation mistake. Source: [107].

In general, the RPC system operates with efficiency above 95% and cluster size smaller than 3 (a good parameter established during the design phase). The importance of the efficiency is a less complicated concept to catch, on the other hand, the cluster size might not be so straight forward. The optimal regime of RPCs operation at CMS is the avalanche mode, in which the

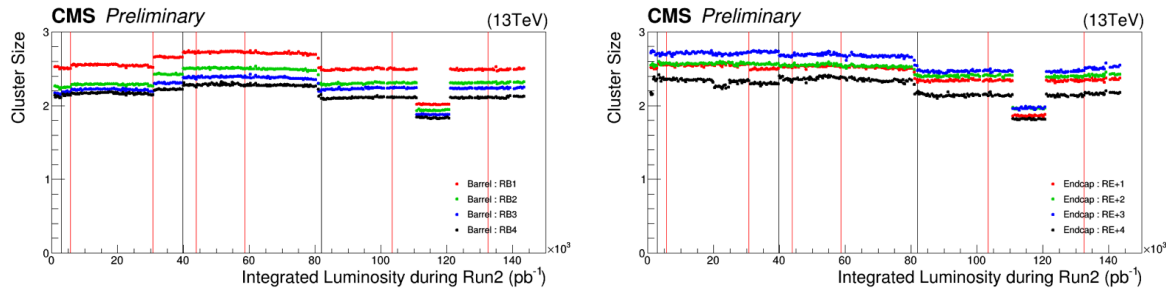


Figure 4.7: RPC cluster size (CLS - per chamber) over Run2 Integrated Luminosity for Barrel (left) and Endcap (right). Red lines indicates technical stops (TS) while grey ones indicates Year-End-Technical stops (YETS). The drop in the cluster size around  $110 \text{ pb}^{-1}$  is related to a known operation mistake. Source: [107].

1448 electrical discharge is constrained in a millimeter level size region. Another operation mode is the  
 1449 streamer mode, in which the initial discharge might trigger secondary ones, e.g. by the emission of  
 1450 unquenched photons. A streamer discharge is capable of fire neighbor strips, increasing the cluster  
 1451 size. Operating in avalanche mode is fundamental to keep the RPCs capable of dealing with the  
 1452 high background environment of CMS.

1453 To keep the mean cluster size under control ( $< 3$ ) is important to guarantees enough spatial reso-  
 1454 lution for the measurements (the geometrical position of a hit is the midpoint of the cluster) and  
 1455 ensures that the system has enough rate capability to operate, since a RPC with a high sensitive  
 1456 front-end electronics (necessary for the avalanche mode operation) could be degraded by pileup of  
 1457 dead time on many channels, including electronics noise, streamers, darks counts and other sources  
 1458 of background.

1459 A third important parameter to be measured and controlled in a RPC system, under the LHC  
 1460 conditions, is the current due to the high voltage applied. This current is known to be proportional  
 1461 to the total charge released in each electrical discharges and to the hit rate on the chamber. The  
 1462 voltage applied is divided, as in a series circuit, between the electrodes and the gap. At increasing  
 1463 background, the current also increases and, since the applied voltage is constant, the voltage across  
 1464 the gap is reduced in favor of the voltage across the electrodes. This reduction of effective voltage  
 1465 on the gas, might have an impact on its gain, imposing a reduction on the detector sensitivity.

1466 Figure 4.8 presents the ohmic currents <sup>2</sup> in different regions of the detector, from 16<sup>th</sup> of April,  
 1467 2018 to 2<sup>nd</sup> of December, 2018. It is clear how the stations subjected to higher background ( $\text{RE}\pm 4$   
 1468 -  $40 \text{ Hz/cm}^2$ ) are subjected to a degrading factor that increases with the luminosity (background  
 1469 rate) and decreases when the detector is powered off. This effect is supposed to be related with  
 1470 the Hydrogen Fluoride (HF) production inside the gap, due to the electrical discharges. HF is a  
 1471 conductivity molecule, which can potentially attach to the internal surface of the gap, reducing  
 1472 the overall resistivity. The HF production can be controlled by properly tuning the gas flow as  
 1473 a function of the background that the chamber is subjected. HF concentration can also lead to

<sup>2</sup>Current at 6500 V, which is below the typical working point of a CMS RPC (around 9500 V). In this region, no charge multiplication effect take place and chamber current is governed only by Ohm's Law.

<sup>1474</sup> permanent degradation of the gap, due to its chemical properties. Keeping the currents levels as  
<sup>1475</sup> low as possible is important for aging proposes.

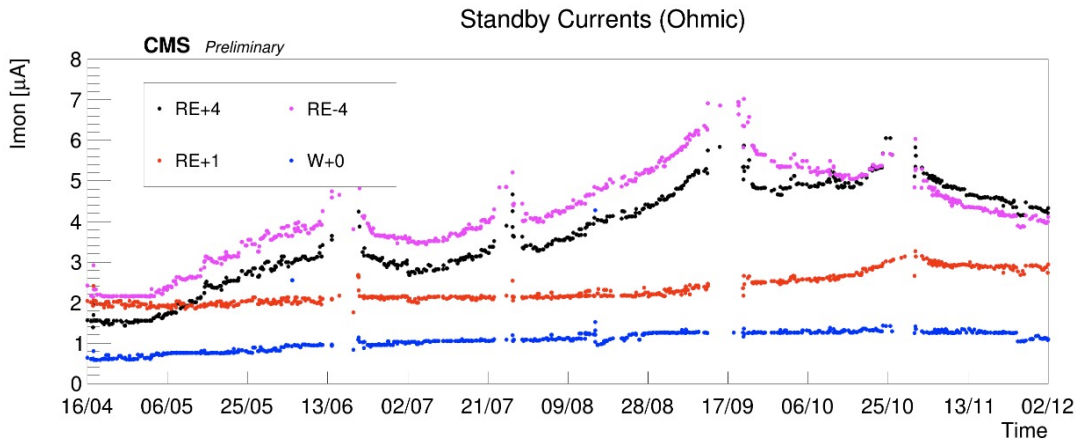


Figure 4.8: Ohmic current history of W+0, RE+1, RE+4 and RE-4. The blank regions, from time to time, corresponds to technical stops (TS), when the detector is off. Source: [107].

<sup>1476</sup> A review of the RPC performance during Run2 can be found at [107].

### <sup>1477</sup> 4.3 Contribution to the CMS RPC project

<sup>1478</sup> During the curse of this study, a head collaboration of our research group and the CMS RPC  
<sup>1479</sup> project was established. Many contributions were given to the project as part of the graduation as a  
<sup>1480</sup> experimental particle physicist, with focus on getting acquaintance with a subsystem technology and  
<sup>1481</sup> give a meaningful collaboration to the detector operation. Those are considered by the community  
<sup>1482</sup> important steps on the student graduation.

<sup>1483</sup> Below it is described the contributions given to the CMS RPC project.

#### <sup>1484</sup> 4.3.1 RPC Operation - Shifts and Data Certification

<sup>1485</sup> The first activities done for the CMS RPC project were shifts for data certification of data taken.  
<sup>1486</sup> This certification is done by specialized people for different CMS subsystems and physics objects  
<sup>1487</sup> groups <sup>3</sup>.

<sup>1488</sup> This certification is done in order to ensure the quality of the date recorded based on the well  
<sup>1489</sup> functionality of each system during the data taking and the reconstruction of the physics objects in  
<sup>1490</sup> the expected matter. A certain collection of data (run) is said certificate when all subsystems and  
<sup>1491</sup> object experts agrees on this.

<sup>3</sup>Groups of reconstruction and performance experts for different high-level reconstructed objects from CMS, i.e. muons, taus, jets/MET, electrons/photons

Figure 4.9 shows, as an example of the luminosity delivered by the LHC, recorded one by CMS and the certified (validated), from the 22nd of April, 2016 to the 27th of October, 2016. Only certified data is available for physics analysis.

Shifts are a continuous weekly activity (specially during the data taking period), performed in a weekly basis, in order to ensure the availability of certified data, as soon as possible.

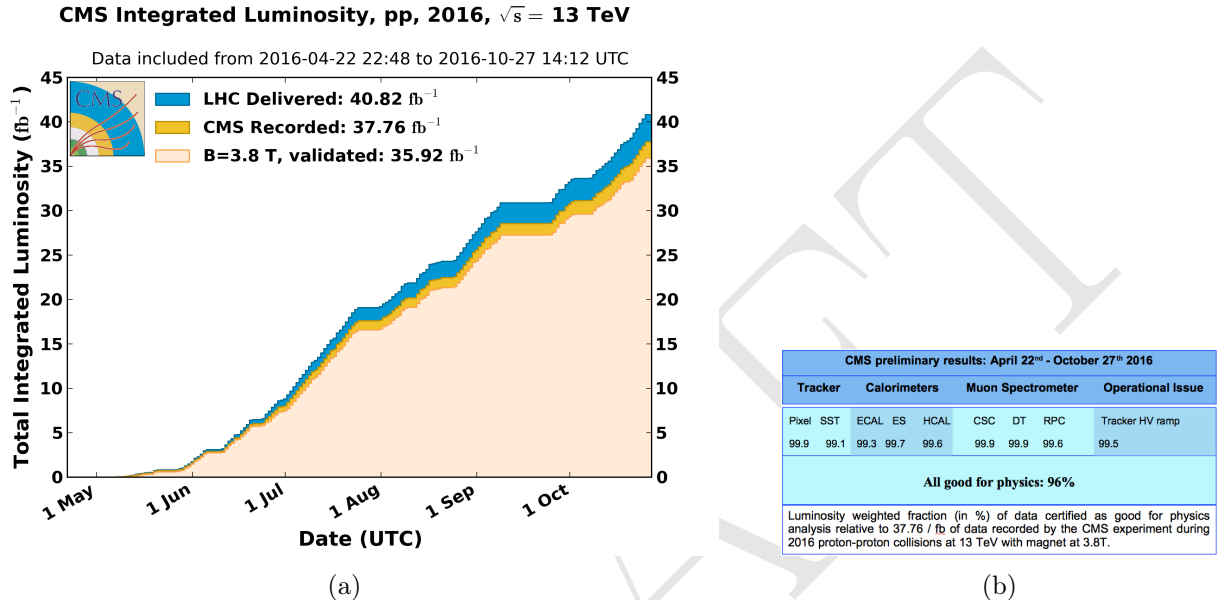


Figure 4.9: (a) Luminosity delivered by the LHC, recorded one by CMS and the certified (validated), from the 22nd of April, 2016 to the 27th of October, 2016. (b) Efficiency of the certification process for each subsystem, from the 22nd of April, 2016 to the 27th of October, 2016. Total CMS efficiency is above 90%. Source: [108]

## 4.4 RPC Online Software

On what concerns the Online Software (OS) of the CMS RPC system, the main contribution given was the upgrade of the Trigger Supervisor libraries.

The Trigger Supervisor is a web-based software, which run over the xDAQ backend and provides, through a modules organized in a tree system, called cells, a standard interface for the operation and monitoring of different system at CMS. In principle only systems which contribute directly to the L1 trigger should have a Trigger Supervisor implementation. This was the case for the RPC during the Run1. Since Run2, RPC contributes to the trigger indirectly, by providing data to the muon processors (CPPF, OMTF and TwinMux). The Trigger Supervisor implementation is a legacy from that period.

Each subsystem is responsible for its own implementation of the Trigger Supervisor, based on the functionalities that it wants to have (requirements). The xDAQ [109] is a middleware, developed by CERN and widely used at CMS, as a tool for control and monitoring of data acquisition system in

1510 a distributed environment. It is capable of providing a software layer for direct access of hardware  
 1511 functionalities and monitoring.

1512 The upgrade made (figure 4.10), consists in upgrade the higher level of the RPC online software.  
 1513 In summary, up to 2017, the online software, was using Scientific Linux 6 as operational system,  
 1514 which executed xDAQ 12, in turn, servers as backend for Trigger Supervisor 2. A upgrade of  
 1515 the operational system to Centos 7, demanded the upgrade to xDAQ 14. On top of that, Trigger  
 1516 Supervisor 2 would not work and had to be updated to Trigger Supervisor 5 in order to be functional  
 1517 in 2018.

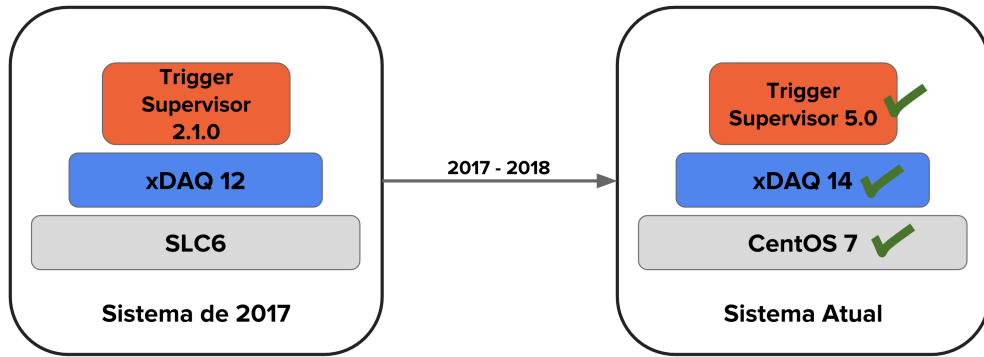


Figure 4.10: Upgrade of the RPC online software.

1518 Between versions 2 and 5 of Trigger Supervisor, part of the source-code had to be reworked, keep  
 1519 the majority of the code structures. Most of the changes were made in the front-end of the system.  
 1520 The standard JavaScript library Dojo [110], used in version2, was deprecated in favor of Google's  
 1521 Polymer[111]. The main reason for this change was to isolate C++ code from HTML, which  
 1522 was impossible with Dojo. This implied to rewrite all the screen of the RPC Trigger Supervisor  
 1523 implementation, as in figure 4.11.

1524 The upgrade was done in time to ensure the control and operation of the RPC for 2018 data taking.

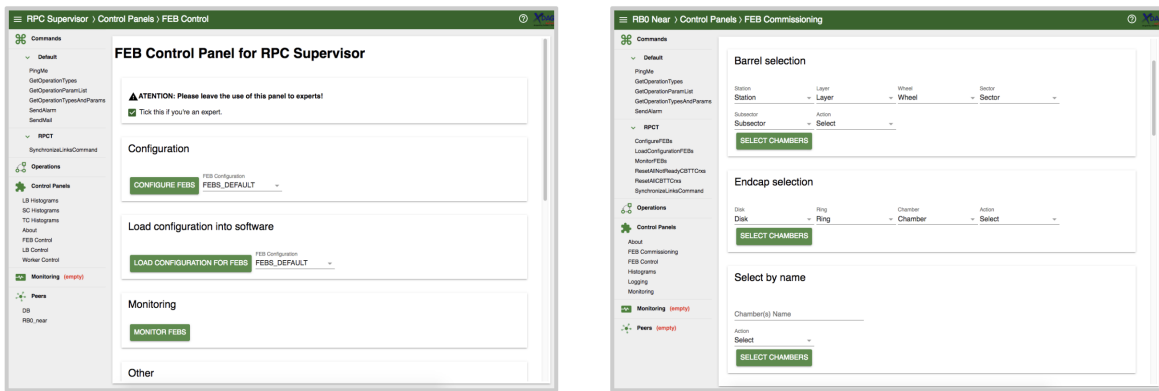


Figure 4.11: Example of the updated screens, using Trigger Supervisor 5.

#### 1525 4.4.1 Improved RPC R&D

1526 For the next 4 year of CMS activities it is foreseen the upgrade of the Muon Systems [78]. These up-  
 1527 grades are planned in order to extend the pseudorapidity coverage ( $\eta$ ) and to guarantee the operation  
 1528 conditions of the present system in the HL-LHC (High Luminosity LHC) era. The RPC (Resistive  
 1529 Plate Chambers) [78] subsystem, it will have maintenance of the present chambers and installation  
 1530 of new chambers in the region of  $|\eta| < 1.8$  para  $|\eta| < 2.4$  [112]. These new chambers (**Improved**  
 1531 **RPC - iRPC**) will be added in the most internal part of the muon spectrometer, RE3/1 e RE4/1,  
 1532 as in Figure 4.12.

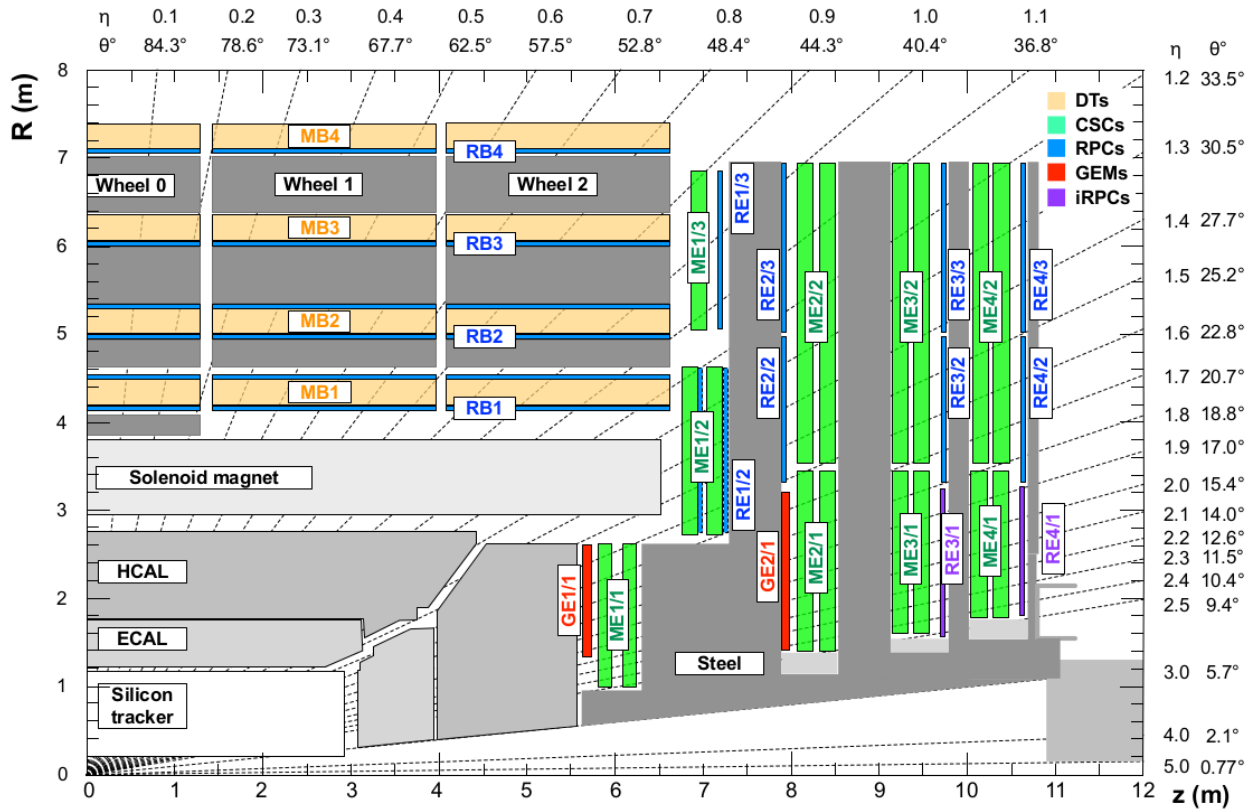


Figure 4.12:  $\eta$  projection of the Muon System subdetectors. In purple, is labeled the iRPCs to be installed during the CMS upgrade.

1533 Even though this region is covered by the CSC detectors CSC (Cathode Strip Chambers), there  
 1534 are some loss of efficiency due to the system geometry. The installation of additional chambers will  
 1535 mitigate this problem and potentially increase the global efficiency of the muon system. The new  
 1536 chamber, called iRPC (*improved RPC*), will be different from the present one. For a luminosity of  
 1537  $5 \times 10^{34} cm^{-2}s^{-1}$  the neutrons, photons, electrons and positrons background in the high  $|\eta|$  region  
 1538 is expected to be around  $700 Hz/cm^2$  (for the chambers in RE3-4/1). Applying a safety factor  
 1539 of 3, the new chambers should support up to  $2 Hz/cm^2$  of gamma radiation and still keep more  
 1540 than 95% of efficiency. Studies indicate, so far, that the use of High Pressure Laminates (HPL) for  
 1541 the double gap chambers is the most suitable choice. In order to reduce the aging and increase the  
 1542 rate capability, the electrodes and the gap size should be reduced in comparison with the present  
 1543 system.

1544 One of the challenges for the R&D of the iRPC chambers is measuring their performance in  
1545 a high radiation environment, as the one for HL-LHC. For this, the CMS RPC project uses the  
1546 Gamma Irradiation Facility (GIF++) [113], at CERN. The GIF++ is located at the H4 beam line  
1547 in EHN1 providing high energy charged particle beams (mainly muon beam with momentum up to  
1548 100 GeV/c), combined with a 14 TBq 137-Cesium source. In the GIFF++ it is possible to achieve  
1549 the HL-LHC total dose in a much reasonable amount of time. With the shutdown of LHC, the  
1550 muon beam source is also off and will stay like this for 3 years. This means that the only muon  
1551 sources for studies in GIF++ are cosmic muons.

1552 In order to create a trigger system for iRPC R&D, the usual procedure is to use scintillators, on the  
1553 top and on the bottom of the chamber. This is effective, but in a high gamma radiation environment,  
1554 scintillators can be very sensitive which could lead to an undesirable amount of fake triggers which  
1555 can degrade the measurements. Also, if one wants to covers a large area with scintillators, this can  
1556 be expensive and they will not provide any means of tracking to measuring not only the global, but  
1557 also the local chamber performance.

1558 To provide a solution, the CMS RPC got in agreement with the LHCb [114] Muon Project to use  
1559 their Multiwire Proportional Chambers (MWPC) [115], which were removed from LHCb, to be  
1560 replaced by new chambers, and use them as trigger and/or tracking system at GIF++. This cham-  
1561 bers, by design, have relatively low gamma sensitivity, already have some 1-dimensional resolution  
1562 ( $O(cm)$ ) and, the biggest advantage, with respect to any other gaseous particle detector option:  
1563 LHCb has hundreds of vacant chambers. Any other detector would have to be build.

1564 Not going in details of the MWPC technology nor the LHCb chamber construction [116], these  
1565 chambers have a total active area of  $968 \times 200 \text{ mm}^2$  divided 2 layers (top and bottom) of 24  
1566 wire pads ( $40 \times 200 \text{ mm}^2$ ) composed of around 25 wires/channel, grouped by construction. Each  
1567 chamber is equipped with 3 FEBs (Front-End Boards) with 16 pads each.

1568 A channel is a logical combination of a top layer (pads) and a bottom layer readout. These readouts  
1569 can be combined in AND or OR logics. One can have 8 channels per FEB, each channel being a  
1570 logical combination of top and bottom pads. In this mode they are called AND2 and OR2. It is  
1571 also possible to have the FEB configured in a 2 channels mode, each one corresponding to one sixth  
1572 of the total readout pads. In this mode, all the pads can be combined in OR (called OR8) or they  
1573 can be AND'ed in top and bottom pads and then group in OR (called OR4AND2). Figures 4.13  
1574 and 4.14 presents a logical diagram for each readout mode.

1575 The nominal gas mixture for these chambers is Ar/CO<sub>2</sub>/CF<sub>4</sub> (40:55:5). For a matter of simplicity,  
1576 it was used an already available similar gas line in the same building, used by CMS CSC (Cathode  
1577 Strip Chamber) [78], which has a similar composition (40:50:10). Optimal conditions are obtained  
1578 with 2 to 4 liters/hour of gas flux and 2.65 kV of applied voltage.

1579 Figure 4.15 shows the setup that was prepared for commissioning of this chambers. It was mounted  
1580 two chambers on top of another (chambers A and B) above an RPC R&D chamber and two other  
1581 chambers on the bottom (chambers C and D). These four MWPC will be used as telescope for  
1582 the RPC chamber. All the services were mounted in rack, as in Figure 4.15. This includes power  
1583 supply (low voltage and high voltage), distribution panel, VME crate and boards for FEB control,

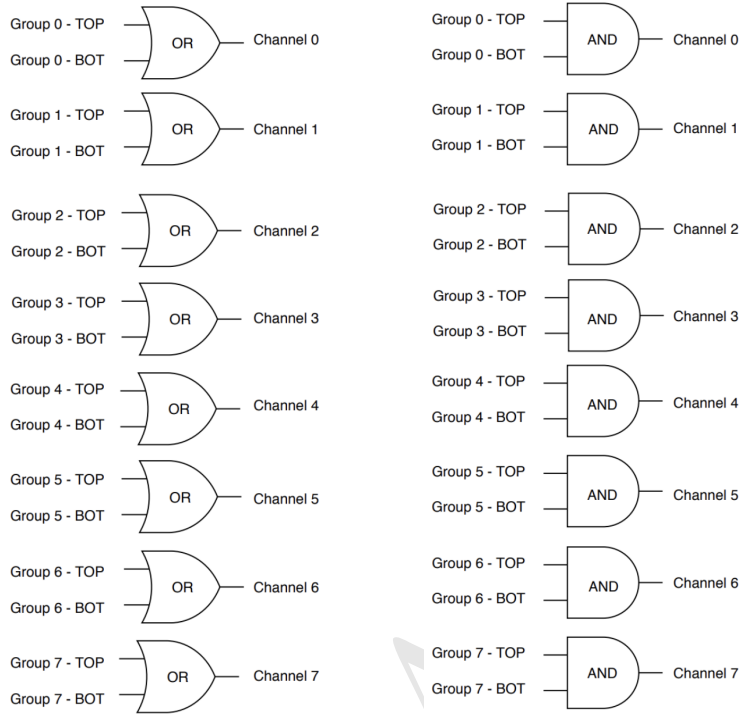


Figure 4.13: FEB configured 8 channels modes. Group should be understood as wire pad. Left: Logical diagram for OR2. Right: Logical diagram for AND2.

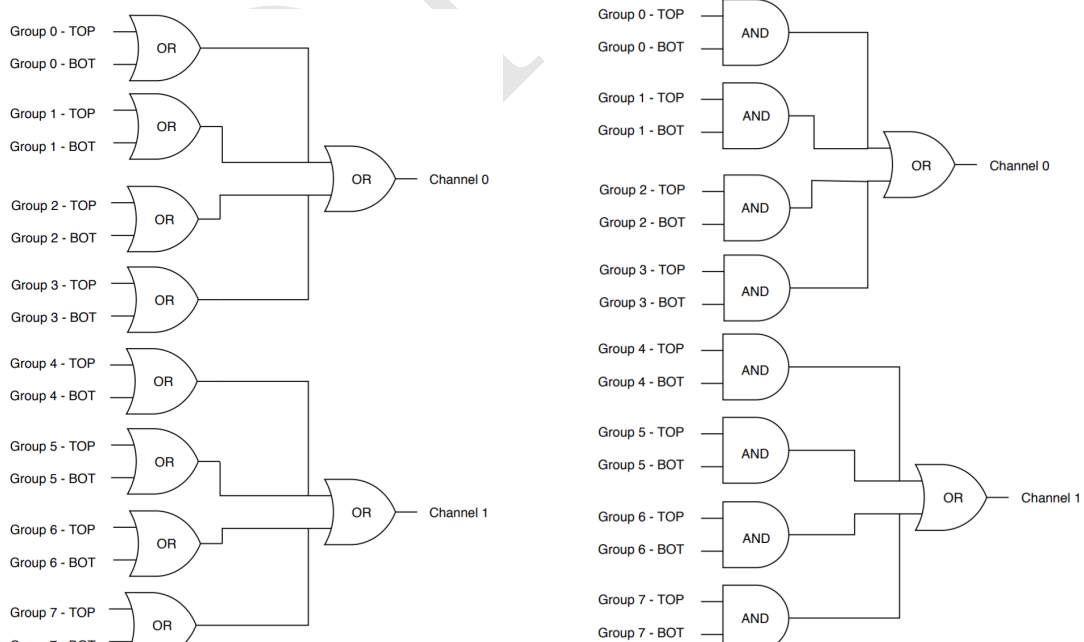


Figure 4.14: FEB configured 2 channels modes. Group should be understood as wire pad. Left: Logical diagram for OR8. Right: Logical diagram for OR4AND2.

1584 computer for control (high voltage, and FEB control) and NIM crate and boards for LVDS to NIM  
 1585 signal conversion, logics and counting.

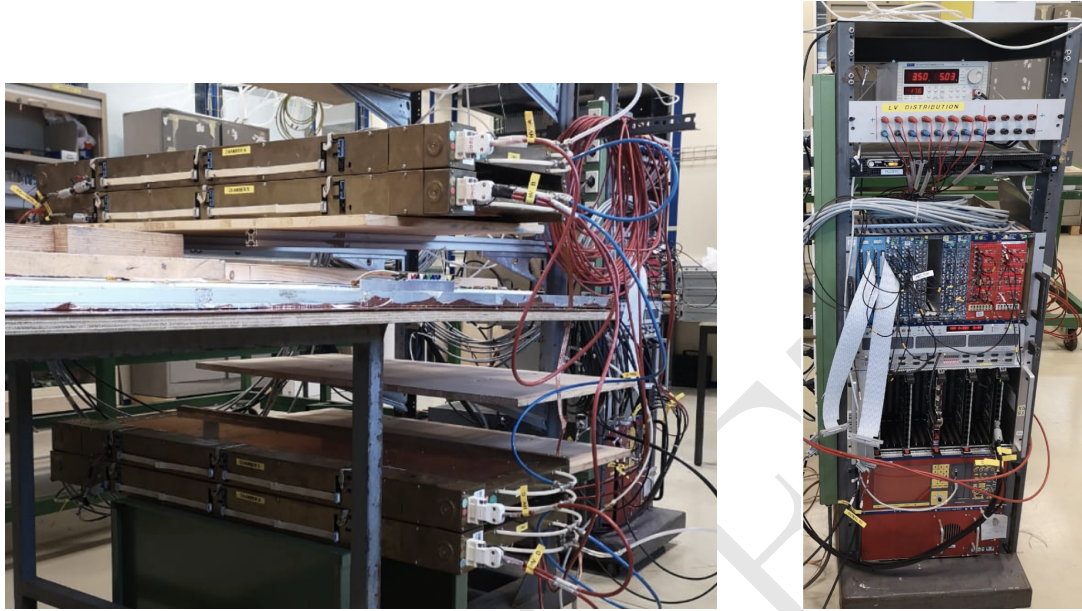


Figure 4.15: Left: Setup mounted for commissioning. Two MWPC chamber on the top (chambers A and B) and two (chambers C and D) on the bottom with a RPC R&D in the middle. Right: Rack with all the services for the operation of these chambers.

1586 Due to the short amount of time available for the commissioning, only two measurements were made  
 1587 with these chambers. They were meant to be a proof of concept for future activities.

1588 The first measurement was to measure the coincidence rate of two chambers as a function of the  
 1589 distance between the two top planes (Figure 4.16). This measurements were done with nominal  
 1590 working point, with one FEB configured in 2 channels mode with 7 pC threshold, in (160 mm x  
 1591 160 mm) area per chamber. One can observe that, if we go for a telescope trigger in the order of  
 1592 1 meter of separation between the chamber, the logical combination chosen has negligible effect in  
 1593 the coincidence rate. Also, the fits can be used to estimate the rate in a configuration with chamber  
 1594 on the roof and under the floor. This could be the case of a universal trigger, to be mounted in  
 1595 GIF++ with these chamber.

1596 The second measurement consists on evaluate the impact of  $\gamma$  background by placing a small Cs-  
 1597 137 source on top of the chamber A (Figure 4.17). For this measurement, the distance between top  
 1598 planes of each pair of chamber (A to B and C to D) is 65 mm, while the distance between the top  
 1599 planes of A and C is 570 mm. It is clear they source has an impact on chamber A rate, but this is  
 1600 negligible when we take into account the coincidence between two chambers.

1601 This two measurements were enough to validate this chambers as possible trigger pro RPC R&D  
 1602 with cosmic muons in the laboratory and at GIF++. The next steps would be use this MWPC  
 1603 chamber to implement a tracking system from triggering. This would demand some developments,  
 1604 since, due to bandwidth restrictions, the signal from each FEB would have to go to a programmable  
 1605 fast electronics, i.e. a FPGA, which would reconstruct muon tracks and provide the trigger to the

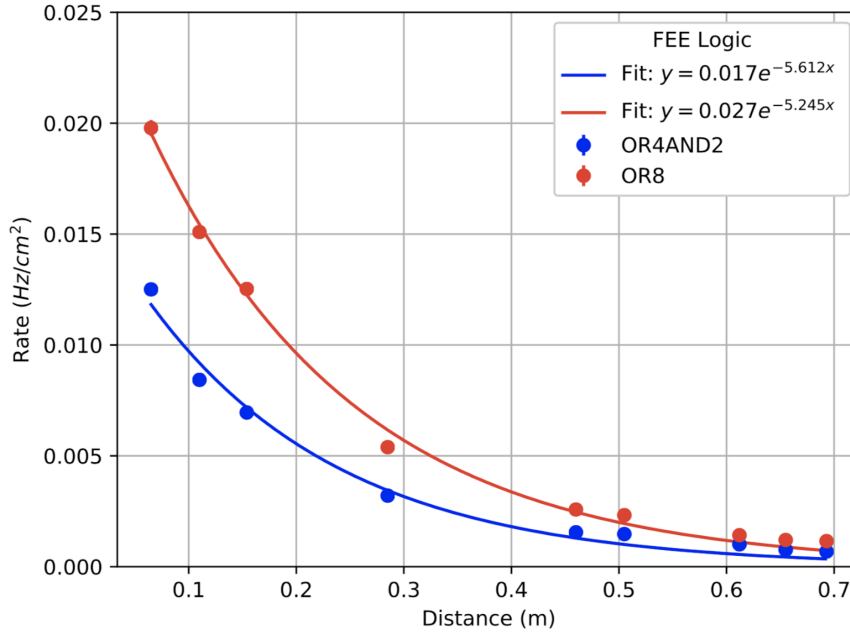


Figure 4.16: Coincidence rate of two chambers with respect to an arbitrary distance between the two top planes. Measured in 10 minutes, for 2 logical combinations (OR8 and OR4AND2). Applied high voltage: 2.65 kV. Threshold: 7 pC. Active area: readout of 160 mm x 160 mm per chamber.

<sup>1606</sup> DAQ system. This can be done by placing the two pair of chambers (AB and CD) in orthogonal  
<sup>1607</sup> configuration and read the signal in a CAEN V2495 board [117].

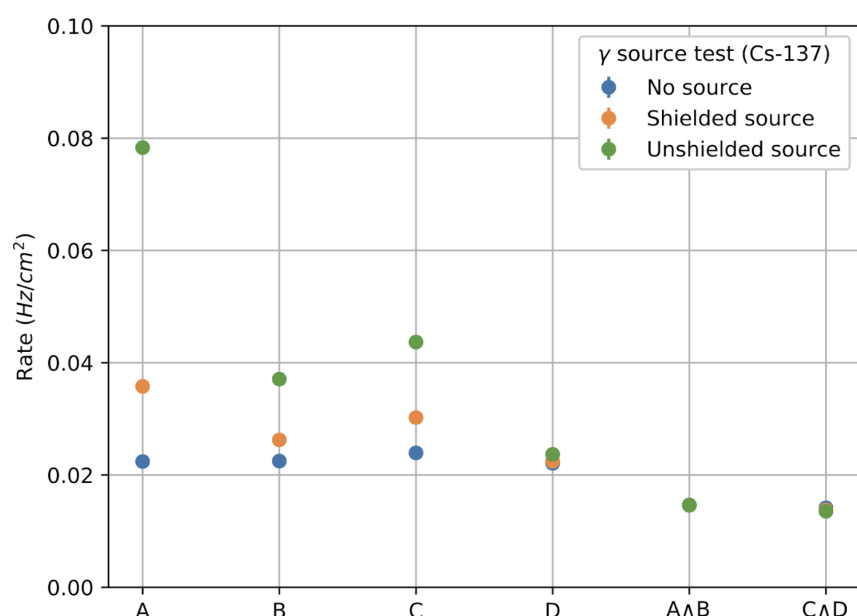


Figure 4.17: Individual rates (chambers A, B, C and D) and coincidence rates for two chambers (A AND B, C AND D), for without  $\gamma$  source (blue), a shielded  $\gamma$  source (orange) and an unshielded  $\gamma$  source (green). Source sitting on top of chamber A. Applied high voltage: 2.65 kV. Threshold: 7 pC. Active area: readout of 160 mm x 320 mm per chamber. Logical combination: AND2

**1608 4.4.2 LS2 and the RPC Standard Maintenance**

1609 In December 2018, the LS2 (Long Shutdown 2) was started. This a period in which the LHC and  
1610 its detectors (CMS included) stop their operation for maintenance and upgrade. The LS2 will go  
1611 up to 2021, when LHC and CMS restart the data taking with the Run3.

1612 During the LS2 it is being installed services for the new chambers (gas pipes, low voltage (LV), cables,  
1613 signal and control optical fibers, high voltage (HV) cable and support equipment, and HV/LV power  
1614 supplies), as well as continuity to the to the RPC R&D studies, besides the reparation of broken  
1615 elements of the present system, i.e. chamber in the barrel region which present gas leak problems,  
1616 maintenance of the LV and HV connectivity and power system, maintenance of the control system  
1617 of problematic chambers (Front-Ends boards, cabling and Distribution Boards) and the dismount  
1618 and reinstallation of four stations in the endcap (RE4) on both sides of CMS [118].

1619 What concerns the standard maintenance of the present RPC system, the main LS2 activities in  
1620 which the student was involved, can be divided in three main tasks: (a) HV maintenance, (b) LV  
1621 and control maintenance and (c) detector commissioning.

**1622 HV maintenance**

1623 A key factor of and RPC performance is the applied high voltage (HV). The CMS RPC achieve  
1624 their optimal performance with, around, 9.5 kV applied in each gap. This voltage is in the range  
1625 of the dielectric breakdown of many gases, which could lead to potential current leakages, if some  
1626 part of the system is damaged, poorly operated or badly installed. If the currents are high enough  
1627 this can make impossible the operation of the chamber. In cases like this, during the operation  
1628 period (data taking), the problematic HV channel is identified and turned off (each chamber has  
1629 two channels, one for each lawyer of gaps). Chambers in this situation are said to be operating in  
1630 single gap mode (SG).

1631 The goal for the HV maintenance is to, now that the CMS is off and the chambers are accessible,  
1632 identify which part of the HV supply system is causing the current leak and fix it the best way  
1633 possible. Usually the problem is beyond the power supply, very often connectors or the gap itself  
1634 are damaged.

1635 The CMS RPCs uses two kind of HV connectors, monopolar and tripolar connector. The monopolar  
1636 are used to connect the chamber to the power supply. If mounted properly, rarely they present  
1637 problems. The connection to the chamber is made by tripolar connectors, in which the ground and  
1638 the HV for both gaps arrives to the chamber in a single connector, for simplicity and to save space in  
1639 the patch panel. Unfortunately these connectors are relatively fragile, and they could be a potential  
1640 source of leak, specially if they were poorly mounted, badly operated or with aging itself. Also,  
1641 since this was a connector made exclusively for the CMS RPC system, some design choices had to  
1642 be improved after the installation of other chamber. Those installed with old batches of tripolar  
1643 connectors are sensitive ones. The reparation of this connectors consists in isolate the connector  
1644 from the chamber and power it up to 15 kV (maximum voltage allowed by the system). If the tested

1645 connector is broken one will observe a very fast increase in the current of the HV channel. The only  
 1646 solution to this kind of problem is to replace the connector.

1647 On the other hand, if the connector is powered isolated and pass the test, the problem beyond  
 1648 the connector (assuming that the power system have already been tested), i.e. inside the chamber.  
 1649 When a chamber is in SG mode it means that a full layer is off, but not necessarily all the gaps  
 1650 in that layer are bad (a RPC can have up to three per layer). In this situation, the procedure  
 1651 consists in cutting the cables that comes from the gaps to the chamber side connector one by one  
 1652 and identify which gap of the problematic layer is the broken by powering it. Once identified, this  
 1653 gap should be solated and the other ones reconnected. The broken gap is unrecoverable, since it is  
 1654 inside the chamber, but 5% to 10 % of efficiency can be retaken, without changing the applied HV  
 1655 and increasing the longevity of the chamber.

1656 Another contribution to the HV maintenance was the proposal of a procedure to replace the prob-  
 1657 lematic tripolar connector by a monopolar (also called jupiter) connector, which are known for being  
 1658 much more stable and reliable. The figure 4.18 (left) show the designed adapter for the chamber  
 1659 patch panel which would made this change possible. Figure 4.18 (right) shows a tryout of a cham-  
 1660 ber in which this procedure was tested. The proposal was presented to the RPC community and  
 1661 approved to be used from now on. Technical drawings and instructions were provided.

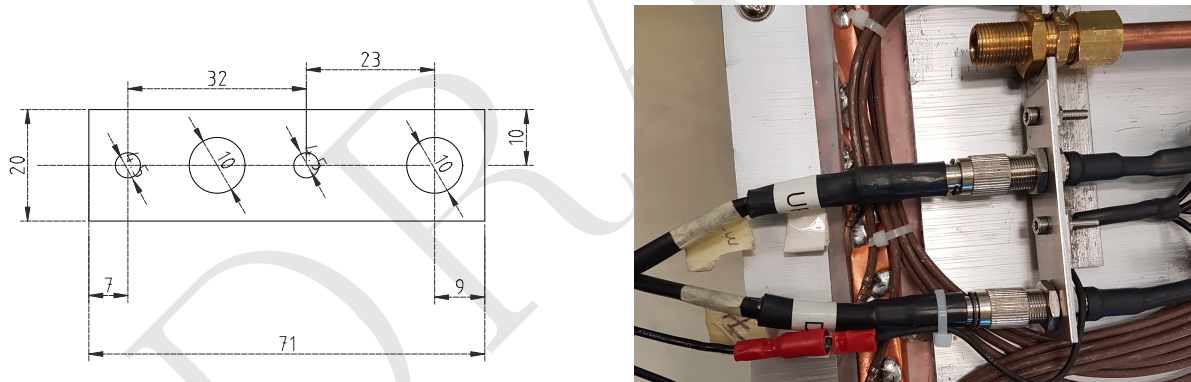


Figure 4.18: Left: Proposed adapter for the chamber patch panel which make it possible to replace a tripolar by a jupiter HV connector. Right: Try out of the proposed HV connector replacement.

## 1662 LV and control maintenance

1663 The low voltage (LV) and control maintenance consists in making sure that the Front-End Boards  
 1664 (FEBs) are powered and configurable, which means that the LV power system is working from  
 1665 supply board to the cable, that the signal cables are in good state and properly connected to the  
 1666 chamber and to the link boards and that the on-detector electronics (FEBs and Distribution Boards  
 1667 - DBs) are working fine.

1668 Usually, this system is very reliable. The weak point, in most of the cases, is the detector electronics.  
 1669 When a FEB [119] (as in Figure 4.19) is problematic it can present regions of very high noise or no  
 1670 signal at all (silent), which can not be recovered by the threshold control. In cases like this, when  
 1671 the FEB is accessible, it can be replaced in order to recover efficiency in the problematic chamber.

1672 This procedure is done by extracting the chamber from inside the detector (only for barrel chamber)  
 1673 and opening its cover to have access to the problematic component. Removed boards are send back  
 1674 to production labs for refurbishment.



Figure 4.19: RPC Front-end board (FEB) used in the barrel chambers.

1675 The most usual problem is a chamber in which the threshold control was lost. For this chamber,  
 1676 most probably, the problem is in the distribution board of the chamber, which is a piece of hardware  
 1677 responsible for distributing the LV power to the FEBs (3 to 6 per chamber) and send the threshold  
 1678 control signal to the FEBs via I2C line. If a chamber has no threshold control, it means that the  
 1679 RPC operation has no control over the signal selection, which can potentially induce performance  
 1680 issues.

1681 For the barrel, this maintenance happens concomitantly with the gas leak reparations on the barrel  
 1682 chamber, since both demands the chamber extraction, which is a complex procedure in terms of  
 1683 operation and demands specialized equipment and manpower. For technical reasons, the gas leak  
 1684 extractions have precedence over LV ones.

### 1685 Detector commissioning

1686 All the LS2 activities demands uncabling of the chamber to be repaired and possibly some neighbor-  
 1687 ing chambers. Also, it can involve the replacement of components of the chamber. To avoid damage  
 1688 to the system a compromising procedure is needed after all this activities. Given the responsibilities  
 1689 of the commissioning it was necessary to: (a) make sure that the RPC system keep tracks of all the  
 1690 interventions, (b) maintain all the algorithms used in the commissioning procedure, (c) together  
 1691 with the RPC Coordination, define a pool of people and a schedule to the commissioning of the  
 1692 system and (d) follow-up, with other CMS RPC experts, the availability of materials and resources  
 1693 for the commissioning operations.

1694 Besides the organizational tasks, the commissioning demanded to establish procedures to ensure the  
 1695 connectivity and functionality of HV and LV connections. For the HV, it is necessary to make sure  
 1696 that the chambers are properly connected, without miscabling <sup>4</sup> and that the currents at stand-by

<sup>4</sup>Mixed cable connections.

- 1697 HV and working point HV are compatible with the ones in the end of last data-taking (end of  
 1698 2018). This activity will start in November/2019, when the CMS RPC Standard Gas Mixture will  
 1699 be available again.
- 1700 For the LV point of view, the LV power cable and signal cables should also be properly connected,  
 1701 and presenting a noise profile compatible with last data-taking. One key point for this task is to  
 1702 make sure that there are no miscabling of signal cable. One RPC chamber can have from 6 to  
 1703 18 signal cable, which are connected very close one to another. There is a good chance that a  
 1704 chamber, after reparation, have its signal cables mixed. In order to diagnose situations like this, it  
 1705 was validated a algorithm present in the RPC Online Software, but never used since LS1, which,  
 1706 by changing the threshold of each component of the RPC system, from very high to very low values  
 1707 (component by component), can spot miscabled chambers. Since the control line is independent of  
 1708 the signal line, a misclabel will present a different noise from what is expected.
- 1709 Besides the validation of this algorithm, it was also implemented a web system (Figure 4.20),  
 1710 developed in Flask [120] wich automatize the execution of the algorithm, making transparent to the  
 1711 shifter (or the one performing the commissioning) the procedure to get miscabling report.

#### FEB Connectivity Test - Analysis

Worker	Date (YY-MM-DD)	Time (HH:MM:SS)	Hash	
RBP2_Far	2019-06-20	23:43:19	387534dst	<a href="#">Run Analyzer</a>
RBP1_Far	2019-06-20	20:12:20	458306dst	<a href="#">Run Analyzer</a>
RBP1_Far	2019-06-20	20:04:46	336162dst	<a href="#">Run Analyzer</a>
RBP1_Near	2019-06-20	19:02:00	377863dst	<a href="#">Run Analyzer</a>
RBP1_Near	2019-06-19	18:59:00	858950dst	<a href="#">Run Analyzer</a>
RBP1_Far	2019-06-19	18:58:26	994787dst	<a href="#">Run Analyzer</a>
YEN3_Far	2019-05-07	10:28:23	176278dst	<a href="#">Run Analyzer</a>
YEN3_Near	2019-05-07	10:28:08	347504dst	<a href="#">Run Analyzer</a>
YEN1_Far	2018-12-07	15:03:24	575561	<a href="#">Run Analyzer</a>
RBO_Far	2018-12-07	14:45:42	101463	<a href="#">Run Analyzer</a>
RBP1_Far	2018-12-07	09:12:00	477689	<a href="#">Run Analyzer</a>

Figure 4.20: RPC FEB Commissioning Analyzer.

- 1712 The LV commissioning is ongoing, since it happens, as much as possible, right after the chamber  
 1713 reparation.

DRAFT

# <sup>1714</sup> 5 Physics Analysis

## Statement of Contribution

During this study, I was the main analysist for the  $H/Z \rightarrow \Upsilon(1S, 2S, 3S) + \gamma$  analysis at CMS. In collaboration with researchers from UNICAMP, UERJ and LIP, I developed an analysis procedure (presented here), a Monte-Carlo generation strategy (since the straightforward approach was not suitable for this decay channel), and a two dimensional modelling for upper limits extraction. This was done in synergy with  $H/Z \rightarrow J/\Psi + \gamma$  analysis team (apart from different selection cuts, characteristic of the decay channel, and the chosen statistical modeling).

The results presented here are derived from the 2016 data only. An analysis of the full Run2 data sample (2016, 2017 and 2018) is being carried out by same team, under the coordination of the Standard Model Physics Group at CMS, in which I am still the main analysist.

<sup>1715</sup>

<sup>1716</sup> The analysis here presented corresponds to the search for rare decays of  $H \rightarrow \Upsilon + \gamma$ , where the  
<sup>1717</sup>  $\Upsilon$  might appear in the states  $1S$ ,  $2S$  or  $3S$ , and shall decay to a pair of muons (from here on,  
<sup>1718</sup> called dimuon system) and the  $\gamma$  will be identified as a offline reconstructed photon. The decay  
<sup>1719</sup> to the dimuon channel offers a very efficient triggering for this process, characteristic of CMS. The  
<sup>1720</sup> analogous process of the  $Z$  boson decays to the same channel is also studied, as a benchmark for  
<sup>1721</sup> the Higgs decay.

<sup>1722</sup> The main process contributing to the accessible phase space of these decays are described in Fig-  
<sup>1723</sup> ure 5.1, in which the different process are represented in a diagram for the reconstructed invariant  
<sup>1724</sup> masses of the muon-muon-photon system ( $\mu\mu\gamma$  - horizontal axis) and the muon-muon system ( $\mu\mu$   
<sup>1725</sup> - vertical axis). The vicinity of the  $H/Z$  mass and  $\Upsilon$  mass regions are represented in the midpoint  
<sup>1726</sup> for each axis. The backgrounds can be divided in **Resonant** and **Non-Resonant** backgrounds.  
<sup>1727</sup> The Non-Resonant might come from two sources, a Full Combinatorial background is composed by  
<sup>1728</sup> the combination of two non-correlated muons with a photon in the final state of the event. This is  
<sup>1729</sup> expected to be spread all over the phase space and in the diagram, it is represented by the color  
<sup>1730</sup> blue. The  $\Upsilon + \gamma$  Combinatorial background is a combination of two correlated muons (e.g.: the  
<sup>1731</sup> decay of a  $\Upsilon$  to a dimuon system) combined with a photon from a secondary process (e.g.: Multiple  
<sup>1732</sup> Particle Interaction - MPI, pileup, a jet mis-identified as a photon). This should be concentrated  
<sup>1733</sup> in the region around the  $\Upsilon(1S, 2S, 3S)$  and it is represented by the gray region.

<sup>1734</sup> The Resonant background is composed by the processes where the boson (Higgs or Z) decays  
<sup>1735</sup> to a  $\mu\mu\gamma$  final state without going through the intermediate meson state. For the Z decays, this  
<sup>1736</sup> background is modeled based on a Drell-Yan to dimuon decays, with a final state radiated (FSR)  
<sup>1737</sup> photon ( $Z \rightarrow \mu\mu\gamma_{FSR}$ ), while for the Higgs decay, a Higgs Dalitz decay ( $H \rightarrow \mu\mu\gamma$ ) is used. The

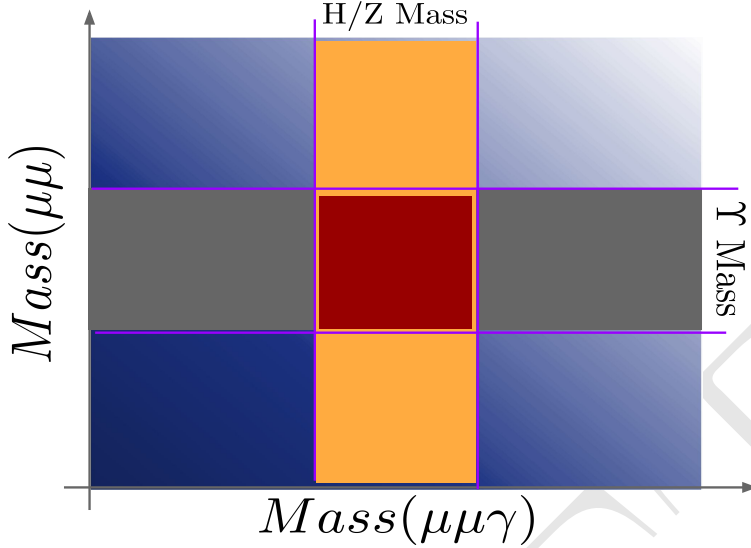


Figure 5.1: A diagram for the reconstructed invariant mass of the  $\mu\mu\gamma$  final state. The blue and gray regions represent the Full Combinatorial and  $\Upsilon + \gamma$  Combinatorial contributions, respectively, while the yellow and red regions represent the Resonant background and the signal region.

1738 Resonant background (also called Peaking Background) is represented in the diagram by the region  
1739 in yellow. The Signal is represented by the red region on the diagram.

1740 Around these representations, the 2-dimensional model of the reconstructed invariant masses ( $m_{\mu\mu\gamma}$   
1741 and  $m_{\mu\mu}$ ) is constructed for each contributing process and tested against the collected data by the  
1742 experiment, by means of a unbinned maximum likelihood fit. No significant excess above the  
1743 background-only model is observed and a upper limit of the signal branch fraction is extracted.  
1744 The following sections describes the data and simulated samples used in this analysis, the event  
1745 selection applied in order to enhance the signal to background ratio and the process to construct  
1746 the statistical models used in the upper limits extraction.

## 1747 5.1 Datasets and simulated events

### 1748 5.1.1 Data samples

1749 The data sample used in this analysis consists of a CMS data sample recorded at 2016, at  $\sqrt{s} =$   
1750 13 TeV, with 25 ns bunch separation. This data sample is composed only by events that were  
1751 certified from all CMS subsystems and reconstruction specialists as good for physics analysis.

1752 This data sample corresponds to  $35.86 \text{ fb}^{-1}$  of integrated luminosity [121].

### 1753 5.1.2 Simulated datasets

1754 Simulation of events at CMS is done via Monte Carlo methods (from here on, simply called MC).  
1755 Pseudo-random events are generated within the physics of the related processes in which we are

interested starting from hard-scattering processes, at parton (constituents of the proton) level, usually with matrix element generators. These handle the incoming and outgoing partons so that they follow some pre-defined theoretical model. The matrix element generator, working on the parton level, allow us to extract the momentum distribution of the parton as a function of the  $q^2$  (transferred momentum) of the collision. MC generators use the so-called parton distribution functions (PDFs) to sample values of momenta and can account for different order of perturbations, like NLO (next-to-leading order), NNLO (next-to-next-to-leading order), and so on.

After the hard-scattering, the **showering** process simulates the radiation emission by gluons and quarks in the initial and final states. Along the hard interaction, the other proton constituents may also interact through soft interaction. This part of the simulation is called **multiple parton interaction** (MPI). The last component of the simulation is the **hadronization**, in which quarks and gluons compose to form hadrons. These can decay according to specific models, as predicted in the case of heavy hadrons, like B hadrons and taus etc. This imposes the QCD confinement to low energy quarks and gluons <sup>1</sup>.

Usually, different generators are used to simulate a process. Each specialized in one or more steps. A summary of the signal and background MC samples used is presented in Table 5.1. These simulated data are comparable with the proton-proton collision using 2016 data conditions and the **pileup** <sup>2</sup> events are added to the simulated event in this step. The pileup events distribution used is modeled as a Poisson pdf (probability distribution function) with mean of 23 events, as recommended by CMS. Detector response in the MC samples is simulated using a detailed description of the CMS detector, based on GEANT4 [122].

The signal MC samples are simulated for the Higgs bosons decaying to  $\Upsilon(nS)(\rightarrow \mu\mu) + \gamma$  channels with POWHEG v2.0 [123–125], at next-to-leading order (NLO) of Feynman graphs computation, for the following production modes: gluon-gluon fusion (ggF), vector boson fusion (VBF), associated production (VH) and associated top production (ttH), with cross-section summarized at table 5.1. A extensive review of these production modes can be found at [126]. The PYTHIA 8 generator [127, 128] is used for hadronization and fragmentation with underlying event tune CUETP8M1 [129]. The parton distribution functions (pdf) NNPDF3.0 [130] are used.

For Z decaying to  $\Upsilon(nS)(\rightarrow \mu\mu) + \gamma$  channels, the signal samples are simulated with MADGRAPH 5 \_MC@NLO 2.6.0 matrix element generator [131] at next leading order and the PYTHIA 8 generator [127, 128] for hadronization and fragmentation with underlying event tune CUETP8M1 [129].

---

<sup>1</sup>QCD forbids coloured objects to exist in non-asymptotic states. They must decays to more complex systems, until they form stable colorless states.

<sup>2</sup>Each LHC collision recorded by CMS, is composed not by a single  $pp$  interaction, but by bunches of protons crossing each other. In this case, a hard interaction is actually surrounded by many soft interaction between adjacent protons. The extra activity produced in these interactions, and caught by the detector, is called **pileup** and has its signal mixed with the hard one. Since, during the data taking, the number of pileup interactions varies according to the instantaneous luminosity, the MC are mixed some soft interaction only sample, called Minimum Bias. The number of mixed soft interaction (pileup events) is governed by a Poisson distribution with a pre-defined mean. The MC samples are then reweighted to match the same distribution of primary vertexes for the corresponding Data. Systematics related to this procedure will be discussed later. A pioneer work on this subject, at CMS, is the master dissertation from Eliza Melo [**tese\_eliza**] - Rio de Janeiro University.

1787 The Drell-Yan process,  $pp \rightarrow Z \rightarrow \mu\mu\gamma_{FSR}$ , results in the same final state as the signal. This  
 1788 process exhibits a peak in the three-body invariant mass,  $m_{\mu\mu\gamma}$ , at the Z boson mass,  $m_Z$ , and it is  
 1789 a resonant background for this channel, therefore referred to as Peaking or Resonant Background.

1790 It is taken into account when deriving the upper limit on the branching fraction for  $Z \rightarrow \Upsilon(nS) + \gamma \rightarrow$   
 1791  $\mu\mu + \gamma$ . The MADGRAPH 5 \_MC@NLO 2.6.0 matrix element generator [131] at leading order,  
 1792 interfaced with PYTHIA 8.226 for parton showering and hadronization with tune CUETP8M1 [129],  
 1793 is used to generate a sample of these resonant background events. The photons in these events are  
 1794 all produced as final-state radiation from the  $Z \rightarrow \mu\mu$  decay and therefore the  $m_{\mu\mu\gamma}$  distribution  
 1795 peaks at the Z boson mass and there is no continuum contribution.

1796 Similarly, the Higgs boson Dalitz decay [132],  $H \rightarrow \gamma^*\gamma \rightarrow \mu\mu + \gamma$ , is a Resonant Background  
 1797 (resonant) to  $H \rightarrow \Upsilon(nS) \rightarrow \mu\mu + \gamma$ . It is simulated at NLO with MADGRAPH 5 \_MC@NLO 2.6.0  
 1798 matrix element generator [131] at next-to-leading order and the PYTHIA 8 generator [127, 128] for  
 1799 hadronization and fragmentation with underlying event tune CUETP8M1 [129]. This Higgs Dalitz  
 1800 Decay sample, was generated only for the ggF production mode, but its cross-section was rescaled  
 1801 to the full Higgs cross-section. This process will present a small contribuition of selected events, so  
 1802 this approximation should be sufficient for the Higgs Resonant Background modeling.

1803 There are also background processes that do not give resonance peaks in the three-body invariant  
 1804 mass spectrum. They are modeled from data, as it will be explained latter in more details.

Table 5.1: Datasets simulated (MC) for 2016 conditions. Assuming that  $\sigma(pp \rightarrow H)$ , taking into consideration all the simulated Higgs production modes, is  $55.13 \text{ pb}$  [133] and  $\sigma(pp \rightarrow Z \rightarrow \mu\mu)$  is  $57094.5 \text{ pb}$ , including the next-to-next-to-leading order (NNLO) QCD contributions, and the next-to-leading order (NLO) electroweak corrections from fewz 3.1 [134] calculated using the NLO PDF set NNPDF3.0, with the phase space selection in invariant mass of the dimuon system of  $m_{\mu\mu} > 50 \text{ GeV}$ . For the Higgs Dalitz  $\sigma$ , we consider only the gluon fusion contribution ( $\sigma_{ggF} = 48.6 \text{ pb}$ ) [133]. The Higgs Dalitz Decay  $BR_{SM}$  and the  $Z \rightarrow \mu\mu\gamma_{FSR}$  were obtained with MCFM 6.6 [135] (as in the CMS search for Higgs Dalitz Decay in at  $\sqrt{s} = 8 \text{ TeV}$  [136]) and with MADGRAPH 5 \_MC@NLO, respectively. The  $BR_{\Upsilon(1S,2S,3S) \rightarrow \mu\mu}^{PDG} = (2.48, 1.93, 2.18) \times 10^{-2}$  is quoted from Particle Data Group report (PDG) [12]. The "Effective  $\sigma$ " for the signal samples is  $\sigma(pp \rightarrow Z(H)) \times BR_{SM} \times BR_{\Upsilon(nS) \rightarrow \mu\mu}^{PDG}$ .

Physics Processes	Branching Ratio ( $BR_{SM}$ )	Effective $\sigma$ (in pb)	Generator	Sample Type
$H \rightarrow \Upsilon(1S) + \gamma$	$5.22 \times 10^{-9}$	$7.14 \times 10^{-9}$	POWHEG 2.0	Signal
$H \rightarrow \Upsilon(2S) + \gamma$	$1.42 \times 10^{-9}$	$1.51 \times 10^{-9}$	POWHEG 2.0	Signal
$H \rightarrow \Upsilon(3S) + \gamma$	$9.10 \times 10^{-10}$	$1.10 \times 10^{-9}$	POWHEG 2.0	Signal
$Z \rightarrow \Upsilon(1S) + \gamma$	$4.88 \times 10^{-8}$	$6.80 \times 10^{-5}$	MADGRAPH 5	Signal
$Z \rightarrow \Upsilon(2S) + \gamma$	$2.44 \times 10^{-8}$	$2.69 \times 10^{-5}$	MADGRAPH 5	Signal
$Z \rightarrow \Upsilon(3S) + \gamma$	$1.88 \times 10^{-8}$	$2.34 \times 10^{-5}$	MADGRAPH 5	Signal
H Dalitz Decay	$3.83 \times 10^{-5}$	$2.13 \times 10^{-3}$	MADGRAPH 5	Resonant Background
$Z \rightarrow \mu\mu\gamma_{FSR}$	—	$7.93 \times 10^{-2}$	MADGRAPH 5	Resonant Background

1805 The number of simulated events is rescaled by the effective  $\sigma$ , from table 5.1, in order to match  
 1806  $35.86 \text{ fb}^{-1}$  of integrated luminosity, from the recorded data. Being  $N = \sigma\mathcal{L}$ ,  $N$  in the number of

1807 events for a process,  $\sigma$  is the cross-section and  $\mathcal{L}$  is the integrated luminosity, the reweighting factor,  
 1808 for a simulated sample is:

$$w_{MC} = \frac{\sigma \mathcal{L}}{N_{sim}}, \quad (5.1)$$

1809 where  $N_{sim}$  is the number of simulated events for a specific process.

1810 The simulated sample are also corrected by the data pileup distribution, since the pileup distribution  
 1811 of MC is different from the pileup distribution of data. The way to correct the MC is to assign a  
 1812 weight to each bin of the MC pileup distribution, with respect to the data. The rescaling is defined  
 1813 as the ratio between normalized pileup (PU) distribution for Data and MC.

$$w_{PU}(n) = \frac{P_{PU}^{Data}(n)}{P_{PU}^{Sim}(n)}, \quad (5.2)$$

1814 where  $n$  is the number of interaction per bunch crossing (pileup).

## 1815 5.2 Contribution of the $\Upsilon(nS)$ polarisation

1816 Measurements of quarkonium polarization observables may yield information about quarkonium  
 1817 production mechanisms that are not available from the study of unpolarized cross sections alone.  
 1818 The three polarization states of a  $J = 1$  quarkonium can be specified in terms of a particular  
 1819 coordinate system in the rest frame of the quarkonium. This coordinate system is often called the  
 1820 "spin-quantization frame".

1821 In a hadron collider,  $\Upsilon(1S, 2S, 3S)$  are reconstructed through their electroweak decays into a lepton  
 1822 pair. The information about the polarization of the quarkonium state is encoded in the angular dis-  
 1823 tribution of the leptons. This angular distribution is usually described in the quarkonium rest frame  
 1824 with respect to a particular spin-quantization frame [137]. The polarization of the  $\Upsilon(1S, 2S, 3S)$   
 1825 is not simulated for signal MC sample and we only apply a reweighting scale factor to each event  
 1826 and so we can emulate the polarization effects [138]. Figure 5.2 present the distributions of  $\cos \Theta$   
 1827 of  $\Upsilon \rightarrow \mu\mu$ , where  $\Theta$  is the angle between the positive muon and the  $\Upsilon$  in the Z (Higgs) rest-frame.  
 1828 At Table 5.2 we show the analytical functions used to describe the extremes scenarios (Unpolarized,  
 1829 Transverse Polarization and Longitudinal Polarization) reweighting, presented in this analysis.

1830 It is worth stating that, for the Higgs decay, only the Transverse Polarization is considered. For  
 1831 the Z decay, because of its spin nature, the Unpolarized scenario is used as the nominal one, and  
 1832 the effects of the two other extremes (Transverse Polarization and Longitudinal Polarization) are  
 1833 quoted as systematics.

Table 5.2: Summary of the impact of reweighted of polarization contribution using several scenarios.

$J_Z$	Polarisation Scenario	Analytic Description
$\pm 1$	Transverse	$3/4 \times (1 + (\cos \Theta)^2)$
0	Longitudinal	$3/2 \times (1 - (\cos \Theta)^2)$

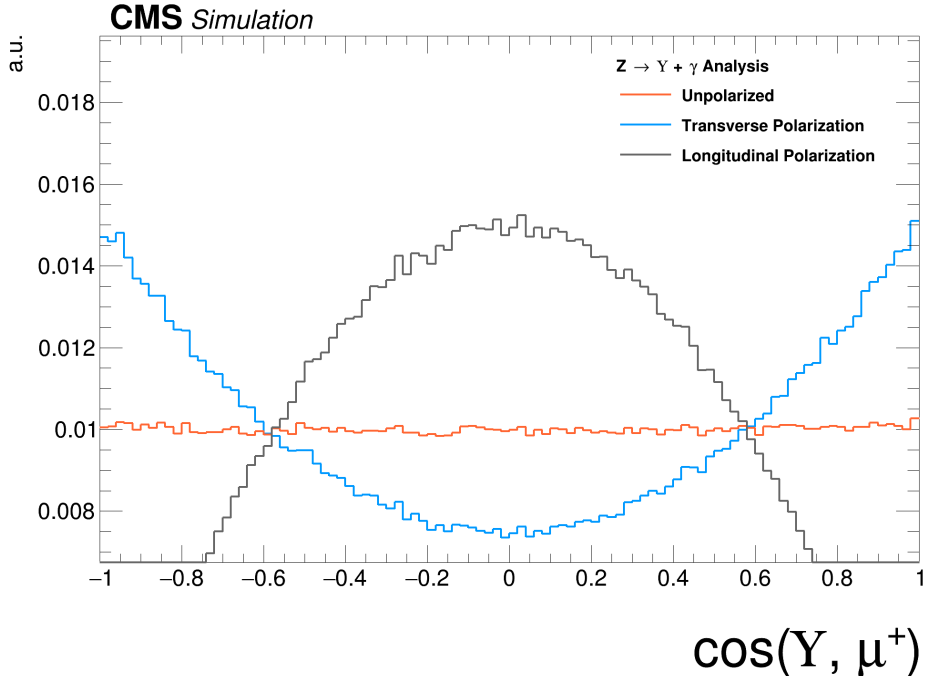


Figure 5.2: Distributions of  $\cos\theta$  of  $\Upsilon \rightarrow \mu\mu$  and  $\gamma^* \rightarrow \mu\mu$ . The orange distribution is the  $Z \rightarrow \Upsilon(1S, 2S, 3S) + \gamma$  sample before reweighting (Unpolarized); the blue and gray distributions are  $Z \rightarrow \Upsilon(1S, 2S, 3S)$  sample after reweighting, for the Transverse and Longitudinal Polarization.

### 1834 5.3 Kinematical studies using MC generator

1835 Using the PYTHIA 8.226 generator, the Monte Carlo signals are produced for Higgs (Z) boson events  
 1836 decaying into ( $\Upsilon(1S, 2S, 3S)$ ) +  $\gamma$ , which are highly boosted. Observing the kinematic generator level  
 1837 distributions in Figure 5.3 for Z boson and Figure 5.4 for Higgs boson, we could conclude that the  
 1838 high- $E_T$  (transverse energy, with respect to the beam line) photon will be back-to-back to the  $\Upsilon$   
 1839 particles being possible to apply an isolation selection to identify a photon in this kinematic topology.  
 1840 Also, we can observe those transverse momenta of the leading/trailing  $p_T$  (transverse momentum,  
 1841 with respect to the beam line) muon <sup>3</sup> and the photon and distances  $\Delta R = \sqrt{\Delta\eta^2 + \Delta\phi^2}$  between  
 1842 the two muons and between the muons and the photon are a good variable that can be used to  
 1843 discriminate the contribution between signal and background events. The leading muon transverse  
 1844 momentum can be greater than 45(30) GeV and trailing muon is greater than 10(20) GeV in Higgs(Z)  
 1845 decay.  $\Delta R$  distributions of the two muons and between the muons and the photon in the both cases  
 1846 show that the two muons are very close and the photon is back-to-back in relation of dimuon system.  
 1847 Another feature of this kinematic topology is that the production vertex between muons produced  
 1848 in  $\Upsilon$  decaying events and the high- $E_T$  photon is measured with high precision.  
 1849 it is worth to mention that discussion above is made only on simulated data samples for this analysis  
 1850 and does not necessarily translate to the real data analysis without further inspection.

<sup>3</sup>In this study we define leading muon and the muon, decaying from the  $\Upsilon$ , with highest  $p_T$ . Trailing muon is the one with the second hight  $p_T$ .

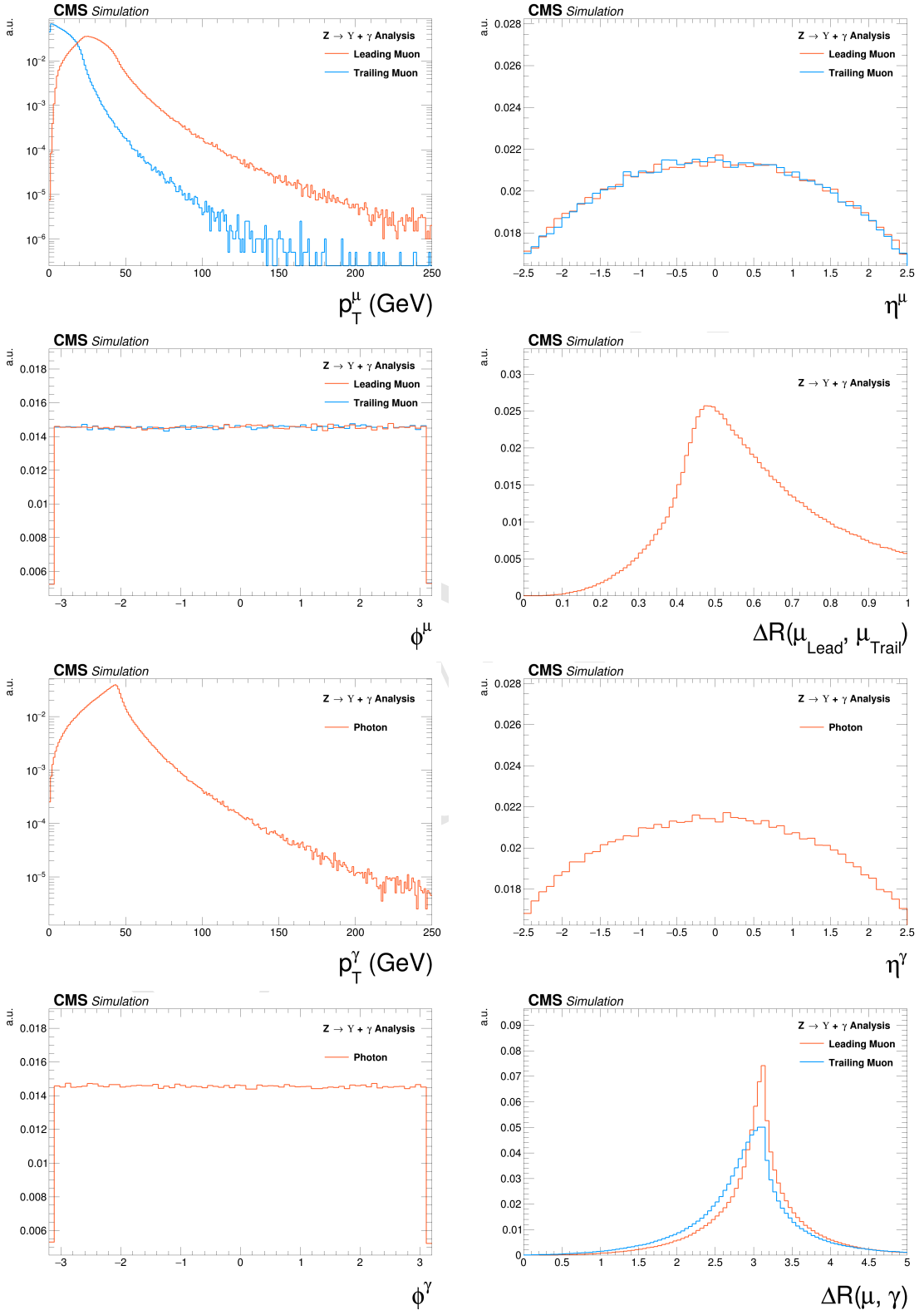


Figure 5.3: Generator level distributions of main variables for  $Z \rightarrow \Upsilon(1S, 2S, 3S) + \gamma$ : Transverse momenta of the leading/trailing  $p_T$  muon and the photon, pseudorapidity ( $\eta$ ) and  $\phi$  of the muons and the photon, distances  $\Delta R$  between the two muons and between the muons and the photon. All the distributions shown in the figure are normalized to the unity of area.

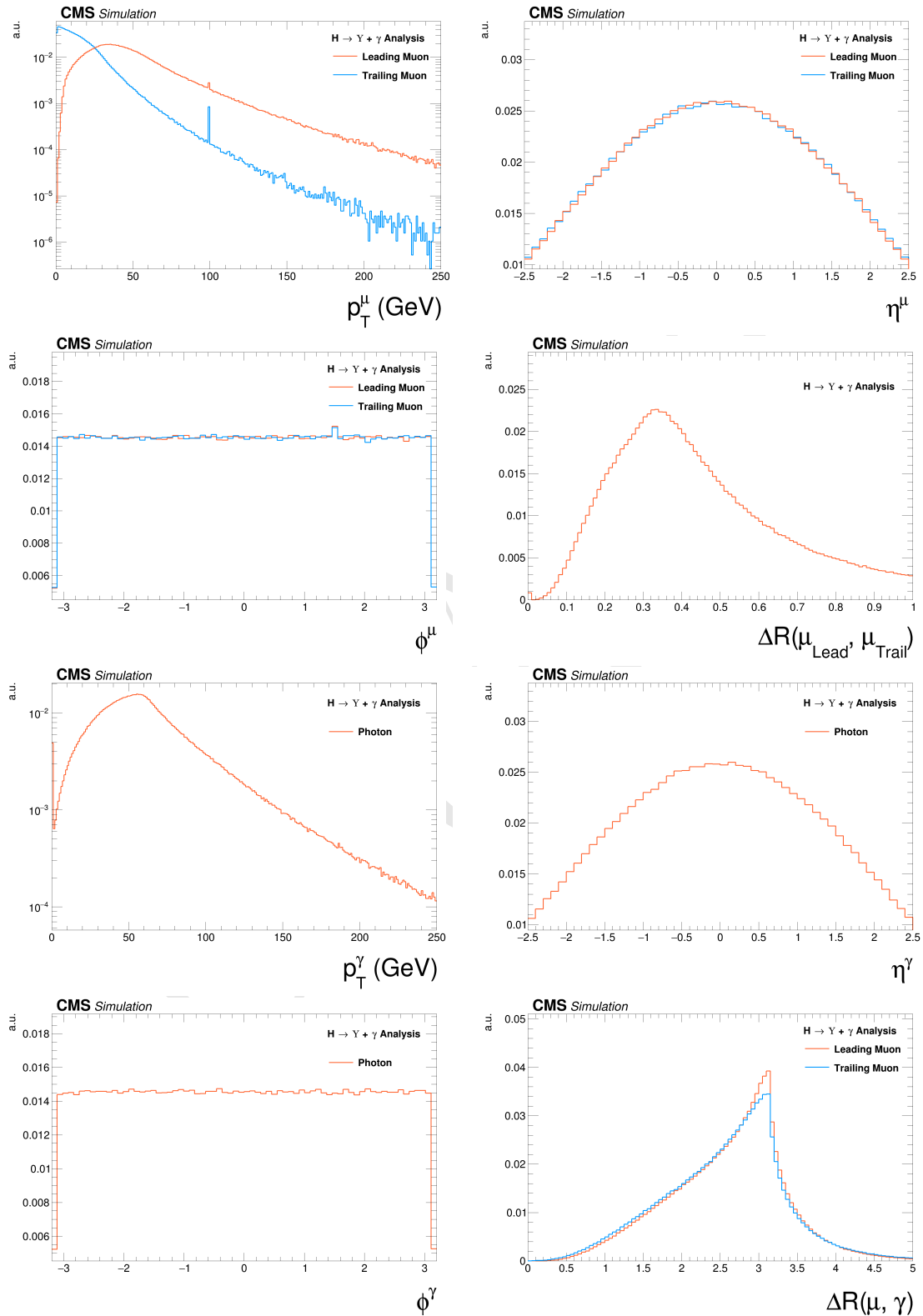


Figure 5.4: Generator level distributions of main variables for  $H \rightarrow \Upsilon(1S, 2S, 3S) + \gamma$ : Transverse momenta of the leading/trailing  $p_T$  muon and the photon, pseudorapidity ( $\eta$ ) and  $\phi$  of the muons and the photon, distances  $\Delta R$  between the two muons and between the muons and the photon. All the distributions shown in the figure are normalized to the unity of area.

## 1851 5.4 Event selection

1852 The event selection is divided in two steps. At first, a set of cuts related to trigger and physics object  
1853 (muons and photons) selection is applied. High level physics objects at CMS are reconstructed based  
1854 of the Particle Flow (PF) algorithm [139]. This selection is called, within this analysis, Group I.  
1855 For the events that pass the Group I selection, another set of cuts is applied, this time focusing on  
1856 kinematical (phase space) event selection, in order to enhance the signal to background ratio. This  
1857 later set is called, within this analysis, Group II. After full selection, three exclusive categories are  
1858 defined, based on the photon's  $\eta$  region and its energy spread shape within the ECAL cells (R9).  
1859 After the full selection, a background and signal modeling process is applied, based on the invariant  
1860 mass distributions, which will be explained in the next section.

## 1861 5.5 Trigger and physics object selection (Group I)

### 1862 5.5.1 Trigger

1863 In this study, the same trigger requirements are applied to both data and simulated samples. For  
1864 the first trigger level (L1), events are selected if they present at least one muon with transverse  
1865 momentum greater than 5 GeV and an isolated <sup>4</sup> photon or electron with transverse momentum  
1866 greater than 18 GeV (at L1, there is no differentiation between photons and electrons). At the  
1867 software level of the trigger system (HLT), the events are required to have at least one muon with  
1868 transverse momentum greater than 17 GeV and a photon with transverse momentum greater than  
1869 30 GeV.  
1870 In order to compensate any difference in the trigger performance between simulated and data  
1871 samples, for every selected MC a proper scale factor is applied, based on the  $p_T$  of the reconstructed  
1872 muon and photon. These scale factor computed by the ratio between efficiency of the trigger for  
1873 the Data sample over the efficiency for a MC sample. These efficiencies are calculated with the tag-  
1874 and-probe method, exploring the resonance of a final state composed by two muon and one photon  
1875 in the vicinity of the  $Z$  boson invariant mass. To this final state, a selection was applied to ensure  
1876 that the photon comes from a Final State Radiation process, allowing us to use the tag-and-probe  
1877 method.  
1878 Considering the similarity of this analysis with the  $H/Z \rightarrow J/\psi + \gamma$  analysis [59], not only in term  
1879 of data samples, but also for triggering and physics object selection, the same scale factors were  
1880 applied. More details are given in the same paper.

---

4The concept of isolation will be detailed later, but in summary, it means a object which has very small activity (above a certain threshold of energy/momentum) around it. In hadron-hadron collider, isolation is a characteristics of hard interactions.

1881 **5.5.2 Muon Identification**

1882 Ahead of any selection, a standard CMS "Ghost Cleaning" procedure is applied to all reconstructed  
 1883 muons in order to avoid that a single physical muon is reconstructed as two or more. For this  
 1884 procedure, reconstructed muons sharing 50% or more segments in the system are arbitrated, in  
 1885 such way, that the ones with lowest quality characteristic is excluded.

1886 After the cleaning, a muon is chosen when it passes a two step identification: the **Loose ID** and  
 1887 the **Tight ID**. Below the muon identification procedure is summarized .

1888 For the Loose ID, each muon is required to:

- 1889 • have transverse momentum greater than 5 GeV, in order to cope with Particle Flow require-  
 1890     ments;
- 1891     • be within the muon system acceptance:  $|\eta| < 2.4$ ;
- 1892     • to have a three dimensional impact parameter uncertainty, with respect to the primary vertex,  
 1893      smaller than 4;
- 1894     • to have transverse distance smaller than 0.5 cm ( $d_{xy} < 0.5$ ), with respect to the primary  
 1895      vertex (PV);
- 1896     • to have longitudinal distance smaller than 1.0 cm ( $d_z < 1$ ), with respect to the primary vertex  
 1897      (PV).

1898 Muons reconstructed only in the muon system, without a correspondence with the tracker, are  
 1899 rejected. The last three requirements of the Loose ID are imposed in order to suppress muons from  
 1900 in-flight decays.

1901 The primary vertex itself, is determined as the reconstructed vertex with the biggest sum of  $p_T^2$  in  
 1902 the event. This sum is performed, considering all the charged PF candidates clustered by the jet  
 1903 finding algorithms [76, 77] and the MET, which is defined as the  $p_T$  vector sum of all the charged  
 1904 and neutral PF candidates associated to that vertex.

1905 For the Tight ID, muons with transverse momentum  $p_T < 200$  GeV, are required to have been  
 1906 reconstructed with the Particle Flow (PF) algorithm. If they have  $p_T > 200$  GeV, they should re-  
 1907 constructed with the Particle Flow (PF) algorithm or satisfy the strict tracker requirements (defined  
 1908 in table 5.3).

Table 5.3: Conditions for a muon to pass the strict tracker requirements.

Requirement	Technical definition
Muon station matching	Muon is matched to segments in at least two stations in the muon system
Good $p_T$ measurement	$\frac{\sigma_{p_T}}{p_T} < 0.3$
Vertex compatibility ( $x - y$ )	$d_{xy} < 2$ mm
Vertex compatibility ( $z$ )	$d_z < 5$ mm
Pixel hits	At least one pixel hit
Tracker hits	Hits in at least six tracker layers

1909 To mitigate spurious signal in the detector that would mimic a muon, the leading muon (the one  
 1910 with highest  $p_T$ ) is required to be isolated within a cone of radius  $\Delta R = \sqrt{\Delta\eta^2 + \Delta\phi^2} < 0.3$  in the  
 1911  $\eta - \phi$  plane. The isolation is evaluated in terms of  $\mathcal{I}^\mu < 0.35$ , defined as:

$$\mathcal{I}^\mu \equiv \left( \sum p_T^{\text{charged}} + \max \left[ 0, \sum p_T^{\text{neutral}} + \sum p_T^\gamma - p_T^{\text{PU}}(\mu) \right] \right) / p_T^\mu. \quad (5.3)$$

1912 The  $\sum p_T^{\text{charged}}$  is the scalar sum of the transverse momenta of charged hadrons originating from the  
 1913 chosen primary vertex of the event. The  $\sum p_T^{\text{neutral}}$  and  $\sum p_T^\gamma$  are the scalar sums of the transverse  
 1914 momenta for neutral hadrons and photons, respectively. Since the isolation variable is particularly  
 1915 sensitive to energy deposits from pileup interactions, a  $p_T^{\text{PU}}(\mu)$  contribution is subtracted, where  
 1916  $p_T^{\text{PU}}(\mu) \equiv 0.5 \times \sum_i p_T^{\text{PU},i}$ , where  $i$  runs over the momenta of the charged hadron PF candidates  
 1917 not originating from the primary vertex, and the factor of 0.5 corrects for the different fraction of  
 1918 charged and neutral particles in the cone.

1919 One should keep in mind that this muon identification process is the same as the one used by the  
 1920  $H \rightarrow ZZ^* \rightarrow 4l$  [140]. This was done in order to keep in phase with other Higgs analysis inside  
 1921 the collaboration. After the muon identification, an appropriate scale factor is applied to the MC  
 1922 events based on the leading muon  $p_T$  and  $\eta$ , in order to correct any possible discrepancy between  
 1923 data and simulated samples. The scale factors were taken from the  $H \rightarrow ZZ^* \rightarrow 4l$  analysis.

1924 In order to cope with trigger requirements, the leading muon should have  $p_T > 20$  GeV and the  
 1925 trailing muon  $p_T > 4$  GeV.

### 1926 5.5.3 Photon Identification

1927 For the photon identification and selection, the standard CMS recommendation are followed. The  
 1928 Multivariate (MVA) Photon identification is used with a working point of 90%, together with a  
 1929 electron veto procedure, to avoid misidentification of electrons as photons. Kinematically, the  
 1930 photons are requested to have transverse energy, with respect to the beam line,  $E_T > 33$  GeV and  
 1931 reconstructed within the CMS acceptance for photons  $|\eta_{SC}| < 2.5^5$ , excluding the Electromagnetic  
 1932 Calorimeter (ECAL) Barrel-Endcap intersections.

1933 The threshold of 33 GeV for the photon transverse energy is driven by the trigger requirements.  
 1934 The selected photon, per event, is the one with highest  $E_T$ .

### 1935 5.5.4 Kinematical distributions

1936 The selection described so far, is called Group I. The plots shown below are related to selected  
 1937 events after this set.

1938 Figures 5.5 to 5.10 present the  $p_T$ ,  $\eta$  and  $\phi$  distributions for the leading muon, trailing muon and  
 1939 the photon, for the Z decaying into  $\Upsilon(1S, 2S, 3S) + \gamma$ .

<sup>5</sup>SC stands for Super Cluster of the reconstructed photon. It is the set of cell in the Electromagnetic Calorimeter used for the photon observation.

Figures 5.11 to 5.13 present the  $p_T$ ,  $\eta$  and  $\phi$  distributions for reconstructed  $\Upsilon(nS)$  ( $\mu\mu$  system) and the reconstructed boson ( $\mu\mu\gamma$  system).

Figures 5.14 to 5.17 present the  $\Delta R = \sqrt{\Delta\eta^2 + \Delta\phi^2}$  between the photon and the muons, the  $\Delta R$  distributions between reconstructed dimuon ( $\mu\mu$ ) system and the photon, the absolute value of the  $\Delta\phi$  between the leading muon and the photon, the ratio for the transverse momentum of the reconstructed Upsilon and the reconstructed Z mass ( $p_T^{\mu\mu}/M_{\mu\mu\gamma}$ ), the ratio for the transverse energy of the reconstructed Photon and the reconstructed Z mass ( $E_T^\gamma/M_{\mu\mu\gamma}$ ) and dimuon mass distribution of the reconstructed  $\Upsilon(nS)$ .

Figures 5.18 to 5.30 present the same variables, but for the Higgs decaying into  $\Upsilon(1S, 2S, 3S) + \gamma$  channel.

In all figures, the black dots are data collect by CMS while the blue distribution is related only to the signal Monte-Carlo generated samples. The observed difference between signal MC and Data is accounted to the lack of full background contribution for these histograms. Only Signal MC is being considered. The key point is to compare the shape of the distributions and how much they match before and after the selection.

For any presented plot, **Data** stands for data collected from real  $pp$  collisions by CMS and **Signal**, stands for the distribution of events from a MC generated sample of signal events, as described in Section 5.1.2.

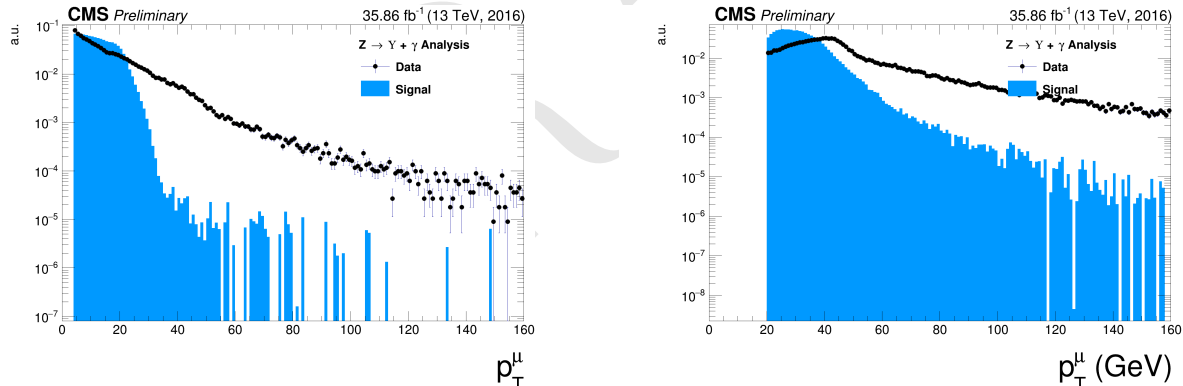


Figure 5.5: The  $p_T$  muon distributions from data and signal events for Z decaying into  $\Upsilon(1S, 2S, 3S) + \gamma$  after Group I of selection cuts, where on left are presenting the trailing muons and on right are the leading muons. The plots are normalized to the unit of area. The black dots are data collect by CMS while the blue distribution is related only to the signal Monte-Carlo generated samples.

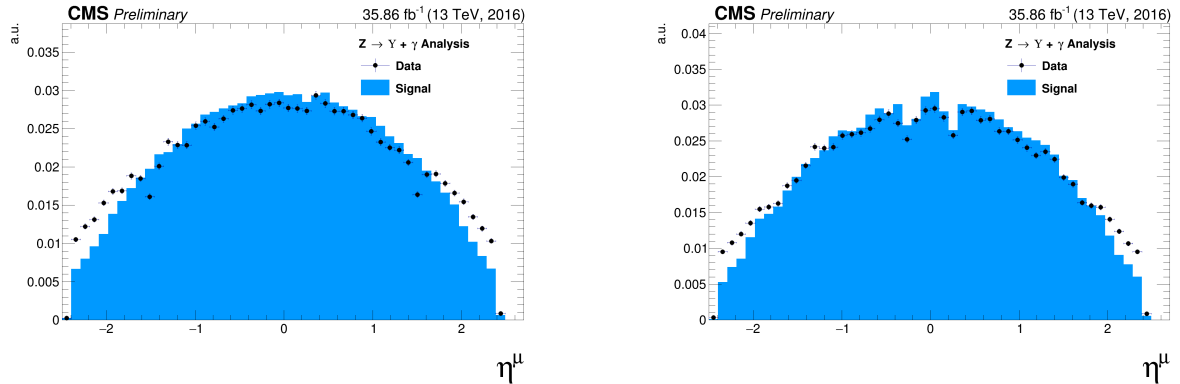


Figure 5.6: The  $\eta$  muon distributions from data and signal events of  $Z$  decaying into  $\Upsilon(1S, 2S, 3S) + \gamma$  after Group I of selection cuts, where on left are presenting the trailing muons and on right are the leading muons. The plots are normalized to the unit of area. The black dots are data collect by CMS while the blue distribution is related only to the signal Monte-Carlo generated samples.

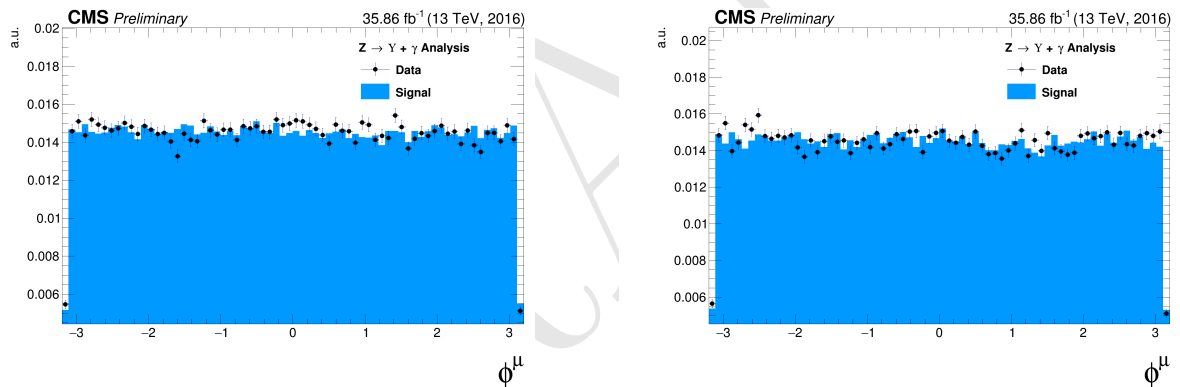


Figure 5.7: The  $\phi$  muon distributions from data and signal events of  $Z$  decaying into  $\Upsilon(1S, 2S, 3S) + \gamma$  after Group I of selection cuts, where on left are presenting the trailing muons and on right are the leading muons. The plots are normalized to the unit of area. The black dots are data collect by CMS while the blue distribution is related only to the signal Monte-Carlo generated samples.

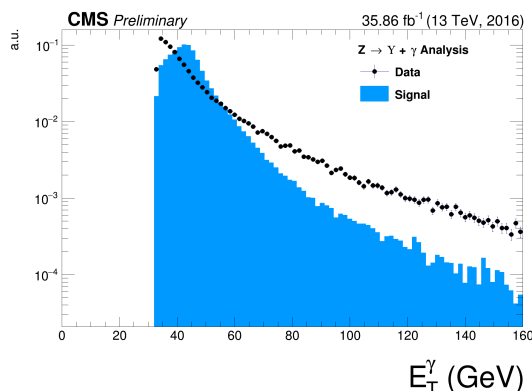


Figure 5.8: The  $p_T$  photon distributions from data and signal events for  $Z$  decaying into  $\Upsilon(1S, 2S, 3S) + \gamma$  Group I of selection cuts. The plots normalized to the unit of area.

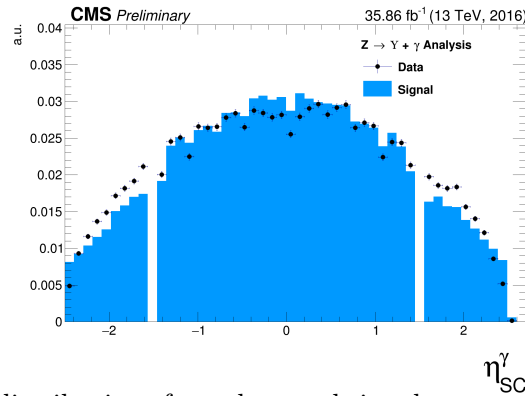


Figure 5.9: The  $\eta$  photon distributions from data and signal events of  $Z$  decaying into  $\Upsilon(1S, 2S, 3S) + \gamma$  after Group I of selection cuts. The plot is normalized to the unit of area.

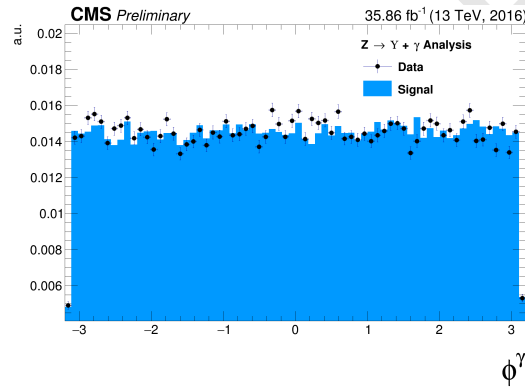


Figure 5.10: The  $\phi$  photon distributions from data and signal events of  $Z$  decaying into  $\Upsilon(1S, 2S, 3S) + \gamma$  after Group I of selection cuts. The plot is normalized to the unit of area.

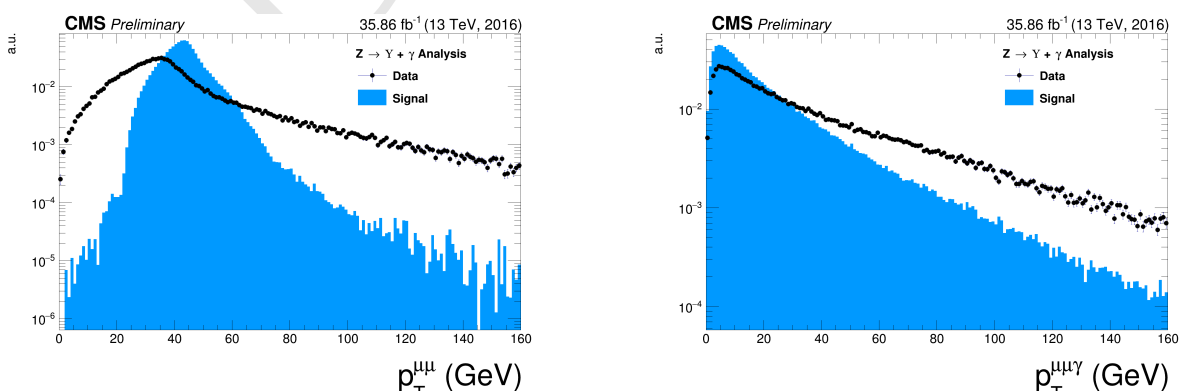


Figure 5.11: The  $p_T$  distributions for the reconstructed  $\Upsilon(1S, 2S, 3S)$  in the left and for  $Z$  in the right from data and signal events for  $Z$  decaying into  $\Upsilon(1S, 2S, 3S) + \gamma$  after Group I of selection cuts. The plots are normalized to the unit of area. The black dots are data collect by CMS while the blue distribution is related only to the signal Monte-Carlo generated samples.

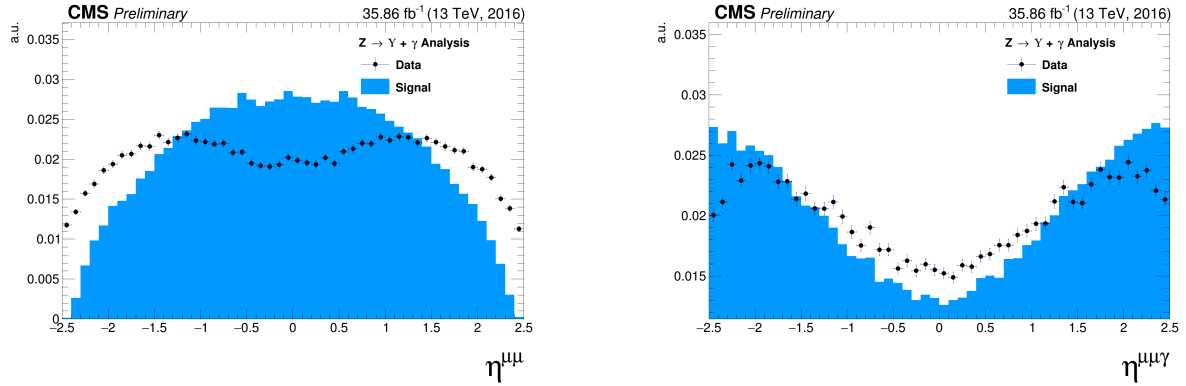


Figure 5.12: The  $\eta$  distributions for  $\Upsilon(1S, 2S, 3S)$  in the left and for  $Z$  in the right from data and signal events for  $Z$  decaying into  $\Upsilon(1S, 2S, 3S) + \gamma$  after Group I of selection cuts. The plots are normalized to the unit of area. The black dots are data collect by CMS while the blue distribution is related only to the signal Monte-Carlo generated samples.

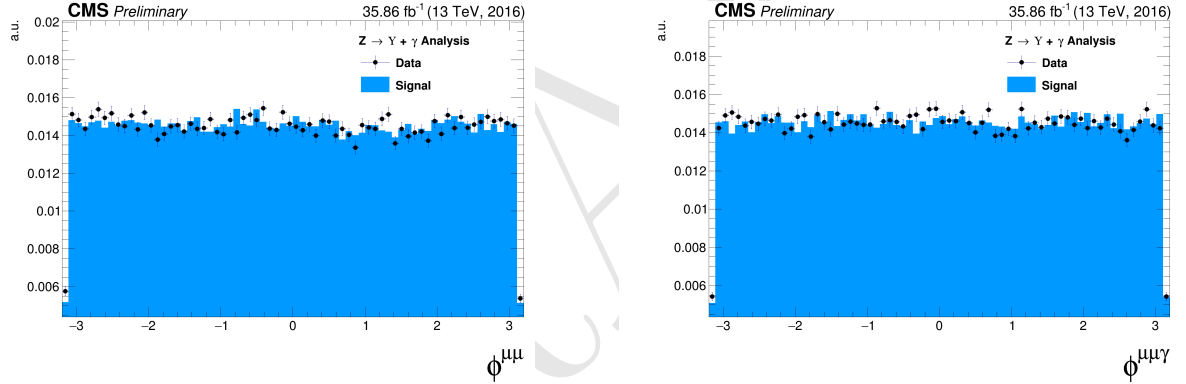


Figure 5.13: The  $\phi$  distributions for  $\Upsilon(1S, 2S, 3S)$  in the left and for  $Z$  in the right from data and signal events for  $Z$  decaying into  $\Upsilon(1S, 2S, 3S) + \gamma$  after Group I of selection cuts. The plots are normalized to the unit of area. The black dots are data collect by CMS while the blue distribution is related only to the signal Monte-Carlo generated samples.

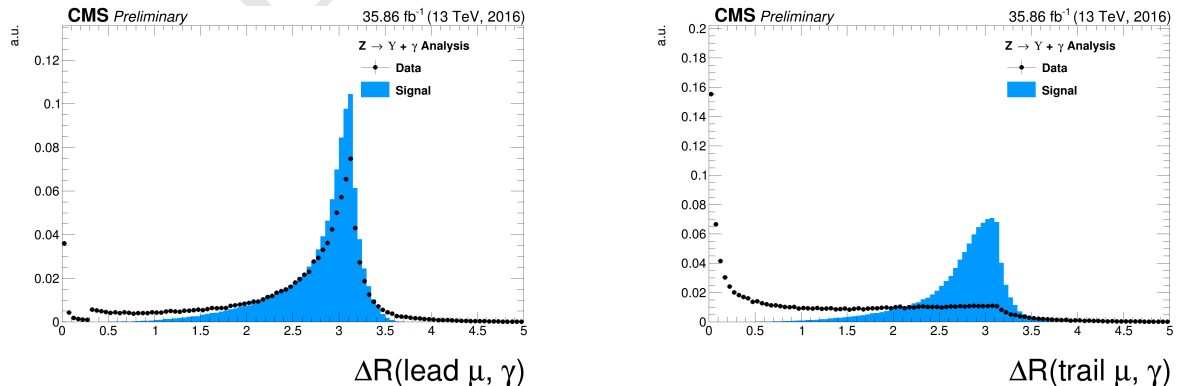


Figure 5.14: The  $\Delta R$  distributions between the photon and the leading muon (left) and the trailing muon (right) for for  $Z$  decaying into  $\Upsilon(1S, 2S, 3S) + \gamma$  from data and signal events after Group I of selection cuts. The plots are normalized to the unit of area. The black dots are data collect by CMS while the blue distribution is related only to the signal Monte-Carlo generated samples.

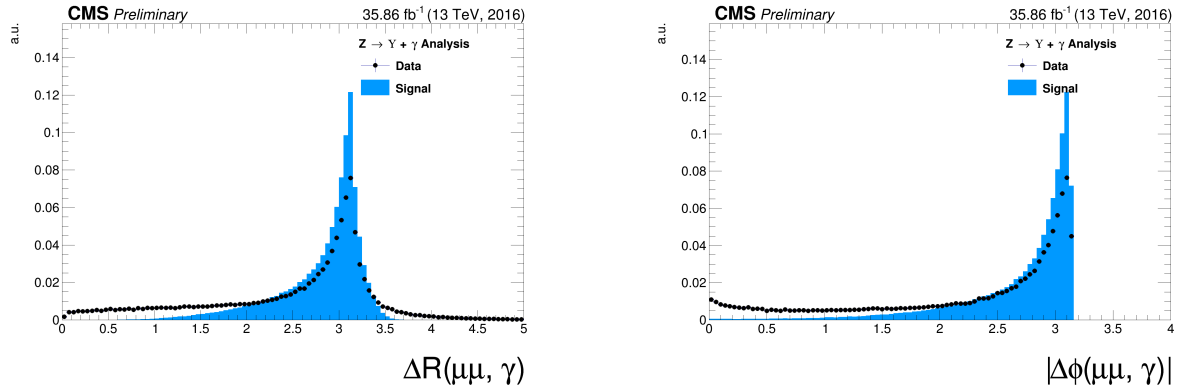


Figure 5.15: Left: The  $\Delta R$  distributions between reconstructed dimuon ( $\mu\mu$ ) system and the photon. Right: absolute value of the  $\Delta\phi$  between the dimuon system and the photon for  $Z$  decaying into  $\Upsilon(1S, 2S, 3S) + \gamma$  from data and signal events after Group I of selection cuts. The plots are normalized to the unit of area. The black dots are data collect by CMS while the blue distribution is related only to the signal Monte-Carlo generated samples.

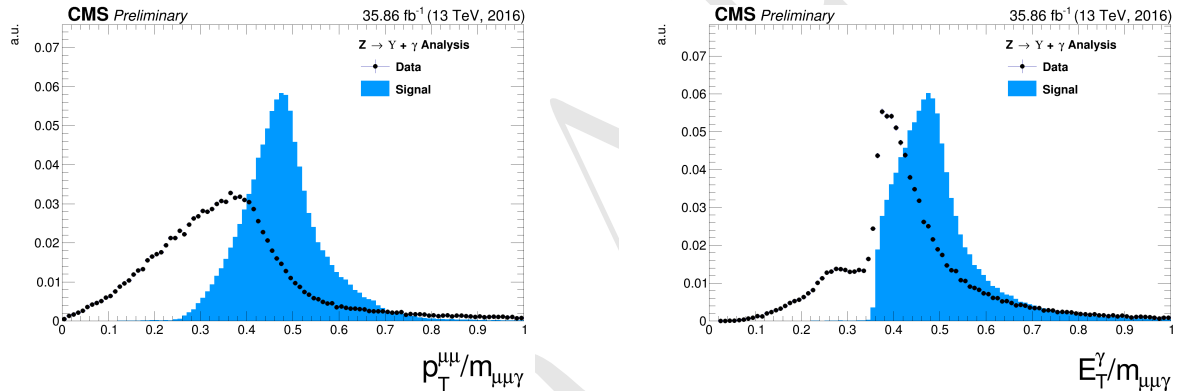


Figure 5.16: The ratio for the transverse momentum of the reconstructed Upsilon and the reconstructed  $Z$  mass ( $p_T^{\mu\mu} / M_{\mu\mu\gamma}$  - left) and the ratio for the transverse energy of the reconstructed Photon and the reconstructed  $Z$  mass ( $E_T^\gamma / M_{\mu\mu\gamma}$  - right) distribution for  $Z$  decaying into  $\Upsilon(1S, 2S, 3S) + \gamma$  from data and signal events after Group I of selection cuts. The plots are normalized to the unit of area. The black dots are data collect by CMS while the blue distribution is related only to the signal Monte-Carlo generated samples.

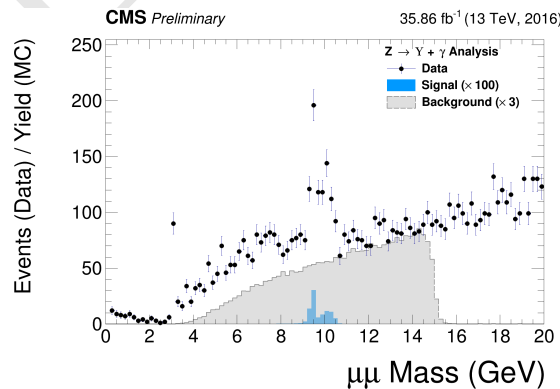


Figure 5.17: The dimuon mass distribution of the reconstructed  $\Upsilon(1S, 2S, 3S)$  from data and signal events for  $Z$  decaying after Group I of selection cuts. The plot is normalized to the number of events. "Signal" stands for the  $Z \rightarrow \Upsilon(1S, 2S, 3S) + \gamma$  sample (scaled by a factor of  $\times 100$ ) and "Background" corresponds to the resonant background ( $Z \rightarrow \mu\mu\gamma_{FSR}$ ) sample (scaled by a factor of  $\times 3$ ).

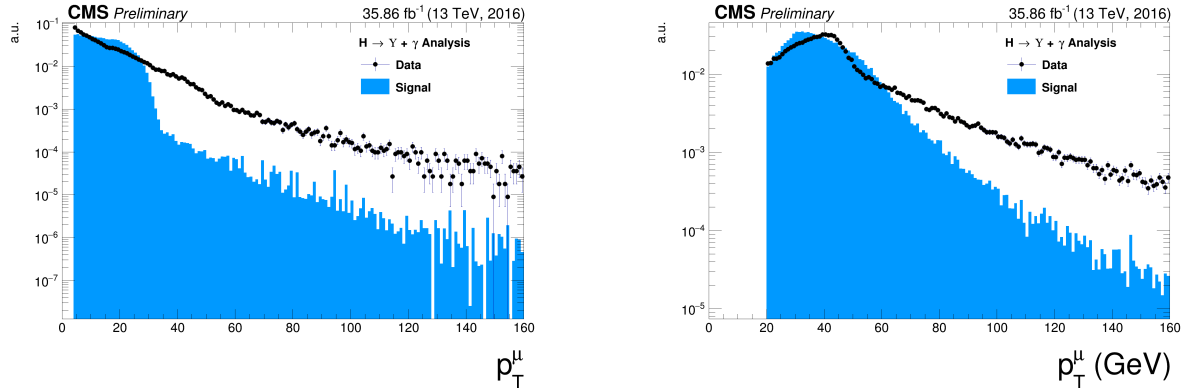


Figure 5.18: The  $p_T$  muon distributions from data and signal events for Higgs decaying into  $\Upsilon(1S, 2S, 3S) + \gamma$  after Group I of selection cuts, where on left are presenting the trailing muons and on right are the leading muons. The plots are normalized to the unit of area. The black dots are data collect by CMS while the blue distribution is related only to the signal Monte-Carlo generated samples.

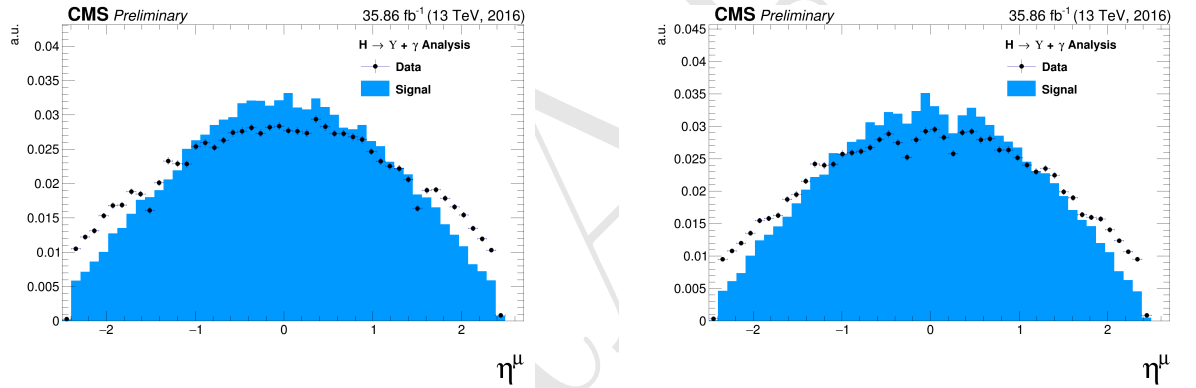


Figure 5.19: The  $\eta$  muon distributions from data and signal events of Higgs decaying into  $\Upsilon(1S, 2S, 3S) + \gamma$  after Group I of selection cuts, where on left are presenting the trailing muons and on right are the leading muons. The plots are normalized to the unit of area. The black dots are data collect by CMS while the blue distribution is related only to the signal Monte-Carlo generated samples.

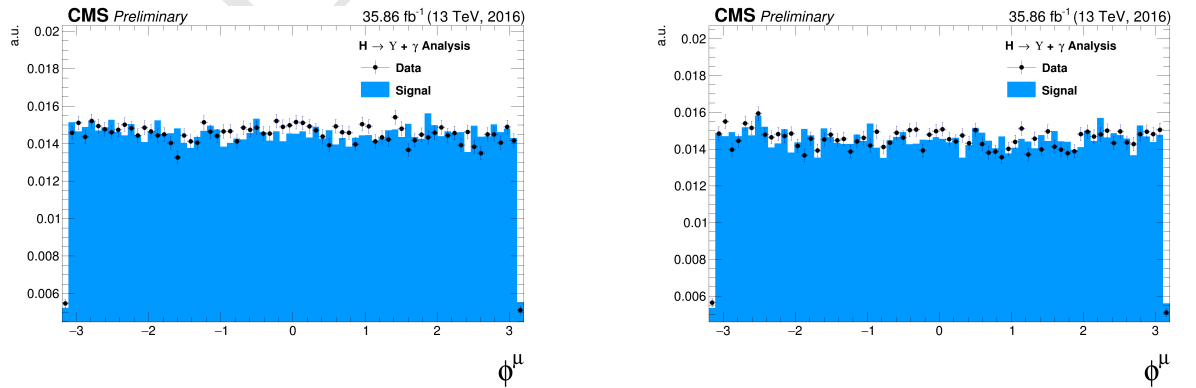


Figure 5.20: The  $\phi$  muon distributions from data and signal events of Higgs decaying into  $\Upsilon(1S, 2S, 3S) + \gamma$  after Group I of selection cuts, where on left are presenting the trailing muons and on right are the leading muons. The plots are normalized to the unit of area. The black dots are data collect by CMS while the blue distribution is related only to the signal Monte-Carlo generated samples.

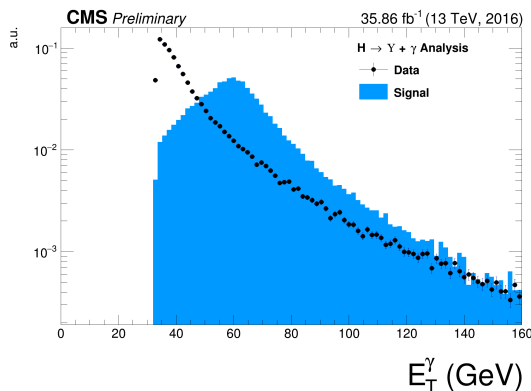


Figure 5.21: The  $p_T$  photon distributions from data and signal events for Higgs decaying into  $\Upsilon(1S, 2S, 3S) + \gamma$  Group I of selection cuts. The plot is normalized to the unit of area.

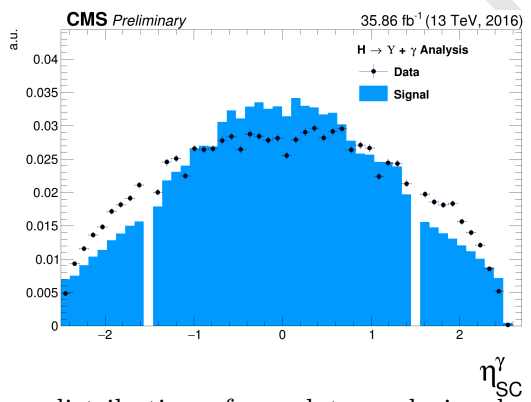


Figure 5.22: The  $\eta$  photon distributions from data and signal events of Higgs decaying into  $\Upsilon(1S, 2S, 3S) + \gamma$  after Group I of selection cuts. The plot is normalized to the unit of area.

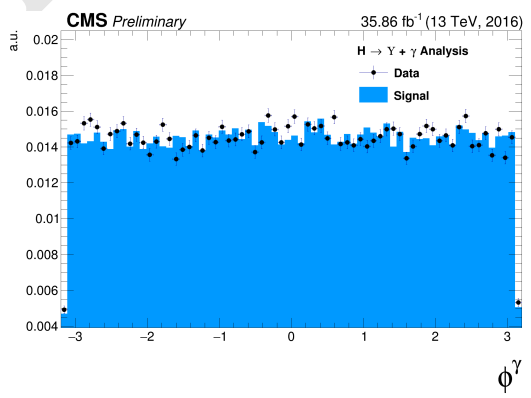


Figure 5.23: The  $\phi$  photon distributions from data and signal events of Higgs decaying into  $\Upsilon(1S, 2S, 3S) + \gamma$  after Group I of selection cuts. The plot is normalized to the unit of area.

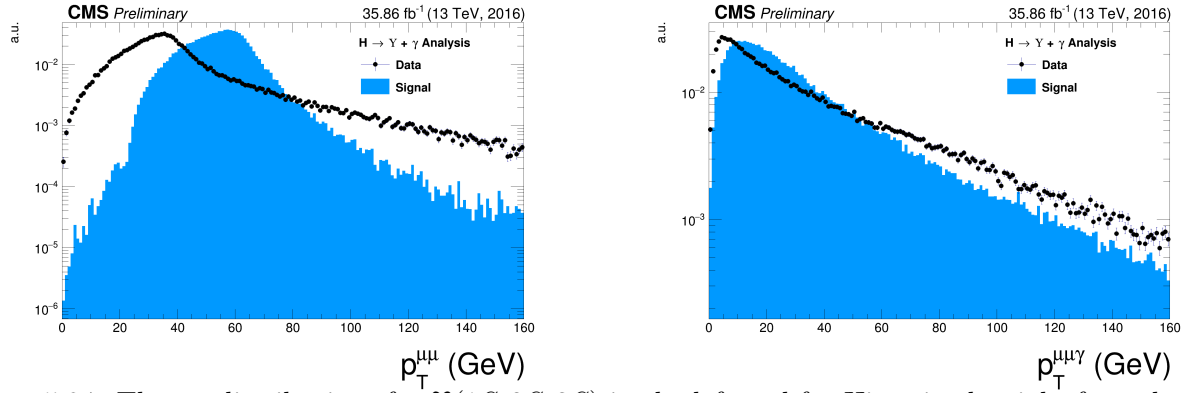


Figure 5.24: The  $p_T$  distributions for  $\Upsilon(1S, 2S, 3S)$  in the left and for Higgs in the right from data and signal events for Higgs decaying into  $\Upsilon(1S, 2S, 3S) + \gamma$  after Group I of selection cuts. The plots are normalized to the unit of area. The black dots are data collect by CMS while the blue distribution is related only to the signal Monte-Carlo generated samples.

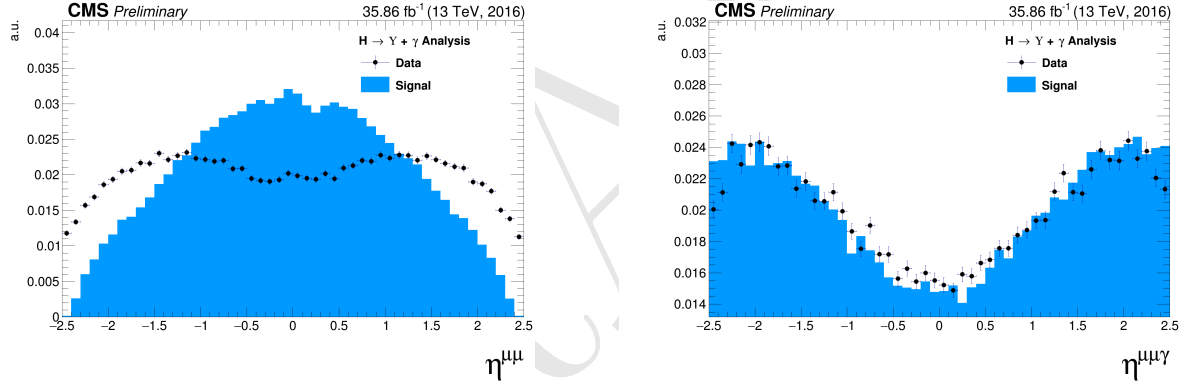


Figure 5.25: The  $\eta$  distributions for  $\Upsilon(1S, 2S, 3S)$  in the left and for Higgs in the right from data and signal events for Higgs decaying into  $\Upsilon(1S, 2S, 3S) + \gamma$  after Group I of selection cuts. The plots are normalized to the unit of area. The black dots are data collect by CMS while the blue distribution is related only to the signal Monte-Carlo generated samples.

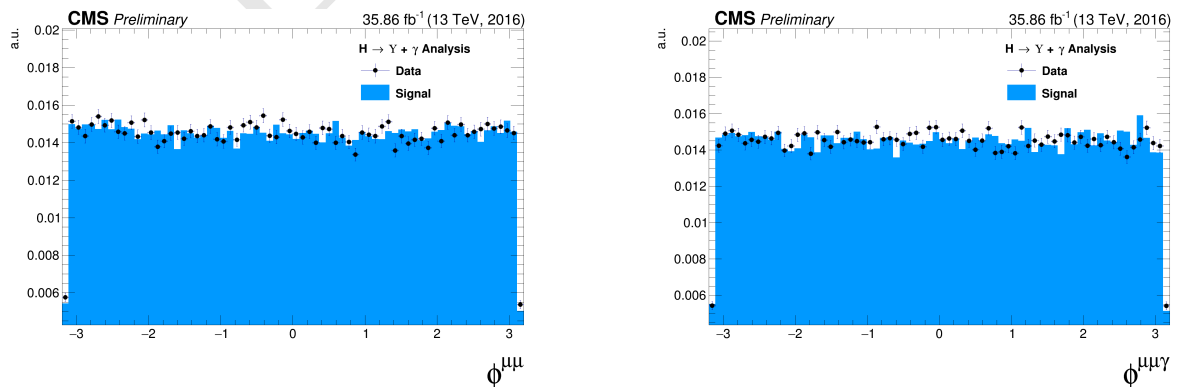


Figure 5.26: The  $\phi$  distributions for  $\Upsilon(1S, 2S, 3S)$  in the left and for Higgs in the right from data and signal events for Higgs decaying into  $\Upsilon(1S, 2S, 3S) + \gamma$  after Group I of selection cuts. The plots are normalized to the unit of area. The black dots are data collect by CMS while the blue distribution is related only to the signal Monte-Carlo generated samples.

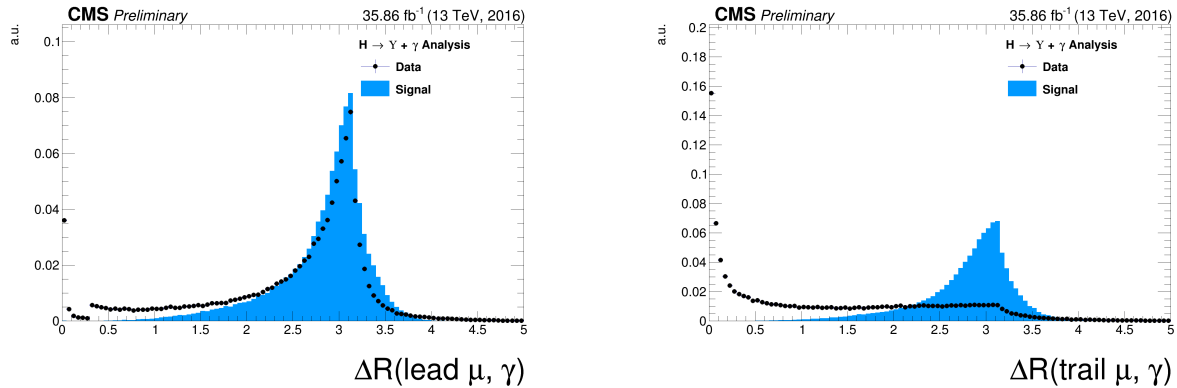


Figure 5.27: The  $\Delta R$  distributions between the photon and the leading muon (left) and the trailing muon (right) for Higgs decaying into  $\Upsilon(1S, 2S, 3S) + \gamma$  from data and signal events after Group I of selection cuts. The plots are normalized to the unit of area. The black dots are data collect by CMS while the blue distribution is related only to the signal Monte-Carlo generated samples.

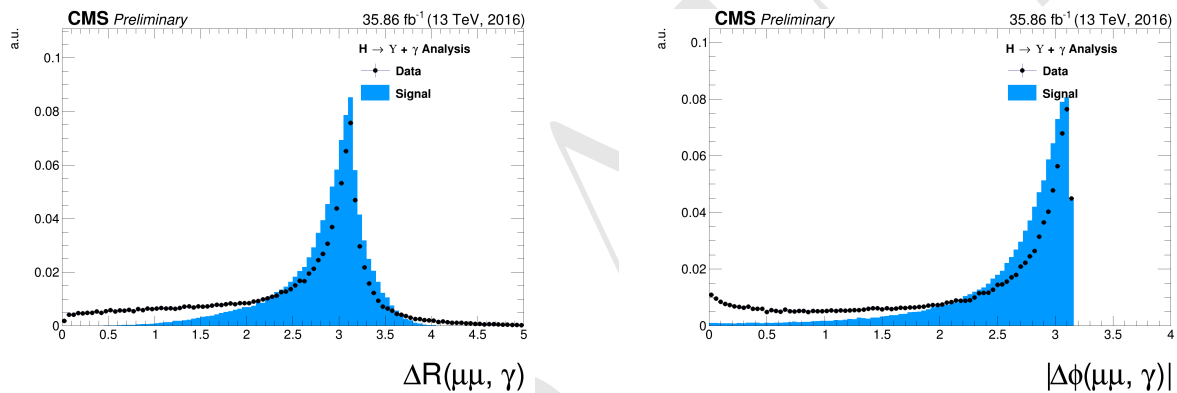


Figure 5.28: Left: The  $\Delta R$  distributions between reconstructed dimuon ( $\mu\mu$ ) system and the photon. Right: absolute value of the  $\Delta\phi$  between the dimuon system and the photon for for Higgs decaying into  $\Upsilon(1S, 2S, 3S) + \gamma$  from data and signal events after Group I of selection cuts. The plots are normalized to the unit of area. The black dots are data collect by CMS while the blue distribution is related only to the signal Monte-Carlo generated samples.

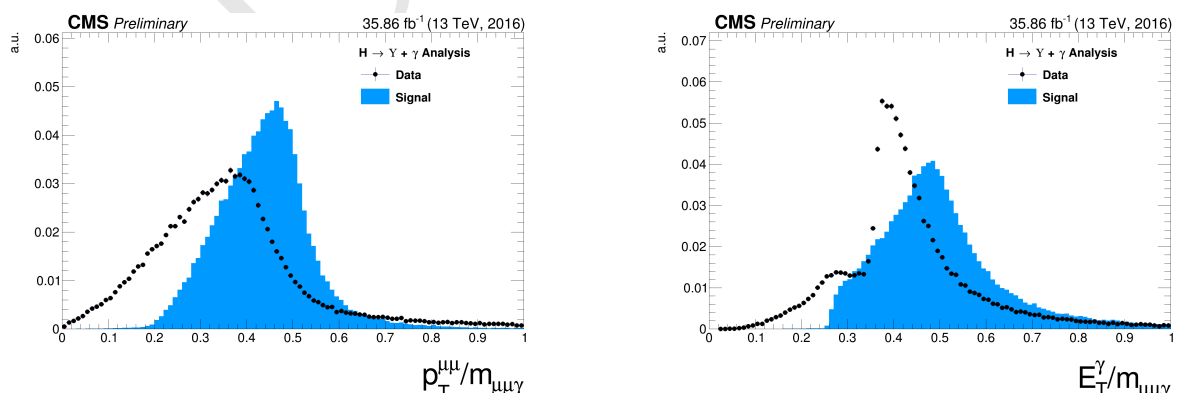


Figure 5.29: The ratio for the transverse momentum of the reconstructed Upsilon and the reconstructed Higgs mass ( $p_T^{\mu\mu}/M_{\mu\mu\gamma}$  - left) and the ratio for the transverse energy of the reconstructed Photon and the reconstructed Higgs mass ( $E_T^\gamma/M_{\mu\mu\gamma}$  - right) distribution for Higgs decaying into  $\Upsilon(1S, 2S, 3S) + \gamma$  from data and signal events after Group I of selection cuts. The plots are normalized to the unit of area. The black dots are data collect by CMS while the blue distribution is related only to the signal Monte-Carlo generated samples.

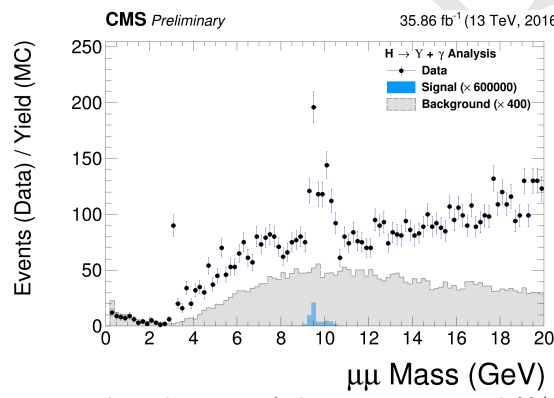


Figure 5.30: The dimuon mass distribution of the reconstructed  $\Upsilon(1S, 2S, 3S)$  from data and signal events for Higgs decaying after Group I of selection cuts. This plot is normalized the expected number of events. "Signal" stands for the  $H \rightarrow \Upsilon(1S, 2S, 3S) + \gamma$  sample (scaled by a factor of  $\times 600000$ ) and "Background" corresponds to the resonant background (Higgs Dalitz Decay) sample (scaled by a factor of  $\times 400$ ).

## 1958 5.6 Kinematical selection (Group II)

1959 After all Trigger and Object Identification cuts, described in before (**Group I**), a set of kinematical  
 1960 cuts are applied in order to improve the signal to background relation. They are

- 1961 •  $\Delta R(\text{leading } \mu, \gamma) > 1;$
- 1962 •  $\Delta R(\text{trailing } \mu, \gamma) > 1;$
- 1963 •  $\Delta R(\mu\mu, \gamma) > 2;$
- 1964 •  $|\Delta\phi(\text{leading } \mu, \gamma)| > 1.5;$
- 1965 •  $8.4 \text{ GeV} < M_{\mu\mu} < 11.1 \text{ GeV};$
- 1966 •  $E_T^\gamma/M_{\mu\mu\gamma} > 35/91.2$  for the Z decay or  $35/125$  for the Higgs decay;
- 1967 •  $p_T^{\mu\mu}/M_{\mu\mu\gamma} > 35/91.2$  for the Z decay or  $35/125$  for the Higgs decay.

1968 The choice of these thresholds were based on the visual inspection of the distributions (besides  
 1969 the invariant mass distribution of the dimuon system  $M_{\mu\mu}$ , which needs to be defined around the  
 1970  $\Upsilon(1S, 2S, 3S)$  mass) and to keep this analysis in phase with other similar analysis within CMS.

1971 Below it is shown the same set of plot shown before, but this time, taking into account the full  
 1972 selection (**Group I+II**).

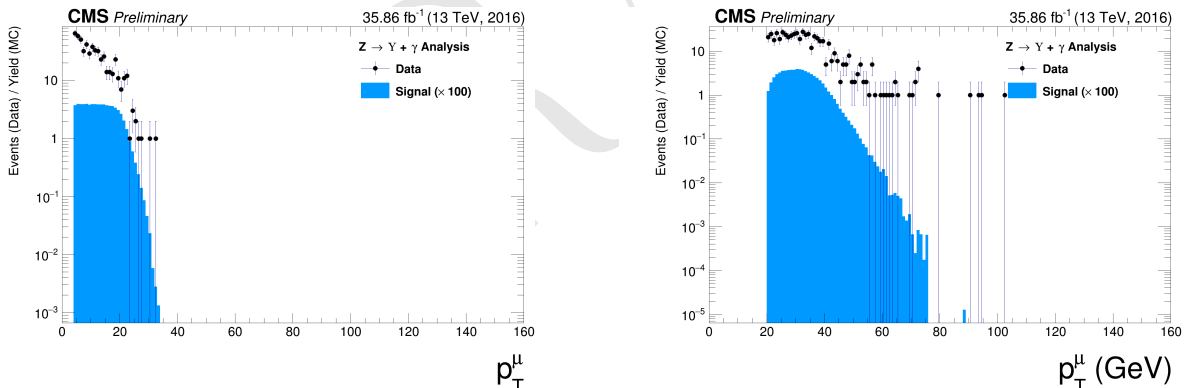


Figure 5.31: The  $p_T$  muon distributions from data and signal events for Z decaying into  $\Upsilon(1S, 2S, 3S) + \gamma$  after Group I+II of selection cuts, where on left are presenting the trailing muons and on right are the leading muons. The plots are normalized to the number of events. Signal sample is scaled by a factor of  $\times 100$ ). The black dots are data collect by CMS while the blue distribution is related only to the signal Monte-Carlo generated samples.

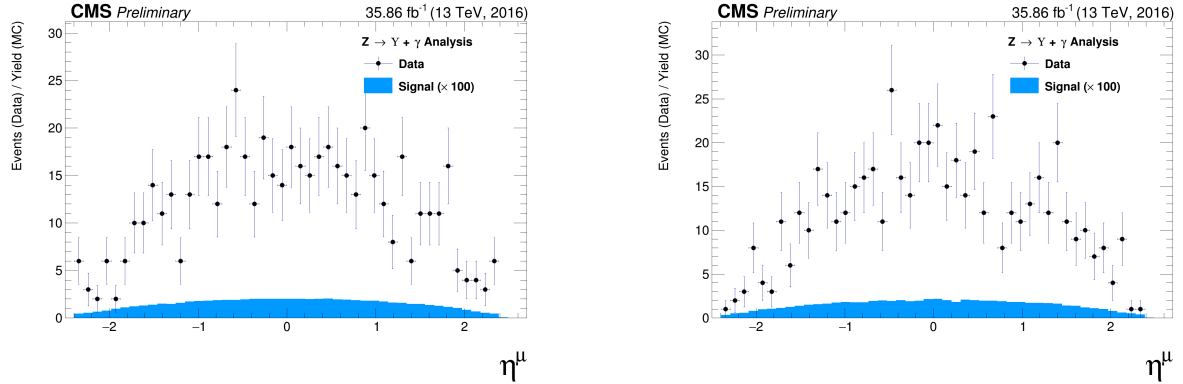


Figure 5.32: The  $\eta$  muon distributions from data and signal events of  $Z$  decaying into  $\Upsilon(1S, 2S, 3S) + \gamma$  after Group I+II of selection cuts, where on left are presenting the trailing muons and on right are the leading muons. The plots are normalized to the number of events. Signal sample is scaled by a factor of  $\times 100$ ). The black dots are data collect by CMS while the blue distribution is related only to the signal Monte-Carlo generated samples.

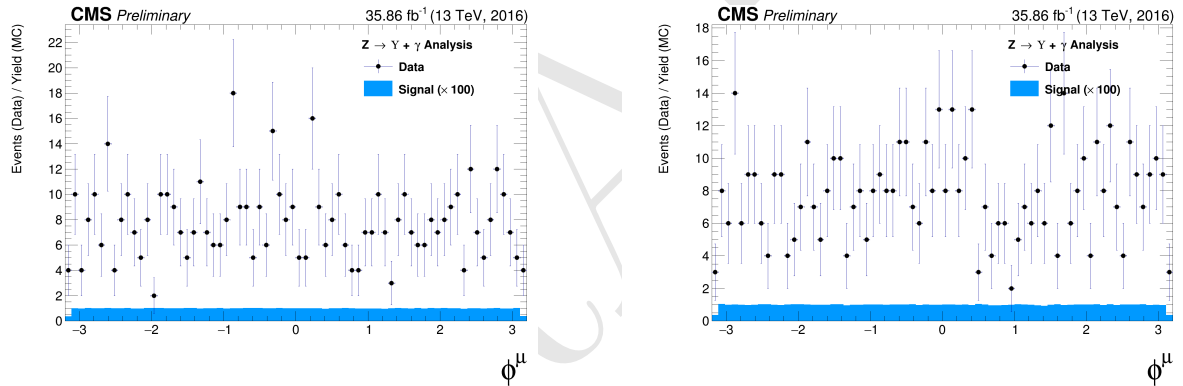


Figure 5.33: The  $\phi$  muon distributions from data and signal events of  $Z$  decaying into  $\Upsilon(1S, 2S, 3S) + \gamma$  after Group I+II of selection cuts, where on left are presenting the trailing muons and on right are the leading muons. The plots are normalized to the number of events. Signal sample is scaled by a factor of  $\times 100$ ). The black dots are data collect by CMS while the blue distribution is related only to the signal Monte-Carlo generated samples.

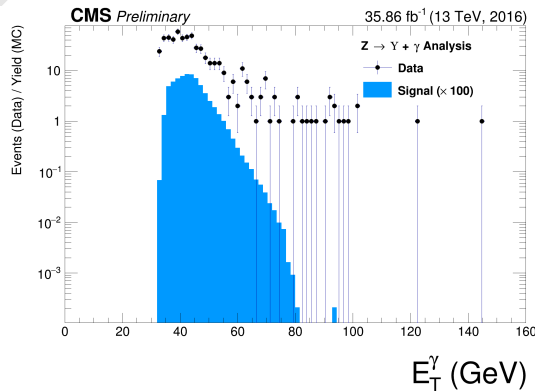


Figure 5.34: The  $p_T$  photon distributions from data and signal events for  $Z$  decaying into  $\Upsilon(1S, 2S, 3S) + \gamma$  all (Group I+II) selection cuts. The plot is normalized to the number of events. Signal sample is scaled by a factor of  $\times 100$ .

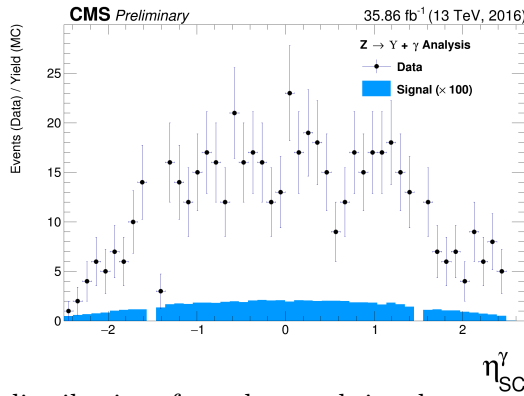


Figure 5.35: The  $\eta$  photon distributions from data and signal events of  $Z$  decaying into  $\Upsilon(1S, 2S, 3S) + \gamma$  after all (Group I+II) selection cuts. The plot is normalized to the number of events. Signal sample is scaled by a factor of  $\times 100$ .

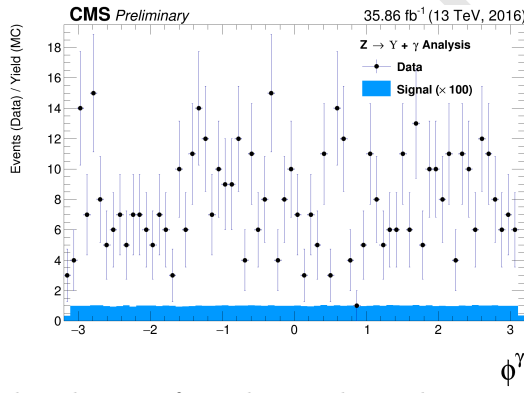


Figure 5.36: The  $\phi$  photon distributions from data and signal events of  $Z$  decaying into  $\Upsilon(1S, 2S, 3S) + \gamma$  after all (Group I+II) selection cuts. The plot is normalized to the number of events. Signal sample is scaled by a factor of  $\times 100$ .

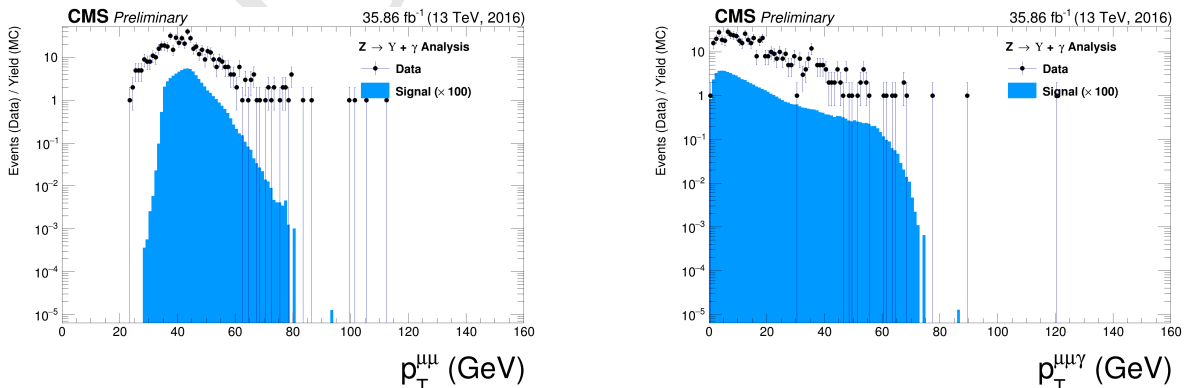


Figure 5.37: The  $p_T$  distributions for  $\Upsilon(1S, 2S, 3S)$  in the left and for  $Z$  in the right from data and signal events for  $Z$  decaying into  $\Upsilon(1S, 2S, 3S) + \gamma$  after all (Group I+II) selection cuts. The plots are normalized to the number of events. Signal sample is scaled by a factor of  $\times 100$ ). The black dots are data collect by CMS while the blue distribution is related only to the signal Monte-Carlo generated samples.

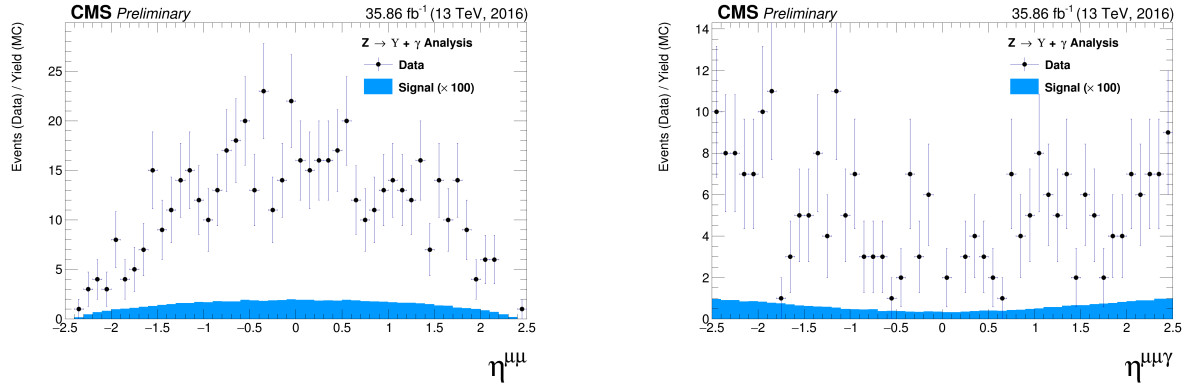


Figure 5.38: The  $\eta$  distributions for  $\Upsilon(1S, 2S, 3S)$  in the left and for  $Z$  in the right from data and signal events for  $Z$  decaying into  $\Upsilon(1S, 2S, 3S) + \gamma$  after all (Group I+II) selection cuts. The plots are normalized to the number of events. Signal sample is scaled by a factor of  $\times 100$ . The black dots are data collect by CMS while the blue distribution is related only to the signal Monte-Carlo generated samples.

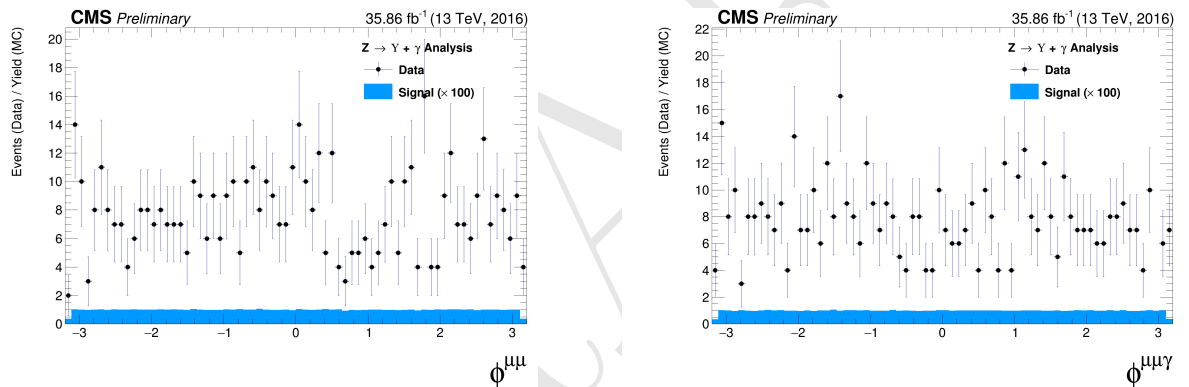


Figure 5.39: The  $\phi$  distributions for  $\Upsilon(1S, 2S, 3S)$  in the left and for  $Z$  in the right from data and signal events for  $Z$  decaying into  $\Upsilon(1S, 2S, 3S) + \gamma$  after all (Group I+II) selection cuts. The plots are normalized to the number of events. Signal sample is scaled by a factor of  $\times 100$ . The black dots are data collect by CMS while the blue distribution is related only to the signal Monte-Carlo generated samples.

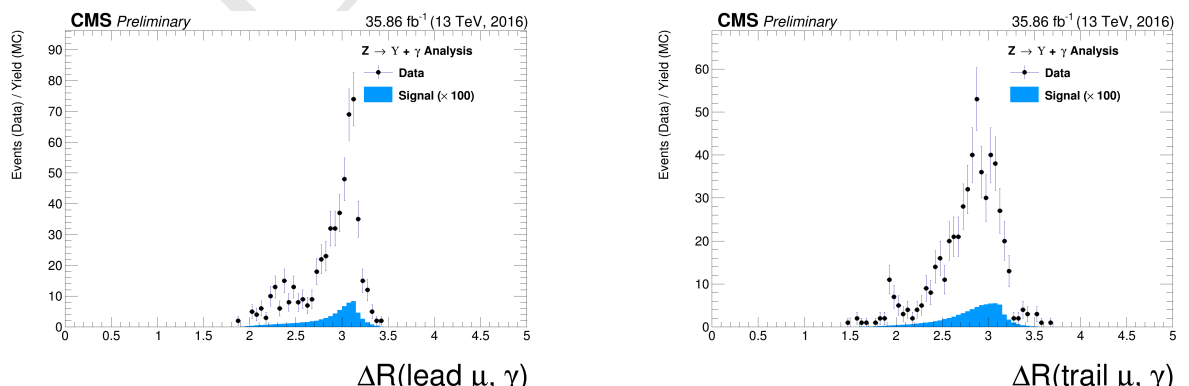


Figure 5.40: The  $\Delta R$  distributions between the photon and the leading muon (left) and the trailing muon (right) for  $\Upsilon(1S, 2S, 3S)$  from data and signal events for  $Z$  decaying after all (Group I+II) selection cuts. The plots are normalized to the number of events. Signal sample is scaled by a factor of  $\times 100$ . The black dots are data collect by CMS while the blue distribution is related only to the signal Monte-Carlo generated samples.

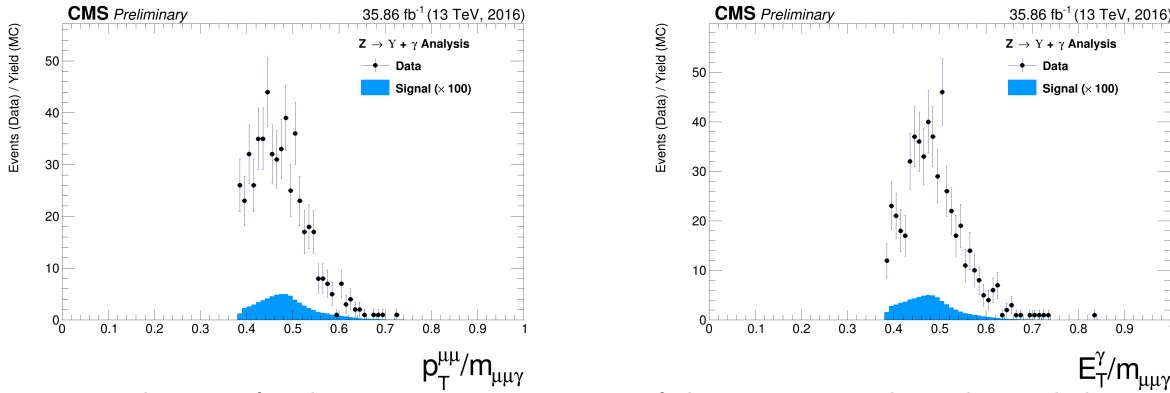


Figure 5.41: The ratio for the transverse momentum of the reconstructed Upsilon and the reconstructed  $Z$  mass ( $p_T^{\mu\mu}/M_{\mu\mu\gamma}$  - left) and the ratio for the transverse energy of the reconstructed Photon and the reconstructed  $Z$  mass ( $E_T^\gamma/M_{\mu\mu\gamma}$  - right) distribution for  $\Upsilon(1S, 2S, 3S)$  from data and signal events for  $Z$  decaying after all (Group I+II) selection cuts. The plots are normalized to the number of events. Signal sample is scaled by a factor of  $\times 100$ ). The black dots are data collect by CMS while the blue distribution is related only to the signal Monte-Carlo generated samples.

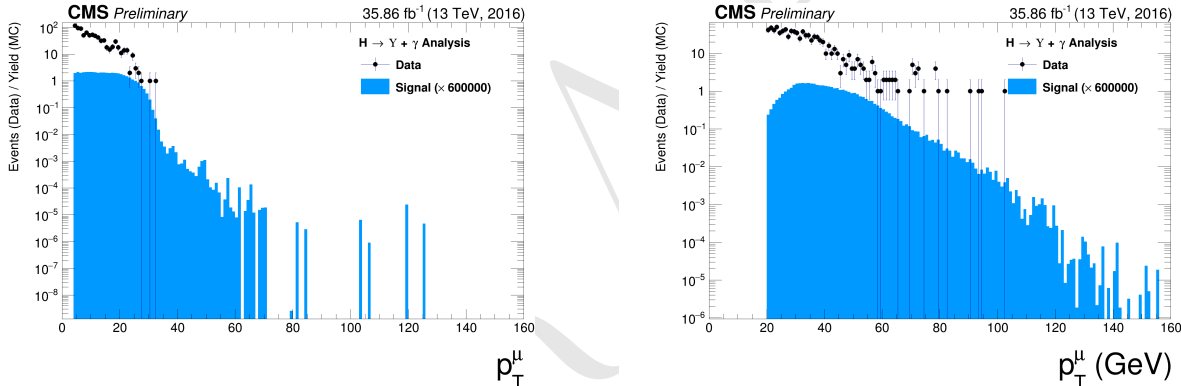


Figure 5.42: The  $p_T$  muon distributions from data and signal events for Higgs decaying into  $\Upsilon(1S, 2S, 3S) + \gamma$  after Group I of selection cuts, where on left are presenting the trailing muons and on right are the leading muons. The plots are normalized to the number of events. Signal sample is scaled by a factor of  $\times 600000$ ). The black dots are data collect by CMS while the blue distribution is related only to the signal Monte-Carlo generated samples.

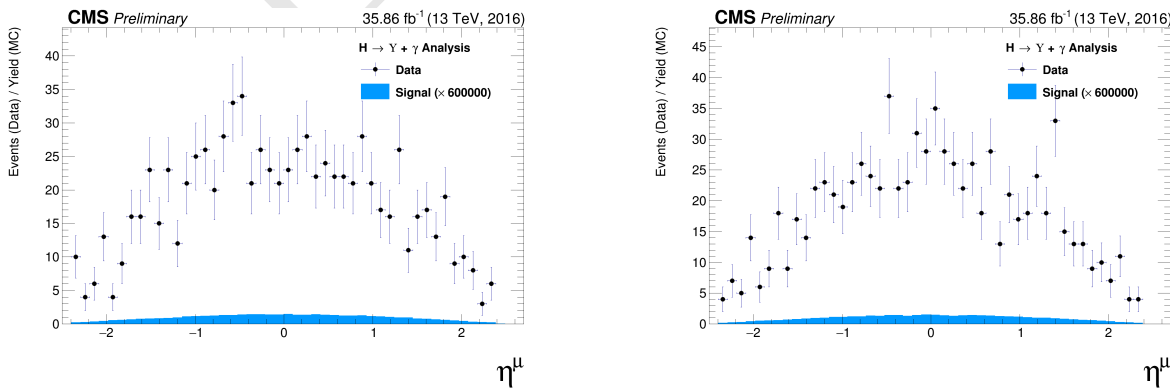


Figure 5.43: The  $\eta$  muon distributions from data and signal events of Higgs decaying into  $\Upsilon(1S, 2S, 3S) + \gamma$  after Group I of selection cuts, where on left are presenting the trailing muons and on right are the leading muons. The plots are normalized to the number of events. Signal sample is scaled by a factor of  $\times 600000$ ). The black dots are data collect by CMS while the blue distribution is related only to the signal Monte-Carlo generated samples.

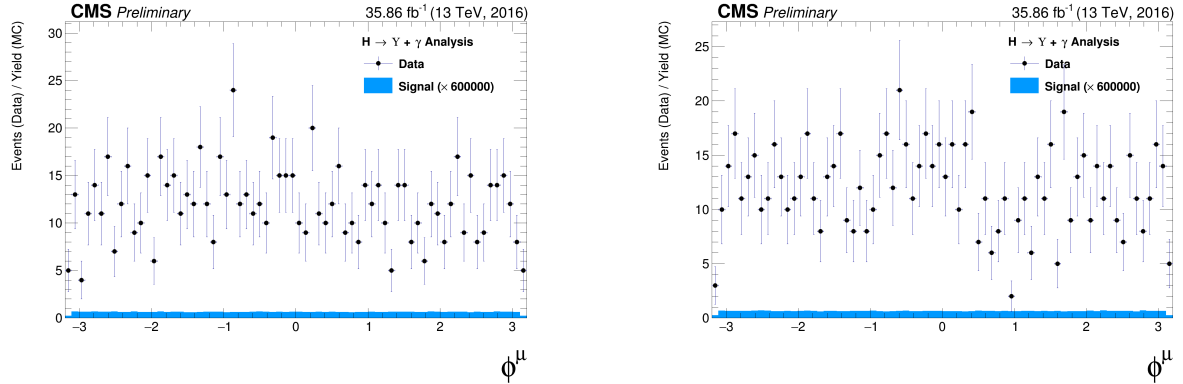


Figure 5.44: The  $\phi$  muon distributions from data and signal events of Higgs decaying into  $\Upsilon(1S, 2S, 3S) + \gamma$  after Group I of selection cuts, where on left are presenting the trailing muons and on right are the leading muons. The plots are normalized to the number of events. Signal sample is scaled by a factor of  $\times 600000$ ). The black dots are data collect by CMS while the blue distribution is related only to the signal Monte-Carlo generated samples.

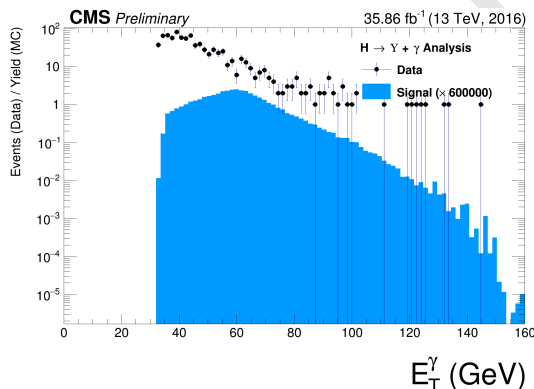


Figure 5.45: The  $p_T$  photon distributions from data and signal events for Higgs decaying into  $\Upsilon(1S, 2S, 3S) + \gamma$  all (Group I+II) selection cuts. The plot is normalized to the number of events. Signal sample is scaled by a factor of  $\times 600000$

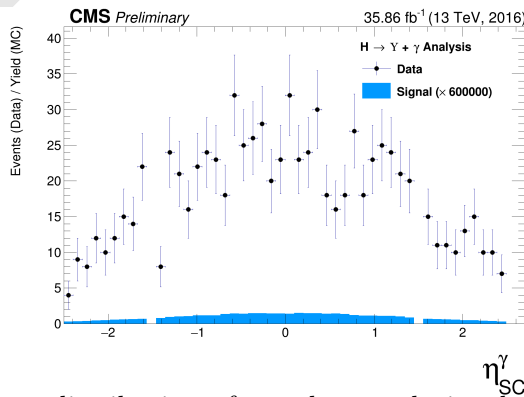


Figure 5.46: The  $\eta$  photon distributions from data and signal events of Higgs decaying into  $\Upsilon(1S, 2S, 3S) + \gamma$  after all (Group I+II) selection cuts. The plot is normalized to the number of events. Signal sample is scaled by a factor of  $\times 600000$ .

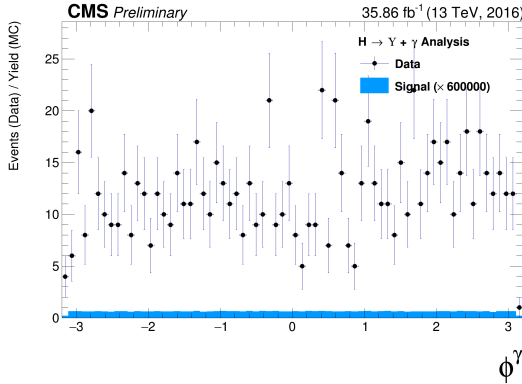


Figure 5.47: The  $\phi$  photon distributions from data and signal events of Higgs decaying into  $\Upsilon(1S, 2S, 3S) + \gamma$  after all (Group I+II) selection cuts. The plot is normalized to the number of events. Signal sample is scaled by a factor of  $c$ .

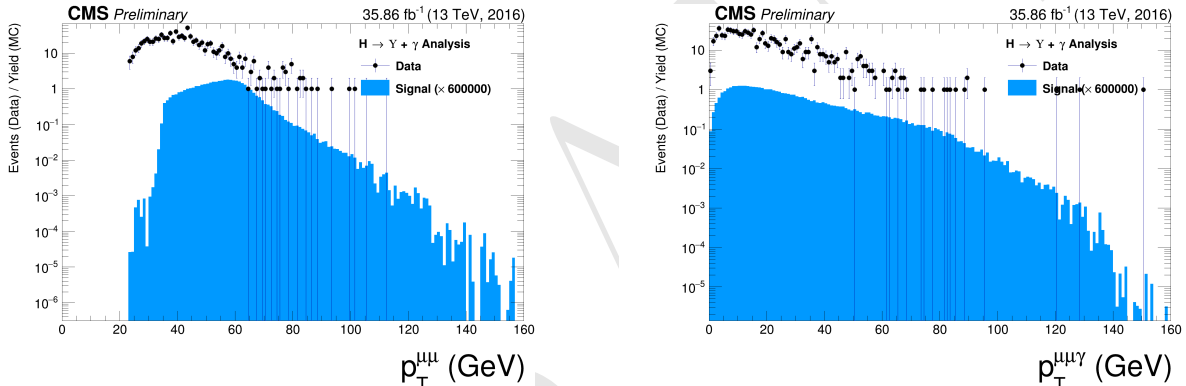


Figure 5.48: The  $p_T$  distributions for  $\Upsilon(1S, 2S, 3S)$  in the left and for Higgs in the right from data and signal events for Higgs decaying into  $\Upsilon(1S, 2S, 3S) + \gamma$  after all (Group I+II) selection cuts. The plots are normalized to the number of events. Signal sample is scaled by a factor of  $\times 600000$ ). The black dots are data collect by CMS while the blue distribution is related only to the signal Monte-Carlo generated samples.

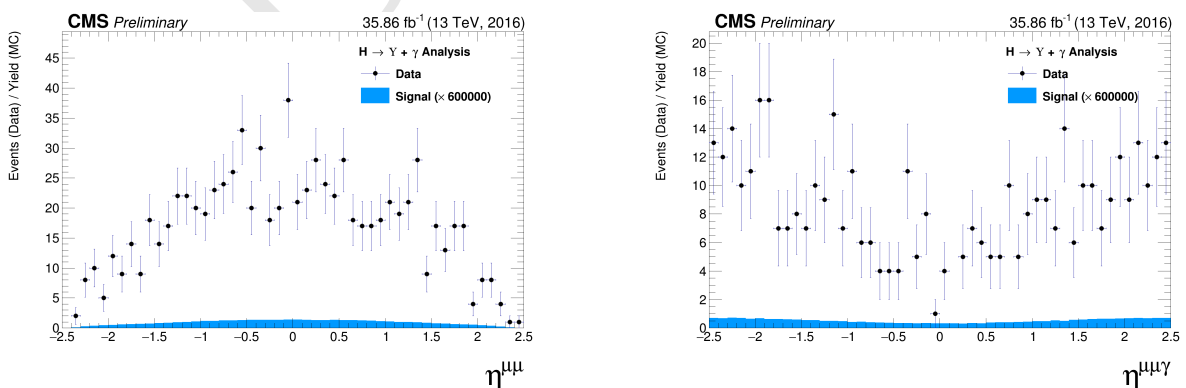


Figure 5.49: The  $\eta$  distributions for  $\Upsilon(1S, 2S, 3S)$  in the left and for Higgs in the right from data and signal events for Higgs decaying into  $\Upsilon(1S, 2S, 3S) + \gamma$  after all (Group I+II) selection cuts. The plots are normalized to the number of events. Signal sample is scaled by a factor of  $\times 600000$ ). The black dots are data collect by CMS while the blue distribution is related only to the signal Monte-Carlo generated samples.

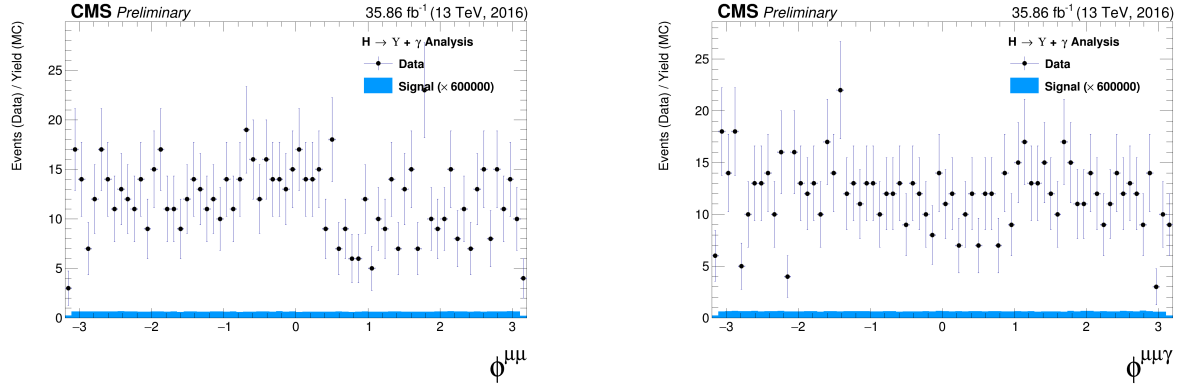


Figure 5.50: The  $\phi$  distributions for  $\Upsilon(1S, 2S, 3S)$  in the left and for Higgs in the right from data and signal events for Higgs decaying into  $\Upsilon(1S, 2S, 3S) + \gamma$  after all (Group I+II) selection cuts. The plots are normalized to the number of events. Signal sample is scaled by a factor of  $\times 600000$ . The black dots are data collect by CMS while the blue distribution is related only to the signal Monte-Carlo generated samples.

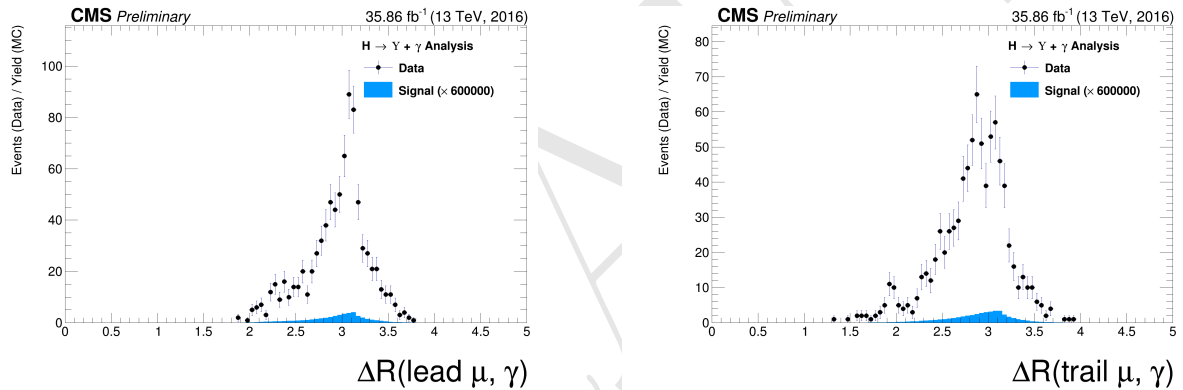


Figure 5.51: The  $\Delta R$  distributions between the photon and the leading muon (left) and the trailing muon (right) for  $\Upsilon(1S, 2S, 3S)$  from data and signal events for Higgs decaying after all (Group I+II) selection cuts. The plots are normalized to the number of events. Signal sample is scaled by a factor of  $\times 600000$ . The black dots are data collect by CMS while the blue distribution is related only to the signal Monte-Carlo generated samples.

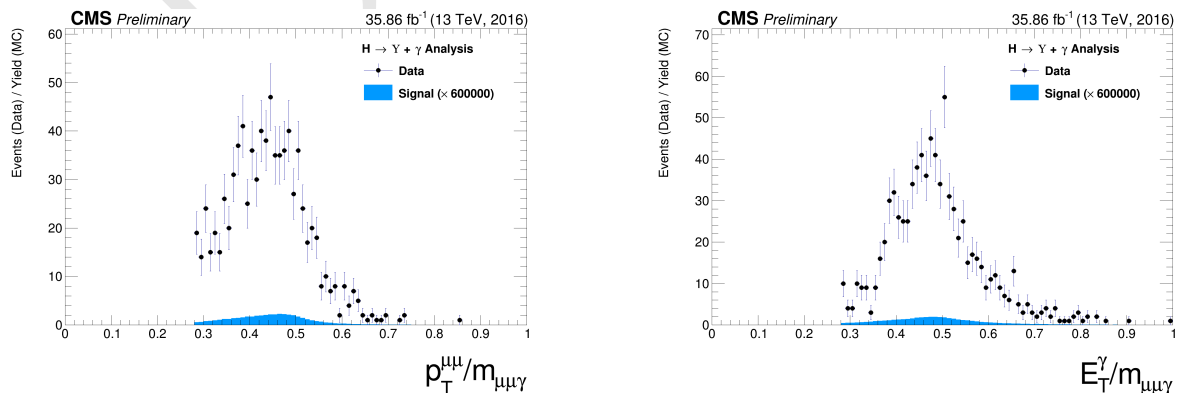


Figure 5.52: The ratio for the transverse momentum of the reconstructed Upsilon and the reconstructed Higgs mass ( $p_T^{\mu\mu}/M_{\mu\mu\gamma}$  - left) and the ratio for the transverse energy of the reconstructed Photon and the reconstructed Higgs mass ( $E_T^\gamma/M_{\mu\mu\gamma}$  - right) distribution for  $\Upsilon(1S, 2S, 3S)$  from data and signal events for Higgs decaying after all (Group I+II) selection cuts. The plots are normalized to the number of events. Signal sample is scaled by a factor of  $\times 600000$ . The black dots are data collect by CMS while the blue distribution is related only to the signal Monte-Carlo generated samples.

## 1973 5.7 Event categorization and yields

1974 In order to increase the sensibility of the analysis, a categorization procedure was applied. They  
 1975 are based on the  $\eta$  and R9 distribution of the reconstructed photon.

1976 The photon R9 is a shower shape variable defined as the fraction of energy deposited in the 5x5  
 1977 square surrounding the Super Cluster seed of the reconstructed photon. A photon that convert  
 1978 before reaching the ECAL tend to have lower values of R9, in comparison with unconverted photons.  
 1979 Converted photons have wider energy resolution and are more likely to be misidentified.

1980 Selected events with the photon reconstructed inside the barrel and with  $R9 > 0.94$  are categorized  
 1981 as "EB High R9"<sup>6</sup>, selected events with the photon reconstructed inside the barrel and with  
 1982  $R9 < 0.94$  are categorized as "EB Low R9" and selected events with the photon reconstructed  
 1983 inside the endcap, regardless of its R9 value, categorized as "EE". This categorization is done in  
 1984 view of increase the analysis sensitivity.

1985 This categorization is implemented only for the Z decay. The Higgs does not present enough  
 1986 statistics to make it profitable, so only the inclusive one is used.

### 1987 5.7.1 R9 reweighting

1988 As spotted by the  $H \rightarrow \gamma\gamma$  analysis, during Run1 [141], there is a disagreement in the R9 distribution  
 1989 of photons in Data and MC. In order to mitigate this difference, a transformation factor is extracted  
 1990 and applied to the reconstructed photons before the categorization.

1991 The same approach of the  $H \rightarrow \gamma\gamma$  analysis is applied, in which the nominal photon selection of this  
 1992 analysis (see section 5.5.3) is used to select photons on Data and MC. Then the two distributions  
 1993 are remapped and the transformation factors are extracted.

1994 Figure 5.53 show the R9 distribution before and after the reweighting, for the Barrel and the Endcap.

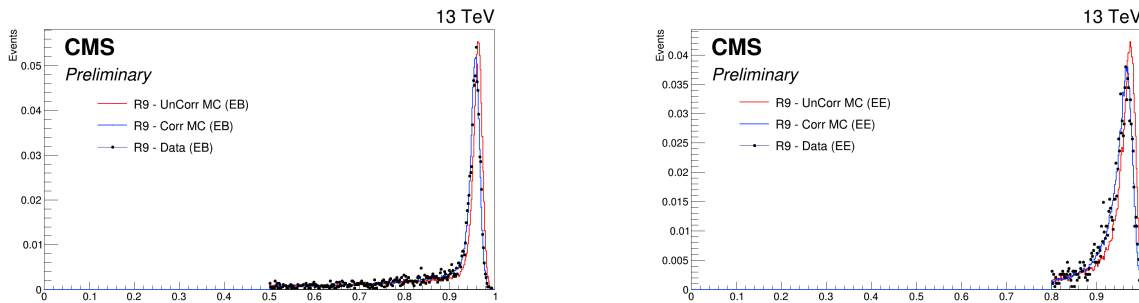


Figure 5.53: Data and MC of the R9 variable, before and after the reweighting. Barrel (left) and Endcap (right).

<sup>6</sup>EB stands for Electromagnetic Barrel

<sup>1995</sup> **5.7.2 Event counting and yields**

<sup>1996</sup> Tables 5.4 and 5.5 show the total number of events before and after the full selection. Two things  
<sup>1997</sup> are important to notice.

Table 5.4: Number of events for the Z decay, before and after the full selection, per categorization scenarios.

	Data	Signal			$Z \rightarrow \mu\mu\gamma_{FSR}$
		$Z \rightarrow \Upsilon(1S) + \gamma$	$Z \rightarrow \Upsilon(2S) + \gamma$	$Z \rightarrow \Upsilon(3S) + \gamma$	
Total (before selection)	169.84 M	3.54	1.4	1.22	$3.33 \times 10^3$
Inclusive	447	0.393	0.157	0.136	176
EB High R9	197	0.172	0.0682	0.0597	78
EB Low R9	146	0.129	0.0519	0.0448	58.5
EE	104	0.0916	0.0365	0.032	39.8

Table 5.5: Number of events for the H decay, before and after the full selection.

	Data	Signal			$H \rightarrow \gamma\gamma^*$
		$H \rightarrow \Upsilon(1S) + \gamma$	$H \rightarrow \Upsilon(2S) + \gamma$	$H \rightarrow \Upsilon(3S) + \gamma$	
Total (before selection)	169.84 M	0.000257	$5.43 \times 10^{-5}$	$3.93 \times 10^{-5}$	136
Inclusive	231	$5.23 \times 10^{-5}$	$1.2 \times 10^{-5}$	$8.96 \times 10^{-6}$	1.22

- <sup>1998</sup> The signal selection efficiency is between 20% and 21% for all  $\Upsilon$  states and categories.
- <sup>1999</sup> When one compares the fraction of selected resonant background, with respect to the selected data  
<sup>2000</sup> events for the Higgs decay ( $1.22/231$ ), the fraction obtained ( $\sim 0.3\%$ ) is irrelevant. On the other  
<sup>2001</sup> hand, the same fraction for the Z decay ( $176/447$ ) is far from irrelevant ( $\sim 39\%$ )<sup>7</sup>. The same  
<sup>2002</sup> relation is not found in the  $H/Z \rightarrow J/\psi + \gamma$  analysis [59], where both decays (Higgs and Z) show  
<sup>2003</sup> neglectable estimations of resonant background contribution to data. The very same behavior was  
<sup>2004</sup> found by ATLAS [56]. It can be explained by the relatively larger cross-section of the Z resonant  
<sup>2005</sup> background ( $Z \rightarrow \mu\mu\gamma_{FSR}$ ), with respect to the Higgs resonant background (Higgs Dalitz Decay).  
<sup>2006</sup> For the  $J/\psi$  channel, it is not an issue since its cross-section is way larger than the resonant  
<sup>2007</sup> background. The figures 5.17 and 5.30 help to clarify these affirmations, for the Z and Higgs decay,  
<sup>2008</sup> respectively. One can easily see how clear the  $J/\psi$  peak is in both decays and how minor the Higgs  
<sup>2009</sup> Dalitz Decay contributions is to the  $\Upsilon$  peak, with respect to the  $Z \rightarrow \mu\mu\gamma_{FSR}$  contribution. It is  
<sup>2010</sup> important to keep in mind the different scaling of the resonant background distributions, the yields  
<sup>2011</sup> are multiplied by  $\times 3$  for the Z and  $\times 100$  for the Higgs. The resonant background to the data due  
<sup>2012</sup> to  $Z \rightarrow \Upsilon(1S, 2S, 3S) + \gamma$  channel is the main motivation to use a 2-dimensional modeling fitting of  
<sup>2013</sup> the signal and background events, in order to add one more layer of differentiation between many  
<sup>2014</sup> backgrounds contributions which will be detailed in the next section.

<sup>7</sup>It is worth to keep in mind that this is a estimation based on MC

## 2015 5.8 Background modeling

2016 The background statistical modeling proposed for this analysis is a two dimensional unbinned maxi-  
 2017 mum likelihood fit on the  $\mu\mu$  and the  $\mu\mu\gamma$  invariant mass distributions. It is considered and modeled,  
 2018 as briefly discussed in 5.1.2, three kinds of backgrounds:

- 2019 • **Full Combinatorial:** any combination of two muon and one photon that pass all the object  
 2020 reconstruction and event selection criteria.
- 2021 •  **$\Upsilon$  Combinatorial:** a  $\Upsilon(1S, 2S, 3S)$ , that decays to a dimuon system, combined with a  
 2022 misidentified photon (misreconstructed, pileup photon, etc.), that pass all the object recon-  
 2023 struction, identification and event selection criteria.
- 2024 • **Resonant background:** a Z (or Higgs) that decays straight to a  $\mu\mu\gamma$ , that pass all the  
 2025 object reconstruction and event selection criteria, without passing through any intermediate  
 2026 state. The main contributions considered for this background are  $Z \rightarrow \mu\mu\gamma_{FSR}$  (a Z decaying  
 2027 to a dimuon system with one of the muons irradiating a photon) or a Higgs Dalitz Decay.

2028 All of them will be modeled from data, with some inputs from the MC (simulated) samples, as  
 2029 explained below. For both invariant mass spectra ( $\mu\mu$  and  $\mu\mu\gamma$ ) the full combinatorial background  
 2030 is expected to behave like a non-resonant distribution. The same behavior is expected for the  
 2031  $\mu\mu\gamma$  mass distribution of the  $\Upsilon$  Combinatorial background and for the  $\mu\mu$  mass distribution of the  
 2032 resonant background.

2033 On the other hand, the  $\mu\mu$  distribution of the  $\Upsilon$  Combinatorial background and the  $\mu\mu\gamma$  mass  
 2034 distribution for the resonant background are expected to behave like a resonant distribution, cen-  
 2035 tered around the  $\Upsilon(1S, 2S, 3S)$  invariant mass (9.46 GeV, 10.02 GeV and 10.35 GeV) [12] and the Z  
 2036 boson invariant mass (91.2 GeV) [12], respectively . Table 5.6 summarizes the background modeling  
 2037 proposed for this analysis.

Table 5.6: Modeling for each background source and mass component.

	$m_{\mu\mu}$	$m_{\mu\mu\gamma}$
<b>Resonant background</b>	Bernstein 1 <sup>st</sup> order	Crystal Ball (Higgs decay) Double Crystal Ball (Z decay)
<b><math>\Upsilon</math> Combinatorial</b>	3 Gaussians (one for each $\Upsilon$ state)	
<b>Full Combinatorial</b>	Chebychev 1 <sup>st</sup> order	Polynomial

2038 For the  $Z \rightarrow \Upsilon(1S, 2S, 3S) + \gamma$  analysis, the resonant background model parameters are extracted  
 2039 by performing a simultaneous 2-dimensional fit over the invariant masses,  $m_{\mu\mu}$  and  $m_{\mu\mu\gamma}$ , of the  
 2040 simulated  $Z \rightarrow \mu\mu\gamma_{FSR}$  MC sample of events that passes the selection described in Section 5.4, as in  
 2041 figure 5.54. Once the parameters are extracted, they are fixed and the *pdf* (Probability Distributions  
 2042 Function) of the 2-Dimensional modeling is stored, leaving only the normalization of the *pdf* as a  
 2043 parameter free to float (this will be determined from data).

2044 In order to describe the 2-dimensional invariant mass distribution of the Resonant Background, as  
 2045 stated in Table 5.6, the  $m_{\mu\mu}$  component is described by a Bernstein polynomial of 1<sup>st</sup> order [142],  
 2046 which is used here just a representation of a linear function. The  $m_{\mu\mu\gamma}$  component is described

2047 by Double Crystal Ball function [143]. A Crystal Ball function is a *pdf* composed by a gaussian  
 2048 distribution and a power-law tail to the left, before certain threshold. The Crystal Ball function was  
 2049 named after the Crystal Ball Collaboration (first to use this *pdf*) and it is widely used in high-energy  
 2050 physics to describe mass distributions that incorporate FSR (final state radiation) effects, via the  
 2051 power-law tail. A Double Crystal Ball is a Crystal Ball function with the power-law tail on both  
 2052 sides.

2053 A Crystal Ball function is defined as:

$$CB(x; \alpha, n, \bar{x}, \sigma) = N \cdot \begin{cases} \exp\left(-\frac{(x-\bar{x})^2}{2\sigma^2}\right), & \text{for } \frac{x-\bar{x}}{\sigma} > -\alpha \\ A \cdot (B - \frac{x-\bar{x}}{\sigma})^{-n}, & \text{for } \frac{x-\bar{x}}{\sigma} \leq -\alpha \end{cases}, \quad (5.4)$$

2054 where,

$$\begin{aligned} A &= \left(\frac{n}{|\alpha|}\right)^n \cdot \exp\left(-\frac{|\alpha|^2}{2}\right), \\ B &= \frac{n}{|\alpha|} - |\alpha|, \\ N &= \frac{1}{\sigma(C + D)}, \\ C &= \frac{n}{|\alpha|} \cdot \frac{1}{n-1} \cdot \exp\left(-\frac{|\alpha|^2}{2}\right), \\ D &= \sqrt{\frac{\pi}{2}} \left(1 + \operatorname{erf}\left(\frac{|\alpha|}{\sqrt{2}}\right)\right), \end{aligned}$$

2055 and  $\operatorname{erf}$  is the error function.

2056 For the three gaussian functions fits, which represent the three  $\Upsilon$  states (1S, 2S and 3S) from the  $\Upsilon$   
 2057 Combinatorial background in the  $m_{\mu\mu}$  component, we use a  $\Upsilon$  control sample in order to extract the  
 2058 fit parameters, including the relative normalization between each  $\Upsilon$  state. This sample is composed  
 2059 by dimuon candidates obtained from data, by selecting the events that passes the same trigger and  
 2060 dimuon selection of the nominal selection and with  $p_T^{\mu\mu} > 35$  GeV (this cut is done in order to  
 2061 keep this selected dimuon candidates compatibles with the  $p_T^{\mu\mu}/M_{\mu\mu\gamma}$  cut applied in the nominal  
 2062 selection). No selection or cuts in the photon are required.

2063 This control sample is fitted with a Chebychev 1<sup>st</sup> order (linear polynomial) for the background  
 2064 support and 3 gaussian with the following constraints:

- 2065 • the mean of each state should be the ones in the PDG [12], but allowed to shift by a float and  
 2066 common (the same for all states) value.
- 2067 • the sigma should be based on the 1S fit of the MC. All other sigma should be the result of  
 2068 the 1S sigma times the state mass over the 1S mass ( $\sigma_{2S,3S} = \frac{m_{2S,3S}}{m_{1S}} \sigma_{1S}$ ).

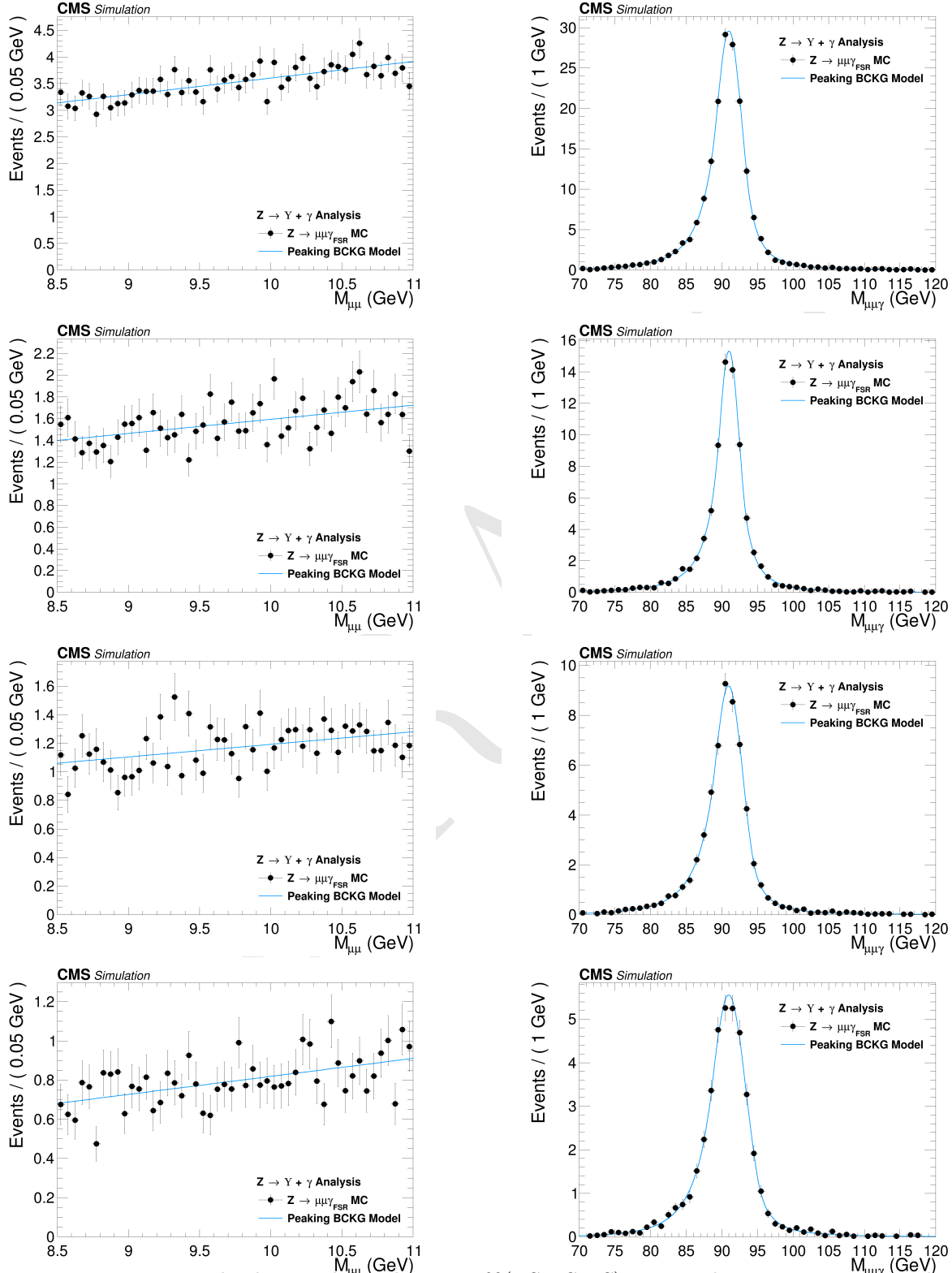


Figure 5.54: Resonant background for the  $Z \rightarrow \Upsilon(1S, 2S, 3S) + \gamma$  analysis.  $\mu\mu$  mass distribution (left) and  $\mu\mu\gamma$  invariant mass distribution (right). From top to bottom categories: Inclusive, EB High R9, EB Low R9, EE.

2069 The idea behind this fit is that scale and resolution (mean and sigma, respectively, of the gaussians)  
 2070 over a sample without a photon selection should be the same as over a sample with photon selection,  
 2071 since these are detector-only dependent effects. The fact that we exclude the photon from this  
 2072 control sample, improves the statistics and gives a better measurement of these variables.

2073 The fit of the  $\Upsilon$  control sample is shown in figure 5.55.

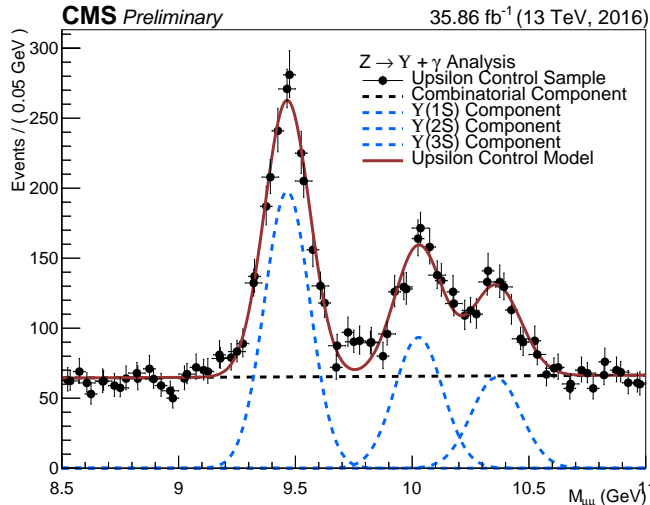


Figure 5.55:  $\Upsilon$  control sample fit with Chebychev 1<sup>st</sup> order for the background support and 3 gaussian for the three  $\Upsilon(1S, 2S, 3S)$  peaks.

2074 Once determined, the fit parameters are fixed, they are used to compose the 2-Dimensional *pdf*. The  
 2075  $m_{\mu\mu}$  component of the full combinatorial background is derived fully from the data fit (described  
 2076 below). In the same sense, the  $m_{\mu\mu\gamma}$  component of the full combinatorial and the  $\Upsilon(nS)$  Combi-  
 2077 torial backgrounds are also fully derived from the data, but following a more complex procedure: a  
 2078 composition with the *pdf* components described above, plus a statistical test, to avoid overfitting  
 2079 within a Discrete Profiling (or "Envelope Method"), as described in [144] and also implemented  
 2080 in [141].

2081 The statistical test consists of, for each category, different orders of a set of polynomial *pdfs* families  
 2082 are tested: a sums of exponentials, sum of polynomials (in the Bernstein basis), a Laurent series  
 2083 and a sums of power-law functions.

- Sums of exponentials:

$$f_N(x) = \sum_{i=1}^N p_{2i} e^{p_{2i+1}x},$$

- Sums of polynomials (in the Bernstein basis):

$$f_N(x) = \sum_{i=0}^N p_i b_{(i,N)}, \text{ where } b_{(i,N)} := \binom{N}{i} x^i (1-x)^{N-i},$$

- Laurent series:

$$f_N(x) = \sum_{i=1}^N p_i x^{-4 + \sum_{j=1}^i (-1)^j (j-1)},$$

- Sums of power-law functions:

$$f_N(x) = \sum_{i=1}^N p_{2i} x^{-p_{2i+1}},$$

2084 where for all  $k$ , the  $p_k$  are a set of floating parameters in the fit.

2085 Twice difference in the negative log-likelihood ( $NLL$ ) between the  $N^{th}$  and the  $(N+1)^{th}$  order of  
 2086 the same polynomial ( $\Delta NLL = 2 \times (NLL_N - NLL_{N+1})$ ) is expected to follow a  $\chi^2$  distribution  
 2087 with  $M$  degrees of freedom, where  $M$  is the increase in degrees of freedom when going from  $N^{th}$  to  
 2088  $(N+1)^{th}$ . This can be shown with the help of the Wilks' theorem [145].

2089 Starting from the lowest order possible, the best choice of order, for each family, is determined when  
 2090 a increase in the order of the polynomial, does not brings a significant improvement in the quality  
 2091 of the fit. Since a model with more fit parameters (higher order polynomials) will always perform,  
 2092 if not the same, better than a simpler one, an optimal choice of the polynomial order, will be the  
 2093 one right before the model becomes too flexible for the data.

2094 Consider a  $p$ -value defined as:

$$\begin{aligned} p\text{-value} &= \int_{\Delta NLL}^{\infty} \chi_M^2(\Delta) d\Delta \\ &= P(\chi_M^2 > \Delta NLL), \end{aligned} \tag{5.5}$$

2095 In the same spirit as the Wilks' theorem, this is the  $p$ -value for a likelihood ratio test between a  
 2096 null hypotheses and an alternative model, where the null hypotheses is the  $N^{th}$  order and  $(N+1)^{th}$   
 2097 order is the alternative one.

$$\begin{aligned} \Delta NLL &= 2 \times (NLL_N - NLL_{N+1}) \\ &= -2 \times \log\left(\frac{\mathcal{L}_N}{\mathcal{L}_{N+1}}\right), \end{aligned} \tag{5.6}$$

2098 where  $\mathcal{L}_N$  is the likelihood for the  $N^{th}$  polynomial order.

2099 The alternative will present a statistically significant improvement, with respect to the null hypothe-  
 2100 ses, if the  $p$ -value is smaller than 0.05, since the probability of obtaining, by chance, considering  
 2101 the null hypotheses is true, a even higher  $\Delta NLL$  is less than 5%. This will give support to chose  
 2102  $(N+1)^{th}$  over  $N^{th}$ .

2103 If the  $p$ -value is greater than 0.05 a higher order is not supported, since the probability of obtaining  
 2104 a  $\Delta NLL$  greater than the one observed is statistically significant (more than 5%). A higher  $\Delta NLL$

means that another data sample, collected and analyzed with strictly the same conditions, would have a probability of more than 5% of giving a better fit improvement than the one observed, again assuming that the null hypotheses is true. This is an indication of overfitting, since the improvements are likely to come from just statistical fluctuations. When testing the  $(N+1)^{th}$  order and this condition is reached, the optimal order should be the  $N^{th}$ .

At first, before any fit to data, the 2-Dimensional model is composed by the five components, as described in Table 5.6 (in which the  $m_{\mu\mu\gamma}$  modeling for the Full Combinatorial Background and the  $\Upsilon$  combinatorial are shared), then, the statistical test described before is ran for each family. It is important to stress that before the statistical test all the other fitting parameters have been fixed. This leaves only the normalizations of the model components and the polynomial coefficients free to float.

Once the optimal order for each *pdf* family is obtained, the composed *pdf* with each choice from statistical test is saved in the same model, providing a discrete variable that indexes the different polynomial *pdf* families. This method is called Discrete Profiling (or "*Envelope Method*") and it allows the analysis algorithm to treat the choice of the *pdf* as a systematics and incorporate its effect in the extracted upper limits. This model, with different choices of polynomial families is called envelope.

The implementation, used in the analysis, of the statistical test and the Discrete Profiling is based on the same algorithm used by the  $H \rightarrow \gamma\gamma$  Run II analysis. An extensive documentation on these methods can be found in  $H \rightarrow \gamma\gamma$  analysis note and physics analysis summary [146, 147] and in the specific reference of the Discrete Profiling [144]. The figures 5.56 and 5.57 show the projection for the  $\mu\mu$  and  $\mu\mu\gamma$  distribution after the statistical test.

For the  $H \rightarrow \Upsilon(1S,2S,3S) + \gamma$  analysis, the same procedure is implemented, except for the resonant background modeling. Since the MC prediction for the contribution of the background is too small, according to the comparison between the final selected events for data and the Higgs Dalitz Decay sample, in order to avoid fitting over statistical fluctuations of the data sample, the Resonant Background, for the Higgs channel, is fully modeled from the MC sample, including its normalization, as shown in figure 5.58, hence it is not included the statistical test, neither in the final background modeling envelope.

The results of the background modeling for the Full Combinatorial and  $\Upsilon$  Combinatorial, can be found at Figures 5.59 and 5.60, for the  $\mu\mu$  and  $\mu\mu\gamma$  distribution, respectively. It is worth to remember that, for the Higgs channel, we are not implementing any categorization.

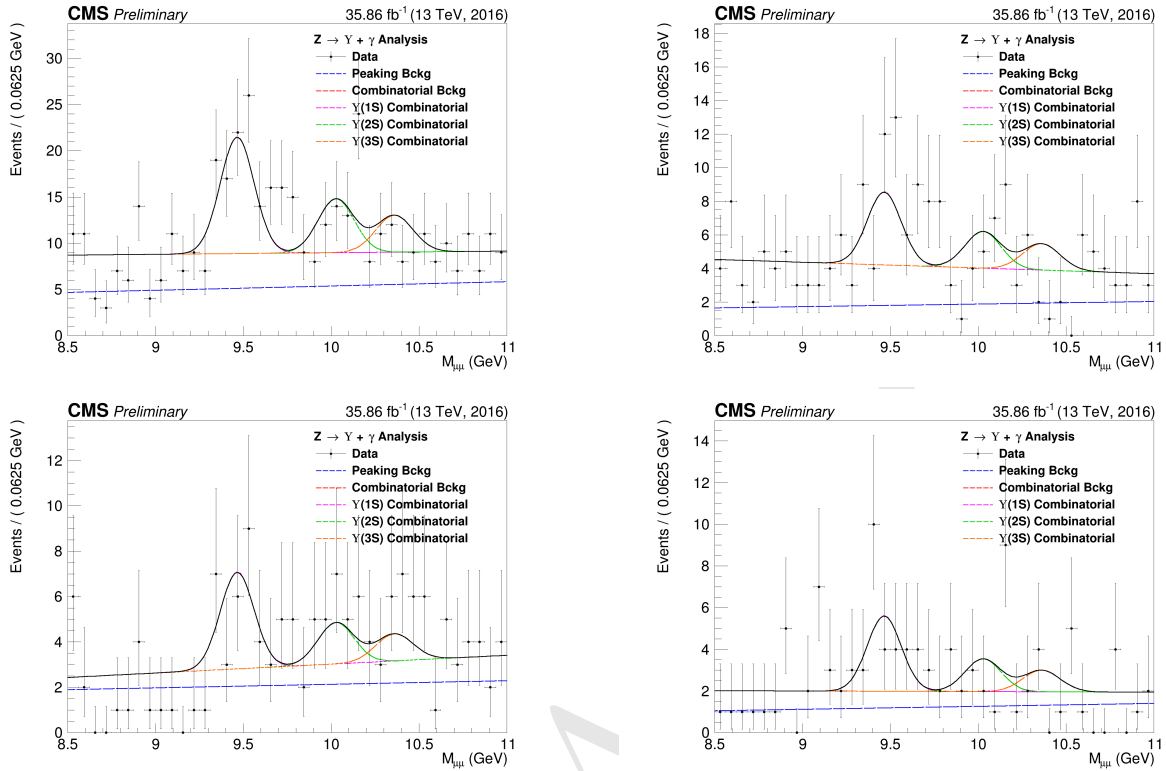


Figure 5.56:  $Z \rightarrow \Upsilon(1S, 2S, 3S) + \gamma$  Background Modeling:  $\mu\mu$  distribution. Inclusive (top left); EB High R9 (top right), EB Low R9 (bottom left), EE (bottom right). The pdfs projections are plotted with respect to the overall best choice of the statistical test.

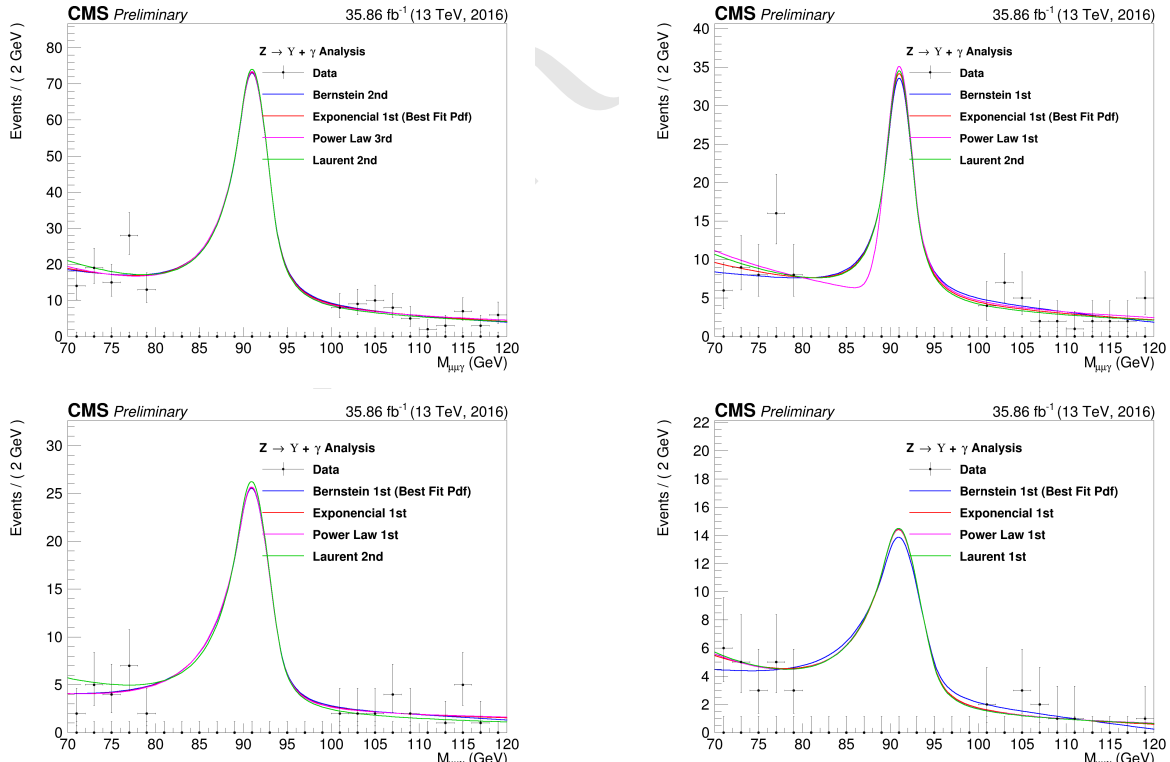


Figure 5.57:  $Z \rightarrow \Upsilon(1S, 2S, 3S) + \gamma$  Background Modeling:  $\mu\mu\gamma$  distribution. Inclusive (top left); EB High R9 (top right), EB Low R9 (bottom left), EE (bottom right). The plotted *pdfs* corresponds to the best choice by the statistical test for each family. The signal region, from 80 GeV to 100 GeV was blinded.

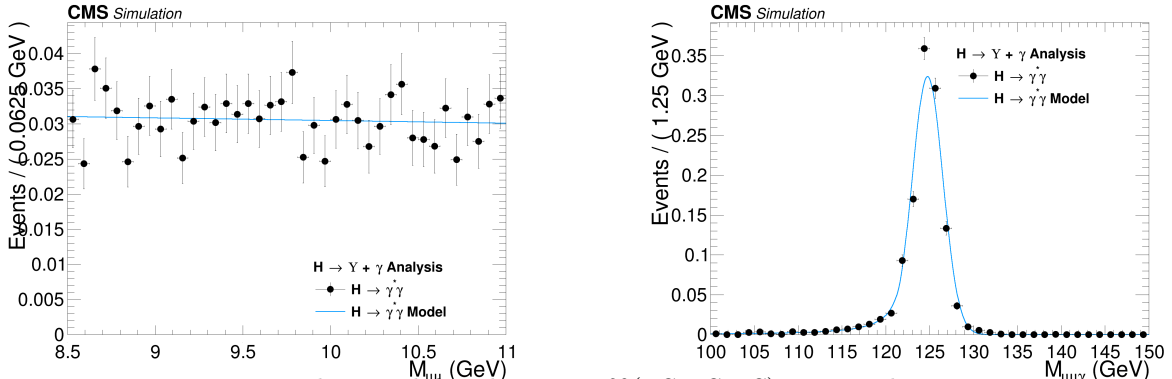


Figure 5.58: Resonant Background for the  $H \rightarrow \Upsilon(1S, 2S, 3S) + \gamma$  analysis.  $m_{\mu\mu}$  invariant mass distribution (left) and  $m_{\mu\mu\gamma}$  invariant mass distribution (right).

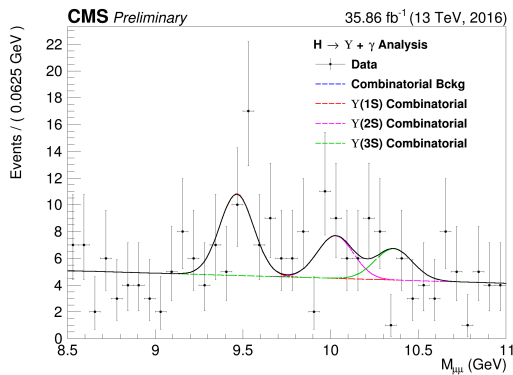


Figure 5.59:  $H \rightarrow \Upsilon(1S, 2S, 3S) + \gamma$  Background Modeling:  $m_{\mu\mu}$  distribution. The *pdfs* projections are plotted with respect to the overall best choice of the statistical test.

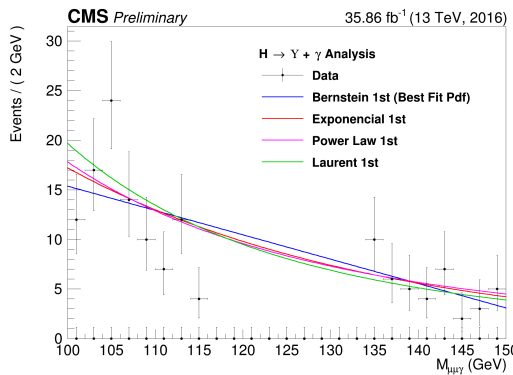


Figure 5.60:  $H \rightarrow \Upsilon(1S, 2S, 3S) + \gamma$  Background Modeling:  $\mu\mu\gamma$  distribution. The plotted *pdfs* corresponds to the best choice by the statistical test for each family. The signal region, from 115 GeV to 135 GeV was blinded.

## 2137 5.9 Signal modeling

2138 Along the same lines as the background modeling (Section 5.8), the signal modeling is implemented  
2139 as a two dimensional unbinned maximum likelihood fit on the  $m_{\mu\mu}$  and the  $m_{\mu\mu\gamma}$  invariant masses  
2140 distributions, but this time, only using the signal simulated MC samples 5.1.2. Since, for the two  
2141 spectra, it is expected a peak-like distribution, one centered in the Z (or Higgs) boson mass and the  
2142 other centered in the  $\Upsilon$  mass, two also peak-like analytics *pdfs* were chosen to compose the signal  
2143 model. The modeling is summarized in table 5.7.

Table 5.7: Modeling for each signal source and mass component.

	$m_{\mu\mu}$	$m_{\mu\mu\gamma}$
$Z \rightarrow \Upsilon(1S, 2S, 3S) + \gamma$	Double Crystal Ball	Double Crystal Ball
$H \rightarrow \Upsilon(1S, 2S, 3S) + \gamma$	Double Crystal Ball	Crystal Ball + Gaussian with the same mean

2144 The projections of the modeling for the Z boson decay channel analysis can be found at figures 5.61,  
2145 5.62, 5.63 and 5.64, for Inclusive, EB High R9, EB Low R9 and EE, respectively. The projection  
2146 on the modeling for the Higgs boson signal can be found at Figure 5.65. A deeper discussion on the  
2147 systematics uncertainties associated to them, will be presented in the next section.

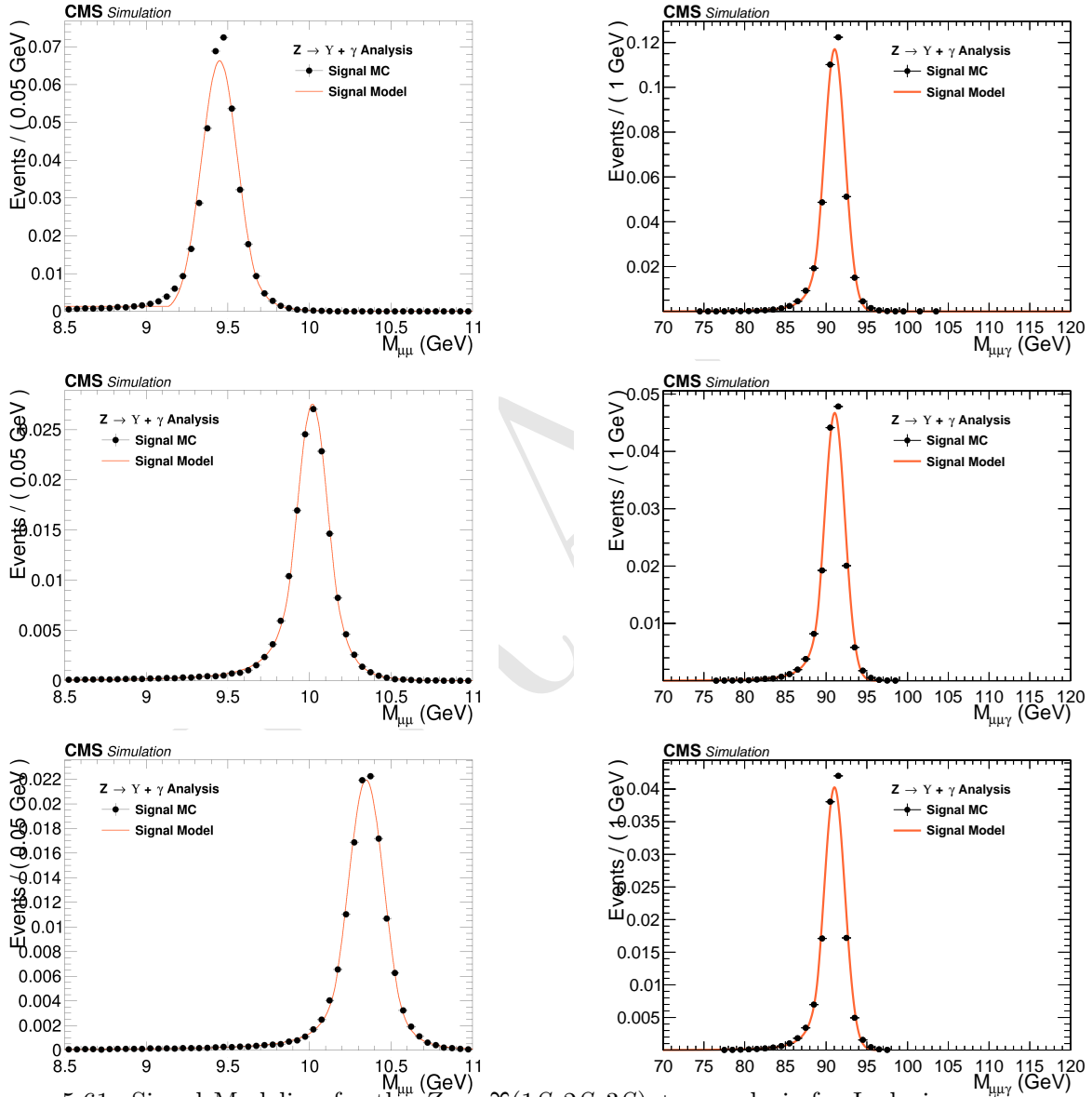


Figure 5.61: Signal Modeling for the  $Z \rightarrow \Upsilon(1S, 2S, 3S) + \gamma$  analysis for Inclusive category.  $m_{\mu\mu}$  mass distribution (left) and  $m_{\mu\mu\gamma}$  mass distribution (right). From top to bottom:  $\Upsilon(1S)$ ,  $\Upsilon(2S)$ ,  $\Upsilon(3S)$ .

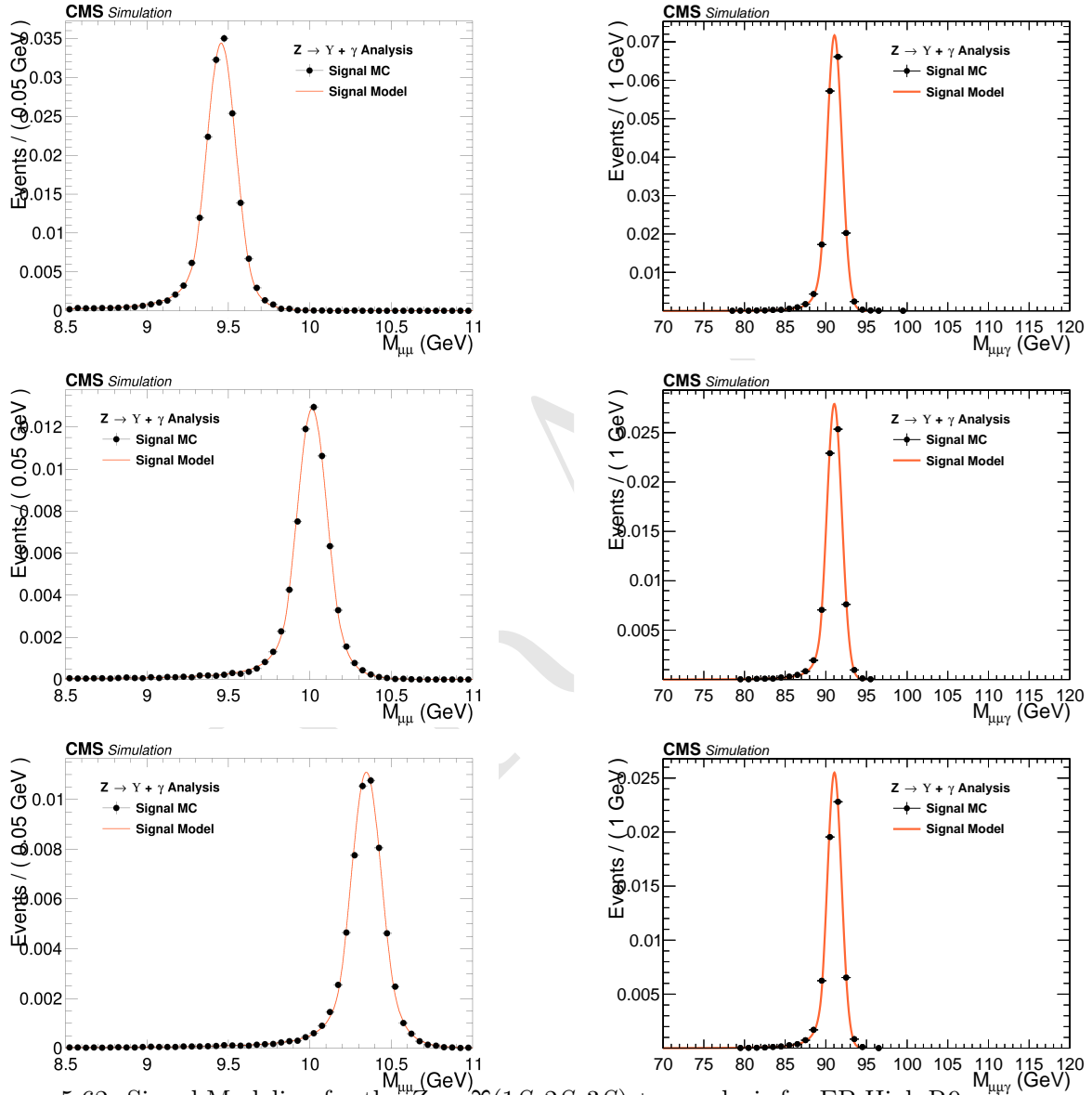


Figure 5.62: Signal Modeling for the  $Z \rightarrow \Upsilon(1S, 2S, 3S) + \gamma$  analysis for EB High R9 category.  $m_{\mu\mu}$  mass distribution (left) and  $m_{\mu\mu\gamma}$  mass distribution (right). From top to bottom:  $\Upsilon(1S)$ ,  $\Upsilon(2S)$ ,  $\Upsilon(3S)$ .

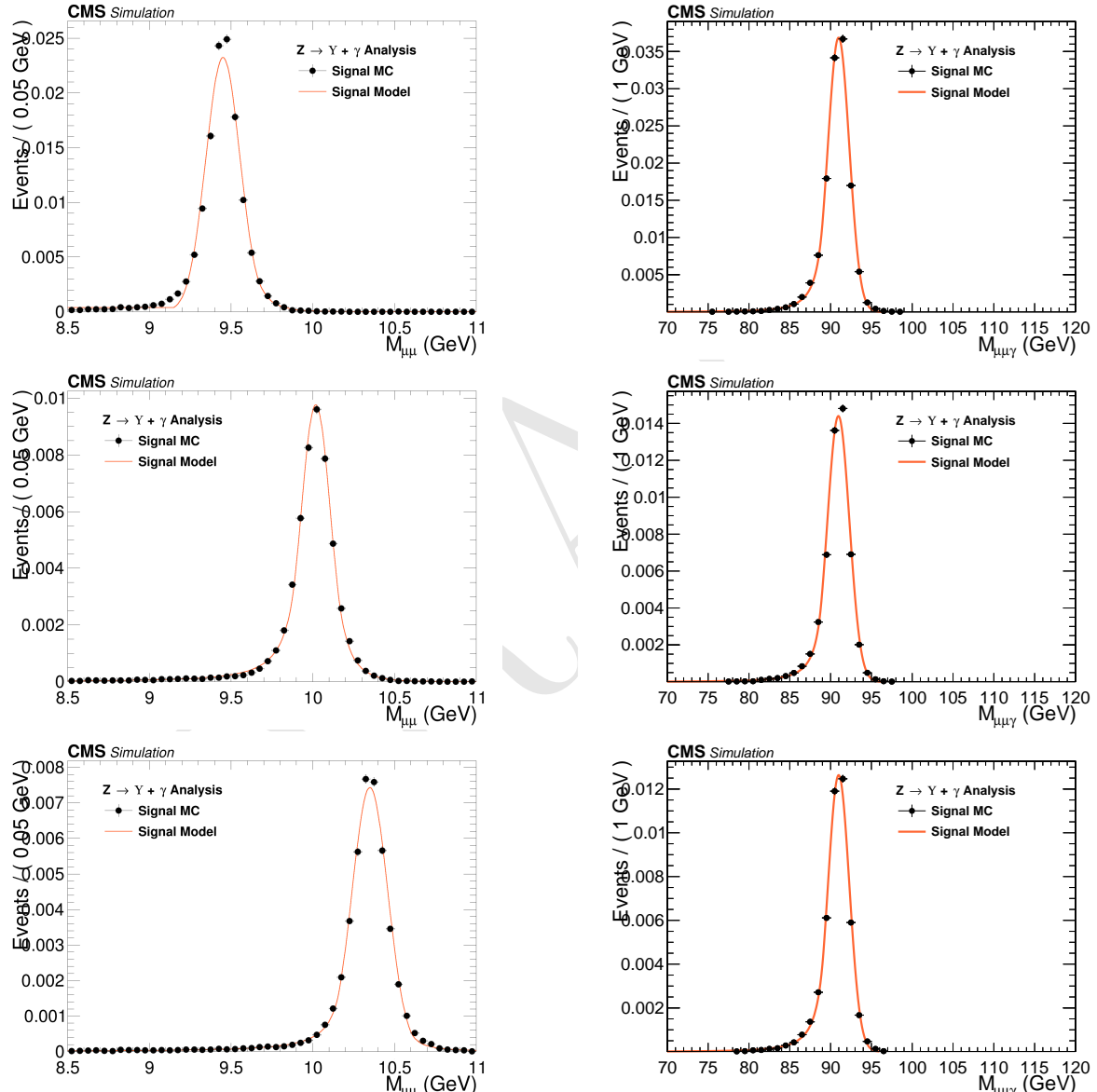


Figure 5.63: Signal Modeling for the  $Z \rightarrow \Upsilon(1S, 2S, 3S) + \gamma$  analysis for EB Low R9 category.  $m_{\mu\mu}$  mass distribution (left) and  $m_{\mu\mu\gamma}$  mass distribution (right). From top to bottom:  $\Upsilon(1S)$ ,  $\Upsilon(2S)$ ,  $\Upsilon(3S)$ .

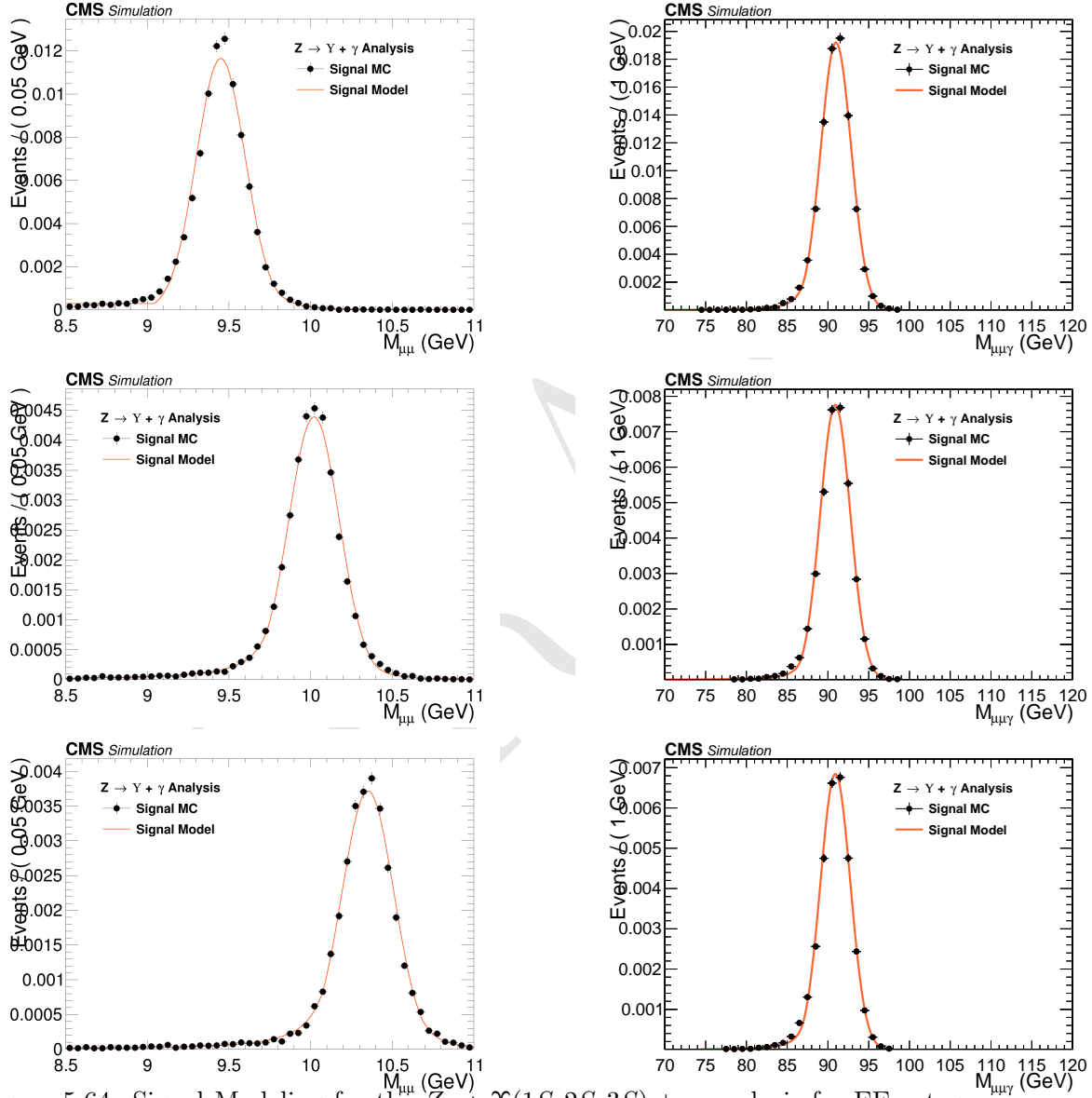


Figure 5.64: Signal Modeling for the  $Z \rightarrow Y(1S, 2S, 3S) + \gamma$  analysis for EE category.  $m_{\mu\mu}$  mass distribution (left) and  $m_{\mu\mu\gamma}$  mass distribution (right). From top to bottom:  $\Upsilon(1S)$ ,  $\Upsilon(2S)$ ,  $\Upsilon(3S)$ .

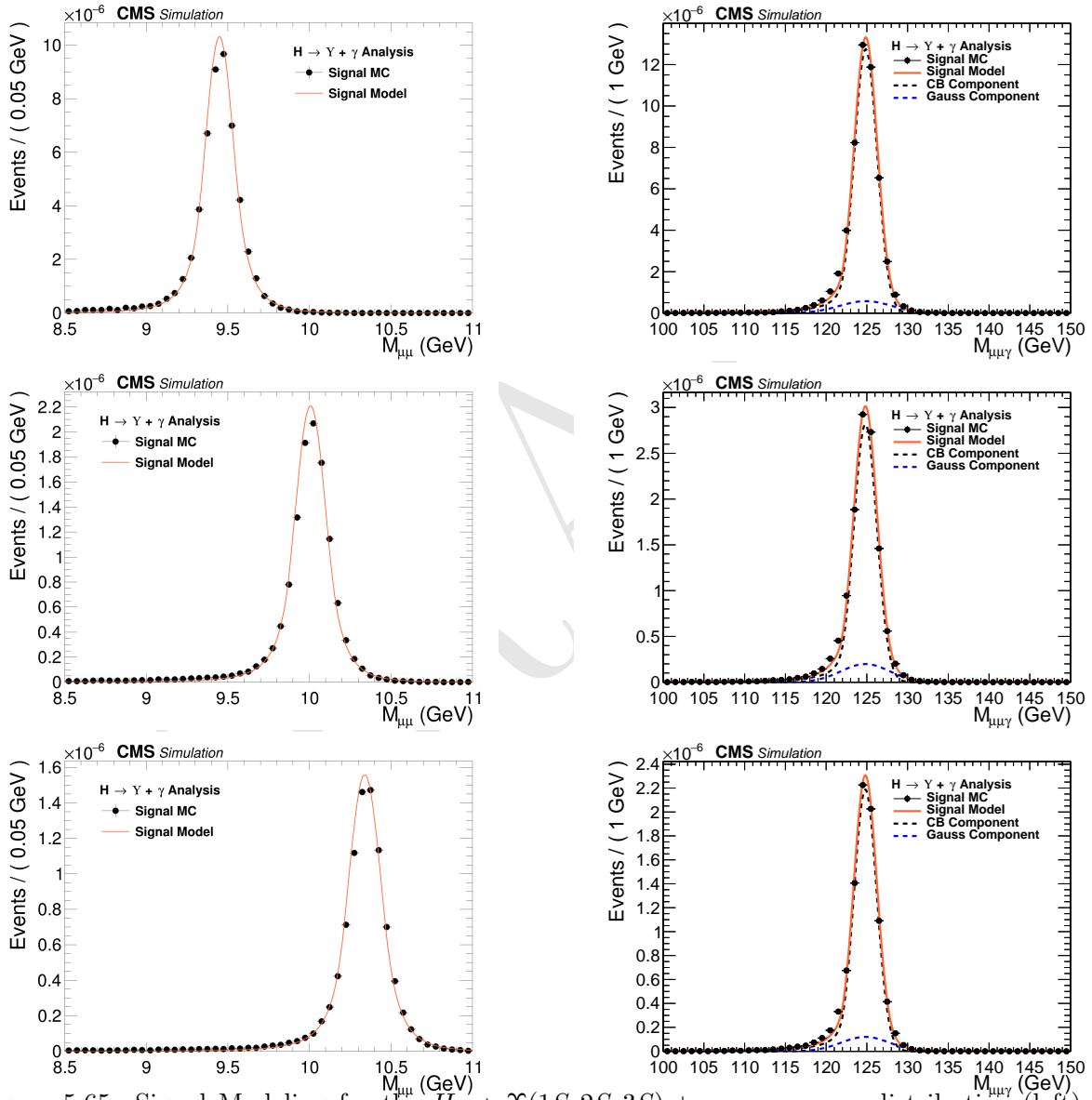


Figure 5.65: Signal Modeling for the  $H \rightarrow \Upsilon(1S, 2S, 3S) + \gamma$ .  $m_{\mu\mu}$  mass distribution (left) and  $m_{\mu\mu\gamma}$  mass distribution (right). From top to bottom:  $\Upsilon(1S)$ ,  $\Upsilon(2S)$ ,  $\Upsilon(3S)$ .

## 2148 5.10 Systematic uncertainties

2149 Two sources of systematics are considered: the ones that affect the predicted yields<sup>8</sup> and the ones  
 2150 that affect the shape of the pdfs used to compose the signal and background model.

2151 Those that affect the predicted yields, presented in Section 5.7.2, it is considered integrated lumi-  
 2152 nosity measurement [121], the pileup description in the Monte-Carlo simulations, the corrections  
 2153 applied to the simulated events in order to compensate for the differences in performance of the some  
 2154 selection criteria, such as trigger, object reconstruction and identification, the  $\Upsilon$  polarization and  
 2155 the theoretical uncertainties, such as the effects of the *parton density functions* (PDF) to the signal  
 2156 cross section [27, 130, 148], the variations of the renormalization and factorization scales [149–153],  
 2157 and the prediction of the decay branching ratios.

2158 For the systematics on the signal modeling, it is considered possible imprecisions of the momentum  
 2159 scale and resolution. They are measured on how they affect the mean ( $\mu$ ) and the standard deviation  
 2160 ( $\sigma$ ) of the signal model. For the background modeling, since it is derived from data, the choice of  
 2161 the *pdf* (Probability distribution function) is the only systematic uncertainties considered. It is  
 2162 treated by the Discrete Profiling method, as described in section 5.8.

2163 The two kinds of systematics uncertainties are described in details below.

### 2164 5.10.1 Uncertainties on the predicted yields

2165 The theoretical sources of uncertainties includes: parton distribution functions uncertainties, strong  
 2166 coupling constant ( $\alpha_s$ ) uncertainty and uncertainty on the  $H \rightarrow \gamma\gamma$  branching fraction (used to derive  
 2167 the Higgs Dalitz Decays cross-section). The values for these theoretical uncertainties are taken from  
 2168 the Higgs Combination Group [133] and also from [152, 154].

2169 An uncertainty value of 2.5% is used on the integrated luminosity of the data samples, as recom-  
 2170 mended by CMS [121]. To evaluate the impact of the pileup reweighting in the final result, the total  
 2171 inelastic cross section of  $69.2\text{ mb}$  is varied by  $\pm 4.6\%$  and the analysis is ran with these extreme  
 2172 values. The systematic uncertainty quoted is the maximum difference in the yields with respect to  
 2173 nominal value, as recommended by CMS.

2174 The impact of the trigger scale factor is evaluated by running this analysis with  $\pm 1\sigma$  on the  
 2175 Trigger Efficiency Scale factors (section 5.5.1). The systematic uncertainty quoted is the maximum  
 2176 difference in the yields with respect to nominal value.

2177 For the final state object identification and isolation associated uncertainty, the scale factors, pro-  
 2178 vided by CMS, to match the performance of MC and Data samples are varied in  $\pm 1\sigma$ . The  
 2179 systematic uncertainty quoted is the maximum difference in the yields with respect to nominal  
 2180 value. This procedure is applied on the scale factors for the Photon MVA ID and the Electron Veto  
 2181 (section 5.5.3) and for Muon Identification and Isolation (section 5.5.2).

---

<sup>8</sup>Number of events, per process, after full selection and corrected by the expected SM cross sections.

Finally, the  $\Upsilon$  Polarization is assessed applying the extremes scenarios of the  $\Upsilon$  polarization (Transverse and Longitudinal Polarization to the signal samples (section 5.2). The systematic uncertainty quoted is the maximum difference in the yields with respect to nominal (Unpolarized) yield. This procedure is applied only for the Z decay. For the Higgs decay, the only polarization considered is the transverse polarization.

The effect of all systematic uncertainties in the signal and resonant background yields are summarized on table 5.8, for the Z decay and table 5.9, for the Higgs decay. Clearly, the main contribution to the systematics uncertainties on the yields is Polarization of the  $\Upsilon(nS)$  (only for the Z decay), around 15%.

### 5.10.2 Uncertainties that affect the signal fits

Smearing and scaling corrections are applied on simulated events since the resolution of Monte Carlo is better than that on data and the detector might not catch all the possible differences in the detector performance, with respect to the data observation. They need to be estimated and included on the systematics. The corrections are:

- **Muon Momentum Scale and Resolution:** extracted by running the analysis with different setups of the official CMS Muon scaling and smearing package [155]. The deviations, with respect to the default correction are summed in quadrature. Once the nominal parameters (mean or sigma) are obtained, the default corrections are shifted by  $\pm 1\sigma$  and the fits are re-done, with the parameters of interest free to float and all others fixed. The systematic uncertainty quoted is the maximum difference of the parameter with respect to nominal value.

- **Photon Energy Scale and Resolution:** extracted by running the analysis with different sets of corrections, provided by the CMS <sup>9</sup>. Once the nominal mean is obtained, the sets are changed and the fits are re-done, with the mean free to float and all others parameters fixed. The corrections are shifted by  $\pm 1\sigma$  on each source of systematics (following standard CMS recommendations). The quoted as systematic uncertainty is the quadrature sum of the maximum deviation within each set.

The effective systematic uncertainty associated with the scale and resolution are the quadrature sum of the muon and photon contributions. The effect of all systematic uncertainties in the Signal fits are summarized on table 5.10, for the Z and Higgs decay.

---

<sup>9</sup>CMS has not published, yet, a paper on the Run2 performance of the Photon reconstruction (This document is under internal review process.). Just as a reference, we cite the Run1 paper [156].

Table 5.8: A summary table of systematic uncertainties in the Z boson decaying into  $\Upsilon(1S, 2S, 3S) + \gamma$ , affecting the final yields of the MC samples.

Source	Uncertainty			
	Signal		Peaking Background	
	$Z \rightarrow \Upsilon(1S)\gamma$	$Z \rightarrow \Upsilon(2S)\gamma$	$Z \rightarrow \Upsilon(3S)\gamma$	$Z \rightarrow \mu\mu\gamma_{FSR}$
Integrated luminosity				
All Categories	2.5%			
SM Z boson $\sigma$ (scale)				
All Categories	3.5%		5.0%	
SM Z boson $\sigma$ (PDF + $\alpha_s$ )				
All Categories	1.73%		5.0%	
Pileup Reweighting				
Inclusive	0.65%	0.68%	0.71%	0.62%
EB High R9	1.01%	1.1%	1.04%	1.06%
EB Low R9	0.17%	0.08%	0.13%	0.11%
EE	1.07%	0.98%	1.26%	0.78%
Trigger				
Inclusive	4.45%	4.46%	4.49%	4.71%
EB High R9	3.5%	3.5%	3.52%	3.71%
EB Low R9	3.55%	3.54%	3.58%	3.72%
EE	7.52%	7.58%	7.56%	8.13%
Muon Identification				
Inclusive	4.82%	4.81%	4.8%	4.52%
EB High R9	4.45%	4.45%	4.44%	4.2%
EB Low R9	4.65%	4.62%	4.63%	4.32%
EE	5.75%	5.75%	5.74%	5.44%
Photon Identification				
Inclusive	1.1%	1.1%	1.09%	1.09%
EB High R9	1.1%	1.09%	1.09%	1.11%
EB Low R9	1.1%	1.1%	1.09%	1.08%
EE	1.1%	1.1%	1.1%	1.09%
Electron Veto				
Inclusive	1.02%	1.02%	1.02%	1.03%
EB High R9	1.2%	1.2%	1.2%	1.2%
EB Low R9	1.2%	1.2%	1.2%	1.2%
EE	0.45%	0.45%	0.45%	0.45%
Polarization				
Inclusive	15.36%	14.78%	14.84%	-
EB High R9	15.6%	14.88%	14.87%	-
EB Low R9	15.01%	14.31%	14.4%	-
EE	15.39%	15.27%	15.39%	-

Table 5.9: A summary table of systematic uncertainties in the Higgs boson decaying into  $\Upsilon(1S, 2S, 3S) + \gamma$ , affecting the final yields of the MC samples.

Source	Uncertainty			
	Signal			Peaking Background
	$H \rightarrow \Upsilon(1S)\gamma$	$H \rightarrow \Upsilon(2S)\gamma$	$H \rightarrow \Upsilon(3S)\gamma$	$H \rightarrow \gamma\gamma^*$
Integrated luminosity	2.5%			
SM Higgs $\sigma$ (scale)	$+4.6\% / -6.7\%$			
SM Higgs $\sigma$ (PDF + $\alpha_s$ )	3.2%			
SM BR $H \rightarrow \gamma\gamma^*$	-			6.0%
Pileup Reweighting	0.61%	0.68%	0.56%	0.9%
Trigger	5.61%	5.47%	5.5%	6.12%
Muon Identification	4.39%	4.36%	4.34%	4.33%
Photon Identification	1.21%	1.22%	1.22%	1.2%
Electron Veto	1.04%	1.04%	1.04%	1.04%

Table 5.10: A summary table of systematic uncertainties in the Z (H) decaying into  $\Upsilon(1S, 2S, 3S) + \gamma$ , affecting the signal fits.

		Z $\rightarrow \Upsilon(nS) + \gamma$			H $\rightarrow \Upsilon(nS) + \gamma$
		Inclusive	EB High R9	EB Low R9	EE
		Mean - Scale			
$\Upsilon(1S)$	Muon Unc.	0.06%	0.05%	0.06%	0.11%
	Photon Unc.	0.21%	0.13%	0.19%	0.26%
	<b>Total Unc.</b>	0.22%	0.14%	0.2%	0.28%
	Sigma - Resolution				
	Muon Unc.	1.12%	0.84%	1.55%	1.14%
	Photon Unc.	2.14%	2.48%	1.95%	2.79%
	<b>Total Unc.</b>	2.42%	2.61%	2.49%	3.01%
$\Upsilon(2S)$	Mean - Scale				
	Muon Unc.	0.07%	0.05%	0.06%	0.13%
	Photon Unc.	0.25%	0.11%	0.2%	0.19%
	<b>Total Unc.</b>	0.26%	0.12%	0.21%	0.23%
	Sigma - Resolution				
	Muon Unc.	1.21%	1.54%	2.65%	1.66%
	Photon Unc.	1.85%	2.67%	3.56%	3.6%
$\Upsilon(3S)$	<b>Total Unc.</b>	2.21%	3.08%	4.44%	3.97%
	Mean - Scale				
	Muon Unc.	0.06%	0.06%	0.06%	0.09%
	Photon Unc.	0.22%	0.14%	0.25%	0.17%
	<b>Total Unc.</b>	0.23%	0.15%	0.26%	0.19%
	Sigma - Resolution				
	Muon Unc.	1.78%	2.38%	2.1%	2.25%
	Photon Unc.	2.51%	4.14%	2.23%	4.08%
	<b>Total Unc.</b>	3.08%	4.77%	3.07%	4.66%

## 5.11 Modeling Cross checks

In order to test the applicability of the statistical (signal and background) modeling proposed in this study, a cross-check procedure is performed by generating a set of pseudo-experiments (toys datasets) based on the signal plus background model, for each decay channel ( $H/Z \rightarrow \Upsilon(1S, 2S, 3S, ) + \gamma$ ) with some signal injected.

The procedure consists of resampling from the signal plus background a number of events, including some extra (injected signal). The amount of injected signal is controlled by the  $\mu_{true}$  variable, where  $\mu_{true} = X$  means inject  $X$  times the expected signal.

Once generated, the toy dataset is refitted to the signal plus background model and the signal strength ( $\mu_{fit}$ ) and its error  $\sigma_{fit}$  are extracted. This procedure is repeated 10000 times and only for the inclusive category. Figures 5.67, 5.66, 5.69 and 5.68 show examples of those fits for the Higgs and Z decay.

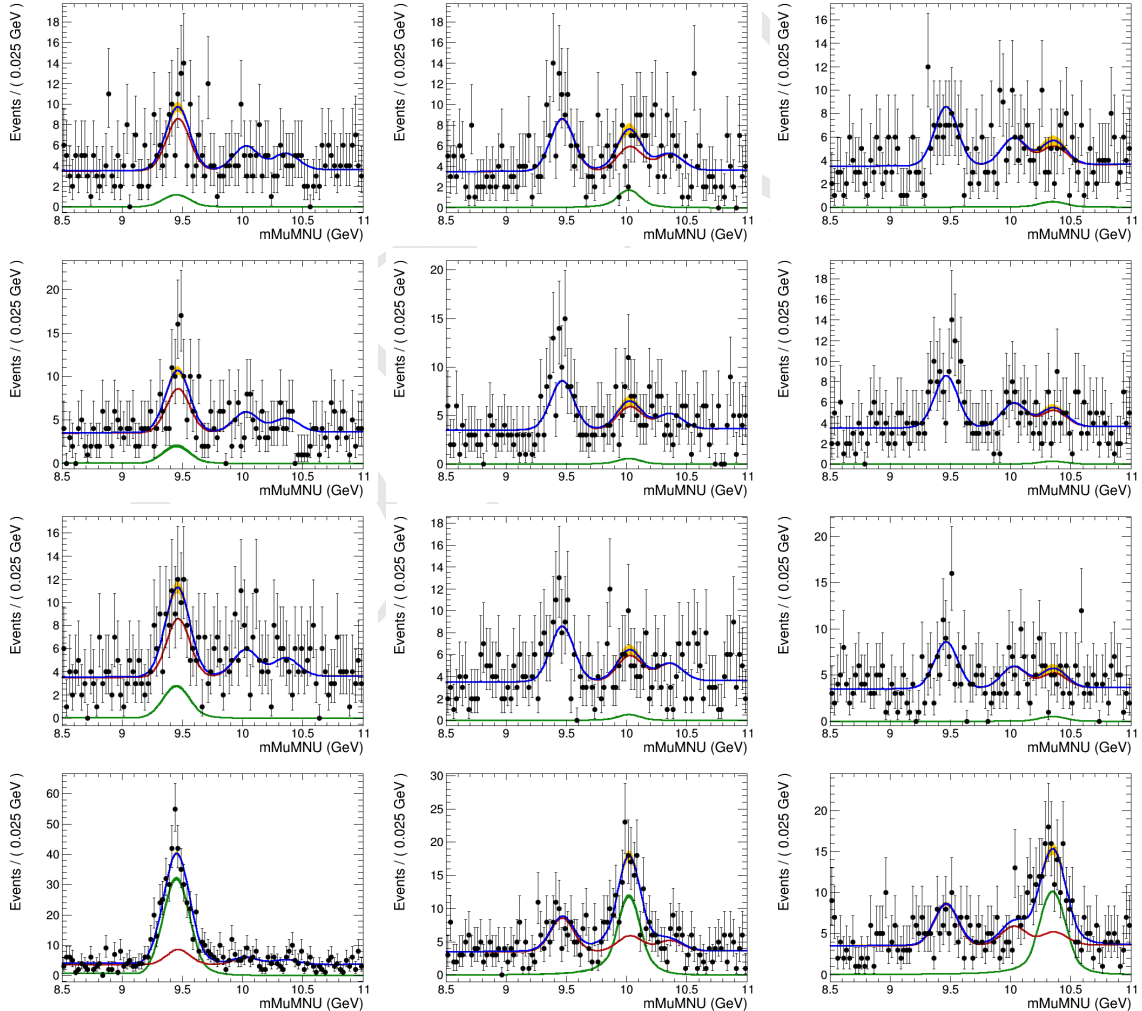


Figure 5.66: Examples of the toy datasets fit ( $M_{\mu\mu}$ ), for the Z decay analysis, after the toy dataset refit, for 1S, 2S and 3S (left to right), with  $\mu_{true}$  equals to 20, 50, 100, 1000 (top to bottom). The red lines corresponds to the background model (B), the green lines to signal model (S), the blue lines to the total (S+B) and the dots is the toy dataset.

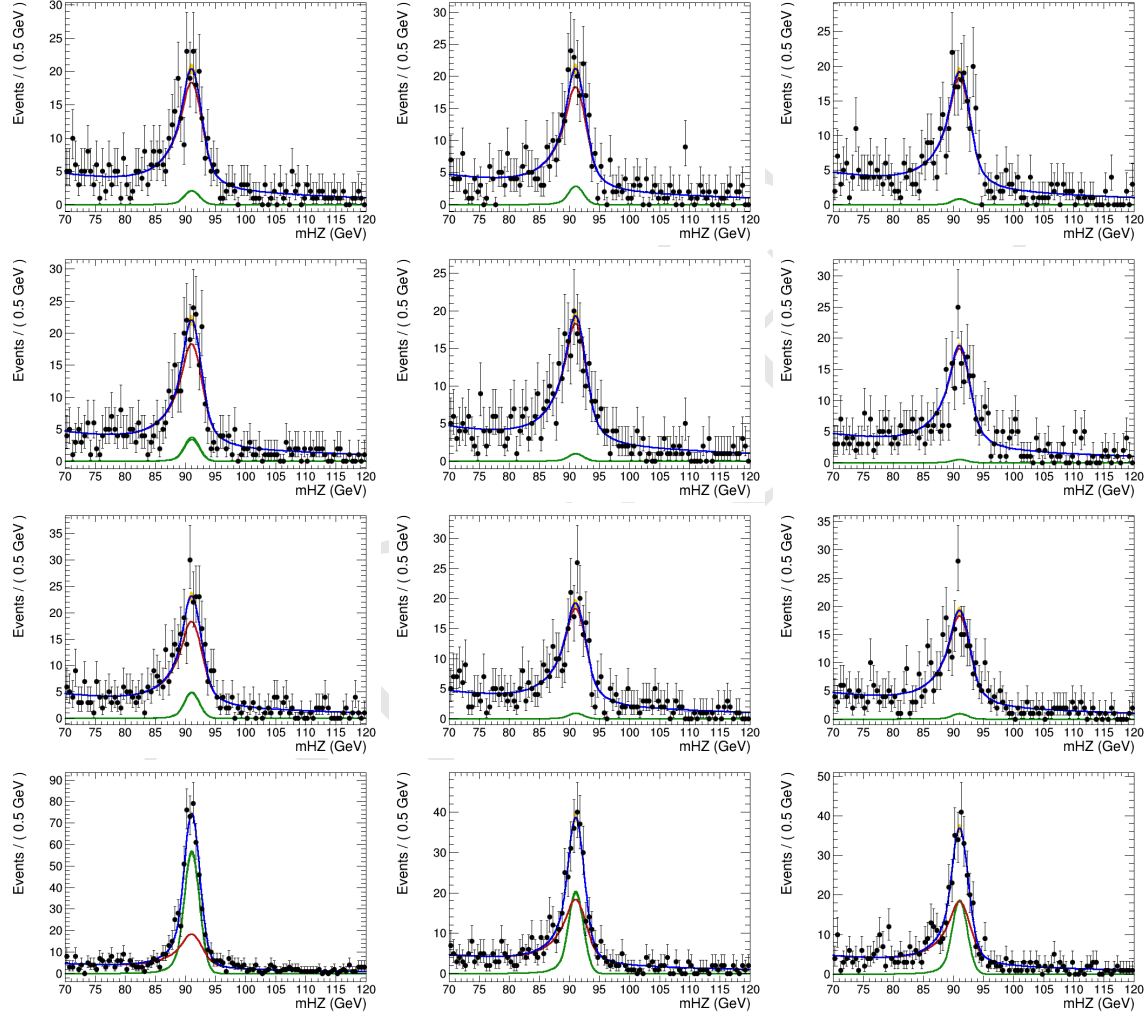


Figure 5.67: Examples of the toy datasets fit ( $M_{\mu\mu\gamma}$ ), for the Z decay analysis, after the toy dataset refit, for 1S, 2S and 3S (left to right), with  $\mu_{true}$  equals to 20, 50, 100, 1000 (top to bottom). The red lines corresponds to the background model (B), the green lines to signal model (S), the blue lines to the total (S+B) and the dots is the toy dataset.

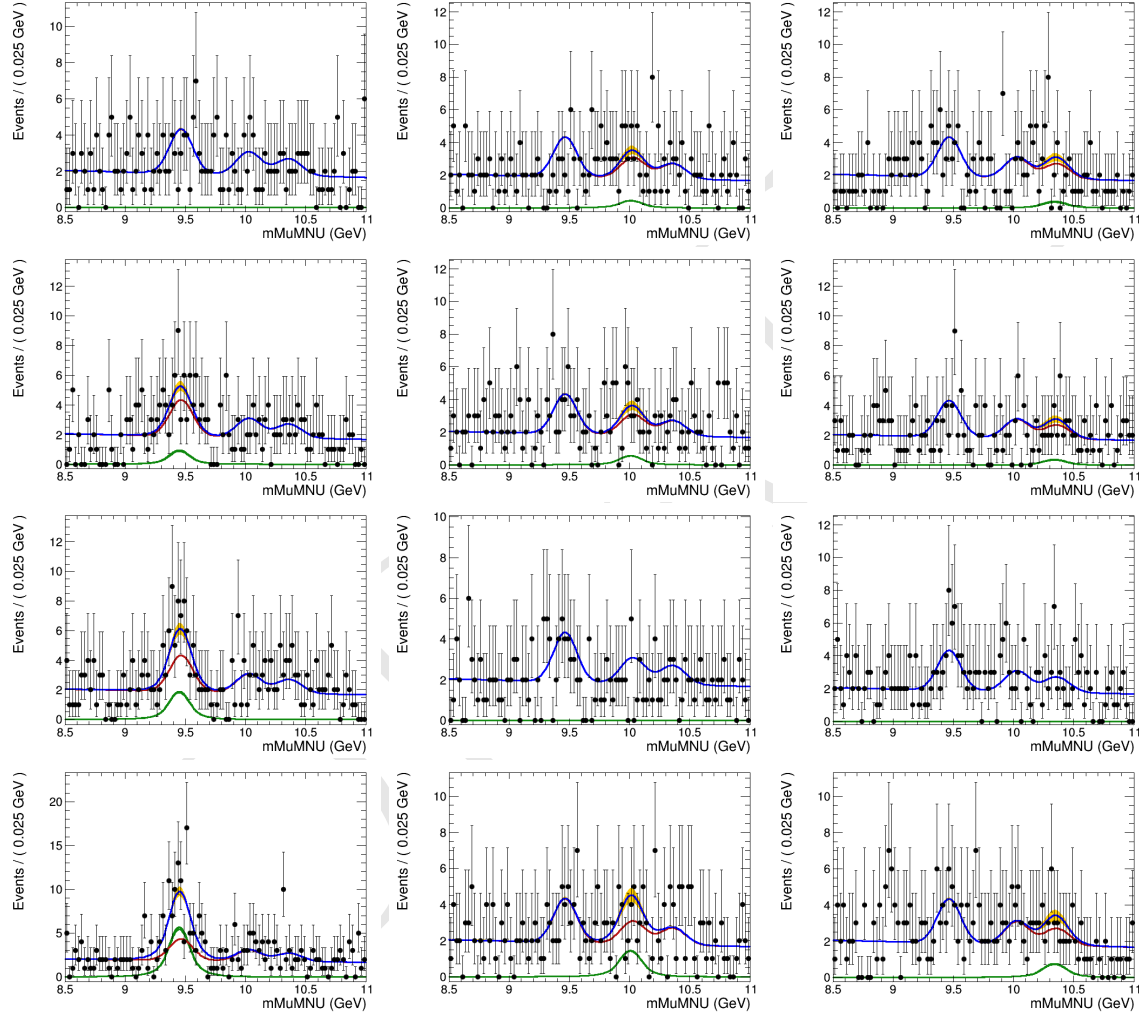


Figure 5.68: Examples of the toy datasets fit ( $M_{\mu\mu}$ ), for the Higgs decay analysis, after the toy dataset refit, for 1S, 2S and 3S (left to right), with  $\mu_{true}$  equals to 100000, 200000, 300000, 1000000 (top to bottom). The red lines corresponds to the background model (B), the green lines to signal model (S), the blue lines to the total (S+B) and the dots is the toy dataset.

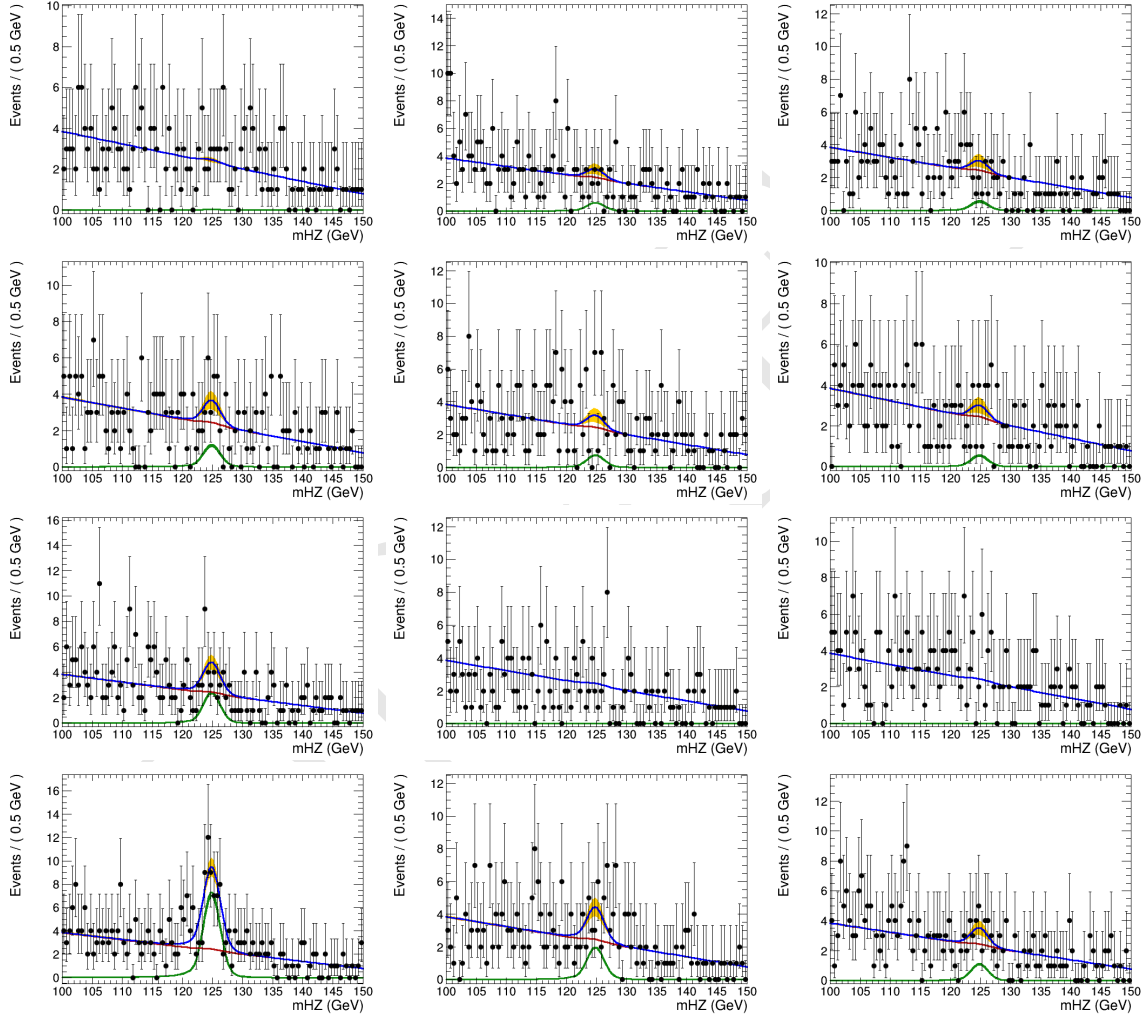


Figure 5.69: Examples of the toy datasets fit ( $M_{\mu\mu\gamma}$ ), for the Higgs decay analysis, after the toy dataset refit, for 1S, 2S and 3S (left to right), with  $\mu_{true}$  equals to 100000, 200000, 300000, 1000000 (top to bottom). The red lines corresponds to the background model (B), the green lines to signal model (S), the blue lines to the total (S+B) and the dots is the toy dataset.

It is expected that the pulls distribution for the fitted signal strength ( $\frac{\mu_{fit} - \mu_{true}}{\sigma_{fit}}$ ) should follow a Gaussian distribution centered in 0 and with  $\sigma$  around 1. Figures 5.70 and 5.71 present those pulls distributions for the Z and Higgs decays, respectively.

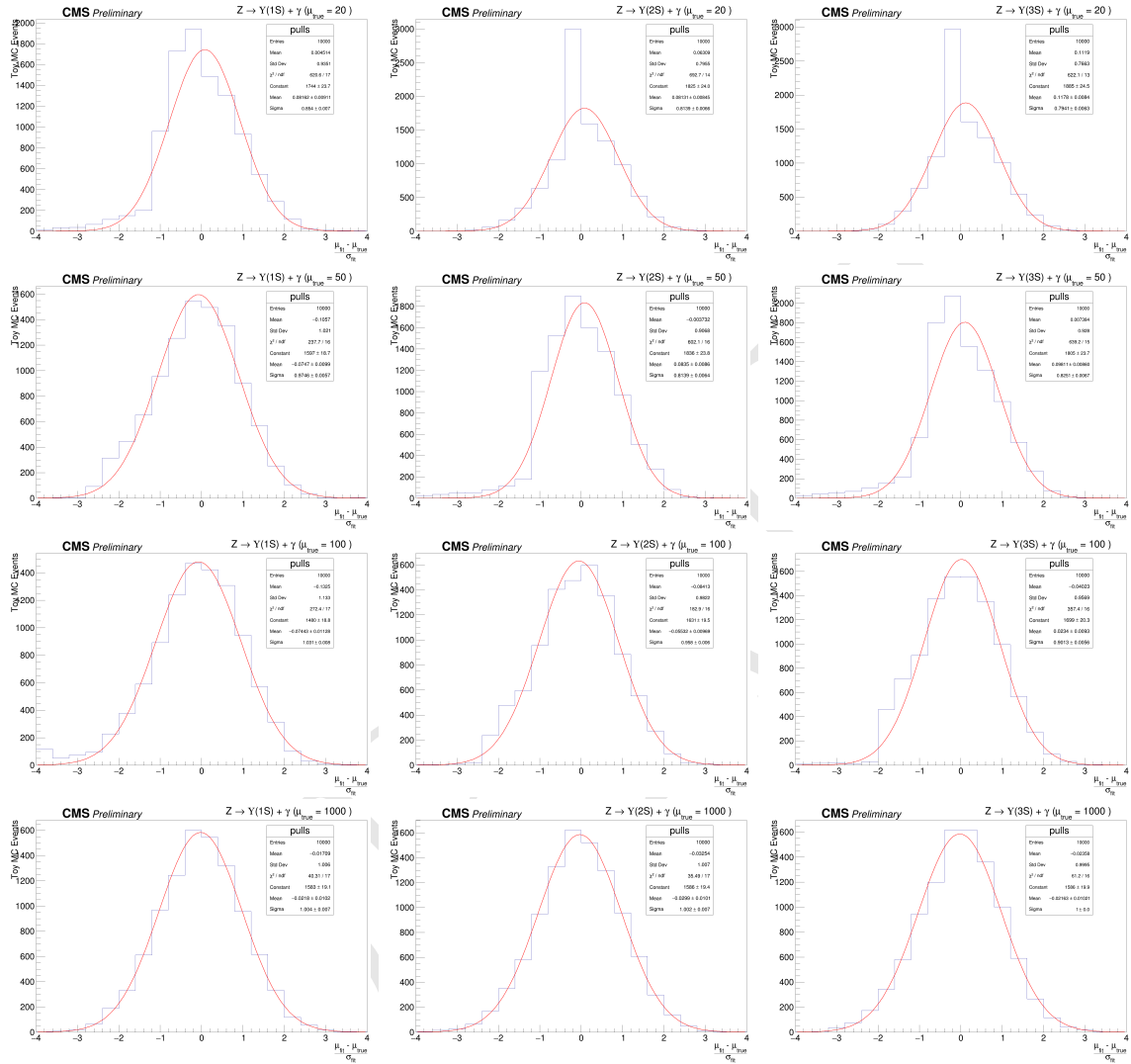


Figure 5.70: Distribution of pulls ( $\frac{\mu_{fit} - \mu_{true}}{\sigma_{fit}}$ ), for the Z decay analysis, after the toy dataset refit, for 1S, 2S and 3S (left to right), with  $\mu_{true}$  equals to 20, 50, 100, 1000 (top to bottom).

As a general conclusion on this cross check, as long as the toy MC generation is able to inject enough signal to be fit, the final modeling of this analysis is able to recover a Gaussian pulls distribution. This, of course, depends on the  $\Upsilon$  state to be considered. For the Z decay, between  $\mu_{true} = 50$  and  $\mu_{true} = 100$  (around a hundred of events passing full selection), while for the Higgs decay, it is needed only a few events after full selection, even thought it means hundreds of thousands times the expected signal, since the very small cross sections for the decay, as shown in Table 5.1.

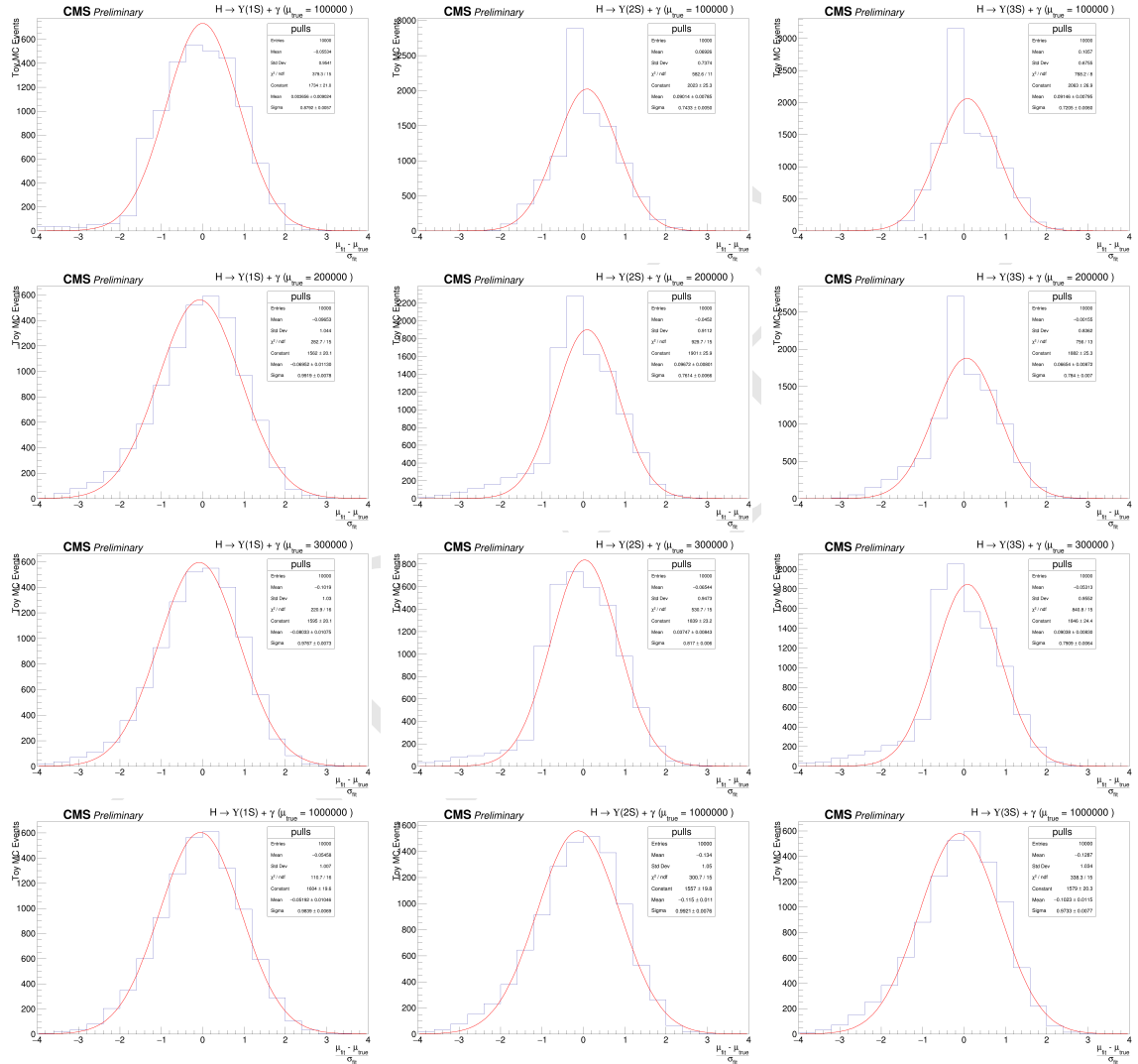


Figure 5.71: Distribution of pulls ( $\frac{\mu_{fit} - \mu_{true}}{\sigma_{fit}}$ ), for the Higgs decay analysis, after the toy dataset refit, for 1S, 2S and 3S (left to right), with  $\mu_{true}$  equals to 100000, 200000, 300000, 1000000 (top to bottom).

## 5.12 Results and conclusion

A two-dimensional (2D) unbinned maximum-likelihood fit to the  $m_{\mu^+\mu^-\gamma}$  and  $m_{\mu^+\mu^-}$  distributions was used to compare the data with background and signal predictions. Search has been performed for a SM Higgs and Z boson decaying into a  $\Upsilon(1S, 2S, 3S)\gamma$ , with  $\Upsilon(1S, 2S, 3S)$  subsequently decaying into  $\mu^+\mu^-$  using data obtained from  $35.9 \text{ fb}^{-1}$  of  $pp$  collisions at  $\sqrt{s} = 13 \text{ TeV}$ .

Since no excess has been observed above the background, the  $CL_s$  formalism is applied, in order to establish an upper limit in the branching fractions for each channel.

### 5.12.1 The $CL_s$ formalism for upper limits setting at CMS

The  $CL_s$  formalism [157] consist in a modified frequentist approach to obtain an upper limit for a certain parameter of a model, with respect to the data, when there is no significant excess that could justify an observation. It is based on the profile-likelihood-ratio test statistic [158] and asymptotic approximations [159]. It is a standard upper limit setting procedure for the LHC experiments [160]. When searching for non-observed phenomena, it is often usual to derive the results as a function of the signal strength modifier  $\mu$ , which is a free parameter of the full model (signal + background). It can be defined such as, the expectation value for the number of events in a bin<sup>10</sup> is:

$$E[n] = \mu s + b, \quad (5.7)$$

where,  $s$  and  $b$  are the expected number of signal and background events, respectively.

The Neyman–Pearson lemma [158] states the likelihood ratio is the optimal test between a null hypothesis and an alternative one (i.e. background-only and signal-plus-background models). On top on this, one could build a likelihood ratio test as:

$$q(\mu) = -2 \ln \left( \frac{\mathcal{L}(\text{data}|\mu s + b)}{\mathcal{L}(\text{data}|b)} \right), \quad (5.8)$$

where the denominator and numerator defines the likelihoods for the background-only and signal-plus-background models, respectively. This was the hypothesis test used by LEP and Tevatron experiments (the former one, with some modifications to include the nuisances effects).

With these two models, i.e. their *pdfs*, one can throw toy MC events in order to construct a distribution of  $q(\mu)$ , namely  $f(q(\mu)|\mu)$ . The *p*-value of  $f(q(\mu)|\mu)$ , as below, can be used to chose between each model.

$$p_\mu = \int_{q(\mu)_\text{data}}^{\infty} f(q(\mu)|\mu) dq(\mu), \quad (5.9)$$

where  $q(\mu)_\text{data}$  is the observed value of  $q(\mu)$  on data, for a given  $\mu$ .

---

<sup>10</sup>A set of common analysis criteria.

2258 If  $p_\mu$  is less than  $\alpha$  (usually 0.05 or 0.1) the background-only model can be excluded in favor of the  
 2259 signal-plus-background model. For the purpose of a confidence interval estimation, the argument  
 2260 can be reversed and one could look for all the values of  $\mu$  that would not be excluded with Confidence  
 2261 Level (CL)  $1 - \alpha$ .

2262 The problem with this definition is that, when the expected signal strength is very small, e.g.  
 2263 a invariant mass distribution in the TeV scale, the null hypothesis and the alternative one are  
 2264 almost indistinguishable. In this situation, a downward fluctuation of the background might lead  
 2265 us to exclude the alternative hypothesis (signal) in a region of low experimental sensitivity region.  
 2266 Putting in number, if we expect 50 background events and 2 signal events, but we observe 40 events,  
 2267 the signal would be easily excluded.

2268 In order to take this effect into account, a modified frequentist approach for upper limits setting, the  
 2269  $CL_s$  was proposed during the Higgs search era at LEP. Lets start by considering a profile likelihood  
 2270 ratio [161] as below:

$$\lambda(\mu) = \frac{\mathcal{L}(\text{data}|\mu, \hat{\theta})}{\mathcal{L}(\text{data}|\hat{\mu}, \hat{\theta})}, \quad (5.10)$$

2271 where,  $\mathcal{L}(\text{data}|\mu, \hat{\theta})$  is the profile likelihood function.

2272 Defining  $\mu$  and the investigated signal strength,  $\hat{\theta}$  is the nuisances that maximizes the likelihood for  
 2273 a given  $\mu$  (fixed) while  $\hat{\mu}$  and  $\hat{\theta}$  are the signal strength and nuisances that, overall, maximizes the  
 2274 likelihood. The advantage of the CMS and ATLAS have a common set of statistical guidelines [162]  
 2275 to ensure the compatibility of the published results. Following these recommendations, the statistics  
 2276 test based on 5.10 is:

$$\tilde{q}_\mu = -2\ln[\lambda(\mu)], \text{ with } 0 \leq \hat{\mu} \leq \mu. \quad (5.11)$$

2277 The left side restriction ( $0 \leq \hat{\mu}$ ) ensure us the proper physical interpretation of  $\mu$  as a positive  
 2278 defined signal strength, i.e., the observation a process would, for a given bin, increase the number  
 2279 of events. The right side restriction  $\hat{\mu} \leq \mu$  secure the interpretation of  $\tilde{q}_\mu$ 's  $p$ -value as a one-sided  
 2280 confidence interval. This is required for a upper limit definition.

2281 The advantage of using the profile likelihood ratio is that, even though it takes into account the  
 2282 effect of nuisances in the likelihood, it is possible to prove that, with the use of Wilk's Theorem [145],  
 2283 that a statistic test defined as  $\tilde{q}_\mu$ , asymptotically follows a chi-square distribution with one degree  
 2284 of freedom (the signal strength) [159]. Thus,  $\tilde{q}_\mu$  is said to be approximately independent of any  
 2285 nuisance and allow a fast computation of its  $p$ -value without the need of toy MC strategies (which  
 2286 can computationally demanding, depending on the complexity of the models), event though this is  
 2287 not the standard CMS/ATLAS recommendation.

2288 Based on  $\tilde{q}_\mu$ , defined at 5.11, one should compute the  $\tilde{q}_\mu^{\text{obs}}$ , also the  $\hat{\theta}_\mu^{\text{obs}}$  and  $\hat{\theta}_{\mu=0}^{\text{obs}}$ , which corresponds  
 2289 to the observed value of  $\tilde{q}_\mu$  on data, the maximum likelihood estimator for the nuisances assuming  
 2290 some signal strength  $\mu$  and assuming a background-only model, respectively. Then, the distributions

of  $f(\tilde{q}_\mu | \mu, \hat{\theta}_\mu^{\text{obs}})$  and  $f(\tilde{q}_\mu | \mu = 0, \hat{\theta}_{\mu=0}^{\text{obs}})$  are generated tossing pseudo-random toy MC. Figure 5.72 presents an example of these two distributions.

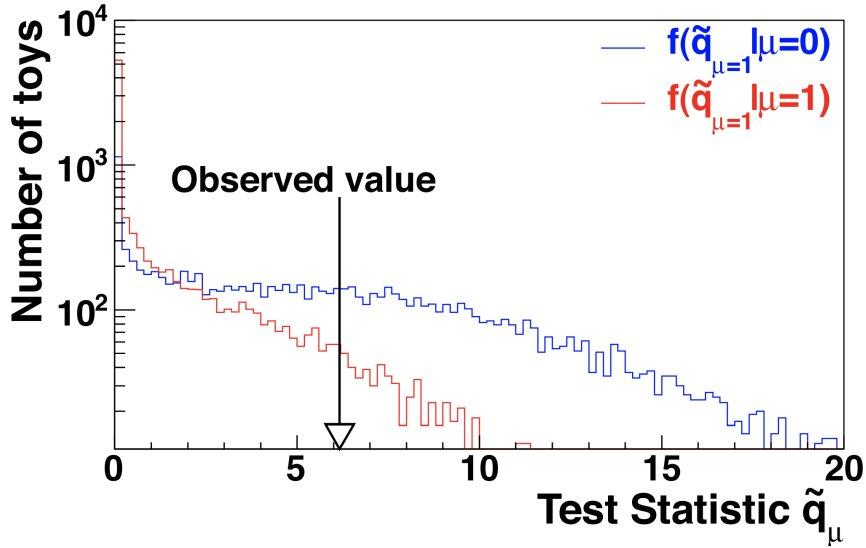


Figure 5.72: Example of  $f(\tilde{q}_\mu | \mu, \hat{\theta}_\mu^{\text{obs}})$   $f(\tilde{q}_\mu | \mu = 0, \hat{\theta}_{\mu=0}^{\text{obs}})$  distributions generated with toy MC. Source: [162].

The  $CL_s$  value is defined as:

$$CL_s(\mu) = \frac{p_{s+b}(\mu)}{1 - p_b}, \quad (5.12)$$

where:

$$p_{s+b}(\mu) = \int_{\tilde{q}_\mu^{\text{obs}}}^{\infty} f(\tilde{q}_\mu | \mu, \hat{\theta}_\mu^{\text{obs}}) d\tilde{q}_\mu \quad (5.13)$$

and

$$p_b = \int_{-\infty}^{\tilde{q}_\mu^{\text{obs}}} f(\tilde{q}_\mu | \mu = 0, \hat{\theta}_{\mu=0}^{\text{obs}}) d\tilde{q}_\mu \quad (5.14)$$

Scanning different values of  $\mu$ , within  $0 \leq \hat{\mu} \leq \mu$ , one would exclude the ones which  $CL_s < \alpha$ . CMS and ATLAS recommends a CL level  $(1 - \alpha)$  of 95%.

The main advantage of the  $CL_s$  approach is that the presence of the denominator  $1 - p_b$  in 5.12 penalizes the exclusion of regions in which the experiment is no sensitive. Figure 5.73 helps to illustrate this. One can notice that a small value of  $p_{s+b}$  (yellow area) is balanced by large value of  $p_b$  (green area). When the experimental sensitivity is higher, the two distributions tend to be far away from each other. Thus leading to a smaller compensation factor ( $p_b$ ) and enhancing the chance of a exclusive  $CL_s$  value.

The expected upper limit and its  $\pm 1\sigma$  and  $\pm 2\sigma$  are determined by generating a large number of toy mc events, for the background-only model ( $\mu = 0$ ), with nuisances free to float, and for each simulation finding  $\mu_{95\%}$ , which defines the confidence level. Once enough samples are generated, one

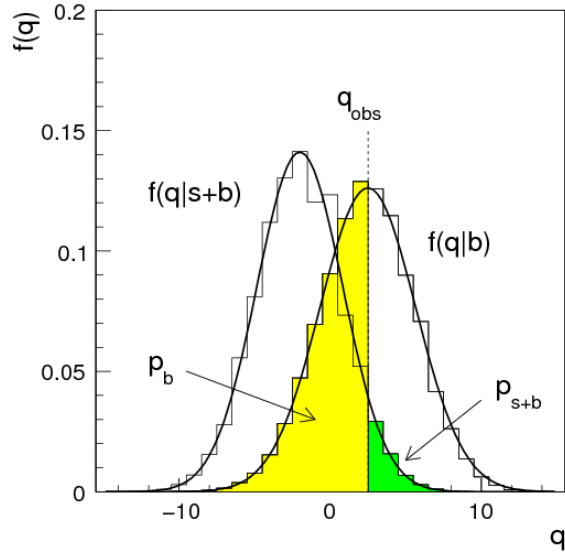


Figure 5.73: Example of  $f(\tilde{q}_\mu|\mu, \hat{\theta}_\mu^{\text{obs}})$ ,  $f(\tilde{q}_\mu|\mu = 0, \hat{\theta}_{\mu=0}^{\text{obs}})$  distributions generated with toy MC. In the figure,  $q$  must be read as  $\tilde{q}$ . The green area shows the  $p_{s+b}$  defined in 5.13, while the yellow one shows  $p_b$  defined in 5.14. Source: [159].

should scan, from left to right, the cumulative distribution of  $\mu_{95\%}$ . The median defines the expected value and the quantiles for 16%, 84% and 2.5%, 97.5% defines the  $\pm 1\sigma$  and  $\pm 2\sigma$ , respectively.

### 5.12.2 Branching fraction upper limits

The results are summarized on table 5.11.

Table 5.11: Summary table for the limits on branching ratio of  $Z \rightarrow \Upsilon(1S, 2S, 3S)\gamma$  and  $H \rightarrow \Upsilon(1S, 2S, 3S)\gamma$  decays.

	95% C.L. Upper Limit		
	$\mathcal{B}(Z \rightarrow \Upsilon\gamma) [\times 10^{-6}]$		
	$\Upsilon(1S)$	$\Upsilon(2S)$	$\Upsilon(3S)$
Expected	$1.6^{+0.8}_{-0.5}$	$2.0^{+1.0}_{-0.6}$	$1.8^{+1.0}_{-0.6}$
Observed	2.9	2.7	1.4
SM Prediction [ $\times 10^{-8}$ ]	4.8	2.4	1.9
	$\mathcal{B}(H \rightarrow \Upsilon\gamma) [\times 10^{-4}]$		
	$\Upsilon(1S)$	$\Upsilon(2S)$	$\Upsilon(3S)$
Expected	$7.3^{+4.0}_{-2.4}$	$8.1^{+4.6}_{-2.8}$	$6.8^{+3.9}_{-2.3}$
Observed	6.9	7.4	5.8
SM Prediction [ $\times 10^{-9}$ ]	5.2	1.4	0.9

The observed(expected) exclusion limit at 95% confidence level on the  $\mathcal{B}(Z \rightarrow \Upsilon(1S, 2S, 3S)\gamma) = 2.9, 2.7, 1.4$  ( $1.6^{+0.8}_{-0.5}, 2.0^{+1.0}_{-0.6}, 1.8^{+1.0}_{-0.6}$ ) $\times 10^{-6}$ , and on the  $\mathcal{B}(H \rightarrow \Upsilon(1S, 2S, 3S)\gamma) = 6.9, 7.4, 5.8$  ( $7.3^{+4.0}_{-2.4}, 8.1^{+4.6}_{-2.8}, 6.8^{+3.9}_{-2.3}$ ) $\times 10^{-4}$ .

2313 As stated before, this analysis was done, for the Z decay, taking into account a mutually excludent  
 2314 categorization of events, based on the reconstructed photon properties ( $\eta_{SC}$  and R9 value), as  
 2315 described in section 5.7.

2316 At table 5.12 we present the results obtained when there is no categorization of events (Inclusive  
 2317 category).

Table 5.12: Summary table for the limits on branching ratio of  $Z \rightarrow \Upsilon(1S, 2S, 3S)\gamma$ , for the two possible categorization scenarios.

95% C.L. Upper Limit - $\mathcal{B}(Z \rightarrow \Upsilon\gamma) [\times 10^{-6}]$			
	without categorization		
	$\Upsilon(1S)$	$\Upsilon(2S)$	$\Upsilon(3S)$
Expected	$1.7^{+0.9}_{-0.5}$	$2.1^{+1.1}_{-0.7}$	$1.9^{+1.0}_{-0.6}$
Observed	2.6	2.3	1.2
with categorization			
	$\Upsilon(1S)$	$\Upsilon(2S)$	$\Upsilon(3S)$
	$1.6^{+0.8}_{-0.5}$	$2.0^{+1.0}_{-0.6}$	$1.8^{+1.0}_{-0.6}$
Observed	2.9	2.7	1.4

2318 It is worth to remember that the categorization takes places only for the Z decay. For the Higgs  
 2319 decay, no categorization is imposed.

2320 By taking, or not, into account any categorization, the numbers presented in both tables (5.11 and  
 2321 5.12), are compatible within themselves and with the results published by the ATLAS collabora-  
 2322 tion [57]. Our interpretation to the lack of improvement of the no categorization scenario with  
 2323 respect to the categorized one, is that, the collected statistics, after full selection, is so small, that  
 2324 the categorization just jeopardize the amount of events available.

## 2325 6 Conclusion and perspectives

2326 In this document it was presented an analysis of the  $H/Z \rightarrow \Upsilon + \gamma$ , with 2016 data sample of the  
2327 CMS detector, at center-of-mass energy  $\sqrt{s} = 13$  TeV. The obtained upper limits, so far, show good  
2328 agreement with the Standard Model predictions and are compatible with previous measurements  
2329 from other LHC experiments. Future developments of this analysis would be the measurement of the  
2330 same upper limits considering the fully available statistics of CMS Run2 (2016, 2017 and 2018), the  
2331 extrapolation of these results to the expected full CMS luminosity ( $3000\text{ fb}^{-1}$ ) and an evaluation,  
2332 using DELPHES [**delphes**], of the sensitivity of future colliders, such as the International Linear  
2333 Collider (ILC) [**ilc**] or the FCC [**fcc**], to this decay.

2334 For the Resistive Plate Chambers, it was presented contributions given to the RPC system of CMS,  
2335 during the development of this study, including its maintenance and R&D. The main challenge  
2336 for the next generation of detector based on this technology is research on new gas mixtures that  
2337 do not included in its composition, green houses gases. There are already developments in this  
2338 direction [**eco\_gas**].

DRAFT

# 2339 Bibliography

- 2340 [1] S. Chatrchyan et al. “The CMS experiment at the CERN LHC”. In: *JINST* 3 (2008), S08004.  
 2341 DOI: [10.1088/1748-0221/3/08/S08004](https://doi.org/10.1088/1748-0221/3/08/S08004).
- 2342 [2] The ATLAS Collaboration et al. “The ATLAS Experiment at the CERN Large Hadron  
 2343 Collider”. In: *Journal of Instrumentation* 3.08 (Aug. 2008), S08003–S08003. DOI: [10.1088/1748-0221/3/08/s08003](https://doi.org/10.1088/1748-0221/3/08/s08003). URL: <https://doi.org/10.1088/1748-0221/2F3%2F08%2Fs08003>.
- 2344 [3] Serguei Chatrchyan et al. “Observation of a new boson at a mass of 125 GeV with the CMS  
 2345 experiment at the LHC”. In: *Phys. Lett. B* 716 (2012), pp. 30–61. DOI: [10.1016/j.physletb.2012.08.021](https://doi.org/10.1016/j.physletb.2012.08.021). arXiv: [1207.7235 \[hep-ex\]](https://arxiv.org/abs/1207.7235).
- 2346 [4] G. Aad et al. “Observation of a new particle in the search for the Standard Model Higgs  
 2347 boson with the ATLAS detector at the LHC”. In: *Physics Letters B* 716.1 (2012), pp. 1–  
 2348 29. ISSN: 0370-2693. DOI: <https://doi.org/10.1016/j.physletb.2012.08.020>. URL:  
<http://www.sciencedirect.com/science/article/pii/S037026931200857X>.
- 2349 [5] NobelPrize.org. *The Nobel Prize in Physics 2013*. 2013. URL: <https://www.nobelprize.org/prizes/physics/2013/summary/>.
- 2350 [6] CMS Collaboration. *Dimuon spectrum 2015*. Tech. rep. CMS-DP-2015-055. Dec. 2015. URL:  
 2351 <http://cds.cern.ch/record/2115428>.
- 2352 [7] Cliff Burgess and Guy Moore. *The Standard Model: A Primer*. Cambridge University Press,  
 2353 2006. DOI: [10.1017/CBO9780511819698](https://doi.org/10.1017/CBO9780511819698).
- 2354 [8] M. Anselmino et al. *Introdução à QCD Perturbativa*. LTC, 2013. ISBN: 9788521622994.
- 2355 [9] F. Halzen and Alan D. Martin. *QUARKS AND LEPTONS: AN INTRODUCTORY COURSE  
 2356 IN MODERN PARTICLE PHYSICS*. Jan. 1984. ISBN: 978-0-471-88741-6.
- 2357 [10] I.J.R. Aitchison and A.J.G. Hey. *Gauge theories in particle physics: A practical introduction.  
 2358 Vol. 2: Non-Abelian gauge theories: QCD and the electroweak theory*. CRC Press, 2012. ISBN:  
 2359 978-1-4665-1307-5.
- 2360 [11] Wikimedia Commons. *Standard Model*. 2020. URL: [https://en.wikipedia.org/wiki/File:Standard\\_Model\\_of\\_Elementary\\_Particles.svg](https://en.wikipedia.org/wiki/File:Standard_Model_of_Elementary_Particles.svg).
- 2361 [12] Particle Data Group et al. “Review of Particle Physics”. In: *Progress of Theoretical and  
 2362 Experimental Physics* 2020.8 (Aug. 2020). 083C01. ISSN: 2050-3911. DOI: [10.1093/ptep/ptaa104](https://doi.org/10.1093/ptep/ptaa104). eprint: <https://academic.oup.com/ptep/article-pdf/2020/8/083C01/33653179/ptaa104.pdf>. URL: <https://doi.org/10.1093/ptep/ptaa104>.
- 2363 [13] A. Salam and J. C. Ward. “On a gauge theory of elementary interactions”. In: *Il Nuovo  
 2364 Cimento (1955-1965)* 19.1 (1961), pp. 165–170. DOI: [10.1007/BF02812723](https://doi.org/10.1007/BF02812723). URL: <https://doi.org/10.1007/BF02812723>.

- [14] RH Dalitz. *Proceedings of the XIIIf International Conference on High Energy Physics*. 1967.
- [15] Wolfgang Ochs. “The Status of Glueballs”. In: *J. Phys. G* 40 (2013), p. 043001. DOI: 10.1088/0954-3899/40/4/043001. arXiv: 1301.5183 [hep-ph].
- [16] Peter W. Higgs. “Broken Symmetries and the Masses of Gauge Bosons”. In: *Phys. Rev. Lett.* 13 (1964). Ed. by J.C. Taylor, pp. 508–509. DOI: 10.1103/PhysRevLett.13.508.
- [17] Peter W. Higgs. “Broken symmetries, massless particles and gauge fields”. In: *Phys. Lett.* 12 (1964), pp. 132–133. DOI: 10.1016/0031-9163(64)91136-9.
- [18] Peter W. Higgs. “Spontaneous Symmetry Breakdown without Massless Bosons”. In: *Phys. Rev.* 145 (1966), pp. 1156–1163. DOI: 10.1103/PhysRev.145.1156.
- [19] F. Englert and R. Brout. “Broken Symmetry and the Mass of Gauge Vector Mesons”. In: *Phys. Rev. Lett.* 13 (1964). Ed. by J.C. Taylor, pp. 321–323. DOI: 10.1103/PhysRevLett.13.321.
- [20] G.S. Guralnik, C.R. Hagen, and T.W.B. Kibble. “Global Conservation Laws and Massless Particles”. In: *Phys. Rev. Lett.* 13 (1964). Ed. by J.C. Taylor, pp. 585–587. DOI: 10.1103/PhysRevLett.13.585.
- [21] T.W.B. Kibble. “Symmetry breaking in nonAbelian gauge theories”. In: *Phys. Rev.* 155 (1967). Ed. by J.C. Taylor, pp. 1554–1561. DOI: 10.1103/PhysRev.155.1554.
- [22] F. Abe et al. “Observation of top quark production in  $\bar{p}p$  collisions”. In: *Phys. Rev. Lett.* 74 (1995), pp. 2626–2631. DOI: 10.1103/PhysRevLett.74.2626. arXiv: hep-ex/9503002.
- [23] S. Abachi et al. “Observation of the top quark”. In: *Phys. Rev. Lett.* 74 (1995), pp. 2632–2637. DOI: 10.1103/PhysRevLett.74.2632. arXiv: hep-ex/9503003.
- [24] John Ellis. “Outstanding questions: physics beyond the Standard Model”. In: *Philosophical Transactions of the Royal Society A: Mathematical, Physical and Engineering Sciences* 370.1961 (2012), pp. 818–830. DOI: 10.1098/rsta.2011.0452. eprint: <https://royalsocietypublishing.org/doi/pdf/10.1098/rsta.2011.0452>. URL: <https://royalsocietypublishing.org/doi/abs/10.1098/rsta.2011.0452>.
- [25] CMS Collaboration. *Summary of the cross section measurements of Standard Model processes*. 2020. URL: <https://twiki.cern.ch/twiki/bin/view/CMSPublic/PhysicsResultsCombined> (visited on 08/21/2020).
- [26] M. Baak et al. “The global electroweak fit at NNLO and prospects for the LHC and ILC”. In: *Eur. Phys. J. C* 74 (2014), p. 3046. DOI: 10.1140/epjc/s10052-014-3046-5. arXiv: 1407.3792 [hep-ph].
- [27] LHC Higgs Cross Section Working Group. “Handbook of LHC Higgs Cross Sections: 4. Deciphering the Nature of the Higgs Sector”. In: (2016). DOI: 10.23731/CYRM-2017-002. arXiv: 1610.07922 [hep-ph].
- [28] Albert M Sirunyan et al. “Combined measurements of Higgs boson couplings in proton–proton collisions at  $\sqrt{s} = 13$  TeV”. In: *Eur. Phys. J. C* 79.5 (2019), p. 421. DOI: 10.1140/epjc/s10052-019-6909-y. arXiv: 1809.10733 [hep-ex].
- [29] A. M. Sirunyan et al. “Observation of Higgs boson decay to bottom quarks”. In: *Phys. Rev. Lett.* 121.12 (2018), p. 121801. DOI: 10.1103/PhysRevLett.121.121801. arXiv: 1808.08242 [hep-ex].

- [30] CMS Collaboration. *Measurement of Higgs boson decay to a pair of muons in proton-proton collisions at  $\sqrt{s} = 13$  TeV*. CMS Physics Analysis Summary CMS-PAS-HIG-19-006. 2019. URL: <http://cdsweb.cern.ch/record/1279362>.
- [31] Albert M Sirunyan et al. “Observation of the Higgs boson decay to a pair of  $\tau$  leptons with the CMS detector”. In: *Phys. Lett. B* 779 (2018), pp. 283–316. DOI: [10.1016/j.physletb.2018.02.004](https://doi.org/10.1016/j.physletb.2018.02.004). arXiv: [1708.00373 \[hep-ex\]](https://arxiv.org/abs/1708.00373).
- [32] Albert M Sirunyan et al. “A search for the standard model Higgs boson decaying to charm quarks”. In: *JHEP* 03 (2020), p. 131. DOI: [10.1007/JHEP03\(2020\)131](https://doi.org/10.1007/JHEP03(2020)131). arXiv: [1912.01662 \[hep-ex\]](https://arxiv.org/abs/1912.01662).
- [33] Albert M Sirunyan et al. “Measurement and interpretation of differential cross sections for Higgs boson production at  $\sqrt{s} = 13$  TeV”. In: *Phys. Lett. B* 792 (2019), pp. 369–396. DOI: [10.1016/j.physletb.2019.03.059](https://doi.org/10.1016/j.physletb.2019.03.059). arXiv: [1812.06504 \[hep-ex\]](https://arxiv.org/abs/1812.06504).
- [34] Albert M Sirunyan et al. “Measurement of the inclusive and differential Higgs boson production cross sections in the leptonic WW decay mode at  $\sqrt{s} = 13$  TeV”. In: (July 2020). DOI: [10.3204/PUBDB-2020-02624](https://doi.org/10.3204/PUBDB-2020-02624). arXiv: [2007.01984 \[hep-ex\]](https://arxiv.org/abs/2007.01984).
- [35] Albert M Sirunyan et al. “A measurement of the Higgs boson mass in the diphoton decay channel”. In: *Phys. Lett. B* 805 (2020), p. 135425. DOI: [10.1016/j.physletb.2020.135425](https://doi.org/10.1016/j.physletb.2020.135425). arXiv: [2002.06398 \[hep-ex\]](https://arxiv.org/abs/2002.06398).
- [36] M. Spira et al. “Higgs boson production at the LHC”. In: *Nucl. Phys. B* 453 (1995), pp. 17–82. DOI: [10.1016/0550-3213\(95\)00379-7](https://doi.org/10.1016/0550-3213(95)00379-7). arXiv: [hep-ph/9504378](https://arxiv.org/abs/hep-ph/9504378).
- [37] CMS Collaboration. *List of CMS Higgs publications*. 2020. URL: <http://cms-results.web.cern.ch/cms-results/public-results/publications/HIG/index.html> (visited on 08/21/2020).
- [38] CMS Collaboration. *List of CMS Higgs public results*. 2020. URL: <http://cms-results.web.cern.ch/cms-results/public-results/preliminary-results/HIG/index.html> (visited on 08/21/2020).
- [39] CMS Collaboration. *Combined Higgs boson production and decay measurements with up to 137 fb<sup>-1</sup> of proton-proton collision data at  $\sqrt{s} = 13$  TeV*. CMS Physics Analysis Summary CMS-PAS-HIG-19-005. 2019. URL: <http://cdsweb.cern.ch/record/1279362>.
- [40] L.D. Landau. “On the angular momentum of a system of two photons”. In: *Dokl. Akad. Nauk SSSR* 60.2 (1948), pp. 207–209. DOI: [10.1016/B978-0-08-010586-4.50070-5](https://doi.org/10.1016/B978-0-08-010586-4.50070-5).
- [41] Chen-Ning Yang. “Selection Rules for the Dematerialization of a Particle Into Two Photons”. In: *Phys. Rev.* 77 (1950), pp. 242–245. DOI: [10.1103/PhysRev.77.242](https://doi.org/10.1103/PhysRev.77.242).
- [42] CMS Collaboration. *List of CMS Higgs publications involving spin-parity tests*. 2020. URL: <http://cms-results.web.cern.ch/cms-results/public-results/publications/HIG/SPIN.html> (visited on 08/21/2020).
- [43] Geoffrey Bodwin et al. “Higgs boson decays to quarkonia and the  $H\bar{c}c$  coupling”. In: *Phys. Rev. D* 88 (5 Sept. 2013), p. 053003. DOI: [10.1103/PhysRevD.88.053003](https://doi.org/10.1103/PhysRevD.88.053003). URL: <https://link.aps.org/doi/10.1103/PhysRevD.88.053003>.
- [44] Geoffrey T. Bodwin et al. “Relativistic corrections to Higgs boson decays to quarkonia”. In: *Phys. Rev. D* 90 (11 Dec. 2014), p. 113010. DOI: [10.1103/PhysRevD.90.113010](https://doi.org/10.1103/PhysRevD.90.113010). URL: <https://link.aps.org/doi/10.1103/PhysRevD.90.113010>.

- [45] G. Aad, B. Abbott, et al. “Combined Measurement of the Higgs Boson Mass in  $pp$  Collisions at  $\sqrt{s} = 7$  and 8 TeV with the ATLAS and CMS Experiments”. In: *Phys. Rev. Lett.* 114 (19 May 2015), p. 191803. DOI: 10.1103/PhysRevLett.114.191803. URL: <https://link.aps.org/doi/10.1103/PhysRevLett.114.191803>.
- [46] Cédric Delaunay et al. “Enhanced Higgs boson coupling to charm pairs”. In: *Phys. Rev. D* 89 (3 Feb. 2014), p. 033014. DOI: 10.1103/PhysRevD.89.033014. URL: <https://link.aps.org/doi/10.1103/PhysRevD.89.033014>.
- [47] M. A. PÉREZ, G. TAVARES-VELASCO, and J. J. TOSCANO. “NEW PHYSICS EFFECTS IN RARE Z DECAYS”. In: *International Journal of Modern Physics A* 19.02 (2004), pp. 159–178. DOI: 10.1142/S0217751X04017100.
- [48] Grossman, Yuval and König, Matthias and Neubert, Matthias. “Exclusive radiative decays of W and Z bosons in QCD factorization”. In: *Journal of High Energy Physics* 2015.4 (Apr. 2015), p. 101. ISSN: 1029-8479. DOI: 10.1007/JHEP04(2015)101. URL: [https://doi.org/10.1007/JHEP04\(2015\)101](https://doi.org/10.1007/JHEP04(2015)101).
- [49] Geoffrey T. Bodwin et al. “ $Z$ -boson decays to a vector quarkonium plus a photon”. In: *Phys. Rev. D* 97 (1 Jan. 2018), p. 016009. DOI: 10.1103/PhysRevD.97.016009. URL: <https://link.aps.org/doi/10.1103/PhysRevD.97.016009>.
- [50] Geoffrey T. Bodwin et al. “Addendum: New approach to the resummation of logarithms in Higgs-boson decays to a vector quarkonium plus a photon [Phys. Rev. D 95, 054018 (2017)]”. In: *Phys. Rev. D* 96 (11 Dec. 2017), p. 116014. DOI: 10.1103/PhysRevD.96.116014. URL: <https://link.aps.org/doi/10.1103/PhysRevD.96.116014>.
- [51] Gino Isidori, Aneesh V. Manohar, and Michael Trott. “Probing the nature of the Higgs-like boson via  $h \rightarrow Vf$  decays”. In: *Physics Letters B* 728 (2014), pp. 131–135. ISSN: 0370-2693. DOI: <https://doi.org/10.1016/j.physletb.2013.11.054>. URL: <http://www.sciencedirect.com/science/article/pii/S037026931300960X>.
- [52] Alexander L. Kagan et al. “Exclusive Window onto Higgs Yukawa Couplings”. In: *Phys. Rev. Lett.* 114 (10 Mar. 2015), p. 101802. DOI: 10.1103/PhysRevLett.114.101802. URL: <https://link.aps.org/doi/10.1103/PhysRevLett.114.101802>.
- [53] Dao-Neng Gao. “A note on Higgs decays into Z boson and  $J/\psi(\Upsilon)$ ”. In: *Physics Letters B* 737 (2014), pp. 366–368. ISSN: 0370-2693. DOI: <https://doi.org/10.1016/j.physletb.2014.09.019>. URL: <http://www.sciencedirect.com/science/article/pii/S0370269314006698>.
- [54] A. M. Sirunyan et al. “Observation of Higgs Boson Decay to Bottom Quarks”. In: *Phys. Rev. Lett.* 121 (12 Sept. 2018), p. 121801. DOI: 10.1103/PhysRevLett.121.121801. URL: <https://link.aps.org/doi/10.1103/PhysRevLett.121.121801>.
- [55] G. Apollinari et al. *High-Luminosity Large Hadron Collider (HL-LHC): Preliminary Design Report*. CERN Yellow Reports: Monographs. Geneva: CERN, 2015. DOI: 10.5170/CERN-2015-005. URL: <https://cds.cern.ch/record/2116337>.
- [56] G. Aad et al. “Search for Higgs and Z Boson Decays to  $J/\psi\gamma$  and  $\Upsilon(nS)\gamma$  with the ATLAS Detector”. In: *Phys. Rev. Lett.* 114 (12 Mar. 2015), p. 121801. DOI: 10.1103/PhysRevLett.114.121801. URL: <https://link.aps.org/doi/10.1103/PhysRevLett.114.121801>.

- [57] Morad Aaboud et al. “Searches for exclusive Higgs and  $Z$  boson decays into  $J/\psi\gamma$ ,  $\psi(2S)\gamma$ , and  $\Upsilon(nS)\gamma$  at  $\sqrt{s} = 13$  TeV with the ATLAS detector”. In: *Phys. Lett. B* 786 (2018), pp. 134–155. DOI: 10.1016/j.physletb.2018.09.024. arXiv: 1807.00802 [hep-ex].
- [58] S. Chatrchyan et al. “The CMS experiment at the CERN LHC”. In: *JINST* 3 (2008), S08004. DOI: 10.1088/1748-0221/3/08/S08004.
- [59] Albert M Sirunyan et al. “Search for rare decays of  $Z$  and Higgs bosons to  $J/\psi$  and a photon in proton-proton collisions at  $\sqrt{s} = 13$  TeV”. In: *Eur. Phys. J. C* 79.2 (2019), p. 94. DOI: 10.1140/epjc/s10052-019-6562-5. arXiv: 1810.10056 [hep-ex].
- [60] Albert M Sirunyan et al. “Search for Higgs and  $Z$  boson decays to  $J/\psi$  or  $\Upsilon$  pairs in proton-proton collisions at  $\sqrt{s} = 13$  TeV”. In: *Phys. Lett. B* 797.arXiv:1905.10408. CMS-HIG-18-025-003 (May 2019). All figures and tables can be found at <http://cms-results.web.cern.ch/cms-results/public-results/publications/HIG-18-025> (CMS Public Pages), 134811. 31 p. DOI: 10.1016/j.physletb.2019.134811. URL: <https://cds.cern.ch/record/2676242>.
- [61] Albert M. Sirunyan et al. “Observation of the  $Z \rightarrow \psi\ell^+\ell^-$  decay in pp collisions at  $\sqrt{s} = 13$  TeV”. In: *Phys. Rev. Lett.* 121.arXiv:1806.04213. CMS-BPH-16-001-003 (June 2018). Submitted to *Phys.Rev.Lett.*, 141801. 17 p. DOI: 10.1103/PhysRevLett.121.141801. URL: <https://cds.cern.ch/record/2623687>.
- [62] Albert M Sirunyan et al. “Search for decays of the 125 GeV Higgs boson into a  $Z$  boson and a  $\rho$  or  $\phi$  meson”. In: (July 2020). DOI: 10.3204/PUBDB-2020-02812. arXiv: 2007.05122 [hep-ex].
- [63] “LHC Machine”. In: *JINST* 3 (2008). Ed. by Lyndon Evans and Philip Bryant, S08001. DOI: 10.1088/1748-0221/3/08/S08001.
- [64] Oliver Sim Brüning et al. *LHC Design Report*. CERN Yellow Reports: Monographs. Geneva: CERN, 2004. DOI: 10.5170/CERN-2004-003-V-1. URL: <http://cds.cern.ch/record/782076>.
- [65] Oliver Sim Brüning et al. *LHC Design Report*. CERN Yellow Reports: Monographs. Geneva: CERN, 2004. DOI: 10.5170/CERN-2004-003-V-2. URL: <http://cds.cern.ch/record/815187>.
- [66] Michael Benedikt et al. *LHC Design Report*. CERN Yellow Reports: Monographs. Geneva: CERN, 2004. DOI: 10.5170/CERN-2004-003-V-3. URL: <http://cds.cern.ch/record/823808>.
- [67] Christiane Lefèvre. “The CERN accelerator complex. Complexe des accélérateurs du CERN”. Dec. 2008. URL: <http://cds.cern.ch/record/1260465>.
- [68] S Baird. *Accelerators for pedestrians; rev. version*. Tech. rep. AB-Note-2007-014. CERN-AB-Note-2007-014. PS-OP-Note-95-17-Rev-2. CERN-PS-OP-Note-95-17-Rev-2. Geneva: CERN, Feb. 2007. URL: <http://cds.cern.ch/record/1017689>.
- [69] Jr. Alves A.Augusto et al. “The LHCb Detector at the LHC”. In: *JINST* 3 (2008), S08005. DOI: 10.1088/1748-0221/3/08/S08005.
- [70] K. Aamodt et al. “The ALICE experiment at the CERN LHC”. In: *JINST* 3 (2008), S08002. DOI: 10.1088/1748-0221/3/08/S08002.
- [71] “High-Luminosity Large Hadron Collider (HL-LHC): Technical Design Report V. 0.1”. In: 4/2017 (Nov. 2017). Ed. by G. Apollinari et al. DOI: 10.23731/CYRM-2017-004.

- [72] Tai Sakuma. “Cutaway diagrams of CMS detector”. In: (May 2019). URL: <http://cds.cern.ch/record/2665537>.
- [73] Serguei Chatrchyan et al. “Description and performance of track and primary-vertex reconstruction with the CMS tracker”. In: *JINST* 9 (2014), P10009. DOI: 10.1088/1748-0221/9/10/P10009. arXiv: 1405.6569 [physics.ins-det].
- [74] Vardan Khachatryan et al. “Performance of electron reconstruction and selection with the CMS detector in proton-proton collisions at  $\sqrt{s} = 8$  TeV”. In: *JINST* 10 (2015), P06005. DOI: 10.1088/1748-0221/10/06/P06005. arXiv: 1502.02701 [physics.ins-det].
- [75] Vardan Khachatryan et al. “Performance of photon reconstruction and identification with the CMS detector in proton-proton collisions at  $\sqrt{s} = 8$  TeV”. In: *JINST* 10 (2015), P08010. DOI: 10.1088/1748-0221/10/08/P08010. arXiv: 1502.02702 [physics.ins-det].
- [76] Matteo Cacciari, Gavin P. Salam, and Gregory Soyez. “The anti- $k_t$  jet clustering algorithm”. In: *JHEP* 04 (2008), p. 063. DOI: 10.1088/1126-6708/2008/04/063. arXiv: 0802.1189 [hep-ex].
- [77] Matteo Cacciari, Gavin P. Salam, and Gregory Soyez. “FastJet User Manual”. In: *Eur. Phys. J.* C72 (2012), p. 1896. DOI: 10.1140/epjc/s10052-012-1896-2. arXiv: 1111.6097 [hep-ph].
- [78] *The CMS muon project: Technical Design Report*. Technical Design Report CMS. Geneva: CERN, 1997. URL: <https://cds.cern.ch/record/343814>.
- [79] A M Sirunyan et al. “Performance of the CMS muon detector and muon reconstruction with proton-proton collisions at  $\sqrt{s} = 13$  TeV”. In: *JINST* 13 (2018), P06015. DOI: 10.1088/1748-0221/13/06/P06015. arXiv: 1804.04528 [physics.ins-det].
- [80] Serguei Chatrchyan et al. “The Performance of the CMS Muon Detector in Proton-Proton Collisions at  $\sqrt{s} = 7$  TeV at the LHC”. In: *JINST* 8 (2013), P11002. DOI: 10.1088/1748-0221/8/11/P11002. arXiv: 1306.6905 [physics.ins-det].
- [81] Fabio Sauli. “The gas electron multiplier (GEM): Operating principles and applications. The gas electron multiplier (GEM): Operating principles and applications”. In: *Nucl. Instrum. Methods Phys. Res., A* 805 (2016), 2–24. 23 p. DOI: 10.1016/j.nima.2015.07.060. URL: <http://cds.cern.ch/record/2262884>.
- [82] Daniel Francois Teyssier. *CMS Drift Tubes performance*. Tech. rep. 2016, pp. 709–713.
- [83] Vardan Khachatryan et al. “The CMS trigger system”. In: *JINST* 12 (2017), P01020. DOI: 10.1088/1748-0221/12/01/P01020. arXiv: 1609.02366 [physics.ins-det].
- [84] A. M. Sirunyan et al. “Particle-flow reconstruction and global event description with the CMS detector”. In: *JINST* 12 (2017), P10003. DOI: 10.1088/1748-0221/12/10/P10003. arXiv: 1706.04965 [physics.ins-det].
- [85] Vardan Khachatryan et al. “Jet energy scale and resolution in the CMS experiment in pp collisions at 8 TeV”. In: *JINST* 12 (2017), P02014. DOI: 10.1088/1748-0221/12/02/P02014. arXiv: 1607.03663 [hep-ex].
- [86] Albert M Sirunyan et al. “Performance of missing transverse momentum reconstruction in proton-proton collisions at  $\sqrt{s} = 13$  TeV using the CMS detector”. In: *JINST* 14 (2019), P07004. DOI: 10.1088/1748-0221/14/07/P07004. arXiv: 1903.06078 [hep-ex].

- [87] Jesse Thaler and Ken Van Tilburg. “Identifying Boosted Objects with  $N$ -subjettiness”. In: *JHEP* 03 (2011), p. 015. DOI: 10.1007/JHEP03(2011)015. arXiv: 1011.2268 [hep-ph].
- [88] Mrinal Dasgupta et al. “Towards an understanding of jet substructure”. In: *JHEP* 09 (2013), p. 029. DOI: 10.1007/JHEP09(2013)029. arXiv: 1307.0007 [hep-ph].
- [89] Jonathan M. Butterworth et al. “Jet substructure as a new Higgs search channel at the LHC”. In: *Phys. Rev. Lett.* 100 (2008), p. 242001. DOI: 10.1103/PhysRevLett.100.242001. arXiv: 0802.2470 [hep-ph].
- [90] Andrew J. Larkoski et al. “Soft drop”. In: *JHEP* 05 (2014), p. 146. DOI: 10.1007/JHEP05(2014)146. arXiv: 1402.2657 [hep-ph].
- [91] Albert M Sirunyan et al. “Pileup mitigation at CMS in 13 TeV data”. In: *JINST* 15 (2020), P09018. DOI: 10.1088/1748-0221/15/09/p09018. arXiv: 2003.00503 [hep-ex].
- [92] R. Santonico and R. Cardarelli. “Development of resistive plate counters”. In: *Nuclear Instruments and Methods in Physics Research* 187.2 (1981), pp. 377–380. ISSN: 0167-5087. DOI: [https://doi.org/10.1016/0029-554X\(81\)90363-3](https://doi.org/10.1016/0029-554X(81)90363-3). URL: <http://www.sciencedirect.com/science/article/pii/0029554X81903633>.
- [93] Marcello Abbrescia, Paulo Fonte, and Vladimir Peskov. *Resistive gaseous detectors: designs, performance, and perspectives*. Weinheim: Wiley-VCH, 2018. DOI: 10.1002/9783527698691.
- [94] A Beroual and I Fofana. “The background of air gap discharge theory”. In: *Discharge in Long Air Gaps*. 2053-2563. IOP Publishing, 2016, 2-1 to 2-22. ISBN: 978-0-7503-1236-3. DOI: 10.1088/978-0-7503-1236-3ch2. URL: <http://dx.doi.org/10.1088/978-0-7503-1236-3ch2>.
- [95] Leonard B. Loeb and John M. Meek. “The Mechanism of Spark Discharge in Air at Atmospheric Pressure. I”. In: *Journal of Applied Physics* 11.6 (1940), pp. 438–447. DOI: 10.1063/1.1712792. eprint: <https://doi.org/10.1063/1.1712792>. URL: <https://doi.org/10.1063/1.1712792>.
- [96] Dong Hyun, Kim. “Work on CMS Muon Detector (RPC) during Long Shutdown 1 (LS1) - Point 5, Cessy, CMS cavern”. CMS Collection. May 2015. URL: <https://cds.cern.ch/record/2016815>.
- [97] P. Bernardini et al. “Precise measurements of drift velocities in helium gas mixtures”. In: *Nuclear Instruments and Methods in Physics Research Section A: Accelerators, Spectrometers, Detectors and Associated Equipment* 355.2 (1995), pp. 428–433. ISSN: 0168-9002. DOI: [https://doi.org/10.1016/0168-9002\(94\)01144-3](https://doi.org/10.1016/0168-9002(94)01144-3). URL: <http://www.sciencedirect.com/science/article/pii/0168900294011443>.
- [98] E. Gorini et al. “Drift velocity measurements in C<sub>2</sub>H<sub>2</sub>F<sub>4</sub> based mixtures”. In: *Proceedings of the 4th International Workshop on Resistive Plate Chamber and Related Detectors, in Napoli, Italy, 15-16 October* (1997).
- [99] G. Bressi et al. “AN APPARATUS TO SEARCH FOR FREE NEUTRON ANTI-NEUTRON OSCILLATIONS”. In: *Nucl. Instrum. Meth. A* 261 (1987), pp. 449–461. DOI: 10.1016/0168-9002(87)90353-6.
- [100] H.L. Ge et al. “The production of residual nuclides in Pb irradiated by 400 MeV/u carbon ions”. In: *Nucl. Instrum. Meth. B* 337 (2014), pp. 34–38. DOI: 10.1016/j.nimb.2014.07.024.

- [101] M. Abbrescia et al. "A Horizontal muon telescope implemented with resistive plate chambers". In: *Nucl. Instrum. Meth. A* 336 (1993), pp. 322–329. DOI: 10.1016/0168-9002(93)91116-5.
- [102] L. Antoniazzi et al. "The E771 RPC muon detector". In: *Nucl. Instrum. Meth. A* 315 (1992), pp. 92–94. DOI: 10.1016/0168-9002(92)90686-X.
- [103] A. Di Ciaccio et al. "Muon tracking and hadron punchthrough measurements using resistive plate chambers". In: *Nucl. Instrum. Meth. A* 315 (1992), pp. 102–108. DOI: 10.1016/0168-9002(92)90688-Z.
- [104] R. de Asmundis. "Performances of the RPC trigger system in the L3 experiment". In: *3rd International Workshop on Resistive Plate Chambers and Related Detectors (RPC 95)*. 1995, pp. 139–155.
- [105] D. Boutigny et al. "BaBar technical design report". In: (Mar. 1995).
- [106] Andrea Gelmi. *Longevity studies for the CMS-RPC system*. Tech. rep. CMS-CR-2018-136. Geneva: CERN, July 2018. URL: <https://cds.cern.ch/record/2634505>.
- [107] M.A. Shah et al. "Experiences from the RPC data taking during the CMS RUN-2". In: *15th Workshop on Resistive Plate Chambers and Related Detectors*. May 2020. arXiv: 2005.12532 [physics.ins-det].
- [108] *Public CMS Data Quality Information*. twiki.cern.ch/twiki/bin/view/CMSPublic/DataQuality. Acessado em: 20/02/2018.
- [109] Johannes Gutleber, Steven Murray, and Luciano Orsini. "Towards a homogeneous architecture for high-energy physics data acquisition systems". In: *Computer Physics Communications* 153.2 (2003), pp. 155–163. ISSN: 0010-4655. DOI: [https://doi.org/10.1016/S0010-4655\(03\)00161-9](https://doi.org/10.1016/S0010-4655(03)00161-9). URL: <http://www.sciencedirect.com/science/article/pii/S0010465503001619>.
- [110] *Dojo*. <https://dojotoolkit.org/>. Acessado em: 20/02/2018.
- [111] *Polymer Project*. Acessado em: 20/02/2018.
- [112] M. I. Pedraza-Morales. *RPC upgrade project for CMS Phase II*. 2018. arXiv: 1806.11503 [physics.ins-det].
- [113] Dorothea Pfeiffer et al. "The radiation field in the Gamma Irradiation Facility GIF++ at CERN". In: *Nuclear Instruments and Methods in Physics Research Section A: Accelerators, Spectrometers, Detectors and Associated Equipment* 866 (2017), pp. 91–103. ISSN: 0168-9002. DOI: <https://doi.org/10.1016/j.nima.2017.05.045>. URL: <http://www.sciencedirect.com/science/article/pii/S0168900217306113>.
- [114] A. Augusto Alves Jr. et al. "The LHCb Detector at the LHC". In: *JINST* 3 (2008), S08005. DOI: 10.1088/1748-0221/3/08/S08005.
- [115] Georges Charpak et al. "The Use of Multiwire Proportional Counters to Select and Localize Charged Particles". In: *Nucl. Instrum. Meth.* 62 (1968), pp. 262–268. DOI: 10.1016/0029-554X(68)90371-6.
- [116] *LHCb Muon Group Home Page*. [Online; accessed 1-October-2019]. 2019. URL: <http://lhcb-muon.web.cern.ch/lhcb-muon/>.
- [117] *CAEN Programmable Logic Unit - V2495*. [Online; accessed 1-October-2019]. 2019. URL: <https://www.caen.it/products/v2495/>.

- 2661 [118] *Resistive Plate Chambers are getting dolled up.* <https://cms.cern/news/resistive-plate-chambers-are-getting-dolled>. Acessado em: 20/09/2019.
- 2662
- 2663 [119] C. Binetti et al. “A new Front-End board for RPC detector of CMS”. In: (Sept. 1999).
- 2664 [120] *Flask (web framework)*. [Online; accessed 1-October-2019]. 2019. URL: <https://palletsprojects.com/p/flask/>.
- 2665
- 2666 [121] CMS Collaboration. *CMS Luminosity Measurements for the 2016 Data Taking Period*. CMS Physics Analysis Summary CMS-PAS-LUM-17-001. 2010. URL: <http://cdsweb.cern.ch/record/1279362>.
- 2667
- 2668
- 2669 [122] S. Agostinelli et al. “GEANT4—a simulation toolkit”. In: A506 (2003), pp. 250–303. DOI: 10.1016/S0168-9002(03)01368-8.
- 2670
- 2671 [123] Paolo Nason. “A New method for combining NLO QCD with shower Monte Carlo algorithms”. In: *JHEP* 11 (2004), p. 040. DOI: 10.1088/1126-6708/2004/11/040. arXiv: hep-ph/0409146 [hep-ph].
- 2672
- 2673
- 2674 [124] Stefano Frixione, Paolo Nason, and Carlo Oleari. “Matching NLO QCD computations with Parton Shower simulations: the POWHEG method”. In: *JHEP* 11 (2007), p. 070. DOI: 10.1088/1126-6708/2007/11/070. arXiv: 0709.2092 [hep-ph].
- 2675
- 2676
- 2677 [125] Simone Alioli et al. “A general framework for implementing NLO calculations in shower Monte Carlo programs: the POWHEG BOX”. In: *JHEP* 06 (2010), p. 043. DOI: 10.1007/JHEP06(2010)043. arXiv: 1002.2581 [hep-ph].
- 2678
- 2679
- 2680 [126] Abdelhak Djouadi. “The anatomy of electroweak symmetry breaking: Tome I: The Higgs boson in the Standard Model”. In: *Physics Reports* 457.1 (2008), pp. 1–216. ISSN: 0370-1573. DOI: <https://doi.org/10.1016/j.physrep.2007.10.004>. URL: <http://www.sciencedirect.com/science/article/pii/S0370157307004334>.
- 2681
- 2682
- 2683
- 2684 [127] Torbjörn Sjöstrand, Stephen Mrenna, and Peter Skands. “A brief introduction to PYTHIA 8.1”. In: *Computer Physics Communications* 178.11 (2008), pp. 852–867. ISSN: 0010-4655. DOI: <https://doi.org/10.1016/j.cpc.2008.01.036>. URL: <http://www.sciencedirect.com/science/article/pii/S0010465508000441>.
- 2685
- 2686
- 2687
- 2688 [128] Torbjörn Sjöstrand et al. “An Introduction to PYTHIA 8.2”. In: *Comput. Phys. Commun.* 191 (2015), pp. 159–177. DOI: 10.1016/j.cpc.2015.01.024. arXiv: 1410.3012 [hep-ph].
- 2689
- 2690 [129] Vardan Khachatryan et al. “Event generator tunes obtained from underlying event and multiparton scattering measurements”. In: *Eur. Phys. J. C*76.3 (2016), p. 155. DOI: 10.1140/epjc/s10052-016-3988-x. arXiv: 1512.00815 [hep-ex].
- 2691
- 2692
- 2693 [130] The NNPDF collaboration et al. “Parton distributions for the LHC run II”. In: *Journal of High Energy Physics* 2015.4 (Apr. 2015), p. 40. ISSN: 1029-8479. DOI: 10.1007/JHEP04(2015)040. URL: [https://doi.org/10.1007/JHEP04\(2015\)040](https://doi.org/10.1007/JHEP04(2015)040).
- 2694
- 2695
- 2696 [131] J. Alwall et al. “The automated computation of tree-level and next-to-leading order differential cross sections, and their matching to parton shower simulations”. In: *Journal of High Energy Physics* 2014.7 (July 2014), p. 79. ISSN: 1029-8479. DOI: 10.1007/JHEP07(2014)079. URL: [https://doi.org/10.1007/JHEP07\(2014\)079](https://doi.org/10.1007/JHEP07(2014)079).
- 2697
- 2698
- 2699
- 2700 [132] Ali Abbasabadi et al. “Radiative Higgs boson decays  $H \rightarrow f\bar{f}\gamma$ ”. In: *Phys. Rev. D* 55 (9 May 1997), pp. 5647–5656. DOI: 10.1103/PhysRevD.55.5647. URL: <https://link.aps.org/doi/10.1103/PhysRevD.55.5647>.
- 2701
- 2702

- [133] D. de Florian et al. *Handbook of LHC Higgs Cross Sections: 4. Deciphering the Nature of the Higgs Sector*. CERN Yellow Reports: Monographs. 869 pages, 295 figures, 248 tables and 1645 citations. Working Group web page: <https://twiki.cern.ch/twiki/bin/view/LHCPhysics/LHCHXSWG>. Oct. 2016. DOI: 10.23731/CYRM-2017-002. URL: <https://cds.cern.ch/record/2227475>.
- [134] Ye Li and Frank Petriello. “Combining QCD and electroweak corrections to dilepton production in the framework of the FEWZ simulation code”. In: *Phys. Rev. D* 86 (9 Nov. 2012), p. 094034. DOI: 10.1103/PhysRevD.86.094034. URL: <https://link.aps.org/doi/10.1103/PhysRevD.86.094034>.
- [135] John M. Campbell and R.K. Ellis. “MCFM for the Tevatron and the LHC”. In: *Nuclear Physics B - Proceedings Supplements* 205-206 (2010). Loops and Legs in Quantum Field Theory, pp. 10–15. ISSN: 0920-5632. DOI: <https://doi.org/10.1016/j.nuclphysbps.2010.08.011>. URL: <http://www.sciencedirect.com/science/article/pii/S0920563210001945>.
- [136] Vardan Khachatryan et al. “Search for a Higgs boson decaying into  $\gamma^*\gamma \rightarrow \ell\ell\gamma$  with low dilepton mass in pp collisions at  $\sqrt{s} = 8$  TeV”. In: *Phys. Lett. B* 753 (2016), pp. 341–362. DOI: 10.1016/j.physletb.2015.12.039. arXiv: 1507.03031 [hep-ex].
- [137] N. Brambilla, S. Eidelman, B.K. Heltsley, et al. “Heavy quarkonium: progress, puzzles, and opportunities”. In: *The European Physical Journal C* 71.2 (Feb. 2011), p. 1534. ISSN: 1434-6052. DOI: 10.1140/epjc/s10052-010-1534-9. URL: <https://doi.org/10.1140/epjc/s10052-010-1534-9>.
- [138] Sandro Palestini. “Angular distribution and rotations of frame in vector meson decays into lepton pairs”. In: *Phys. Rev. D* 83 (3 Feb. 2011), p. 031503. DOI: 10.1103/PhysRevD.83.031503. URL: <https://link.aps.org/doi/10.1103/PhysRevD.83.031503>.
- [139] A.M. Sirunyan et al. “Particle-flow reconstruction and global event description with the CMS detector”. In: *Journal of Instrumentation* 12.10 (2017), P10003. URL: <http://stacks.iop.org/1748-0221/12/i=10/a=P10003>.
- [140] Albert M Sirunyan et al. “Measurements of properties of the Higgs boson decaying into the four-lepton final state in pp collisions at  $\sqrt{s} = 13$  TeV”. In: *JHEP* 11 (2017), p. 047. DOI: 10.1007/JHEP11(2017)047. arXiv: 1706.09936 [hep-ex].
- [141] V. Khachatryan et al. “Observation of the diphoton decay of the Higgs boson and measurement of its properties”. In: *The European Physical Journal C* 74.10 (Oct. 2014), p. 3076. ISSN: 1434-6052. DOI: 10.1140/epjc/s10052-014-3076-z. URL: <https://doi.org/10.1140/epjc/s10052-014-3076-z>.
- [142] S. Bernstein. “Démonstration du théorème de Weierstrass fondée sur le calcul des probabilités”. In: *Commun. Soc. Math. Kharkov* 13.1–2 (1912).
- [143] John Erthal Gaiser. “Charmonium Spectroscopy From Radiative Decays of the  $J/\psi$  and  $\psi'$ ”. PhD thesis. SLAC, 1982. URL: <http://www-public.slac.stanford.edu/sciDoc/docMeta.aspx?slacPubNumber=slac-r-255.html>.
- [144] P. D. Dauncey et al. “Handling uncertainties in background shapes: the discrete profiling method”. In: *JINST* 10.04 (2015), P04015. DOI: 10.1088/1748-0221/10/04/P04015. arXiv: 1408.6865 [physics.data-an].

- [145] S. S. Wilks. "The Large-Sample Distribution of the Likelihood Ratio for Testing Composite Hypotheses". In: *Ann. Math. Statist.* 9.1 (Mar. 1938), pp. 60–62. DOI: 10.1214/aoms/1177732360. URL: <https://doi.org/10.1214/aoms/1177732360>.
- [146] Higgs to Gamma Gamma Working Group. *Further measurement of  $H \rightarrow \gamma\gamma$  at  $\sqrt{s} = 13$  TeV*. CMS Note 2016/209. CERN, 2016. URL: [http://cms.cern.ch/iCMS/jsp/db\\_notes/noteInfo.jsp?cmsnoteid=CMSPAS-HIG-16-020](http://cms.cern.ch/iCMS/jsp/db_notes/noteInfo.jsp?cmsnoteid=CMSPAS-HIG-16-020).
- [147] *Updated measurements of Higgs boson production in the diphoton decay channel at  $\sqrt{s} = 13$  TeV in pp collisions at CMS*. CMS Physics Analysis Summary CMS-PAS-HIG-16-020. Geneva: CERN, 2016. URL: <http://cds.cern.ch/record/2205275>.
- [148] Jon Butterworth et al. "PDF4LHC recommendations for LHC Run II". In: *J. Phys.* G43 (2016), p. 023001. DOI: 10.1088/0954-3899/43/2/023001. arXiv: 1510.03865 [hep-ph].
- [149] A. D. Martin et al. "Parton distributions for the LHC". In: *Eur. Phys. J.* C63 (2009), pp. 189–285. DOI: 10.1140/epjc/s10052-009-1072-5. arXiv: 0901.0002 [hep-ph].
- [150] Hung-Liang Lai et al. "New parton distributions for collider physics". In: *Phys. Rev.* D82 (2010), p. 074024. DOI: 10.1103/PhysRevD.82.074024. arXiv: 1007.2241 [hep-ph].
- [151] Sergey Alekhin et al. "The PDF4LHC Working Group Interim Report". In: (2011). arXiv: 1101.0536 [hep-ph].
- [152] Michiel Botje et al. "The PDF4LHC Working Group Interim Recommendations". In: (2011). arXiv: 1101.0538 [hep-ph].
- [153] Richard D. Ball et al. "Impact of Heavy Quark Masses on Parton Distributions and LHC Phenomenology". In: *Nucl. Phys.* B849 (2011), pp. 296–363. DOI: 10.1016/j.nuclphysb.2011.03.021. arXiv: 1101.1300 [hep-ph].
- [154] Giampiero Passarino. "Higgs Boson Production and Decay: Dalitz Sector". In: *Phys. Lett.* B727 (2013), pp. 424–431. DOI: 10.1016/j.physletb.2013.10.052. arXiv: 1308.0422 [hep-ph].
- [155] A.M. Sirunyan et al. "Performance of the CMS muon detector and muon reconstruction with proton-proton collisions at  $\sqrt{s}=13$  TeV". In: *Journal of Instrumentation* 13.06 (June 2018), P06015–P06015. DOI: 10.1088/1748-0221/13/06/p06015. URL: <https://doi.org/10.1088/1748-0221/13/06/p06015>.
- [156] Vardan Khachatryan et al. "Performance of photon reconstruction and identification with the CMS detector in proton-proton collisions at  $\sqrt{s} = 8$  TeV". In: *JINST* 10.CMS-EGM-14-001. CMS-EGM-14-001. CERN-PH-EP-2015-006 (Feb. 2015). Comments: Submitted to JINST, P08010. 59 p. DOI: 10.1088/1748-0221/10/08/P08010. URL: <http://cds.cern.ch/record/1988093>.
- [157] A L Read. "Presentation of search results: the CL<sub>st</sub> technique". In: *Journal of Physics G: Nuclear and Particle Physics* 28.10 (Sept. 2002), pp. 2693–2704. DOI: 10.1088/0954-3899/28/10/313. URL: <https://doi.org/10.1088/0954-3899/28/10/313>.
- [158] J. Neyman and E. S. Pearson. "On the Problem of the Most Efficient Tests of Statistical Hypotheses". In: *Philosophical Transactions of the Royal Society of London. Series A, Containing Papers of a Mathematical or Physical Character* 231 (1933), pp. 289–337. ISSN: 02643952. URL: <http://www.jstor.org/stable/91247>.

- 2784 [159] Glen Cowan et al. “Asymptotic formulae for likelihood-based tests of new physics”. In: *The*  
2785 *European Physical Journal C* 71.2 (Feb. 2011), p. 1554. ISSN: 1434-6052. DOI: 10.1140/  
2786 [epjc/s10052-011-1554-0](https://doi.org/10.1140/epjc/s10052-011-1554-0). URL: <https://doi.org/10.1140/epjc/s10052-011-1554-0>.
- 2787 [160] *Procedure for the LHC Higgs boson search combination in Summer 2011*. Tech. rep. CMS-  
2788 NOTE-2011-005. ATL-PHYS-PUB-2011-11. Geneva: CERN, Aug. 2011. URL: <https://cds.cern.ch/record/1379837>.
- 2790 [161] David H. Annis. “Kendall’s Advanced Theory of Statistics, Vol. 1: Distribution Theory (6th  
2791 ed.). Alan Stuart and J. Keith Ord; Kendall’s Advanced Theory of Statistics, Vol. 2A: Clas-  
2792 sical Inference and the Linear Model (6th ed.). Alan Stuart and J. Keith Ord, and Steven  
2793 F. Arnold”. In: *Journal of the American Statistical Association* 101 (2006), pp. 1721–1721.  
2794 URL: <https://EconPapers.repec.org/RePEc:bes:jnlasa:v:101:y:2006:p:1721-1721>.
- 2795 [162] *Procedure for the LHC Higgs boson search combination in Summer 2011*. Tech. rep. CMS-  
2796 NOTE-2011-005. ATL-PHYS-PUB-2011-11. Geneva: CERN, Aug. 2011. URL: <https://cds.cern.ch/record/1379837>.